

DTRA-TR-10-66

DEFENSE THREAT REDUCTION AGENCY Scientific & Technical Review Information

1 Oct 10-01

PA CONTROL NUMBER:

PA 10-555 50010

SUSPENSE:

Oct 15, 2010

PM / PHONE / EMAIL:

Michael Robinson / michael.robinson@dtra.mil

DATE:

9/30/2010

BRANCH CHIEF / PHONE / EMAIL:

DATE:

DIVISION CHIEF / PHONE:

Michael Robinson 767-3706

DATE:

9/30/2010

DIRECTORATE / DIRECTOR / PHONE:

RD/BA Joan Pierre / 767-3510

DATE:

9/30/2010

ENTERPRISE / OFFICE / PHONE:

RD / Eugene Stokes / 767-2826

DATE:

10/5/10

PUBLIC AFFAIRS:

Richard M. Cole (Chief, PA) J. Kearnes

DATE:

10/7/10

1. TTLE: FINAL REPORT

CONTRACT NUMBER


HDTRA1-07-1-0010

ORIGINATOR NJ INSTITUTE OF TECHNOLOGY

2. TYPE OF MATERIAL: ☐ PAPER ☐ PRESENTATION ☐ ABSTRACT ☒ OTHER FINAL GRANT REPORT3. OVERALL CLASSIFICATION: ☐ CONTRACTOR ☐ PROJECT MANAGER

UNCLASSIFIED

A. Review authority for unclassified material is the responsibility of the PM. Your signature indicates the material has undergone technical and security review.


4 OCT 2010

B. Warning Notices/Caveats:

☐ RD☐ FRD☐ CNWDI☐ NATO RELEASABLE☐ SUBJECT TO EXPORT CONTROL LAWS

C. Distribution Statement:

☒

A. Approved for public release; distribution is unlimited (unclassified papers only).

☐

B. Distribution authorized to U.S. Government agencies only; (check the following):

☐ Contractor Performance Evaluation
☐ Foreign Government Information
☐ Administrative or Operational Use
☐ Specific Authority
☐ Premature Dissemination

☐ Proprietary Information
☐ Test and Evaluation
☐ Software Documentation
☐ Critical Technology

RD-BA OPSEC Review
Keith A. Simmers
KEITH A. SIMMERS
MAJ, USA
23 SEP 10

**CLEARED
for public release**

☐

C. Distribution authorized to U.S. Government agencies and their contractors; (check the following):

☐ Critical Technology
☐ Specific Authority
☐ Administrative or Operational Use

☐ Software Documentation
☐ Foreign Government Information

OCT - 7 2010

☐

D. Distribution authorized to the Department of Defense and U.S. DoD Contractors only; (check the following):

☐ Foreign Government Information
☐ Critical Technology
☐ Administrative or Operational Use

☐ Software Documentation
☐ Foreign Government Information

PA Ops
Defense Threat Reduction Agency

☐

E. Distribution authorized to DoD Components only; (check the following):

☐ Administrative or Operational Use
☐ Premature Dissemination
☐ Critical Technology
☐ Foreign Government Information
☐ Direct Military Support

☐ Software Documentation
☐ Specific Authority
☐ Proprietary Information
☐ Test and Evaluation
☐ Contractor Performance Evaluation
☐

F. Further dissemination only as directed.

☐

X. Distribution authorized to U.S. Government agencies and private individuals or enterprises eligible to obtain export-controlled technical data in accordance with DoD Directive 5230.25 (unclassified papers only).

4. MATERIAL TO BE: ☐ Presented ☒ Published Date Required: 15 Oct 2010

Name of Conference or Journal: DTIC, NTIS

Remarks:

OPSEC REVIEW/DATE

Approved 10/7/2010

REPORT DOCUMENTATION PAGE					<i>Form Approved</i> <i>OMB No. 0704-0188</i>	
<small>The public reporting burden for this collection of information is estimated to average 1 hour per response, including the time for reviewing instructions, searching existing data sources, gathering and maintaining the data needed, and completing and reviewing the collection of information. Send comments regarding this burden estimate or any other aspect of this collection of information, including suggestions for reducing the burden, to the Department of Defense, Executive Services and Communications Directorate (0704-0188). Respondents should be aware that notwithstanding any other provision of law, no person shall be subject to any penalty for failing to comply with a collection of information if it does not display a currently valid OMB control number.</small>						
PLEASE DO NOT RETURN YOUR FORM TO THE ABOVE ORGANIZATION.						
1. REPORT DATE (DD-MM-YYYY) 01/10/2010		2. REPORT TYPE Final Technical Report			3. DATES COVERED (From - To) October 2006 - August 2010	
4. TITLE AND SUBTITLE Mechanistic Models for Ignition and Combustion of Metallic Powder in Different Environments					5a. CONTRACT NUMBER	
					5b. GRANT NUMBER HDTRA1-07-1-0010	
					5c. PROGRAM ELEMENT NUMBER	
6. AUTHOR(S) E.L. Dreiziin					5d. PROJECT NUMBER	
					5e. TASK NUMBER	
					5f. WORK UNIT NUMBER	
7. PERFORMING ORGANIZATION NAME(S) AND ADDRESS(ES) Otto H. York Department of Chemical Biological and Pharmaceutical Engineering New Jersey Institute of Technology, Newark, NJ 07102					8. PERFORMING ORGANIZATION REPORT NUMBER	
9. SPONSORING/MONITORING AGENCY NAME(S) AND ADDRESS(ES) DTRA-R&D Enterprise 8725 John J. Kingman Rd Ft. Belvoir, VA 22060					10. SPONSOR/MONITOR'S ACRONYM(S) DTRA	
					11. SPONSOR/MONITOR'S REPORT NUMBER(S)	
12. DISTRIBUTION/AVAILABILITY STATEMENT						
13. SUPPLEMENTARY NOTES						
14. ABSTRACT						
15. SUBJECT TERMS						
16. SECURITY CLASSIFICATION OF:			17. LIMITATION OF ABSTRACT UU	18. NUMBER OF PAGES 105	19a. NAME OF RESPONSIBLE PERSON E.L. Dreizin	
a. REPORT Unclassified	b. ABSTRACT Unclassified	c. THIS PAGE Unclassified			19b. TELEPHONE NUMBER (Include area code) (973) 596-5751	

Reset

Mechanistic Models for Ignition and Combustion of Metallic Powders in Different Environments

Basic Research Initiative grant project

Supported by Defense Threat Reduction Agency
Grant # HDRTA1-07-1-0010

Final report

Period of Performance: October 1, 2006 – August 14, 2010

Prepared by Professor E.L. Dreizin
Principal Investigator
Otto H. York Department of Chemical, Biological and Pharmaceutical Engineering
New Jersey Institute of Technology
Newark NJ 07102

September 17, 2010

Table of Contents

ABSTRACT	4
1. BACKGROUND: DESCRIPTIONS OF ALUMINUM IGNITION AND COMBUSTION PROCESSES.....	5
REFERENCES.....	6
2. OBJECTIVES AND APPROACH.....	7
3. OXIDATION OF ALUMINUM PARTICLES IN THE PRESENCE OF WATER	7
3.1. INTRODUCTION	7
3.2. EXPERIMENTAL	8
3.3. RESULTS	9
3.4. DISCUSSION	15
3.5. CONCLUSIONS.....	17
3.6. REFERENCES.....	18
4. ALUMINUM POWDER OXIDATION IN CO₂ AND MIXED CO₂/O₂ ENVIRONMENTS ...	19
4.1. INTRODUCTION	19
4.2. EXPERIMENTAL	19
4.3. EXPERIMENTAL RESULTS	20
4.4. OXIDATION KINETICS.....	24
4.5. DISCUSSION	30
4.6. CONCLUSIONS.....	30
4.7. REFERENCES.....	31
5. OXIDATION OF ALUMINUM PARTICLES IN MIXED CO₂/H₂O ATMOSPHERES	32
5.1. INTRODUCTION	32
5.2. EXPERIMENTAL	32
5.3. RESULTS	34
5.4. REACTION KINETICS	36
5.5. DISCUSSION	41
5.6. CONCLUSIONS.....	42
5.7. REFERENCES.....	42
6. HEATING AND IGNITION OF METALLIC PARTICLES BY A CO₂ LASER.....	43
6.1. INTRODUCTION	43
6.2. TECHNICAL APPROACH.....	44
6.3. EXPERIMENTAL	45
6.4. HEAT TRANSFER MODEL	47
6.5. RESULTS AND DISCUSSION	52
6.6. CONCLUSIONS.....	55
6.7. REFERENCES.....	56
7. ALUMINUM PARTICLE IGNITION IN DIFFERENT OXIDIZING ENVIRONMENTS	57
7.1. INTRODUCTION	57
7.2. EXPERIMENTAL	58
7.3. SIMULATION OF GAS MIXING FOR IGNITION EXPERIMENTS.....	61
7.4. EXPERIMENTAL DATA PROCESSING.....	64
7.5. RESULTS AND DISCUSSION	67
7.6. ARRHENIUS MODEL PARAMETER FOR AL IGNITION IN DIFFERENT ENVIRONMENTS	73
7.7. CONCLUSIONS.....	75
7.8. REFERENCES.....	76
8. OXIDATION OF ALUMINUM POWDERS AT HIGH HEATING RATES.....	77

8.1. INTRODUCTION	77
8.2. EXPERIMENTAL	77
8.3. RESULTS AND DISCUSSION	78
8.4. REFINING AND VALIDATION OF THE OXIDATION MODEL	85
8.5. CONCLUSIONS.....	92
8.6. REFERENCES.....	92
9. ON POSSIBILITY OF VAPOR-PHASE COMBUSTION FOR FINE ALUMINUM PARTICLES	93
9.1. INTRODUCTION	93
9.2. A SIMPLIFIED HEAT TRANSFER MODEL FOR AN AL PARTICLE BURNING IN THE VAPOR PHASE	94
9.3. MAXIMUM VAPOR PHASE FLAME DIAMETER FOR AL PARTICLES BURNING IN DIFFERENT ENVIRONMENTS	96
9.4. DISCUSSION	98
9.5. CONCLUSIONS.....	100
9.6. REFERENCES.....	100
10. COMBUSTION TIMES AND EMISSION PROFILES OF MICRON-SIZED ALUMINUM PARTICLES BURNING IN DIFFERENT ENVIRONMENTS	101
10.1. INTRODUCTION	101
10.2. EXPERIMENTAL	103
10.3. RESULTS	106
10.4. DISCUSSION	115
10.5. CONCLUSIONS.....	118
10.6. REFERENCES.....	119
11. CHARACTERISTICS OF ALUMINUM COMBUSTION OBTAINED FROM CONSTANT VOLUME EXPLOSION EXPERIMENTS	120
11.1. INTRODUCTION	120
11.2. EXPERIMENTAL	120
11.3. THERMODYNAMIC EQUILIBRIUM CALCULATIONS	121
11.4. EXPERIMENTAL RESULTS	122
11.5. DISCUSSION	128
11.6. CONCLUSIONS.....	135
11.7. REFERENCES.....	135

ABSTRACT

This effort addressed ignition and combustion of aluminum particles in different environments. The focus was on identifying quantifiable characteristics of aluminum ignition and combustion that are useful for development and validation of the respective reaction models.

It was shown that aluminum ignition in any oxidizing environment is governed by changes in the diffusion resistance of the protective surface layer of alumina and that these changes occur rapidly when the alumina film undergoes polymorphic phase changes. It was also shown that presence of water as an oxidizer dramatically affects alumina properties, in particular resulting in the disruption of the film continuity upon aluminum melting. It was further shown that the effect is amplified in mixed H_2O/CO_2 environments. Finally, the model of aluminum oxidation is expanded and validated in high-heating rate thermo-analytical measurements. This model is directly applicable for describing thermally activated ignition of aluminum powders.

A new experimental technique is developed to investigate combustion dynamics of individual metal particles in the size range of 2 – 15 μm . The technique is applied to study combustion of Al in different oxidizers. It is observed that stages reported earlier to be distinguished in combustion of coarse Al particles can also be observed for fine particles. A transition from the vapor phase to surface combustion regime was observed when the Al particle sizes decreased. The change in the combustion regime was explained by analyzing the heat transfer for a single Al particle combusting in room temperature air, and accounting for a transition heat transfer regime in vicinity of the micron-sized particles with dimensions comparable to the mean free path of the gas molecules. Burn times for Al particles were measured as a function of particle size for different oxidizers.

1. Background: descriptions of aluminum ignition and combustion processes

Aluminum and other metal powders are widely used as fuels or fuel additives in explosives, propellants, and pyrotechnics. However, metal ignition processes crucial for accurate modeling of metallized energetic materials remain poorly understood. For example, aluminum, the most common reactive metal additive, is known to ignite after the integrity of a protective Al_2O_3 layer is disrupted. A quantitative description of the processes leading to such a disruption is lacking. In most practical models, it is simply assumed that the oxide coating stops being protective at a fixed temperature close to the melting point of Al_2O_3 . Recent research involving ignition of powders with different size distributions and, in particular, nanopowders, showed that the value of the fixed ignition temperature must be adjusted as a strong function of particle size [1]. One hypothesis posed that the disruption of integrity of the Al_2O_3 layer occurs as a result of thermal expansion mismatch between Al and Al_2O_3 , and led to the suggestion that ignition should be triggered by aluminum melting, when this mismatch is at its maximum [2, 3]. However, this hypothesis did not explain many reports of much higher ignition temperatures measured for micron-sized Al powders and somewhat lower than melting point ignition temperatures for nano-sized Al powders. Furthermore, multiple thermal analysis studies with micron-sized and nano-sized Al powders [4 – 6] showed no accelerated Al oxidation during melting, contradicting the expected higher oxidation rate that would be caused a non-continuous Al_2O_3 layer.

A new model of heterogeneous oxidation of Al powder leading to ignition was recently developed and quantified for reaction of aluminum in environments containing oxygen as the only oxidizer [6 – 8]. This model considers the oxidation process that is limited by the rates of diffusion of aluminum and oxygen ions through the growing layer of aluminum oxide. Most importantly, this model considers the changing properties of the aluminum oxide layer at elevated temperatures, including polymorphic phase transitions accompanied by substantial changes in the oxide density. The model predicts a broad range of ignition temperatures for aluminum powders of different sizes, consistent with many available experimental reports. The quantitative description is currently available for ignition of aluminum particles in air [7] but not in the many practically interesting environments, in which H_2O and CO/CO_2 molecules serve as primary oxidizers.

Aluminum combustion has been studied broader than ignition and one critical parameter of aluminum combustion, universally important for all applications and identified in many studies is the particle burn time, τ_b , as a function of the particle diameter, D . For practical purposes the burn time is commonly expressed as a power law $\tau_b \sim D^n$, with the exponent n and pre-exponent factor depending on the oxidizing environment, temperature, and pressure, e.g., [9 – 12]. Various D^n type trends were reported by different authors based on a diverse set of experiments. Generally, laboratory experiments in well-characterized environments reported in the literature can be broadly divided into two groups: experiments using individual metal particles, e.g., [13 – 18], and experiments employing aerosolized powders or clouds, e.g., [11, 19 – 23]. For individual particles, the measurements of combustion times are often direct, while indirect methods and data analyses are used to extract the information on particle burn times or burn rates

from the cloud combustion experiments. It is also worth noting that single metal particle combustion experiments in general, and direct measurements of combustion times for individual aluminum droplets in particular, were restricted to relatively large particles, with sizes 50 μm or greater. However, most practical applications deal with finer aluminum powders with particle sizes on the order of, or finer than, 20 μm . It is also interesting that in many experimental configurations, aluminum particles burn in combustion products of hydrocarbon fuels. In such cases, the oxidizers are mixtures of CO_2 , H_2O , and O_2 in various proportions. While this situation imitates some practical applications, the specific oxidizer mixtures produced in laboratory burners and in practical energetic formulations differ from one another substantially. Laboratory experiments with mixed oxidizers are also not particularly useful for extracting the information about efficiency of individual oxidizing species, which is required to model the practical configurations. The information on aluminum combustion in CO_2 and H_2O is very limited [13, 23, 24], with most data coming from experiments in mixed oxidizers, where the effects of different oxidizers are somewhat difficult to uncouple.

References

1. Trunov, M.A., Schoenitz, M., and Dreizin, E.L. *Propellants Explosives and Pyrotechnics*, V. 40, No 1, pp. 36-43 (2005)
2. V.I. Rozenband, N.I. Vaganova, *Combustion and Flame*, 88 (1), 113-118 (1992)
3. V.I. Rozenband *Combustion and Flame*, 137, 366-375 (2004)
4. C. Johnson, T. Parr, D. Hanson-Parr, R. Hollins, S. Fallis, K. Higa, Proc. 37-th JANNAF Combust. Subcom. Meeting (November 2000), 2000, pp. 539-55
5. Bulian, C.J., Kerr, T.T., Puszynski, J.A. *Proceedings of the Thirty-First International Pyrotechnics Seminar*, F.J. Schelling - Editor, IPSUSA Seminars, Inc., Fort Collins, CO, pp. 327-338 (2004)
6. M.A. Trunov, M. Schoenitz, E.L. Dreizin *Combustion and Flame* V. 140 No 4, pp. 310-318 (2005)
7. Trunov, M.A., Schoenitz, M., Dreizin, E.L. *Combustion Theory and Modeling*, 10 (4) pp. 603-624 (2006)
8. Trunov, M.A., Umbrajkar, S.M., Schoenitz, M. Mang, J.T., Dreizin, E.L. *Journal of Physical Chemistry B*, 110(26), pp. 13094-13099 (2006)
9. M.W. Beckstead, *Combustion Explosions and Shockwaves* 41 (2005) 533-546.
10. P. Lynch, H. Krier, N. Glumac, *Proceedings of the Combustion Institute*. 32 (2009) 1887-1893.
11. Y.L. Shoshin, E.L. Dreizin, *Combustion and Flame* 145 (2006) 714-722.
12. Y. Huang, G.A. Risha, V. Yang, R.A. Yetter, *Combustion and Flame* 156 (2009) 5-13.
13. P. Bucher, R.A. Yetter, F.L. Dryer, E.P. Vicenzi, T.P. Parr, D.M. Hanson-Parr *Combustion and Flame* 117 (1999) 351-361.
14. S.E. Olsen, M.W. Beckstead, *Journal of Propulsion and Power* 12 (1996) 662-671.
15. E.L. Dreizin, *Combustion and Flame* 117 (1999) 841-850.
16. E.L. Dreizin, *Combustion and Flame*, 116 (1999) 323-333.

17. E.L. Dreizin, *Combustion and Flame*, 105 (1996) 541-556.
18. Y. Huang, G.A. Risha, V. Yang, R.A. Yetter, *Proceedings of the Combustion Institute*. 31 II (2007) 2001-2009.
19. N.I. Poletaev, A.V. Florko, *Combustion Explosions and Shockwaves* 44 (2008) 437-443.
20. S. Goroshin, M. Kolbe, J.H.S. Lee, *Proceedings of the Combustion Institute*. 28 (2000) 2811-2817.
21. S. Goroshin, J. Mamen, A. Higgins, T. Bazyn, N. Glumac, H. Krier, *Proceedings of the Combustion Institute*. 31 II (2007) 2011-2019.
22. Y. Shoshin, E. Dreizin, *Combustion and Flame*, 133 (2003) 275-287.
23. S. Rossi, E.L. Dreizin, C.K. Law, *Combustion Science and Technology* 164 (2001) 209 – 237.
24. J. Servaites, H. Krier, J.C. Melcher, R.L. Burton, *Combustion and Flame* 125 (2001), 1040-1054.

2. Objectives and approach

The main objective of this effort was to develop adequate and useful descriptions of metal particle ignition and combustion in practically interesting environments. Specific objectives were:

1. Characterize kinetics of aluminum oxidation in $\text{H}_2\text{O}/\text{O}_2/\text{CO}_2$ gases that are available as oxidizing species in the combustion products of common high explosives.
2. Develop a quantitative ignition model for aluminum particles in varied environments.
3. Characterize combustion dynamics and burn rates of single aluminum particles and aerosolized aluminum powders in different environments.

The approach of this effort was based on detailed experimental characterization of Al ignition and combustion processes. The main tool in characterization of oxidation reactions leading to ignition was thermal analysis. Thermo-analytical experiments and respective ignition descriptions were validated in experiments exploiting rapid heating of Al particles in a laser beam. The laser ignition experiment was further modified to characterize the rates of particle combustion as a function of the particle size. Furthermore, Al combustion was studied for aerosolized clouds, in a constant volume explosion apparatus. All experiments emphasized the effects of oxidizing environments and were focused on generating quantitative descriptions of the ignition and combustion processes.

3. Oxidation of Aluminum Particles in the Presence of Water

3.1. Introduction

Ignition and combustion of aluminum particles continues to be studied extensively [1 - 4]. Different mechanisms, based on the disruption of a protective Al_2O_3 layer on aluminum particles, have been proposed for ignition of aluminum powder [5 - 12].

Recent research investigated related processes of aluminum powder oxidation in dry air [5 - 7]. However, practical applications involve ignition and combustion of aluminum particles in mixed environments involving CO₂ and H₂O species as primary oxidizers [13 - 15]. A description of Al ignition behavior in water containing atmospheres requires reliable information regarding the reaction rates involved. This necessitates a quantitative mechanistic model of the processes involved in aluminum powder oxidation in H₂O. Specifically, similarities with and differences from the previously proposed model of aluminum powder oxidation in dry oxygen developed based on thermal analysis experiments [5] need to be identified. In dry oxygen, the rate of aluminum oxidation was determined to be governed by the diffusion of oxygen, and to some extent, diffusion of aluminum, through the surface oxide layer, as well as by polymorphic phase changes in the oxide layer. No connection was established to the melting of aluminum metal.

The present study aims to provide the experimental data needed to develop a quantitative oxidation (and eventually ignition) model for aluminum powder in atmospheres that contain steam. Experimental results are presented, and the implications for an oxidation model are discussed.

3.2. Experimental

Aluminum powder (Alfa Aesar, 3-4.5 μm nominal size, 97.5 % pure) was heated in a Netzsch STA409PG thermal analyzer using a thermogravimetric sample carrier with a 17 mm diameter flat corundum plate to hold the sample. The furnace of the STA409PG is connected to a pressurized boiler, which is held at 180 °C, and the connecting lines are also all heated to temperatures above 150 °C to prevent condensation. The gas flow pattern of the STA409PG was modified from its default configuration to increase homogeneity of the purge gas. The oxidizers, steam and oxygen, were fed into the furnace from the same port, allowing them to mix before they entered the sample location while in the original setup, different gases are fed into the furnace at opposite ends, leading to potential mixing problems. Initial experiments established that above the melting point, the aluminum particles tended to coalesce into droplets with sizes in the 0.5 – 1 mm range. To mitigate the associated drastic loss in surface area, the powders in subsequent measurements were ultrasonically mixed with 150-nm α -alumina powder (Inframat Advanced Materials, 99.8 % pure) to contain approximately 25 wt-% free Al. For the blend of alumina and aluminum powders, coalescence was not observed on heating.

In all experiments, argon, steam, and oxygen were present in varying proportions. Argon is introduced into the furnace in two locations. The first, and invariant gas flow of 20 mL/min serves to protect the thermobalance from any condensation. It enters the furnace from below. Due to the furnace geometry, it has a negligible contribution to the atmosphere that the sample is exposed to. The second argon flow was used as a carrier gas for steam, entering the furnace from above; its flow rate can be widely varied. The steam flow rate could also be varied over a wide range. In experiments where oxygen was required, it replaced part of the argon carrier gas flow.

Initial experiments established the salient differences between oxidation in oxygen and in steam, using respectively similar oxidizer concentrations. Several experiments in steam/argon mixtures with fixed concentration were performed at heating

rates of 1, 5, 10, and 20 K/min. Finally, two experimental series were conducted where the amounts of the oxidizers steam and oxygen were systematically varied. In the first series, the argon carrier gas flow was kept constant, while steam and oxygen were balanced against each other. In the second series, steam was kept constant, while argon and oxygen were balanced.

The behavior in steam was expected to be comparable to that in dry oxygen, at least to some extent. Therefore, in analogy to previously published work [5, 6], partially oxidized samples that were heated to intermediate temperatures were recovered for further analysis by X-ray diffraction. The diffraction patterns were collected on a Philips X'pert MRD diffractometer operated at 45 kV and 40 mA. Samples were held on a zero-background quartz plate. The specific samples recovered for XRD analysis were not blended with α -alumina, in order to avoid introducing a potential oxidation product. Quantitative x-ray analysis was not attempted, therefore the loss of surface area due to coalescence was not a concern.

3.3. Results

Figure 3.1 shows thermogravimetric (TG) curves illustrating the differences between oxidation in steam and oxygen. Note that due to the nature of the steam generation, there is more experimental noise in the data than expected for dry atmospheres. The origin of the occasional noise, observed especially at high steam concentration, is not entirely understood. It has been suggested by the manufacturer that water may condense at the furnace exhaust, and block the exhaust momentarily. This explanation is consistent with the type of noise seen. Aside from this, the experiments are reproducible, and the noise was not found to have any influence on the conclusions drawn below. Figure 3.1 shows that in both environments, aluminum oxidizes in several distinct stages. In steam, initial slow oxidation between 300 – 500 °C is followed by a stepwise weight increase of less than 10 % near 550 °C. An additional, relatively sharp, oxidation step is observed near the aluminum melting point of 660 °C. These initial two oxidation steps are followed by a spread-out oxidation reaction that terminates when the material is fully oxidized above 1000 °C.

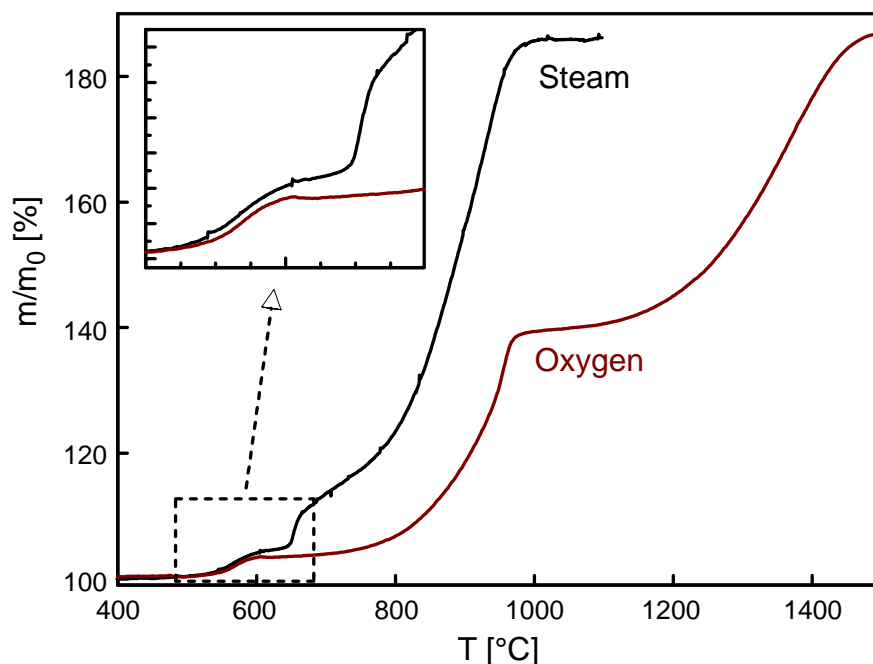


Fig. 3.1. Thermogravimetric curves for aluminum particles oxidizing in steam and oxygen. The gas concentrations were 27 vol % H_2O , and 21 vol-% O_2 , respectively. The balance was argon in both cases.

The most striking difference from oxidation in dry oxygen is the sharp oxidation step near the Al melting temperature. The second important difference is that in steam the oxidation is complete at a much lower temperature than it is in dry oxygen.

Material recovered after the complete heating cycle was analyzed by XRD, and showed α -alumina as the only oxide phase present. To determine whether the step around 660 °C is caused by any structural transition in the surface oxide layer, samples were heated to temperatures below the Al melting point (580 °C) as well as above the Al melting point (680 °C). The samples were kept for approximately 30 minutes in order to accumulate oxide in quantities that are detectable by powder XRD, and subsequently cooled to room temperature and recovered. The XRD patterns of these samples are shown in Fig. 3.2. The only crystalline alumina phase that could be detected in either sample was γ -alumina, and furthermore, no difference was seen between the two samples. This suggests that the oxidation step near the Al melting point is not related to any readily detectable structural change in the oxide layer.

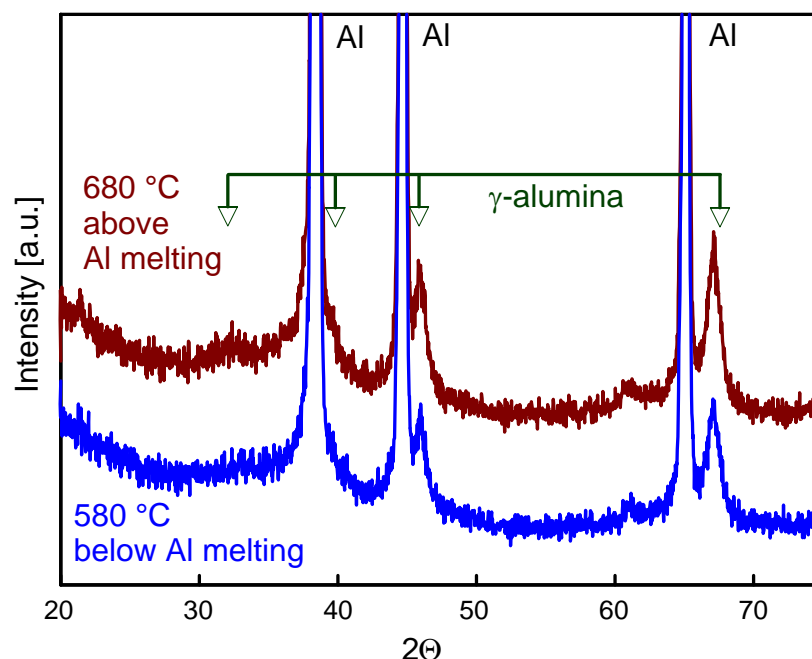


Fig. 3.2. XRD patterns of partially oxidized aluminum powders.

To further test whether the surface oxide is structurally different when grown in dry vs. wet environments, and that it may therefore mechanically respond differently to stress caused by the melting of the Al metal, a sample was heated in dry oxygen to 850 °C to grow a significant amount of γ -alumina on its surface. If this surface oxide, grown under dry conditions, is structurally different from the oxide grown in the presence of water, then that sample should not exhibit a stepwise weight increase on Al melting when it is re-heated in steam. The result of this experiment is illustrated in Fig. 3.3. The sample pre-heated in dry oxygen shows no weight increase (and thus, no appreciable additional oxidation) upon its reheating in steam until the melting temperature of aluminum is reached. However, the TG curve for the re-heated sample clearly shows a stepwise weight increase upon aluminum melting. This suggests that there is no significant difference in the structure of the surface oxide whether it formed in the presence or absence of water. Additionally, although structural differences can not be rigorously ruled out due to the inherent resolution limits of thermogravimetry, the conclusion is reasonably well supported for the purpose of describing oxidation rates.

Measurements at varying heating rates are shown in Fig. 3.4. The onset temperature of the oxidation step near the aluminum melting point does not change systematically with the heating rate. This suggests that at least initially, this oxidation step is caused by an equilibrium reaction as opposed to a thermally activated non-equilibrium process, such as diffusion.

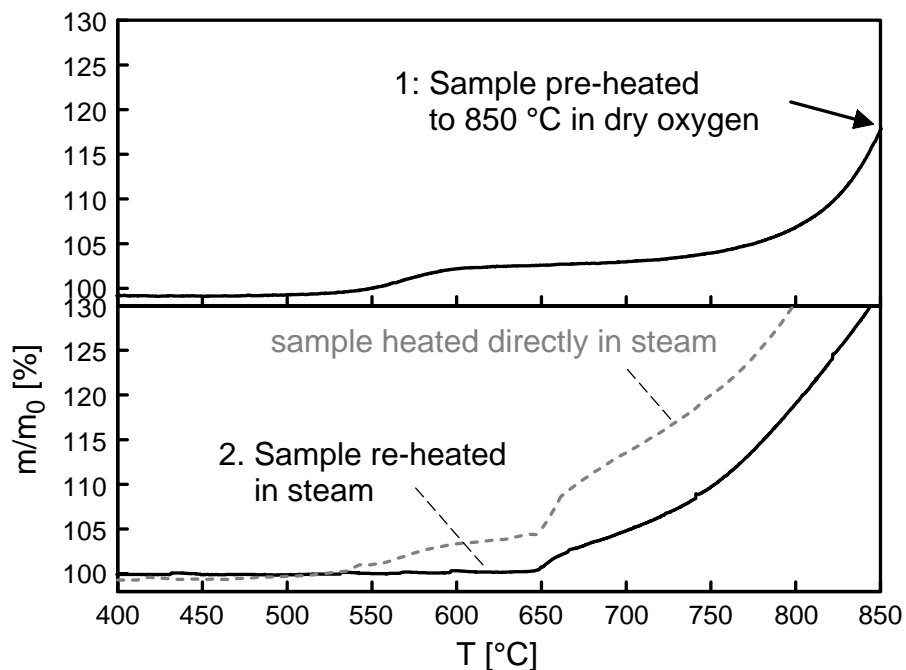


Fig. 3.3. Repeat heating in steam of a sample pre-oxidized in dry oxygen. A sample heated directly in steam is shown for comparison.

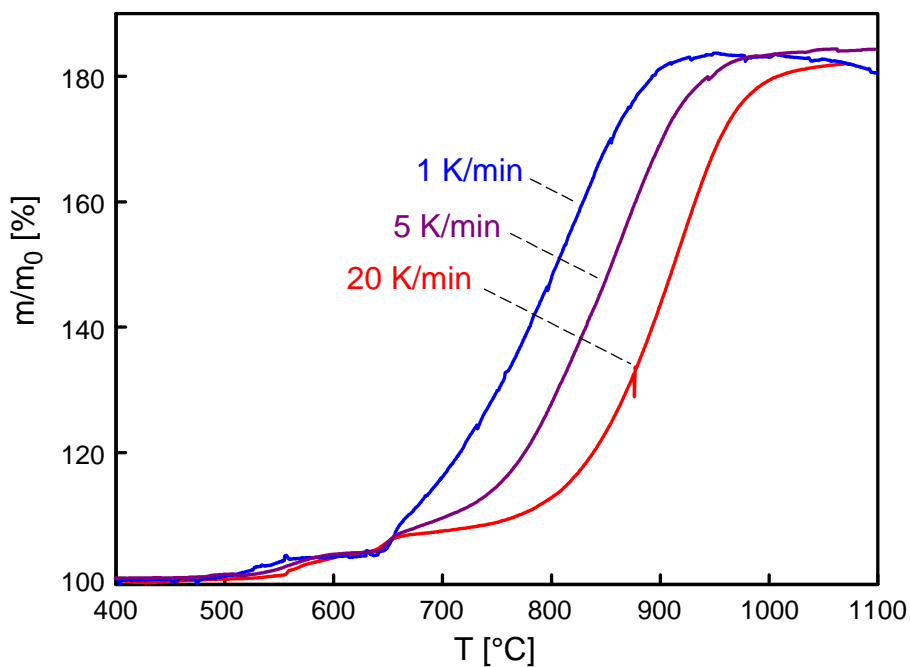


Fig. 3.4. TG traces of Al powders oxidized in 27 vol-% steam (balance Ar) at varying heating rates.

The results of oxidation in atmospheres with variable composition are shown in Figure 3.5. All atmospheres were mixtures of H_2O , O_2 , and Ar. In the series shown in Fig. 3.5, the concentration of argon was kept constant, while the flow rates of steam and oxygen were balanced against each other. For the purpose of comparison, three weight

change reference points were distinguished in these measurements: an initial increase near 550 °C (referred to as “1st step” below), a sharp step near the Al melting point, 660 °C, and the total weight change between approximately 400 °C and 900-1100 °C. In most cases, the first step and the Al melting step overlapped to some extent. To separate the individual contributions, the procedure described below and illustrated in Fig. 3.6 was applied consistently for all measurements. Initial and final baselines were identified as sections where the TG signal could be approximated by a straight line. Then, a temperature was identified where the difference between the TG signal and the initial baseline was half the difference between the initial and final baselines. The difference between the baselines at that temperature was then taken as the weight change corresponding to this step. Figure 3.7A shows the processed results that correspond to the measurements shown in Fig. 3.5. This procedure is routinely applied to step transitions, see for instance Ref. [16].

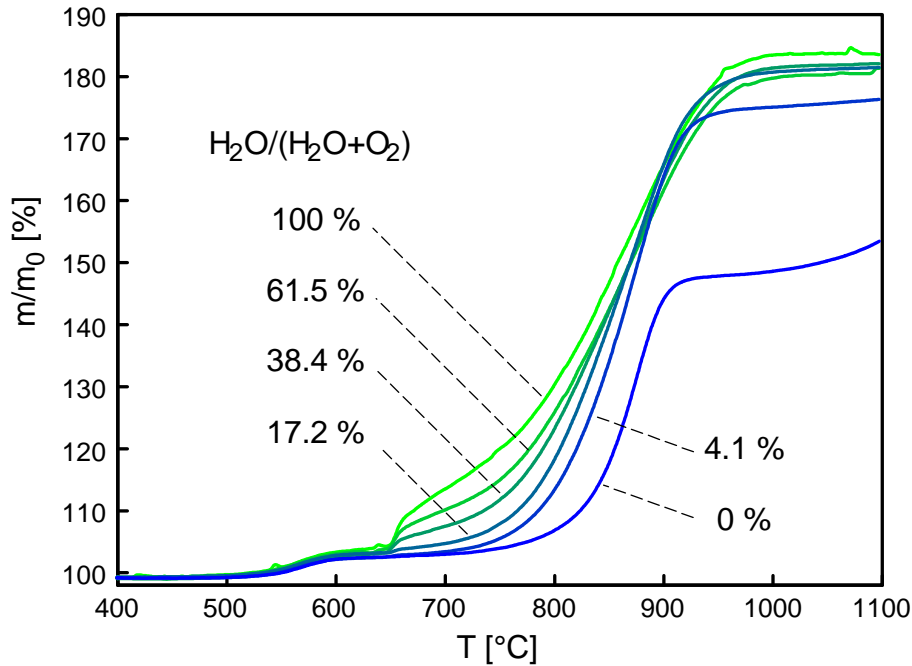


Fig. 3.5. TG traces of Al powders oxidized in systematically varied H₂O/O₂/Ar atmospheres. The numbers on the graph indicate the ratio H₂O/(H₂O + O₂).

As Figs. 3.5 and 3.7A show, the composition of the atmosphere has little effect on the oxidation behavior below the Al melting point. Conversely, the relative weight increase near Al melting does show a distinct dependence on the concentration of water in the atmosphere. Absent in a dry environment, the weight change increases with increasing water concentration. The total weight change, observed above 1000 °C, only depends on water concentration in relatively dry atmospheres. The dry measurement behaves as previously reported [5, 6] with a significantly slowed oxidation above ~900 °C, and less than 50 % relative weight change at 1100 °C. Slightly more water in the atmosphere brings the weight change close to what is expected for complete oxidation ($\Delta m/m_0 = 89\%$), and the measurement with H₂O/(H₂O + O₂) = 17.2 % already shows the same final sample mass as the other, more water-rich measurements. The variations

in final sample mass observed for experiments in the more water-rich atmospheres do not show a systematic trend, and are attributed to minor compositional variations in the initial Al/Al₂O₃ mixtures.

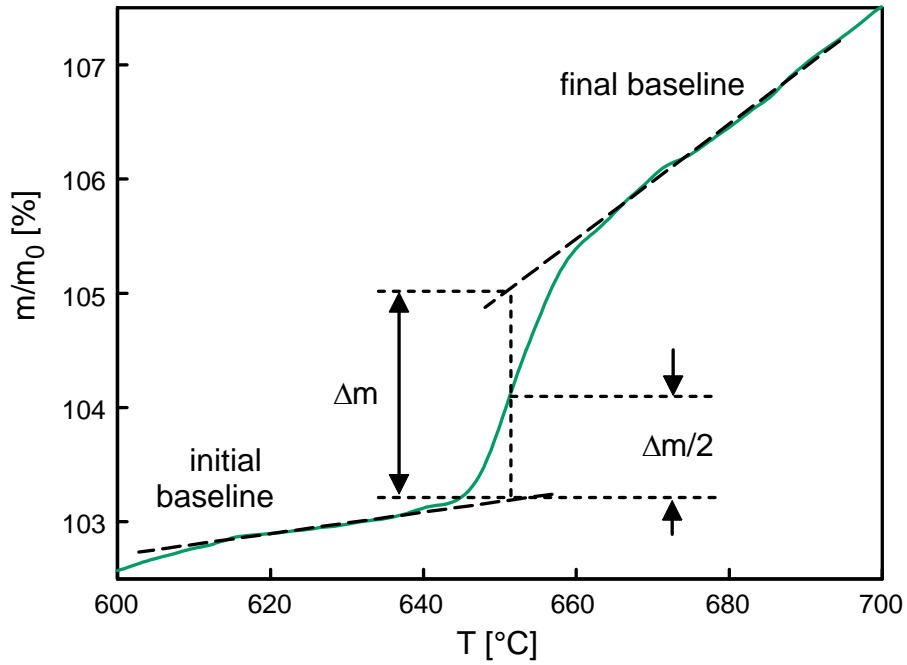


Fig. 3.6. Procedure to consistently assign weight changes to observed oxidation steps.

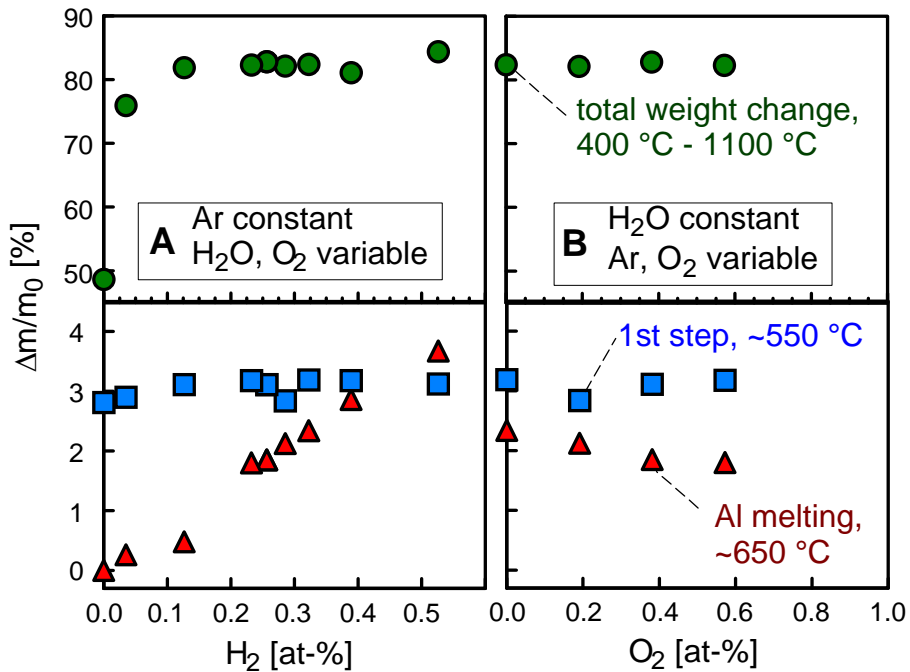


Fig. 3.7. Observed weight changes for various atmospheric compositions. A: Left column: Ar constant, H₂O and O₂ vary; B: right columns: H₂O constant, Ar and O₂ vary.

In an attempt to gain insight in the processes behind the sharp weight change near the Al melting point, the oxidizer concentrations were further systematically varied in a second set of experiments. The flow rate of steam was kept constant, while the concentrations of oxygen and argon were balanced against each other to keep the total gas flow rate constant. The measurements were processed like described above, and the results are shown in Fig. 3.7B. None of the weight changes showed a marked dependence on the oxygen flow rate, and therefore on the total oxidizer concentration. This result clearly shows that the mass change at the Al melting point at least primarily correlates only with the concentration of steam in the atmosphere. This could suggest that hydrous species diffuse more easily through the oxide layer when it is stressed due to the volume increase of the melting aluminum core. However, the effect could also be caused by transient porosity, where the degree of porosity depends on the concentration of steam in the atmosphere. A clear distinction can not be drawn based on the observations in this study.

3.4. Discussion

Reaction mechanism

As noted above, two significant differences between aluminum oxidation in steam and in dry oxygen were observed. The first is the step-wise increase in the oxidation rate correlating with aluminum melting that is observed in steam and not in dry oxygen. The second is the difference in the temperature at which complete oxidation is observed in the TG experiments: about 1000 °C in steam vs. 1500 °C in dry oxygen.

A sharp increase in the oxidation rate associated with disruption of the oxide shell caused by the expansion of the aluminum core, particularly on melting, has been hypothesized to occur in previous papers, e.g., [8 - 12]. Despite this hypothesis, such an increase in the oxidation rate at the Al melting point has never been observed with dry oxygen serving as oxidizer in previous studies. In this paper, a sharp increase in the oxidation rate is unambiguously observed to occur, and it correlates with aluminum melting when the oxidizer contains water. There is some evidence in the literature that spinel-based transition aluminas—specifically δ -alumina, which is structurally similar to the γ polymorph—may be stabilized by the adsorption of H_2O on its surface, resulting in the preferred formation of fresh alumina surface, and a corresponding reduction in the oxide's crystallite size [17]. This could conceivably cause the oxide layer to exhibit no resistance to breaking up under stress in the presence of H_2O , leading, if not to actual porosity, so at least to a dense network of grain boundaries through which diffusion can be significantly faster than through bulk γ -alumina. Due to the surface stabilization of the transition alumina by water adsorption, the degree of porosity would likely depend on the concentration of steam in the atmosphere. Therefore, the oxide layer would act as a membrane the permeability of which is controlled by the steam concentration. Further, a stabilized and porous γ -alumina layer may allow the complete oxidation of the material before the onset of α -alumina formation.

Conversely, the oxidation step could also be caused by preferential diffusion of hydrous species through the stressed oxide layer. Both cases – porosity and accelerated

diffusion of hydrous species – are functionally equivalent and can not be distinguished based on the observations available.

Prior to aluminum melting, oxidation in wet and dry environments proceeds in a similar way. A step-wise oxidation step observed for dry oxygen and assigned earlier to the polymorphic phase change from amorphous to γ -Al₂O₃ [5 - 7] is clearly observed in steam. After aluminum melting, the oxidation in dry oxygen is separated into at least two well-identifiable steps assigned previously to growth of transitional alumina polymorphs (γ -Al₂O₃ with possible transformations into other polymorphs with similar densities, such as δ -Al₂O₃ and θ -Al₂O₃), and transformation to and growth of the much denser α -Al₂O₃, respectively [5]. In dry oxygen, the transformation to α -Al₂O₃ is accompanied by a substantial reduction in the oxidation rate. A similar reduction in the oxidation rate is not observed for oxidation in steam. This can be readily explained by the stabilization of γ -Al₂O₃ polymorph in presence of water [17], so that the formation of α -Al₂O₃ is delayed to higher temperatures. However, the powder is completely oxidized before such higher temperatures are attained.

Reaction kinetics

This study is part of a larger scale effort aimed to establish a quantitative description of the oxidation of aluminum in various oxidizers, and especially at high heating rates. Therefore, one motivation for this study is to provide the experimental background for a quantitative description of aluminum oxidation and oxidation rate in steam. To this end, preliminary kinetic processing of the TG results was performed. Measurements performed at the heating rates of 2, 5 and 10 K/min were processed by an isoconversion algorithm [18]. The algorithm was chosen because it has the advantage that it does not depend on a strict temperature program in the experiments, i.e. linear heating, while also being relatively insensitive to noisy experimental data. For further details on this algorithm, please see Ref. [18]. For this present study, the algorithm was implemented in MATLAB. The preliminary result, an apparent activation energy that varies with the degree of oxidation, or reaction progress defined as $\alpha = (m - m_0)/(m_f - m_0)$, where m is the sample mass at a given temperature, and m_0 and m_f are initial and final sample masses, respectively, is shown in Fig. 3.8.

At least two regions can be distinguished. The melting of aluminum near 660 °C (933.15 K) is an equilibrium transition, not a thermally activated reaction, and an activation energy can not be meaningfully assigned. The activation energy in the region at lower values of α , and at lower temperatures, is near 200 kJ/mol. Above the Al melting point, the activation energy increases from about 200 kJ/mol to approximately 320 kJ/mol. The interpretation of these results is not straightforward, and the results must be considered preliminary. In a strict sense, the activation energy only applies to the specific type of material used here – spherical aluminum with a nominal size of 3-4.5 μ m. Further, it describes the bulk oxidation of the material, which is not directly applicable to, for instance, single particle oxidation and ignition, unless the specific particle size distribution is accounted for. Work to address this, and to derive more generally applicable kinetic parameters, e.g., diffusion coefficients, is currently in progress.

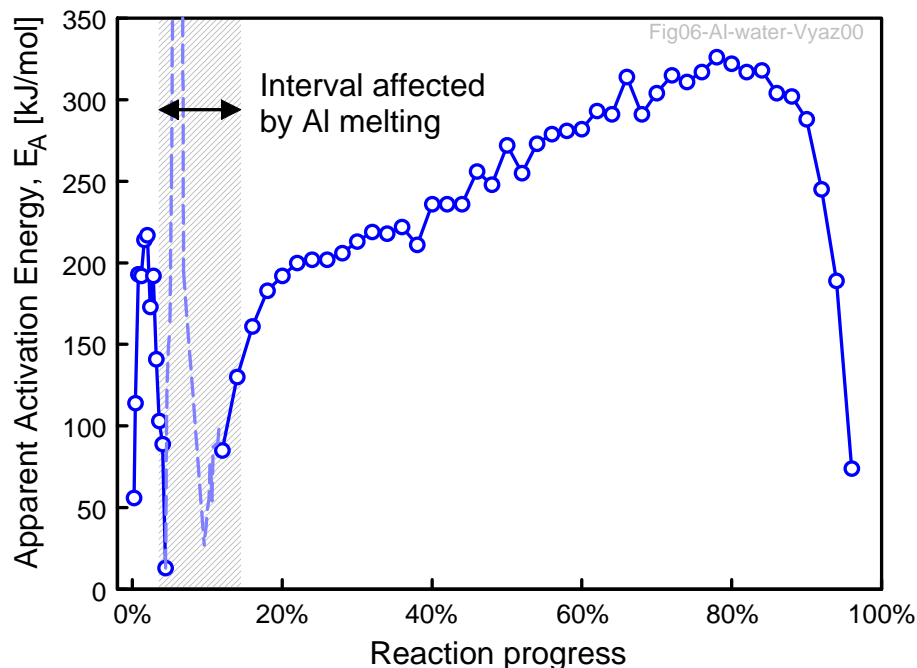


Fig. 3.8. Apparent activation energy for aluminum oxidation in steam/argon gas mixtures.

With the above caveats, the activation energies determined here can be compared to previously determined values. In Ref [5], an aluminum particle ignition-oxidation model was established, where the oxidation of aluminum to form the γ polymorph of alumina was found to be described best with an activation energy of 227 kJ/mol. This is broadly consistent with the 200-320 kJ/mol range seen above the Al melting point in the present study. Comparison of the oxidation below Al melting is not straightforward. The model established in [5] states that at low heating rates, between 550 and 600 °C, formation of amorphous alumina ($E_{am} = 120$ kJ/mol [5]) competes with the transition of amorphous to γ alumina ($E_{am-\gamma} = 458$ kJ/mol [5]). Although the value of ~ 200 kJ/mol determined here falls within this range, the current resolution of the isoconversion processing is insufficient to distinguish individual processes.

The isoconversion method used here to process the thermoanalytical data is currently considered state-of-the-art; however the current results are preliminary, as previously stated. Resolving individual oxidation processes, that could not be achieved based on the present data processing, is important for development of practically useful oxidation models. A processing approach enabling one to better separate individual oxidation steps was previously discussed in the literature [5] and used to describe oxidation of aluminum in oxygen. While its application requires detailed analysis of each individual TG curve and is outside the scope of the present manuscript, such processing is planned in the future to establish a more rigorous kinetic model.

3.5. Conclusions

Systematic differences between aluminum powder oxidation in wet and dry environments were observed. In wet environments, oxidation is complete at significantly lower temperatures compared to dry oxygen. Further, an additional sharp, stepwise weight

increase occurs in presence of steam. This stepwise weight increase clearly correlates with the Al melting point. The size of this oxidation step correlates with the concentration of steam, although it is independent of the total oxidizer concentration in the mixed steam/oxygen/argon environments. It is proposed that the γ -alumina polymorph is stabilized in the presence of water, allowing the oxidation to complete before the γ -to- α transition drastically limits diffusion rates. It is further proposed that γ -alumina when stressed when the aluminum core expands upon its melting may act as a semipermeable membrane, where OH can diffuse at much higher rates compared with oxygen. Alternatively, it is possible that the stressed γ -alumina layer temporarily becomes porous, and that the degree of porosity depends on the concentration of steam in the atmosphere.

Preliminary estimates for activation energies associated with the overall oxidation reaction occurring in the presence of steam were determined to be broadly consistent with values previously determined for aluminum powder oxidation in dry oxygen.

3.6. References

1. Friedman, R., Maček A.; *Combust. Flame*, **1962**, 6, 9
2. Trunov, M.A., Schoenitz, M., Dreizin, E.L.; *Propellants Explosives and Pyrotechnics*, **2005**, 30, 3.
3. Beckstead, M.W.; *Combustion, Explosion and Shock Waves*, **2005**, 41, 533.
4. Beckstead, M.W., Liang, Y., Pudduppakkam, K.V.; *Combustion, Explosion and Shock Waves*, **2005**, 41, 622.
5. Trunov, M.A., Schoenitz, M., Dreizin, E.L.; *Combustion Theory and Modelling*, **2006**, 10, 603.
6. Trunov, M.A., Schoenitz, M., Zhu X., Dreizin, E.L.; *Combust. Flame*, **2005**, 140, 310.
7. Trunov, M.A., Umbrajkar, S.M., Schoenitz, M., Mang, J.T., Dreizin, E.L.; *J. Phys. Chem. B*, **2006**, 110, 13094.
8. Rai, A.; Lee, D.; Park, K.; Zachariah, M. R.; *J. Phys. Chem. B*, **2004**; 108, 14793.
9. Gurevich, M. A.; Ozerov, E. S.; Yurinov, A. A.; *Fizika Goreniya i Vzryva*, **1978**, 14, 50 (in Russian.)
10. Rozenband, V.I., Vaganova, N.I.; *Combust. Flame*, **1992**, 88, 113.
11. Rozenband, V.I.; *Combust. Flame*, **2004**, 137, 366.
12. Gremyachkin, V. M.; Ereemeev, P. M.; *Khimicheskaya Fizika*, **2006**, 25, 42. (in Russian.)
13. Servaites, J., Krier, H., Melcher, J. C., Burton, R. L.; *Combust. Flame*, **2001**, 125, 1040.
14. Olsen, S.E., Beckstead, M.W. *Journal of Propulsion and Power*, **1996**, 12, 662
15. Sarou-Kanian, V., Rifflet, J.C., Millot, F., Gökalp I.; *Combust. Flame*, **2006**, 145, 220.
16. TA Instruments, User Manual for "Universal Analysis 2000" software package, version 4.5 (2007)
17. Łodziana, Z. Topsøe, N.-Y., Nørskov, J.K. *Nature Materials*, **2004**, 3, 289.
18. Vyazovkin, S.; *Journal of Computational Chemistry*, **2001**, 22, 178.

4. Aluminum powder oxidation in CO₂ and mixed CO₂/O₂ environments

4.1. Introduction

Aluminum and other metal powders are widely used as fuels or fuel additives in explosives, propellants, and pyrotechnics [1 – 3]. However, metal ignition processes crucial for accurate modeling of metallized energetic materials remain poorly understood. For example, aluminum, the most common reactive metal additive, is thought to ignite after the integrity of a protective Al₂O₃ layer is disrupted. A quantitative description of the processes leading to such a disruption is lacking. In most practical models, it is simply assumed that the oxide coating stops being protective at a fixed temperature selected between the melting points of Al and Al₂O₃ [4, 5]. Recent research involving ignition of powders with different size distributions and, in particular, nanopowders, showed that the value of the fixed ignition temperature must be adjusted as a strong function of particle size [6]. One hypothesis posed that the disruption of integrity of the Al₂O₃ layer occurs as a result of thermal expansion mismatch between Al and Al₂O₃, and led to the suggestion that ignition should be triggered by aluminum melting, when this mismatch is at its maximum [7, 8]. However, this hypothesis did not explain many reports of much higher ignition temperatures measured for micron-sized Al powders and somewhat lower than melting point ignition temperatures for nano-sized Al powders. Furthermore, multiple thermal analysis studies with micron-sized and nano-sized Al powders [9 – 12] showed no accelerated Al oxidation during melting, contradicting the expected higher oxidation rate that would be caused by a non-continuous Al₂O₃ layer.

A model of heterogeneous oxidation of Al powder leading to ignition was recently developed and quantified for reaction of aluminum in environments containing oxygen as the only oxidizer [10 – 12]. This model considers the oxidation process that is limited by the rates of diffusion of aluminum and oxygen ions through the growing layer of aluminum oxide. Most importantly, this model considers the changing properties of the aluminum oxide layer at elevated temperatures, including polymorphic phase transitions accompanied by substantial changes in the oxide density. The model predicts a broad range of ignition temperatures for aluminum powders of different sizes, consistent with many available experimental reports. The quantitative description is currently available for ignition of aluminum particles in air [11] but not in the many practically interesting environments, in which H₂O and CO/CO₂ molecules serve as primary oxidizers. To extend this model, one needs to understand how the change in the gaseous oxidizer affects processes of oxidation for aluminum powder. In particular, the changes in the reaction rates of individual oxidation stages need to be quantified. This paper presents an experimental study of aluminum powder oxidation with CO₂ and CO₂/O₂ mixtures serving as oxidizers. The oxidation processes are characterized experimentally and respective reaction rates are recovered from the obtained measurements.

4.2. Experimental

Aluminum powder (Alfa Aesar, 3-4.5 μm nominal size, 97.5 % pure) was heated in a Netzsch STA409PG thermal analyzer using a thermogravimetric (TG) sample carrier with a 17 mm diameter flat corundum plate to hold the sample. Large diameter TG

sample holders enhance access of the oxidizing gas to the powdered sample; also sintering of the powder upon heating is minimized. The furnace with TG sample holders was calibrated using a set of certified pure metals, the melting points of which were recovered from the recorded sample temperature as a function of time. The TG balance was continuously flushed with ultra high purity argon by Matheson at 20 ml/min. In all experiments, argon, carbon dioxide, and oxygen were present in varying proportions. The experiments systematically addressed aluminum powder oxidation in environments with varied CO₂ concentration balanced with argon and argon/oxygen mixtures. Partially oxidized samples were cooled from several selected temperatures, recovered, and analyzed using x-ray diffraction. The diffraction patterns were collected on a Philips X'pert MRD diffractometer operated at 45 kV and 40 mA. Samples were held on a zero-background quartz plate. The kinetics of aluminum oxidation in CO₂ was studied using experiments at varied heating rates. Two different methods were used to process experimental results and obtain respective descriptions of the oxidation kinetics.

Initial TG experiments established that above the melting point, the aluminum particles tended to coalesce into droplets with sizes in the 0.5 – 1 mm range. To mitigate the associated drastic loss in surface area, the powders in subsequent measurements were ultrasonically mixed with 150-nm α -alumina powder (Inframat Advanced Materials, 99.8 % pure) to contain approximately 25 wt-% free Al.

4.3. Experimental results

TG oxidation curves measured at a fixed heating rate of 5 °C/min for the aluminum powder heated in Ar/CO₂ mixtures with different concentrations of CO₂ and in an Ar/O₂ mixture are shown in Fig. 4.1. The total gas flow rate in all experiments shown in Fig. 4.1 was fixed at 100 mL/min. The characteristic stepwise oxidation behavior reported earlier for aluminum oxidation in oxygen [9 – 12] is clearly observed in all cases. As was earlier proposed for oxidation of aluminum in oxygen, the oxidation process can be broken down into four stages, as schematically shown at the bottom of Fig. 4.1 (the beginnings and the ends of individual stages are only shown approximately and vary from one TG trace to another). Note that the oxidation during stage I is barely noticeable for these relatively coarse powders mixed with aluminum oxide.

All TG curves nearly coincide for the stages I and II, and at the beginning of stage III, for temperatures under 800 °C. At higher temperatures, when stage III continues and a clear second oxidation step is observed in Fig. 4.1, oxidation occurs noticeably faster in the Ar/O₂ mixture. However, for the experiment in Ar/O₂ mixture this oxidation stage ends at a lower temperature (around 900 °C) than it does for Ar/CO₂ mixtures (around 1000 °C). As a result, by 1000 °C, the oxidation is substantially more complete by the end of stage III for the experiments in Ar/CO₂ as compared to Ar/O₂ environments. As expected, the completeness of aluminum oxidation by the end of stage III increases with the increase in the CO₂ concentration. By the end of the heating cycle, the sample is at about 1450 °C and the oxidation completeness is nearly the same for experiments performed in all environments.

Figure 4.2 shows a similar set of TG traces collected at a heating rate of 5 °C /min when mixed Ar/O₂/CO₂ environments were used. The total gas flow rate was again set to 100 ml/min and the argon flow rate was fixed at 50 ml/min. The balance between the O₂ and CO₂ flows was varied. For comparison, Ar/CO₂ and Ar/O₂ traces shown in Fig. 4.1 are also shown in Fig. 4.2 as dashed lines. Oxidation in the presence of oxygen occurs identically for all samples at temperatures below ~ 900 °C. However, for the sample heated to this temperature in the absence of CO₂, the oxidation step ends here, while in the presence of CO₂ it is extended by about 50 °C resulting in a higher degree of oxidation achieved around 1000 °C. No meaningful difference in the oxidation behavior could be detected when the O₂/CO₂ ratio was varied from 15/35 to 35/15.

In previous work, the stepwise oxidation pattern of aluminum in oxygen was found to correlate with the polymorphic phase changes in the alumina produced on the surface of the powder particles [10 – 12]. To establish whether similar phase transitions occur in oxidation of aluminum in CO₂, a set of samples was oxidized to selected temperatures, cooled, and recovered for X-ray diffraction analysis. Note that in these experiments, the starting aluminum powder was not mixed with alumina so that the oxidation was affected by partial sintering occurring after melting. Figure 4.3 shows the TG traces recorded for the quenching experiments, which effectively coincide for all four runs, with the temperatures at which the samples were quenched labeled by stars. The effect of admixed alumina powder is illustrated by the dashed line in Fig. 4.3, recorded under identical conditions with the Al/Al₂O₃ blend. Figure 4.4 shows sections of the obtained X-ray diffraction patterns, in which the peaks produced by different alumina polymorphs can be distinguished. Consistently with our previous results [10 – 12], formation of γ -Al₂O₃ is observed after the first oxidation step occurring before aluminum melting (referred to as Stage II oxidation). Stage III starts with the growth of the thickness of the γ -Al₂O₃ layer. At higher temperatures, formation of θ -Al₂O₃ is observed. Finally, before the stage III oxidation is completed, formation of α -Al₂O₃ is also detected.

The effect of heating rate on the oxidation behavior of aluminum powder in CO₂ is shown in Fig. 4.5. As in the previous experiments, the total gas flow rate was set to 100 ml/min with a fixed 50 ml/min Ar flow and the Ar/CO₂ ratio fixed at 1/1. Generally, the traces shift to higher temperatures at increased heating rates, as anticipated for the thermally activated oxidation processes. A minor irregularity is observed for the traces recorded at 5 and 10 °C/min at higher temperatures, most likely caused by partial sintering in the samples occurring above the Al melting point despite dilution of aluminum powder with alumina.

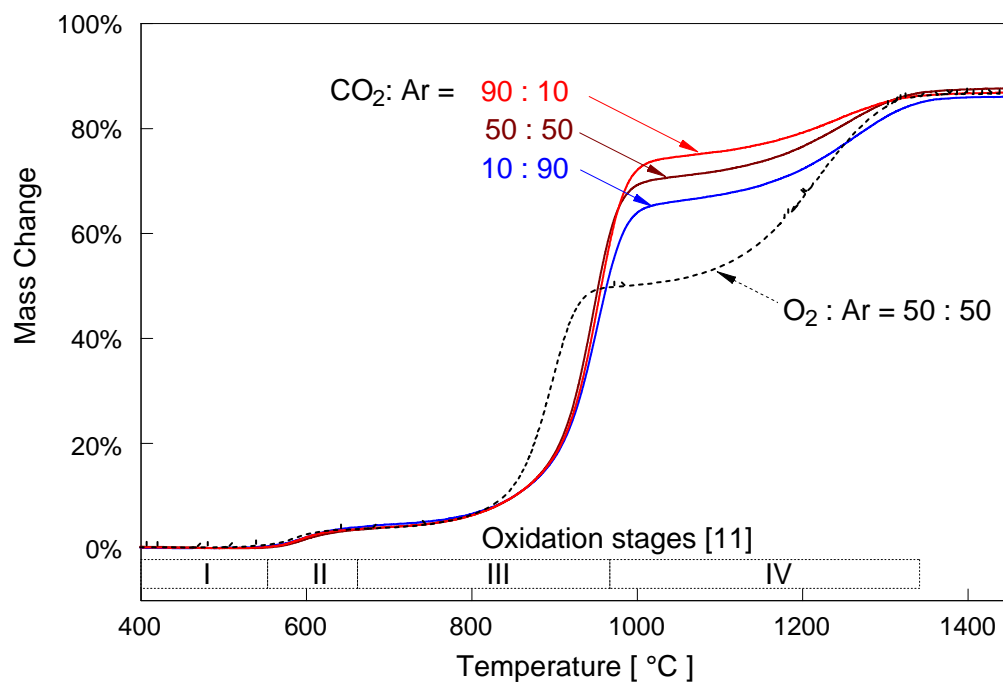


Fig. 4.1. TG traces recorded for aluminum oxidation in Ar/CO₂ and Ar/O₂ gas mixtures. The heating rate is fixed at 5 °C /min, the total gas flow rate is 100 ml/min.

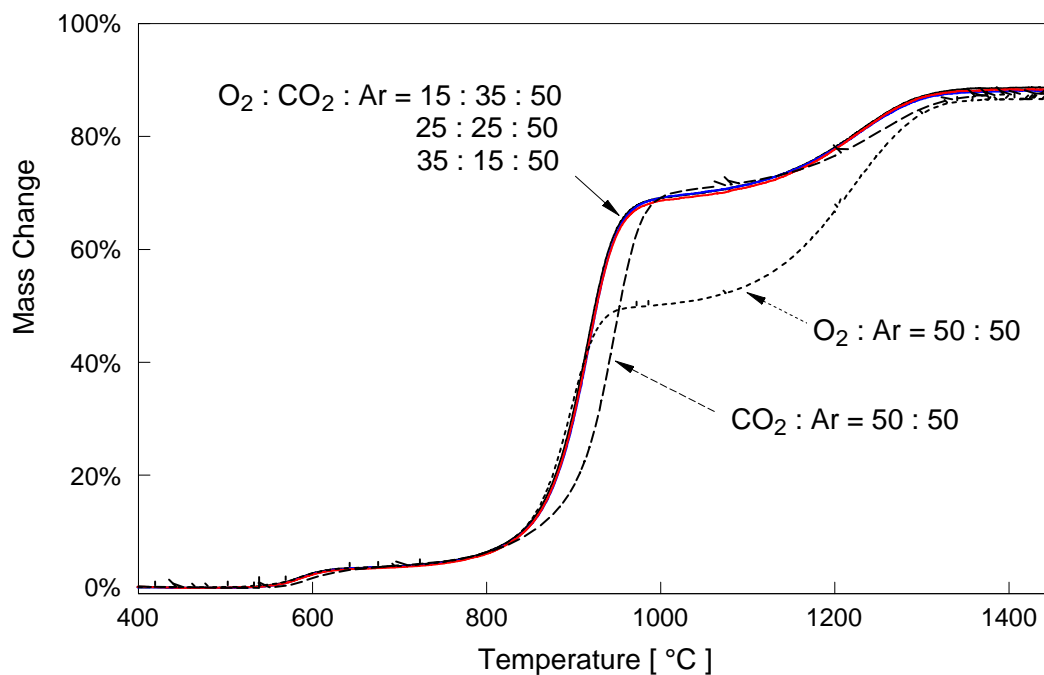


Fig. 4.2. TG traces recorded for aluminum oxidation in Ar/CO₂/O₂ and Ar/O₂ gas mixtures. The heating rate is fixed at 5 °C /min, the total gas flow rate is 100 ml/min.

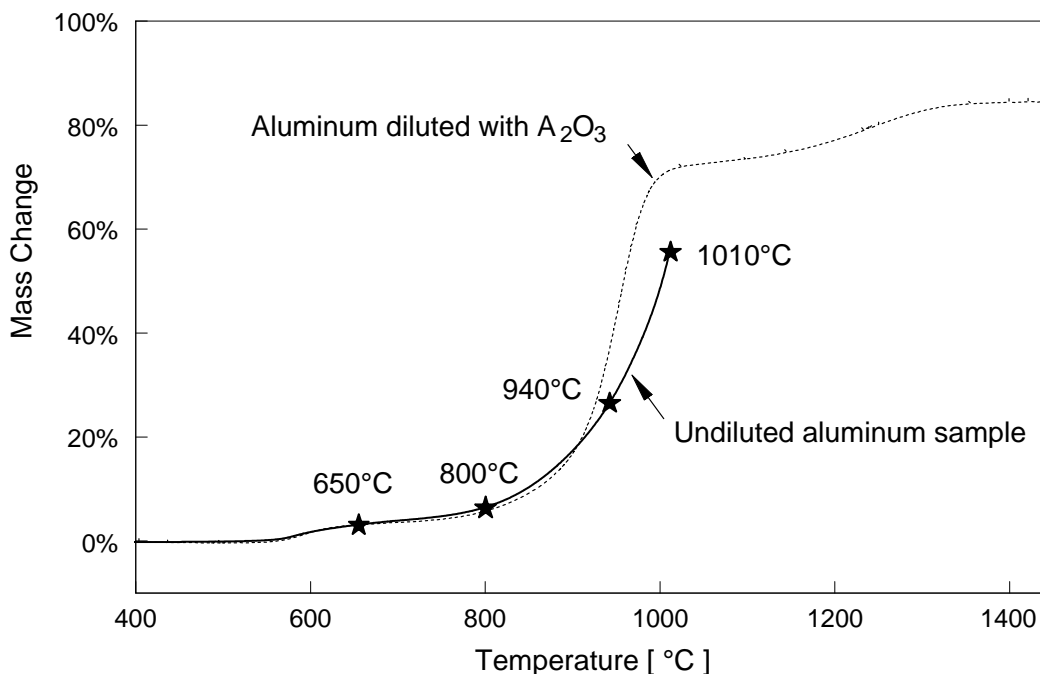


Fig. 4.3. TG traces recorded for the samples heated to and cooled from specific temperatures for subsequent product analysis by x-ray diffraction. For reference, a trace for aluminum powder diluted with alumina is also shown. The heating rate is 5 °C /min, the environment is a CO_2/Ar mixture with the flow rates of 90/10 ml, respectively.

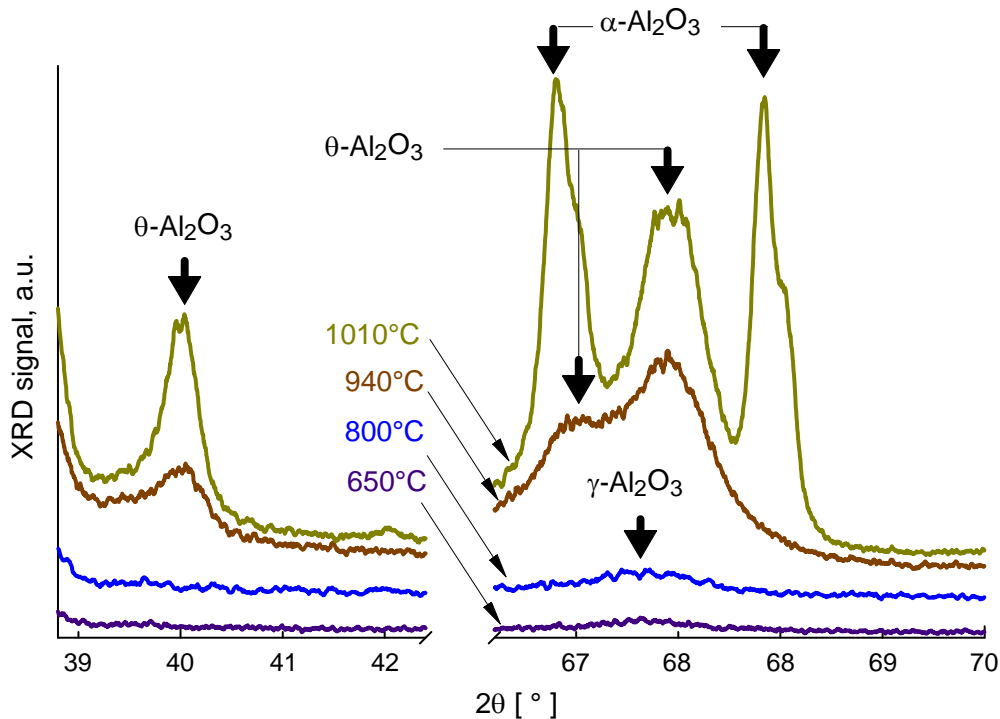


Fig. 4.4. Segments of the XRD patterns for the samples quenched at different temperatures. The 2θ range is selected to show the relatively weak peaks produced by aluminum oxide polymorphs.

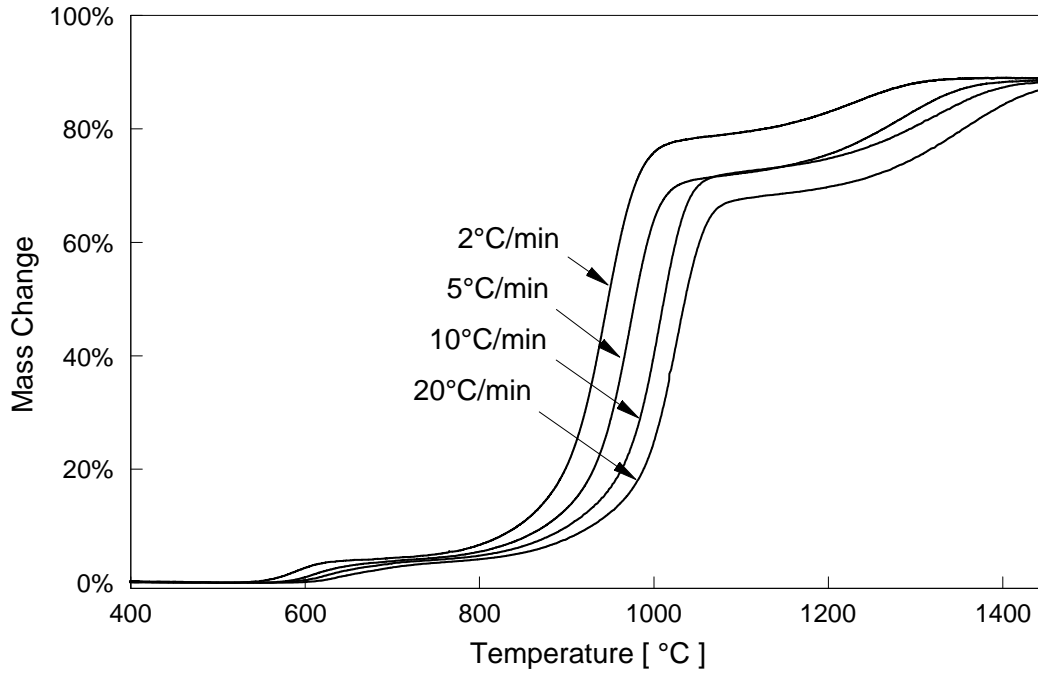


Fig. 4.5. TG traces recorded for aluminum oxidation in Ar/CO₂ gas mixture at varied heating rates. The total gas flow rate is 100 ml/min.

4.4. Oxidation kinetics

The kinetics of oxidation processes in CO₂ was quantified using two different signal processing techniques.

The first technique used a recently developed isoconversion algorithm described in detail elsewhere [13]. The algorithm was chosen because it has the general advantage that it does not depend on a strict temperature program in the experiments, i.e., linear heating, while also being relatively insensitive to noisy experimental data. For this present study, the algorithm was implemented in MATLAB and applied to process simultaneously all four measurements shown in Fig. 4.5. The result, an apparent activation energy that varies with the degree of oxidation, or reaction progress, defined as $\alpha = (m - m_0)/(m_f - m_0)$, where m is the sample mass at a given temperature, and m_0 and m_f are initial and final sample masses, respectively, is shown in Fig. 4.6. The initial range of α , corresponding to stage II (or the first oxidation step observed in Figs. 4.1, 4.2, and 4.5) is resolved poorly. The activation energy varies substantially, and no consistent value could be assigned to the respective oxidation processes. Relatively little variation in the activation energy is observed for $10\% < \alpha < 60\%$. This range of the reaction progress generally corresponds to the stage III reaction or the second oxidation step visible in the TG curves, in Figs. 4.1, 4.2, and 4.5. During this oxidation stage the thickness of the γ -Al₂O₃ increases and θ -Al₂O₃ forms. It is also apparent that the activation energy increases at $\alpha \approx 20\%$. A sharp decrease in the activation energy at α close to 70-80% correlates with

the initial formation of $\alpha\text{-Al}_2\text{O}_3$ and transition to the oxidation stage IV, and does not reflect an actual change in the activation energy.

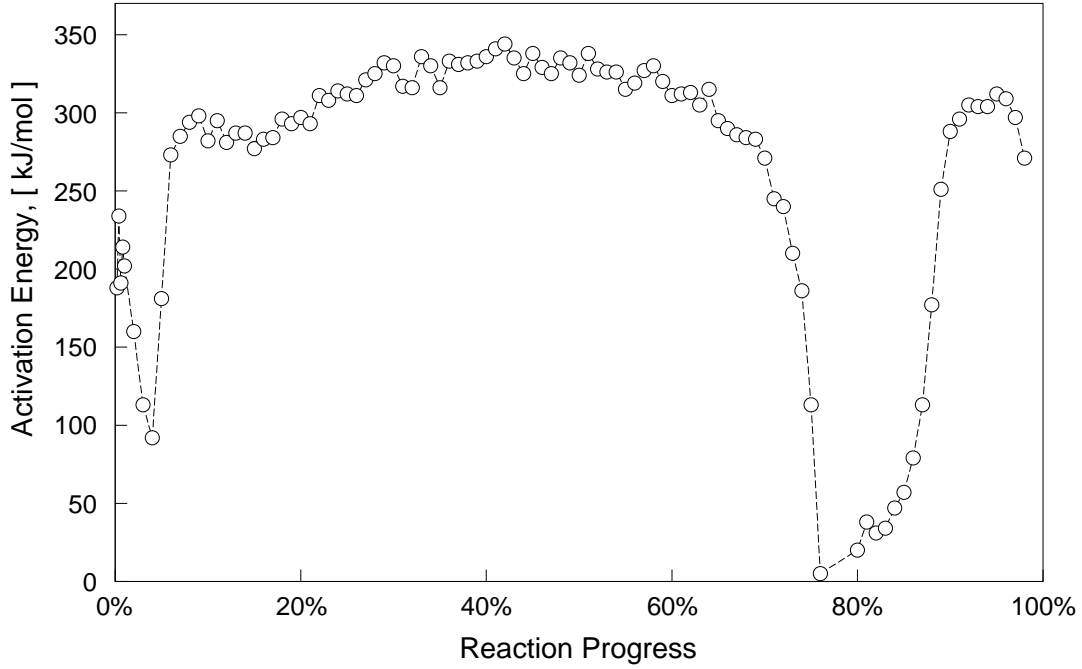


Fig. 4.6. Activation energy as a function of reaction progress obtained by isoconversion processing developed in ref. [13] applied for the TG traces measured for four heating rates (2, 5, 10, and 20 °C/min) shown in Fig. 4.5.

The second technique used to quantify the reaction kinetics relied on processing individual TG curves. It was described in detail elsewhere [11] and used to process similar experiments on oxidation of aluminum powders in oxygen. It is only briefly described below. Particles are assumed to be spherical and oxidation is assumed to occur as a series of individual processes. Thus, it is assumed that at any given time the rate of oxidation is limited by a single thermally activated mass transfer process, such as diffusion of one species, A . With these assumptions, at any given moment the rate of sample mass change, $\frac{dm}{dt} = \frac{dm}{dT} \frac{dT}{dt}$, can be described as:

$$\frac{dm}{dT} = \frac{C_A^* \exp\left(-\frac{E}{RT}\right)}{\frac{1}{r_{Al}} - \frac{1}{r_{ox}}} \frac{1}{\beta} \quad (4.1)$$

where T is temperature, t is time, C_A^* is the combined oxidation constant depending on the reaction stoichiometry, the initial sample mass, and the type of the species A ; r_{Al} and r_{ox} are the radii of the aluminum core and oxide shell, respectively; E is the activation energy; R is the universal gas constant, and $\beta = dT/dt$ is the heating rate. In this analysis it is expected that each process occurring during oxidation can be characterized by its

specific activation energy. The values of these process-specific activation energies can be found from the differential TG curves (i.e., from $\frac{dm}{dT}$ as a function of temperature):

$$\frac{E}{RT} = \ln C_A^* - \ln\left(\frac{dm}{dT}\right) - \ln(\beta) - \ln\left(\frac{1}{r_{Al}} - \frac{1}{r_{ox}}\right) \quad (4.2)$$

The radii r_{Al} and r_{ox} at different temperatures are also readily derived from the current sample mass m obtained from the TG [11]. Therefore, the right side of Eq. (4.2) depends only on the experimental sample mass. In this processing technique, a function, $Y(TG)$, equivalent to the right side of Eq. (4.2) is determined from the TG signal and is plotted vs. inverse temperature. A typical plot is shown in Fig. 4.7. Portions of this function approaching straight lines are identified and interpreted as parts of the oxidation process for which the activation energy remains constant and equal to the slope of the line. Data for experiments with different heating rates are processed independently. The results of the processing of multiple TG curves are summarized in Table 4.1. For each value of activation energy corresponding to a portion of the function $Y(TG)$, the range of values of the reaction progress, α , corresponding to the same portion of $Y(TG)$ is also shown. The activation energies determined from different experiments should coincide for the same ranges of α if the same oxidation processes control the reaction during the oxidation stages observed in the TG traces.

The activation energy for the stage I oxidation could only be obtained from several experiments performed with undiluted aluminum samples due to limits in the resolution of the measurement. These experiments were interrupted at higher temperatures, so that the activation energies corresponding to the other oxidation stages are not available.

Stage II is characterized by a relatively high activation energy, consistent for all experiments. This stage was earlier assigned to the transformation from amorphous to γ - Al_2O_3 . Although this high activation energy was obtained consistently from the individual runs, it is not supported by the processing shown in Fig. 4.6, which is based on simultaneous evaluation of measurements with different heating rates.

Stage III consistently comprises two straight segments with distinct slopes (cf. ranges III-a and III-b in Fig. 4.7). This suggests two processes occurring in series. Once again, these processes could not be meaningfully resolved from the processing in Fig. 4.6. The temperatures of transition between these processes, T^* (when the slope of the straight line fit for the function $Y(TG)$ changes) are shown in an Arrhenius-type plot of the logarithm of the average heating rate vs. inverse temperature in Fig. 4.8 for both Ar/O₂ and Ar/CO₂ environments. For the Ar/O₂ environments [10 – 11], experimental data reported earlier were reprocessed to obtain the respective values of T^* . Analysis of the samples heated and quenched in the CO₂/Ar environment (cf. Fig. 4.4) suggests that the change in the slope of the function $Y(TG)$ can be correlated with the onset of formation of θ - Al_2O_3 . Note that based on the available XRD results it is difficult to separate clearly the onsets of formation of θ - and α - Al_2O_3 polymorphs. From Fig. 4.8, the activation energy associated with the transition can be roughly estimated with the assumption that the

slopes represent E_a/R [14]. The activation energy of the transition in oxygen is 559 ± 48 kJ/mol, which is consistent with activation energies that have been reported for generalized γ -to- α transitions [15]. In contrast, the transition in CO_2 appears to be characterized by a much lower activation energy of 207 ± 19 kJ/mol. A number of mechanisms for the structural transitions among transition aluminas and from transition aluminas to the stable α alumina have been proposed. In ref. [16] Zhou and Snyder propose that θ -alumina is a necessary precursor of α -alumina, that therefore the γ polymorph will not transform to the α phase without first undergoing the structural change that leads to the formation of θ . This scenario is consistent with the close association of θ and α phases in the present XRD results.

The presence of carbon in the system could potentially stabilize the transition aluminas by the absorption of CO or CO_2 onto the alumina surface [17]. Therefore, the rate of the observed transition may be determined by a combination of the structural transition between the alumina polymorphs and the desorption kinetics of CO/ CO_2 from the surface of γ or θ alumina, which are characterized by much lower activation energies [17].

In summary, the activation energies obtained by this second technique for different oxidation stages from individual experiments are in reasonably good agreement between themselves for the experiments performed at different heating rates or with varied environments. While the processing is labor-intensive and involves analysis of each individual trace, the results allow a relatively straightforward assignment of activation energies to the stages clearly detected in the TG traces. These activation energies are expected to be useful for detailed modeling of aluminum oxidation in CO_2 and mixed CO_2/O_2 oxidizers.

To allow some comparison between the data processing methods, Table 4.1 also shows the ranges of the reaction progress α for which respective straight line segments were identified. Those ranges should be relatively consistent between measurements, but they also should ideally correspond to identifiable sections of the plot shown in Fig. 4.6. However, comparison is difficult. When the oxidation slows down, e.g., after stage II and IIIb, the lower reaction results in a substantial variation in the reaction progress for different heating rates. This variation influences the activation energy calculated by method 1 over significant intervals of α : from about 2 % to 10 %, and again between 70 % and 90 %, the activation energy is depressed, and can not be taken as a meaningful representation of the oxidation process. This may be the main reason that the changes in the activation energy are detected better in the processing method based on individual measurements. The values shown in Fig. 4.6 vary between 200 and 350 kJ/mol, while the values in Table 4.1 range from 190 to 630 kJ/mol and are likely to represent better the activation energies corresponding to different processes occurring during powder oxidation.

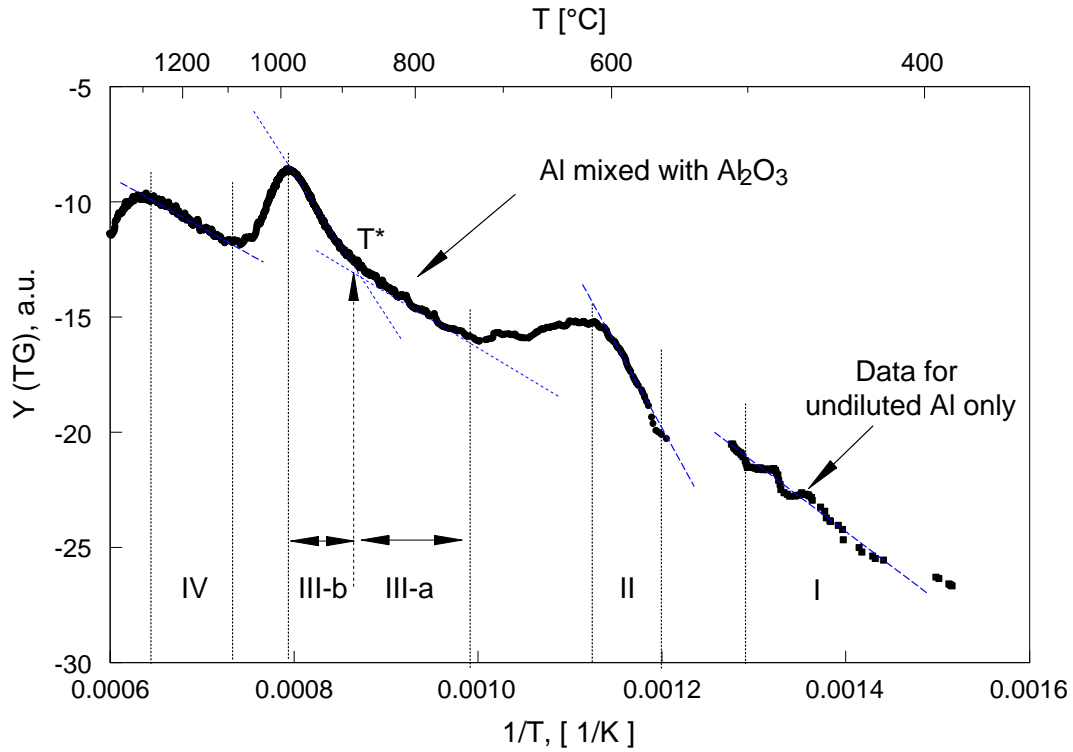


Fig. 4.7. TG trace processing for recovery of the activation energies for different parts of the oxidation process. The trace processed here corresponds to an experiment performed at a heating rate of 5 °C/min in Ar/CO₂ (10/90) environment.

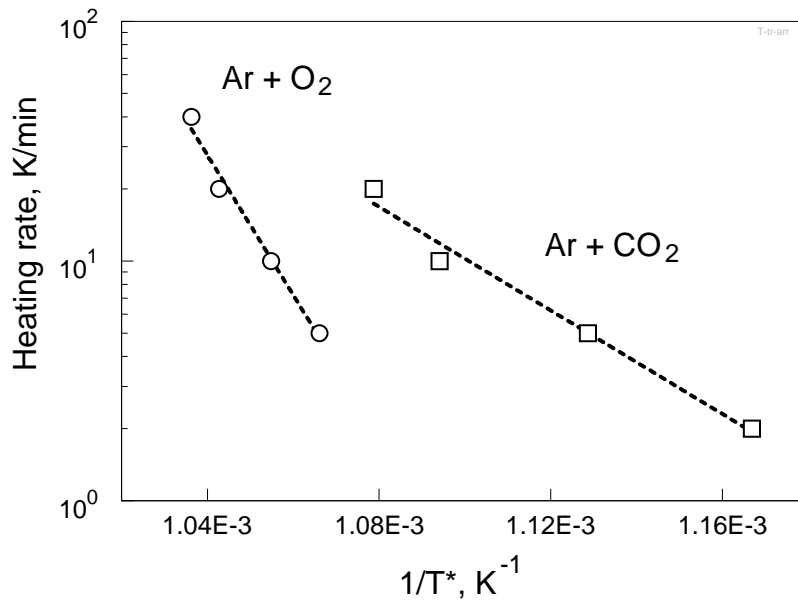


Fig. 4.8. Effect of heating rate on the temperature T^* at which the slope of the function $Y(TG)$ changes for different oxidizing environments. The experimental data reported in ref. [10 – 11] for Ar/O₂ environments were reprocessed here to obtain one of the data sets shown.

Table 4.1. Activation energies for different oxidation stages obtained by interpretation of the function Y(TG) described in Eq. (4.2).

Materials	CO ₂ :O ₂ :Ar flow rates [ml/min]	Heating rate [K/min]	E _a [kJ/mol] (reaction progress α in parentheses)				
			I	II	III-a	III-b	IV
Aluminum (3-4.5 μm)	90 : 0 : 10	5	108 (0.9-1.0)	425 (1.2-2.1)	206 (7.3-31)	-	-
	90 : 0 : 10	5	89 (0.9-1.0)	430 (1.4-2.5)	196 (7.8-61)	-	-
	90 : 0 : 10	5	59 (0.9-1.0)	431 (1.5-2.2)	-	-	-
	90 : 0 : 10	5	78 (0.7-0.8)	390 (1.5-3.3)	-	-	-
		<i>Average</i>	<i>84 ± 20</i>	<i>419 ± 20*</i>	<i>201 ± 7*</i>		
Aluminum (3-4.5 μm) diluted with alumina	0 : 50 : 50	5	-	-	202 (4.2-11)	520 (11-41)	257 (56-85)
	10 : 0 : 90	5	-	360 (0.4-2.3)	229 (5.4-18)	483 (18-51)	211 (75-91)
	50 : 0 : 50	5	-	631 (0.2-1.8)	268 (4.7-14)	622 (14-58)	187 (80-91)
	90 : 0 : 10	5	-	515 (0.3-2.2)	236 (5.0-19)	601 (19-57)	188 (85-92)
	50 : 0 : 50	2	-	460 (0.3-2.8)	284 (5.2-15)	551 (15-77)	189 (90-99)
	50 : 0 : 50	5	-	631 (0.2-1.8)	268 (4.7-14)	622 (14-58)	187 (80-91)
	50 : 0 : 50	10	-	577 (0.2-1.3)	243 (5.3-16)	617 (16-75)	199 (85-96)
	50 : 0 : 50	20	-	579 (0.2-1.0)	240 (4.4-14)	577 (14-58)	233 (78-91)
		<i>Average</i>		<i>562 ± 72</i>	<i>259 ± 21</i>	<i>592 ± 34</i>	<i>202 ± 21</i>
	15 : 35 : 50	5	-	546 (0.3-2.0)	271 (4.1-12)	550 (12-60)	209 (78-94)
	25 : 25 : 50	5	-	582 (0.3-2.4)	239 (4.7-12)	663 (12-67)	210 (79-93)
	35 : 15 : 50	5	-	506 (0.4-2.5)	226 (5.6-14)	696 (14-65)	206 (78-96)
		<i>Average</i>		<i>545 ± 38</i>	<i>245 ± 23</i>	<i>636 ± 77</i>	<i>208 ± 2</i>

* Lower accuracy measurements because of the effect of particle coalescence upon melting

4.5. Discussion

The oxidation of aluminum powder in CO₂ containing environments is generally similar to that observed in oxygen. The main distinctive feature observed in CO₂ is the extended Stage III oxidation resulting in a greater degree of reaction at about 1000 °C. This indicates stabilization of the transition alumina phases (γ and θ - Al₂O₃) in the presence of CO₂. On the other hand, the beginning of the Stage III oxidation is slower when CO₂ is the only oxidizer in the system. This could be due to the lower effective oxygen concentration, since both, O and CO are species diffusing through the growing oxide layer. In the presence of both O₂ and CO₂ as oxidizers, the Stage III oxidation begins as fast as in O₂ but, like in CO₂ it is extended to higher temperatures than in O₂. The comparison of activation energies determined in this work for Stages I, II, III, and IV with those reported in ref. [11] for oxidation of aluminum powder in oxygen is presented in Table 4.2.

Table 4.2. Comparison of oxidation stages and reaction kinetics for aluminum powder oxidation in O₂ and CO₂

Environment	Activation energy, E _a [kJ/mol]				
	Growth of amorph. Al ₂ O ₃	Formation of γ	Growth of transition aluminas		Growth of α
			Growth of γ	Formation and growth of	
				θ and α	
	I	II	III-a	III-b	IV
Ar/O ₂ [11]	120	458	227	394	306
Ar/CO ₂	84	562	259	592	202

Considering a relatively large error typically expected from the activation energy values obtained from TG or similar experiments, the results are consistent between each other. The relatively large differences in the activation energies observed for stages III-b and IV can be attributed to real differences in the oxidation rates in different environments.

4.6. Conclusions

Oxidation of aluminum powders in CO₂ occurs in several stages, qualitatively similar to that in oxygen. Aluminum oxidation rates are effectively the same for O₂ and CO₂ oxidizers for the low-temperature oxidation processes controlled by the growth of the initial amorphous oxide, its transformation to γ -Al₂O₃ polymorph, and initial growth of γ -Al₂O₃. At higher temperatures, the growth of transition alumina in oxygen occurs faster than it does in CO₂. However, the thermal area of stability of the transition alumina polymorphs, primarily for θ -Al₂O₃ is extended to higher temperatures in presence of CO₂. Therefore, in presence of CO₂, the denser α -Al₂O₃ polymorph that has a higher diffusion resistance forms later, allowing for a higher degree of oxidation to be achieved at lower temperature as compared to the environments containing oxygen as the only oxidizer. In mixed, CO₂/O₂ oxidizers, the initial growth of γ -Al₂O₃ is observed to proceed as fast as with oxygen only, while the region of stability of transition alumina polymorphs remains extended to higher temperatures. Activation energies for individual aluminum powder oxidation steps observed in CO₂ are determined from processing

the measured TG traces and compared to the activation energies reported earlier for aluminum oxidation in oxygen.

4.7. References

1. Price, E.W. Combustion of Metalized Propellants. Progress in Astronautics and Aeronautics 90, pp. 479-513, 1984
2. Gogulya, M.F., Makhov, M.N., Dolgoborodov, A.Yu., Brazhnikov, M.A., Arkhipov, V.I., Shchetinin, V.G. Mechanical sensitivity and detonation parameters of aluminized explosives. Combustion, Explosion and Shock Waves 40 (4), pp. 445-457 2004
3. Pourmortazavi, S. M.; Hajimirsadeghi, S. S.; Kohsari, I.; Fathollahi, M.; Hosseini, S. G. Thermal decomposition of pyrotechnic mixtures containing either aluminum or magnesium powder as fuel. Fuel, 2008, 87(2), 244-251.
4. Benkiewicz, K., Hayashi, A.K. Parametric studies of aluminum combustion model for simulations of detonation waves 2006 AIAA Journal 44 (3), pp. 608-619
5. DesJardin, P.E., Felske, J.D., Carrara, M.D. Mechanistic model for aluminum particle ignition and combustion in air 2005 Journal of Propulsion and Power 21 (3), pp. 478-485
6. Trunov, M.A., Schoenitz, M., and Dreizin, E.L., "Ignition of Aluminum Powders under Different Experimental Conditions" *Propellants Explosives and Pyrotechnics*, V. 40, No 1, pp. 36-43 (2005)
7. V.I. Rozenband, N.I. Vaganova, *Combustion and Flame*, 88 (1), 113-118 (1992)
8. V.I. Rozenband *Combustion and Flame*, 137, 366-375 (2004)
9. Jones, D.E.G., Brousseau, P., Fouchard, R.C., Turcotte, A.M., Kwok, Q.S.M. Thermal characterization of passivated nanometer size aluminium powders 2000 Journal of Thermal Analysis and Calorimetry 61 (3), pp. 805-818
10. Trunov, M.A., Schoenitz, M., Zhu, X., Dreizin, E.L., "Effect of Polymorphic Phase Transformations In Al_2O_3 Film on Oxidation Kinetics of Aluminum Powders" *Combustion and Flame*, V. 140 No 4, pp. 310-318 (2005)
11. Trunov, M.A., Schoenitz, M., Dreizin, E.L., "Effect of Polymorphic Phase Transformations in Alumina Layer on Ignition of Aluminum Particles" *Combustion Theory and Modeling*, 10 (4) pp. 603-624 (2006)
12. Trunov, M.A., Umbrajkar, S.M., Schoenitz, M. Mang, J.T., Dreizin, E.L. "Oxidation and Melting of Aluminum Nanopowders" *Journal of Physical Chemistry B*, 110(26), pp. 13094-13099 (2006)
13. Vyazovkin, S.; *Journal of Computational Chemistry*, **2001**, 22, 178.
14. Starink, M.J.; *Thermochimica Acta* 404 (2003), 163-176
15. Burtin, P., Brunelle, J.P., Pijolat, M., and Soustelle, M.; *Applied Catalysis*, 34 (1987) 239-254
16. Zhou, R-S, and Snyder, R.L, "Structures and transformation mechanisms of the η , γ , θ transition aluminas" *Acta Cryst. B* 47 (1991), 617-630
17. Dewaele, O., and Froment, G.F., "TAP study of the sorption of CO and CO_2 on $\gamma\text{Al}_2\text{O}_3$ " *Applied Catalysis A* 185 (1999) 203-21

5. Oxidation of aluminum particles in mixed CO₂/H₂O atmospheres

5.1. Introduction

Advances in computational capabilities enable increasingly more detailed modeling of combustion dynamics in various energetic systems. Respective fluid dynamics and heat transfer processes are being described more and more accurately using both novel modeling approaches [1-3] and detailed numerical schemes [4, 5].

However, contemporary combustion models still rely on very simplified and often inaccurate submodels to describe the dynamics of ignition and combustion of metals present in energetic formulations. For aluminum, the most common metallic additive in both propellants and explosives, ignition is commonly described by a somewhat arbitrarily chosen fixed ignition temperature as reviewed in ref. [6] and combustion is modeled to fit the “d-power law” inferred from a modified hydrocarbon droplet combustion model [7]. Many experimental studies, e.g., [8-10] have shown such simplified descriptions for both ignition and combustion of aluminum to be inadequate. In particular, recent research on aluminum particle ignition has shown that it is controlled by diffusion processes of oxygen and aluminum through the surface oxide, and that this diffusion is critically affected by polymorphic phase changes occurring in alumina upon heating [11,12]. A quantitative oxidation model was developed [12] describing ignition of aluminum particles in O₂/N₂ environments reasonably well [13]. It is interesting that aluminum melting, often hypothesized to result in “cracking” of the oxide film due to the difference in the thermal expansion coefficients for aluminum and its oxide [14], plays effectively no role in the model proposed in ref. [12], which was based on thermo-analytical experiments performed in O₂/Ar environments. In such experiments, aluminum melting was clearly registered, but it did not correlate in any way with the observed oxidation processes.

Further development of this reaction model is desired to describe aluminum oxidation and ignition kinetics in practical environments. This is the main objective of the present study. Most energetic formulations include hydrocarbon energetic compounds, which react or gasify faster than aluminum, so that the igniting aluminum particles are surrounded by the respective reaction products, including H₂O and CO₂. Recent research expanding on the thermo-analytical studies [11,12] addressed oxidation kinetics for aluminum powders in H₂O [15] and CO₂ [16] serving as oxidizers instead of, or in addition to oxygen. In all oxidizers, aluminum oxidation can be described as a sequence of relatively well-defined stages. The presence of H₂O causes an additional oxidation step to occur, which is clearly associated with aluminum melting, unlike in cases when the oxidizers are either O₂ or CO₂ or respective mixtures. In H₂O/O₂ environments, the magnitude of the oxidation step occurring upon Al melting correlates with the concentration of H₂O, but is effectively independent on the concentration of O₂ [15]. The mechanism of this oxidation step is poorly understood and warrants further investigation. This paper continues the experimental study begun in refs. [11,12,15,16], and addresses oxidation reactions and their kinetics for aluminum powders in mixed O₂/CO₂/H₂O oxidizers.

5.2. Experimental

Experiments were organized similar to the previous experiments performed in H₂O, CO₂, and mixed H₂O/O₂ and CO₂/O₂ oxidizers [15,16]. Spherical aluminum powder (Alfa Aesar, 3-4.5 μm nominal size, 97.5 %) was heated in a Netzsch STA409PG thermal analyzer using a thermogravimetric (TG) sample carrier with a 17 mm diameter flat corundum plate to hold the

sample. To study the effect of particle size, spherical aluminum with nominal sizes of 4.5-7 μm (Alfa Aesar, 97.5 %), and 10-14 μm (Alfa Aesar, 98 %) were used in a subset of the experiments.

The furnace of the STA409PG is connected to a pressurized boiler, which is held at 180 $^{\circ}\text{C}$. The connecting lines are also all heated above 150 $^{\circ}\text{C}$ to prevent condensation. The gas flow pattern of the STA409PG was modified from its default configuration to increase homogeneity of the purge gas. The oxidizers steam, carbon dioxide, and oxygen, were fed into the furnace from the same port, allowing them to mix before they entered the sample location while in the original setup, different gases are fed into the furnace at opposite ends, leading to potential mixing problems. Argon is introduced into the furnace in two locations. The first, and invariant, gas flow of 20 mL/min, serving to protect the thermobalance from condensation, enters the furnace from below. Due to the furnace geometry, it has a negligible contribution to the atmosphere that the sample is exposed to. The second argon flow was used as a carrier gas for steam, entering the furnace from above; its flow rate could be widely varied. The steam flow rate could also be varied over a wide range. In experiments where carbon dioxide or oxygen was required, part of the argon carrier gas flow was replaced with the respective oxidizing gas. In all experiments, argon, carbon dioxide, water, and oxygen were present in varying proportions. The total gas flow was in the range of 100-200 mL/min. Figure 5.1 shows an overview of the gas compositions used in this study.

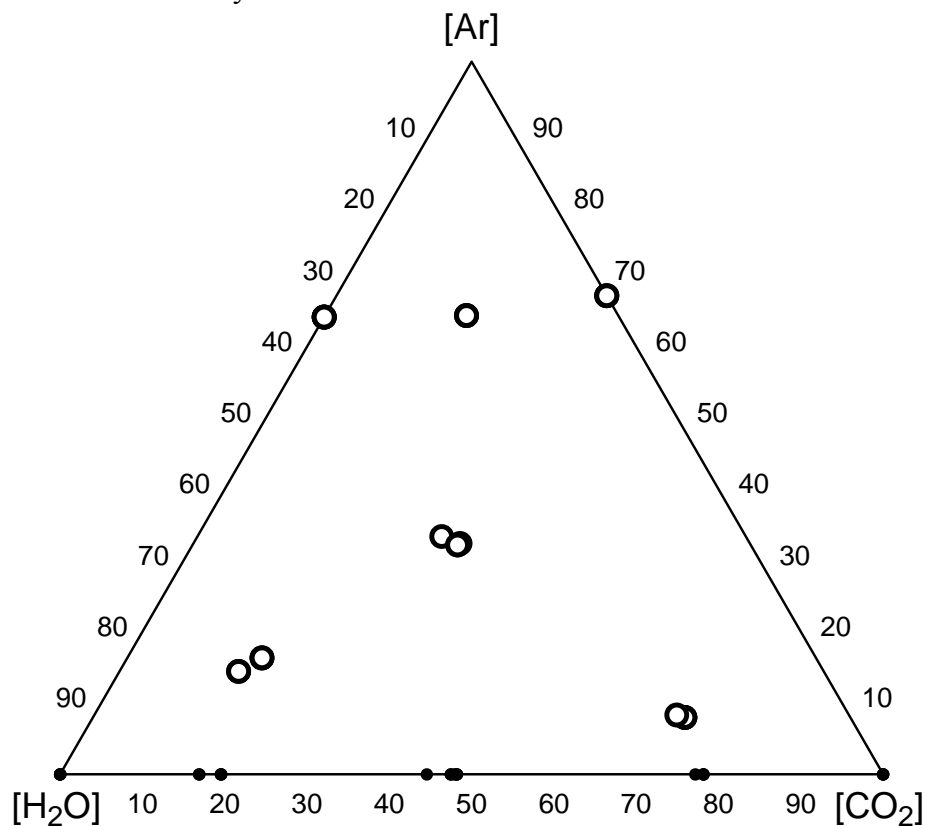


Fig. 5.1. Open circles are the compositions in vol-% of the atmospheres used in this work. Smaller filled symbols along the bottom edge are projections of the actual compositions onto the H₂O-CO₂ binary system.

To mitigate substantial loss in the surface area of aluminum upon melting and associated particle coalescence, the samples were prepared as mixtures of aluminum with 150-nm α -alumina powder (Inframat Advanced Materials, 99.8 %). The powders were mixed using an ultrasonic bath and the final samples contained approximately 25 wt-% free Al. The furnace with TG sample holder was calibrated using a set of certified pure metals, the melting points of which were recovered from the recorded sample temperature as a function of time.

Heating rates were varied from 2 to 20 K/min.

5.3. Results

Qualitative differences of aluminum oxidation observed in H_2O , CO_2 , and mixed $\text{H}_2\text{O}/\text{CO}_2$ environments are illustrated in Fig. 5.2. To make comparison easier, the bold lines show measurements at 5 K/min for each environment, while other heating rates are shown as thin lines. The oxidation in all environments shown in Fig 5.1 proceeds nearly identically until about 900 K. The stepwise weight increase between about 750 K and 900 K has been previously observed in dry oxygen, and was attributed to the transition of the surface oxide from its amorphous form to the more stable γ polymorph [11,12]. Following this step, the oxidation rate decreases in CO_2 [16], as it does in O_2 [11], and gradually increases over the temperature range 1000 – 1250 K. At this point the surface oxide transforms to the α polymorph, which reduces the reaction rate once more. In CO_2 , like in O_2 , aluminum powder does not oxidize completely until temperatures above ~ 1700 K are reached. In contrast to this behavior, an additional stepwise weight increase is observed in steam near the melting point of aluminum at 933 K. The size of this step was previously found to correlate with the water concentration in $\text{H}_2\text{O}-\text{O}_2$ -Ar mixed atmospheres [15]. This step was attributed to higher diffusion rates through the oxide layer modified by the presence of water as it is stressed by the volume change of aluminum melting.

Further, oxidation in steam is complete at temperatures as low as 1250 K. These qualitative changes in oxidation behavior were attributed to changed properties of the γ -alumina surface layer in the presence of water [15].

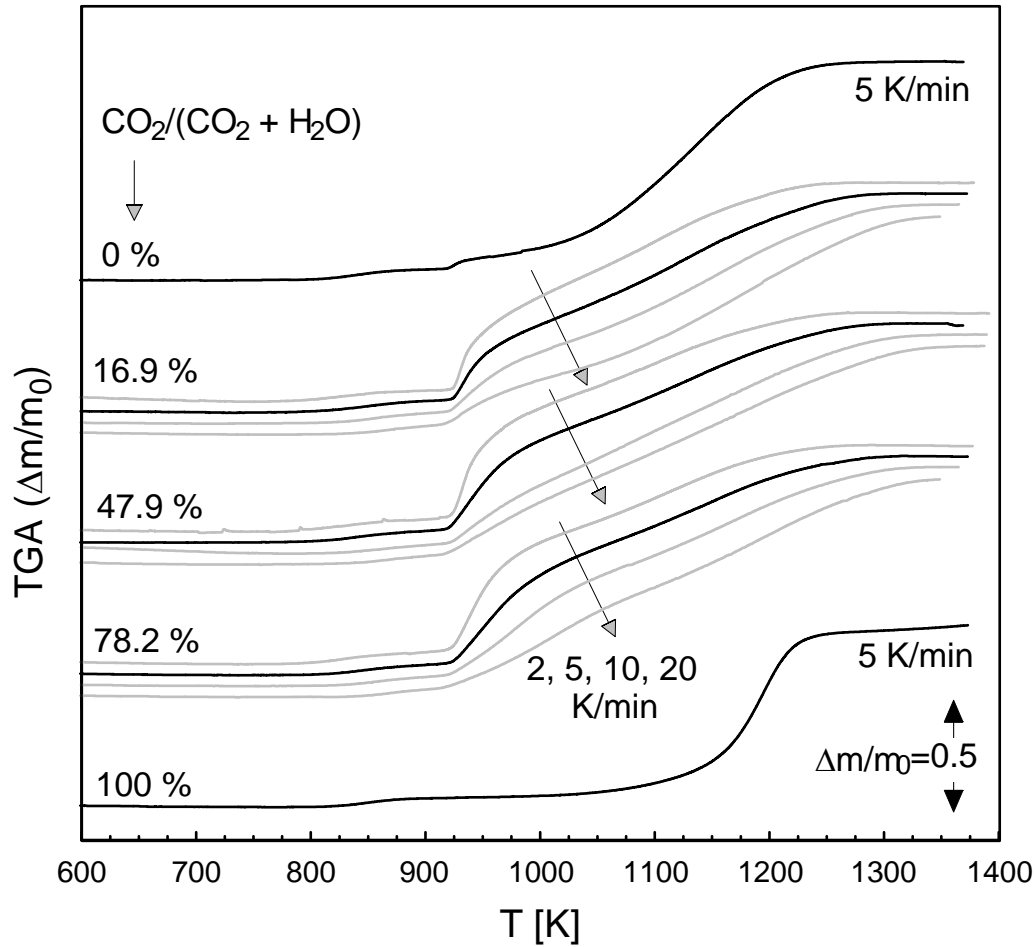


Fig. 5.2. Oxidation of aluminum with 3-4.5 μm nominal size in various oxidizing atmospheres. Measurements are grouped by oxidizer composition, and varying heating rates are shown within each group. Although the measurements are offset for clarity, the vertical scaling is the same.

In $\text{H}_2\text{O}/\text{CO}_2$ gas mixtures, oxidation is qualitatively similar to oxidation in steam: a stepwise weight change is observed at the aluminum melting point, and oxidation is complete at comparatively low temperatures. However, the weight change associated with aluminum melting is much larger than observed in steam in the absence of CO_2 , while the oxidation rate following this step is slightly lower than in either CO_2 or H_2O alone. The size of this step increases with increasing concentration of CO_2 , although it is not observed at all when H_2O is completely absent.

Figure 5.3 shows measurements at 5 K/min for aluminum powders with different particle sizes.

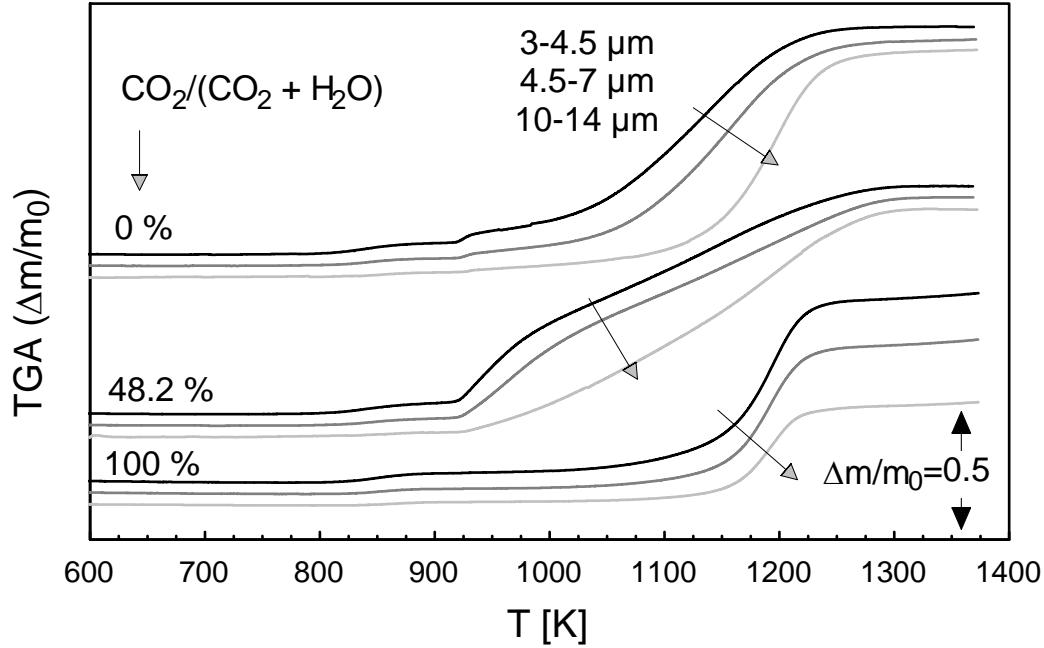


Fig. 5.3. Oxidation of aluminum with varying particle sizes in various oxidizing atmospheres. Measurements are grouped by oxidizer composition, and nominal particle sizes are shown within each group. Although the measurements are offset for clarity, the vertical scaling is the same.

5.4. Reaction kinetics

Measurements at varying heating rates are shown as thin lines in Fig. 5.2. In order to quantitatively relate the new measurements to previous investigations of oxidation of aluminum powder, oxidation kinetics were determined according to a formalism [12] first introduced for aluminum oxidation in oxygen. Particles are assumed to be spherical and oxidation is assumed to occur as a series of individual diffusion processes through the growing surface oxide layer. In this model, at any given time the rate of oxidation is limited by a single, thermally activated mass transfer process, such as diffusion of one species. The recorded TGA traces are processed according to the following equation:

$$\frac{E}{RT} = \ln C_A^* - \ln \left(\frac{dm}{dt} \right) - \ln \left(\frac{1}{r_{Al}} - \frac{1}{r_{ox}} \right) \quad (5.1)$$

where T is temperature, t is time, C_A^* is the combined oxidation constant depending on the reaction stoichiometry, the initial sample mass, and the type of the diffusing species; r_{Al} and r_{ox} are the radii of the aluminum core and oxide shell, respectively; E is the activation energy, and R is the universal gas constant. For details of the derivation, please see Ref. [12].

The right side of Eq. (5.1) depends only on the experimental sample mass, and is readily plotted vs. inverse temperature to identify regions that can be described by a positive slope. This is shown in Fig. 5.4. For each such region, the assumptions used to derive Eq. (5.1) are considered valid so that the slopes represent the activation energies of the specific reaction processes governing oxidation at the respective values of the reaction progress. Fig. 5.4 also shows that despite numerical smoothing, the continuously calculated “instantaneous activation energy” is very noisy, although relatively constant regions can be identified at low and high

temperatures, respectively. To aid classifying the results, all experiments that were performed were therefore processed identically. Intervals in $1/T$ were identified where the slope of the plot of the RHS of Eq. (5.1) vs. $1/T$ was continuously positive. The assumptions for Eq. (5.1) were considered valid in these intervals; therefore respective values of $1/T$ above the 10th percentile were averaged, and the standard deviation was calculated. Three such intervals were identified for each measured TG trace. They were assigned to the growth of amorphous alumina, reaction associated with aluminum melting, and growth of γ -alumina, occurring respectively at decreasing values of $1/T$ or increasing temperatures, similar to earlier observations [15, 16]. These intervals in $1/T$ correspond to specific intervals in temperature, and in the degree of oxidation, α . Therefore, the end points in T and in α of these intervals were also recorded. Figure 5.5 shows these intervals for experiments performed at different heating rates and in different environments. Fig. 5.6 shows activation energies corresponding to the growth of amorphous and γ -alumina corresponding to the first and third of these intervals.

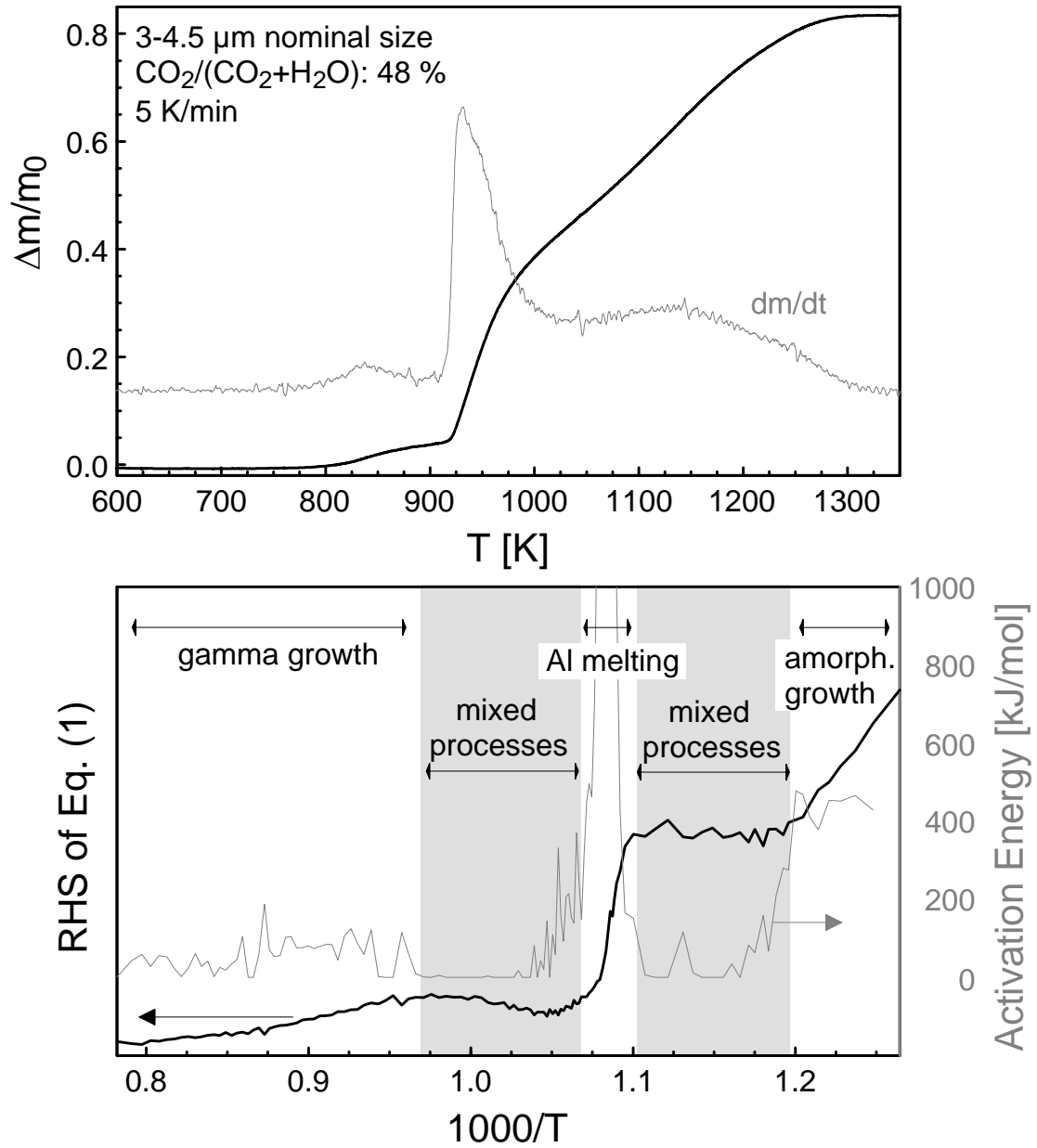


Fig. 5.4. Kinetic processing of a measurement at 5 K/min with an intermediate CO_2 concentration. The first panel shows the measurement and its derivative, while the bottom panel shows the RHS of Eq. (5.1) plotted vs. inverse temperature. Also shown is the derivative, indicating the “instantaneous activation energy”.

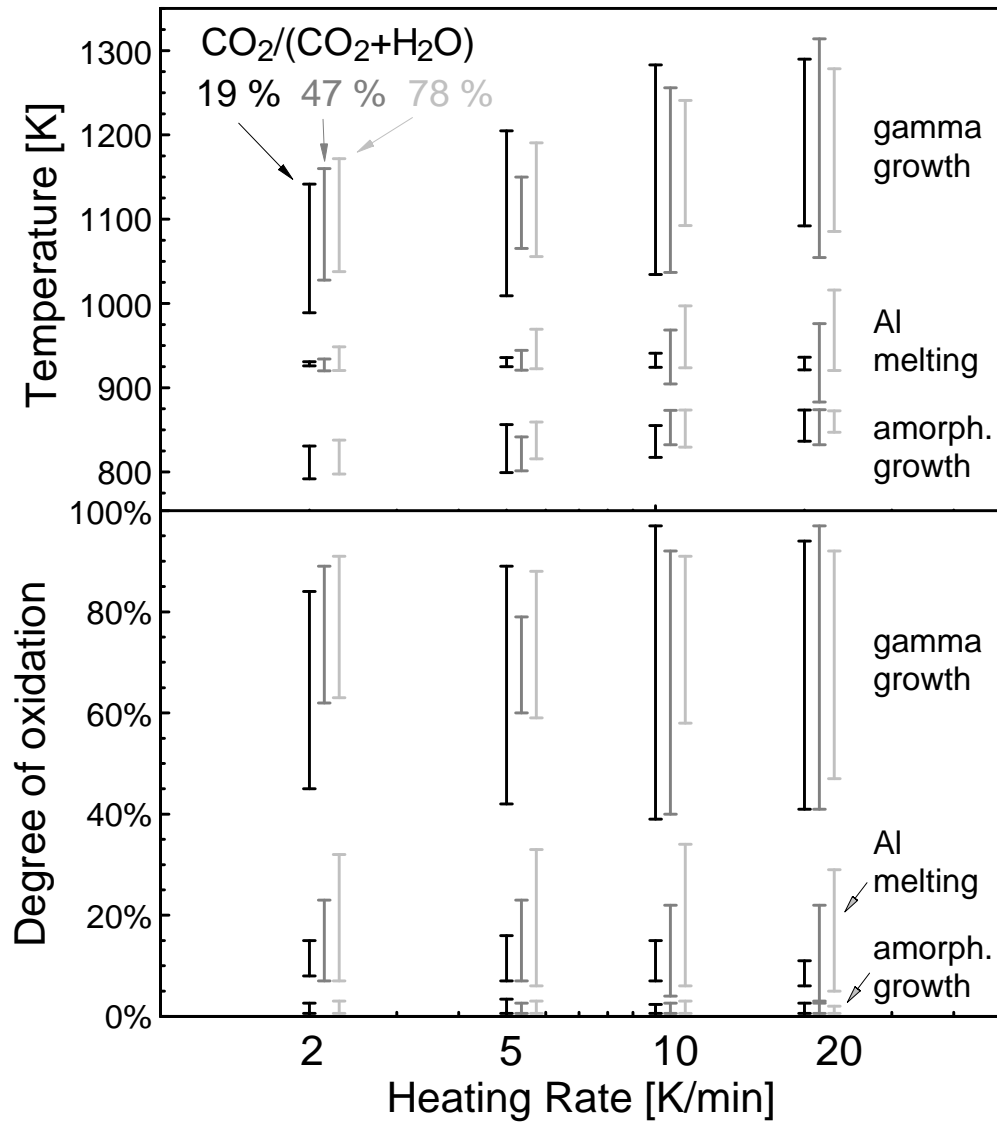


Fig. 5.5. Intervals where the RHS of Eq. (5.1) shows a consistently positive slope vs. $1/T$. Shown are all measurements from Fig. 5.2 where multiple heating rates were available. Different oxidizer compositions are offset for clarity, although the heating rates for each group is the same.

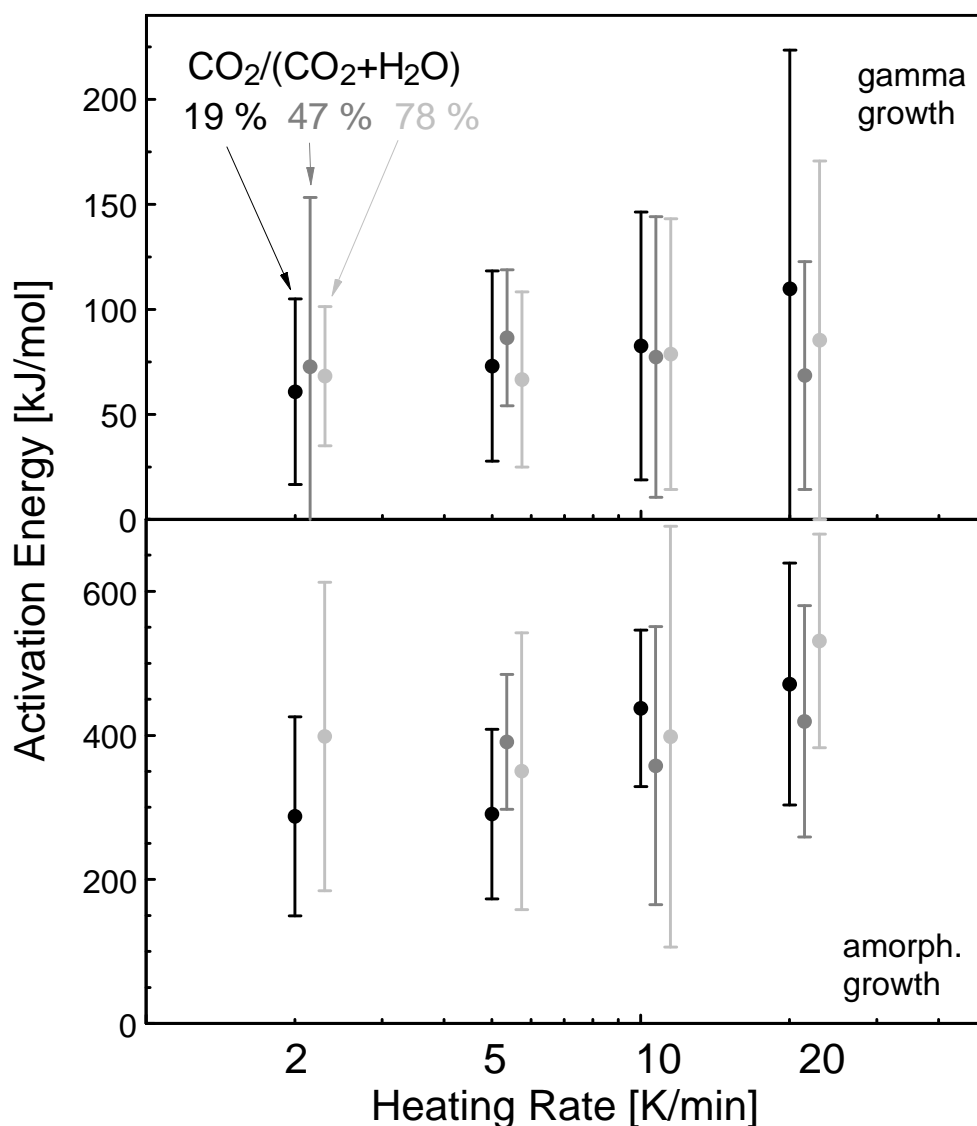


Fig. 5.6. Activation energies calculated for different oxidation stages, heating rates, and oxidizer composition. See text for a detailed explanation. Different oxidizer compositions are offset for clarity, although the heating rates for each group is the same.

It is observed that in the first and final oxidation phases (growth of amorphous alumina corresponding to the reaction progress below 5 % and growth of γ -alumina occurring at reaction progress above 50 %, respectively), the results for different heating rates largely overlap. For large reaction progress values, the resulting activation energy is consistently between 50 and 100 kJ/mol for different runs, suggesting that for that stage the oxidation rate is controlled by a single process. For the initial stages of reaction, the resulting activation energy increases slightly from about 300 to about 450 kJ/mol as the heating rate increases from 2 to 20 K/min. This is likely an indication that the reaction rate during this step is limited by more than a single process.

The stage associated with Al melting includes a sharp initial peak, caused by the Al melting itself, and, and a lower shoulder at higher reaction progress values, which is again consistent between heating rates. Calculating activation energies in this range is not meaningful,

but it can be noted that both, the temperature interval and the range of the degree of oxidation increase with increasing CO₂ concentration as well as with increasing heating rate.

5.5. Discussion

Despite the fact that the oxidation step at the Al melting point has been observed before when water was the only oxidizer, the behavior in combined CO₂/H₂O oxidizers is quantitatively different. As Fig. 5.2 illustrates, the oxidation step at moderate H₂O concentrations is much more pronounced in the presence of CO₂, than at higher H₂O concentrations in the absence of CO₂. In a previous study on mixed H₂O/O₂ oxidizers, it was found that the size of this oxidation step only correlates with the concentration of H₂O, and is independent of the concentration of O₂ [15]. It has therefore been hypothesized that water may play a structural role in the growing surface layer of γ -alumina, and that this changes the transport properties of the surface oxide. A possible mechanism for this is that H₂O could thermodynamically stabilize the surface of the continuously forming alumina, so that its most stable form is not the bulk material but nm-sized crystallites [17]. A surface layer consisting of such crystallites may not pose any mechanical resistance to breaking up under the stress imposed by the melting aluminum core.

CO₂, on the other hand, in the absence of water does not cause increased oxidation rates when aluminum melts, suggesting that CO₂ may not influence the permeability of the surface oxide [16]. However, it was also found that the transformation rates between transition aluminas was influenced by the presence of CO₂, likely via surface adsorption [16,18] suggesting that CO₂ could affect the stability of the surface oxide. Therefore, the following scenario becomes possible. Water may stabilize small alumina crystallites, which when the surface oxide is stressed, aids the penetration by all oxidizers, including CO₂. Stabilization of nano-sized alumina crystallites by adsorbed CO₂ or its decomposition products (CO and C) effectively delays their eventual sintering and shifts the healing of the oxide layer to temperatures higher than in the absence of CO₂.

Another possibility is that the hydrogen that is generated by the reaction of aluminum and water proceeds to react with fresh CO₂ to form CO and water. This may substantially increase the effective local H₂O concentrations, especially in the porous samples used in this TGA study. The locally increased availability of H₂O could amplify the effect of water on the growing γ -alumina layer. Note that local production of water directly on the surface of alumina in this scenario may be more effective in modifying the alumina structure than increase in the water concentration in the oxidizing gas.

The ranges for activation energies observed for the oxidation of aluminum powder in mixed CO₂/H₂O atmospheres are broadly consistent with previous observations. In O₂, as in CO₂, the first oxidation step, attributed to the initial formation of γ -alumina, was associated with activation energies of 458 kJ/mol, and 562 kJ/mol, respectively [12,16]. In Fig. 5.6, the first observed oxidation phase below 5 % reaction progress falls approximately in that range.

The following growth phase of the γ polymorph was associated with activation energies in the 200-250 kJ/mol range in O₂ and CO₂ [12,16]. From Fig. 5.4 it is evident that the oxidation stage that includes the step on Al melting involves at least two separate processes. The melting of Al itself is an equilibrium process, and therefore has an infinite activation energy, visible as the initial peak with an unphysical maximum. The ensuing oxidation is thermally activated, and the corresponding activation energy can be determined from the shoulder towards

higher reaction progress values. Observed activation energies are in the 200-300 kJ/mol range, consistent with γ oxide growth in O_2 and CO_2 .

The only unexplained feature in CO_2/H_2O mixed oxidizers is the final oxidation phase identified in Fig. 5.5 above 50-60 % reaction progress. Activation energies are near 100 kJ/mol throughout, contrary to what was observed previously for the growth of either γ alumina or of other transition polymorphs [12, 16].

5.6. Conclusions

The oxidation of spherical aluminum powder was investigated by thermogravimetry in mixed CO_2/H_2O atmospheres. The oxidation process is qualitatively similar to previous observations where H_2O was the only oxidizer. An initial stepwise weight increase of less than 5 % is followed by a more pronounced step at the Al melting point. The size of this step is larger than what was observed for pure H_2O , it depends on the oxidizer composition with the observed maximum at high CO_2 and low H_2O concentrations. Oxidation is complete at temperatures as low as 1250 K.

Activation energies were evaluated for all oxidation steps using an explicit kinetic model describing the diffusion of oxidizing species through a growing surface oxide layer. Values for activation energies determined in this study are broadly consistent with values previously reported for oxidation in the respective component oxidizers O_2 , CO_2 , and H_2O .

Future work will incorporate the observations presented here in a quantitative oxidation model that will be used to describe oxidation and ignition of aluminum particles in oxidizers of arbitrary compositions and over a range of heating rates of interest for combustion applications.

5.7. References

1. Frost, D.L., Ornthanalai, C., Zarei, Z., Tanguay, V., Zhang, F. 2007 Journal of Applied Physics 101 (11), art. no. 113529
2. Baer, M. R. Thermochimica Acta 384 351–367 (2002)
3. Eakins D.E., N.N. Thadhani, N.N., Acta Materialia 56 1496–1510 (2008)
4. Fang, T. 2008 Journal of Thermophysics and Heat Transfer 22 (2), pp. 313-315
5. Yoh, J.J., Kim, K.-H. 2008 Journal of Applied Physics 103 (11), art. no. 113507
6. Trunov, M.A., Schoenitz, M., and Dreizin, E.L., “Ignition of Aluminum Powders under Different Experimental Conditions” Propellants Explosives and Pyrotechnics, V. 40, No 1, pp. 36-43 (2005)
7. Beckstead, M.W. 2005 Combustion, Explosion and Shock Waves 41 (5), pp. 533-546
8. Dreizin, E.L., "Experimental Study of Stages in Aluminum Particle Combustion in Air", Combustion and Flame, 105:541-556 (1996)
9. Dreizin, E.L., "On the Mechanism of Asymmetric Aluminum Particle Combustion", Combustion and Flame 117:841-850 (1999)
10. Brooks, Kristen P., Beckstead, Merrill W. "Dynamics of aluminum combustion" Journal of Propulsion and Power 11 (4), pp. 769-780 (1995)
11. Trunov, M.A., Schoenitz, M., Zhu, X., Dreizin, E.L., “Effect of Polymorphic Phase Transformations In Al_2O_3 Film on Oxidation Kinetics of Aluminum Powders” Combustion and Flame, V. 140 No 4, pp. 310-318 (2005)

12. Trunov, M.A., Schoenitz, M., Dreizin, E.L., “Effect of Polymorphic Phase Transformations in Alumina Layer on Ignition of Aluminum Particles” *Combustion Theory and Modeling*, 10 (4) pp. 603-624 (2006)
13. Mohan, S., Trunov, M.A., and Dreizin E.L. “Heating and Ignition of Metallic Particles by a CO₂ Laser” *Journal of Propulsion and Power* 24 (2) pp. 199 – 205 (2008)
14. Rozenband, V.I., Vaganova, N.I. A strength model of heterogeneous ignition of metal particles 1992 *Combustion and Flame* 88 (1), pp. 113-118
15. Schoenitz, M., Chen, C. and Dreizin, E. L., “Oxidation of Aluminum Particles in the Presence of Water”, *J. Phys. Chem. B*, in press (2009)
16. Zhu, X., Schoenitz, M. and Dreizin, E. L., “Aluminum Powder Oxidation in CO₂ and Mixed CO₂/O₂ Environments”, *J. Phys. Chem. C*, in press (2009)
17. Łodziana, Z. Topsøe, N.-Y., Nørskov, J.K. *Nature Materials*, (2004), 3, 289.
18. Dewaele, O., and Froment, G.F., “TAP study of the sorption of CO and CO₂ on γ Al₂O₃” *Applied Catalysis A* 185 (1999) 203-210

6. Heating and Ignition of Metallic Particles by a CO₂ Laser

6.1. Introduction

Reactive metals and metalloids, e.g., Al, B, Mg, Zr, Ti, Li, etc., as well as their alloys are promising ingredients for high energy density compositions used in propulsion systems, explosives, and pyrotechnics. Metallic powder fuel additives enable one to achieve higher combustion enthalpies and reaction temperatures. In most practical systems, metal ignition and combustion occur in environments with rapidly changing temperatures and gas compositions. On the other hand, most of the available quantitative characteristics describing ignition and combustion of metal particles were obtained from laboratory experiments in which the environment temperature and composition were carefully controlled. Thus, ignition of metallic particles has been often characterized by a predetermined ignition temperature [1, 2]. Ignition is also commonly assumed to occur after an ignition delay, which is estimated as the time required to preheat the particle up to the ignition temperature. The ignition temperature is classically understood in terms of the Semenov’s thermal theory as the minimum environment temperature which leads to self-sustaining combustion of an inserted particle [3, 4]. This definition has been successfully used for applications where the heating rates are characteristically low, e.g., dealing with fire safety and ignition of solid fuels in large furnaces [5, 6]. However, it becomes inadequate for applications in which the particles are heated rapidly, and the particle’s temperature can exceed the classically defined ignition temperature before the self-sustaining combustion is established. Furthermore, the whole concept of ignition temperature appears inadequate considering the nature of heterogeneous oxidation leading to ignition of most metals. For example, for aluminum, the thermally accelerated heterogeneous oxidation producing the heat necessary for a self-sustaining combustion also accelerates the growth of a protective oxide layer, which could prevent the combustion from occurring. This situation is typical for metal particle ignition in explosives, propellants and pyrotechnics. Thus, to describe ignition for such application, it is necessary to analyze specific transient heat transfer problems in which one or more of the exothermic processes leading to the particle ignition are considered. Such analyses require quantitative descriptions of these, typically thermally controlled, exothermic processes

balanced by the conventional heat transfer terms of convection and radiation. The kinetics of exothermic reactions in related energetic materials is commonly characterized by thermal analysis, where the heating rates are very low, on the order of 1 – 50 K/min. The extrapolation of the identified kinetics to the high heating rates is difficult and requires direct experimental verification. This difficulty led to development of new experimental approaches to directly characterize ignition kinetics for the heating rates in the range of $10^3 - 10^4$ K/s [7, 8]. However, the practically interesting heating rates of 10^6 K/s range have not been achieved. Also, there is a critical difficulty in the interpretation of all the experimental data dealing with ignition of metal powders, which is caused by the presence of particles of different sizes. The heating rates are different for particles of different sizes, and so must be the rates of the thermally controlled processes leading to ignition. Therefore, interpretation of the experimental data obtained with regular, polydispersed metal powders is difficult while experiments with highly monodispersed particles are impractical.

This study presents a new experimental technique and the corresponding heat transfer model that enables one to quantify ignition kinetics for reactive particles heated at varied heating rates approaching to or exceeding 10^6 K/s. Therefore, the identified ignition kinetics must be directly useful in modeling ignition of such particles in practical applications involving rapid heating. The proposed experimental technique uses CO₂ laser heating of aerosolized powders, which is particle size sensitive. As a result, only particles in a narrow range of sizes are effectively heated and ignited. This allows interpreting the results using a detailed heat transfer model for the specific, effectively heated particle size, even though a commonly available polydispersed powder is used in experiments. The laser is fired at a minimum possible power at which ignition starts to be observed, so that only the most effectively heated particles are ignited. The technique allows achieving different particle heating rates by varying the speed of particles fed into the laser beam. The paper describes the developed experimental technique, the heat transfer model, and experiments aimed to calibrate the model using a metal powder with well-established ignition kinetics.

6.2. Technical Approach

The technical approach is based on feeding individual micron-sized metal particles into a focused CO₂ laser beam. Because the CO₂ laser wavelength (10.6 μm) is comparable to the particle diameter, the laser heating is particle size dependent and is most effective for the particles of about 3.4 μm in diameter (as discussed in detail below). The experiment is conducted in an oxidizing environment, so that if the laser power exceeds a specific threshold, the heated particles of 3.4 μm diameter start igniting when they cross the laser beam. A detailed heat transfer model is developed, taking into account heating of metal particles in the laser beam, thermally controlled heterogeneous exothermic reactions leading to ignition, convection, and radiation terms. The model needs to consider only the specified above particle diameter, while experiments are conducted with a commercial polydispersed Al powder. The model includes one adjustable parameter that is effective diameter of the focused laser beam. Specifically, it is the standard deviation for the Gaussian function describing the energy distribution across the laser beam. An experimentally determined laser power ignition threshold obtained for spherical Al particles, for which the kinetics of exothermic reactions leading to ignition has been recently described [9 – 12] is used to determine the adjustable parameter and thus to calibrate the model.

The calibrated model is validated by experiments conducted with the same particles but at different heating rates. The validated model can be used to determine ignition kinetics of different materials igniting in various environments.

6.3. Experimental

The powder used in these experiments was spherical, 99% pure aluminum with nominal average particle size of 4.5 – 7 μm by Alfa Aesar. The experimental setup is shown in Fig. 6.1 and includes a generator of an aerosol jet, a 125 W CO₂ laser (Synrad, Evolution 125) with a ZnSe convex lens (0.75" aperture and 4" focal length), and a modulated green laser (SUWTECH model DPGL-3000 by Photop Technologies, Inc) operated with a set of a semi-cylindrical and convex glass lenses to produce a laser sheet for the jet visualization. Also, not shown in the Fig. 6.1 but employed in the experiments were a digital camera (Panasonic GS-35), used to obtain particle streaks, and a photomultiplier tube (PMT) used to identify events of particle ignition. In addition, a power meter (Synrad, POWER WIZARD 250), was used to measure the laser beam energy and verify the accuracy of the pre-set laser power.

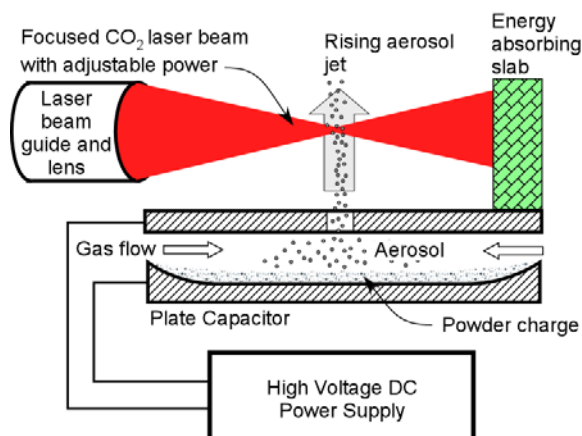


Fig. 6.1. Schematic diagram of the experimental setup.

The aerosol jet generator uses electrostatic aerosolization described elsewhere [13]. In this technique, a conductive (e.g., metal) powder is placed between the electrodes of a parallel plate capacitor. A high DC voltage in a range of 1-15 kV is applied and conductive particles acquire electric charge. They are repelled from the bottom electrode and attracted to the top electrode, at which they re-charge upon collision. The motion of the charging and re-charging particles continues so that an aerosol is produced in the space between the capacitor's electrodes. The applied voltage can be used to control the particle number density in the produced aerosol. In the device used in this project, a small opening (nozzle) was made in the center of the top electrode to allow formation of a thin aerosol jet escaping from the capacitor. The number density of the produced aerosol was maintained small so that the number of particles fed into aerosol jet was of the order of 1000 per second. The space between the capacitor's electrodes was enclosed in a chamber. A controlled air flow, measured by a gas flow meter (M-200SCCM-D by Alicat Scientific Inc.), was fed into the chamber to adjust the speed of the escaping laminar

aerosol jet. The speed could be readily controlled in the range of 0.1 - 3 m/s. An additional, slow (~ 0.1 m/s) shroud air flow (not shown in 6.1) was also produced around the aerosol jet which was found to enhance the jet's stability [13].

The aerosol jet was illuminated by a vertical green laser sheet. To enable particle image velocimetry, the laser sheet was modulated at 600, 1500 and 2000 Hz, depending on the jet speed. Produced particle streaks were recorded using the digital camera and the streak lengths were measured to determine the jet velocity.

The CO₂ laser was focused about 1.5 cm above the jet nozzle using an auxiliary red laser aligned with the CO₂ laser beam and the ZnSe lens. Once a stable aerosol jet was established, the CO₂ laser was fired continuously for 8 seconds, at a preset power level. The visible radiation, generated by heating and/or ignition of particles, was monitored using a photomultiplier connected to a PC-based data acquisition system. The streaks of heated particles were also visualized by a digital camera operated with a shutter open for the entire duration of the laser firing. The experiment was repeated with gradually increased laser powers until ignition was clearly observed. The peaks recorded by the PMT were analyzed to determine the minimum laser power needed for ignition for each specific aerosol jet velocity.

The images recoded by the digital camera showed short and bright streaks of particles crossing the laser beam. However, discrimination between the streaks produced by luminous particles that did not ignite and those that ignited and burned was ambiguous. Thus, using the PMT with a temporal resolution of 20 μ s was necessary for clear identification of the ignition events. Typical examples of PMT peaks produced by different particles crossing the laser beam are shown in Fig. 6.2. Figure 6.2 (a) shows a peak produced by a particle that ignited and burned. A sharp voltage rise is followed by small changes in the radiation signal occurring during the particle combustion. On the other hand, the peak shown in Fig. 6.2b shows the heating and cooling of the particle that never ignited, and the voltage rise is immediately followed by the voltage decrease as the particle exits from the beam. The minimum ignition threshold was determined if at least one ignition event was detected during an 8-s period the laser was fired. An 8-s experiment was performed at least three times for each laser power setting.

The experiment was performed for three different particle velocities, so that the igniting particles were heated at three different rates. Both the jet velocity and the laser power measurements were repeated immediately before and after each ignition experiment.

In a separate measurement, the effective diameter of the focused laser beam was evaluated. Because the laser energy is distributed across the beam according to a Gaussian profile [14], the laser beam diameter is poorly defined. However, experimentally this diameter was roughly assessed by firing the laser on a ceramic surface and measuring the diameter of the produced impression.

Figure 6.3 shows magnified images of the impressions obtained at 12.5 W, 25 W and 62.5 W laser powers with exposure time of 90 ms, 15 ms and 3 ms respectively. Minimum exposure times required to obtain an impression were used for each laser power setting. The sizes of the external and internal circles observed on the obtained impressions did not change as a function of the laser power and could indicate the diameters of the zone of thermal influence and of the laser beam, respectively. The diameter of the inner circle was measured to be close to 330 μ m. This size was considered as an initial approximation for the beam diameter. As described below, the width of the Gaussian distribution of the laser beam energy profile was used as an adjustable parameter in the developed heat transfer model. The measurement using the

laser beam impressions served as a guide for the reasonable range, in which the adjustable parameter could vary.

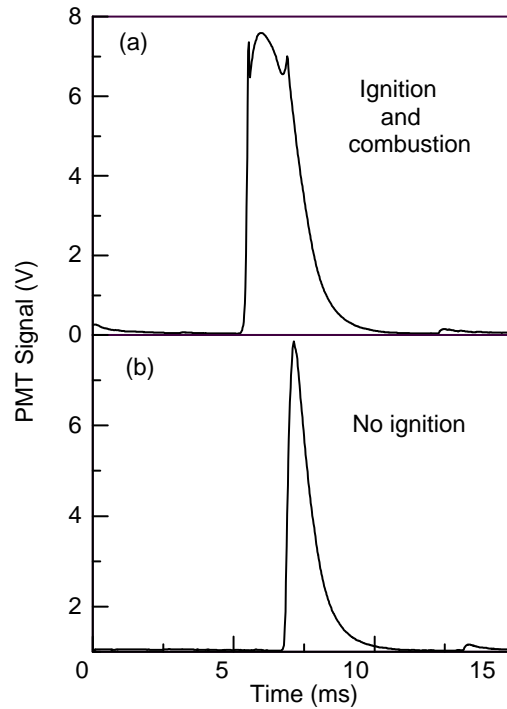


Fig. 6.2. PMT signal from micron size Al particles crossing the CO₂ laser beam. The aerosol jet velocity is 2.4 m/s and the laser power is 37.7 W: (a) Signal corresponding to ignition and combustion of a particle; (b) Signal corresponding to heating and cooling of an unignited particle.

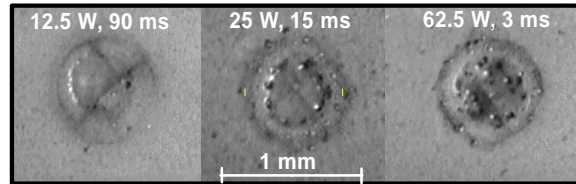


Fig. 6.3. CO₂ laser beam impressions on a ceramic plate obtained at different laser power levels. The impressions are painted over with a dark marker to improve contrast. The laser powers and exposure times are shown for each impression.

6.4. Heat Transfer Model

The model calculates the temperature history of a single particle heated by a focused CO₂ laser beam. The experimental aerosol jet is assumed to be sufficiently thin to neglect the interaction between the particles. The velocimetry data suggests the particle in the jet separated by few millimeters which is 1000 times the particle diameter. The particles are heated while crossing the laser beam, so that the characteristic particle heating times, determined by the

particle speed and the beam diameter are in the range of 0.1 – 3 ms. These times are much longer than the characteristic time of temperature equilibration within the particle, $\tau \approx D^2/\alpha \sim 0.1 \mu\text{s}$, where D is the particle diameter and α is the metal's thermal diffusivity. Thus, the temperature gradients within metal particles are neglected. The model considers only the particles of a selected diameter that are heated by the CO₂ laser most effectively. This diameter is determined below while analyzing the interaction of the laser irradiation with the metal particle.

The particle's temperature history is calculated using the heat balance:

$$MC \frac{\partial T_p}{\partial t} = \dot{Q}_{Laser} + \dot{Q}_{Chemical} - \dot{Q}_{Radiation} - \dot{Q}_{Convection} \quad (6.1)$$

where M is the particle mass, C is its specific heat, and T_p is its temperature; \dot{Q}_{Laser} is the heat transfer rate to the particle from the laser beam, $\dot{Q}_{Chemical}$ is the chemical heat generation rate, which is the term describing an exothermic process responsible for ignition, and $\dot{Q}_{Radiation}$ and $\dot{Q}_{Convection}$ are the radiation and convection heat transfer rates, respectively. The overall goal of the proposed experimental methodology and this model is to determine the term $\dot{Q}_{Chemical}$ as a function of temperature, and thus obtain the quantitative description of the ignition kinetics. Therefore, all the other heat transfer terms must be readily calculated. The radiation term is readily determined from the Stefan-Boltzmann law:

$$\dot{Q}_{Radiation} = \varepsilon \sigma_{SB} (\pi D^2) (T_p^4 - T_g^4) \quad (6.2)$$

where ε is emissivity, σ_{SB} is Stefan-Boltzmann constant, T_p and T_g are the particle and ambient air temperatures, respectively, and D is the particle diameter. The radiation heat loss does not play any significant role in determining particle temperature as it is always less than 1 % of the laser power absorbed by the particle.

The calculation of terms $\dot{Q}_{Convection}$ and \dot{Q}_{Laser} is less straightforward. The convection term was calculated considering that for micron-sized particles, the mean free path of the gas molecules is comparable to the particle diameter. As a result, a transition regime heat transfer model based on Fuchs' model [15 – 18] was used. The laser absorption efficiency of the particle was estimated by taking into account the absorption and scattering of the laser beam, due to comparable particle size and laser wavelength [19-21]. A theoretical analysis describing the laser heating of micron-sized metal particles was reported in the literature [19]. However, the effects of particle melting and the specific distribution of the laser power across the beam have not been considered. The analysis presented in Refs. [19-21] was reproduced and expanded in this paper. The width of the laser beam was difficult to determine and it was treated as an adjustable parameter. In order to find this parameter, in these experiments aluminum particles igniting in air were used, for which the ignition kinetics relations were reported recently [9 – 12]. Therefore, the term $\dot{Q}_{Chemical}$ was known so that the comparison of the predicted by this model and experimental results was used to fully define the laser heat input to the particle. The developed model and the fully quantified term \dot{Q}_{Laser} can be used to determine unknown $\dot{Q}_{Chemical}$ terms for different powders ignited in different environments.

Convection Term

For a 3.4 μm diameter particle in an atmospheric pressure air at room temperature, the value of Knudsen number (Kn) is close to 0.03. The conventional, continuum convection model is only valid for $\text{Kn} < 0.01$, and at greater values of Kn, a transition model needs to be considered. The correction for the dimensionless heat transfer coefficient or Nusselt number (Nu) is shown in Fig. 6.4 for a specific combination of the particle and gas temperatures as relevant to this work. It is clear that the correction is significant compared to $\text{Nu} \approx 2$ for continuum heat transfer. Recently, detailed Monte-Carlo simulations [15, 16] validated a simplified heat transfer model proposed by Fuchs [17, 18] for transition heat transfer regime. In the Fuchs' model, a particle is assumed to be surrounded by a hypothetical Langmuire's layer with thickness δ . The thickness of this layer is very close to the molecular mean free path in the ambient gas, λ_{MFP} , calculated in Ref. [15] as:

$$\delta \approx \lambda_{\text{MFP}} = \frac{4}{5} \frac{k_g(T_g)T_g}{P_g} \sqrt{\frac{m_g}{2K_B T_g}} \quad (6.3)$$

where k_g is the gas thermal conductivity, P_g is the gas pressure, m_g is the mass of the gas molecule, and K_B is the Boltzmann constant. Heat transfer within the Langmuire's layer is calculated using a free-molecular expression:

$$\dot{q} = \dot{q}_{\text{Free molecular}} = A\pi D^2 P_g \sqrt{\frac{k_B T_\delta}{8\pi m_g}} \frac{\gamma^* + 1}{\gamma^* - 1} \left(\frac{T_p}{T_\delta} - 1 \right) \quad (6.4)$$

where A is the accommodation coefficient, T_δ is the temperature at the boundary of the Langmuire's layer, and γ is the adiabatic index of the gas. The superscript '*' indicates that the value of γ is averaged over the temperature range of $(T_p - T_\delta)$, as described in Ref. [15].

Outside the Langmuire's layer, the heat transfer is calculated using a continuum regime heat transfer expression:

$$\dot{q} = \dot{q}_{\text{Continuum}} = \frac{4\pi(\delta + D/2)k_g(T_g)T_g}{i+1} \left[\left(\frac{T_\delta}{T_g} \right)^{i+1} - 1 \right] \quad (6.5)$$

where i is the power law dependence coefficient for the gas thermal conductivity (taken as $1/2$ for a mono-atomic gas). For a quasi-steady temperature profile, that can be used in this case, equations (6.4) and (6.5) are solved iteratively for the temperature at the boundary of the Langmuire's layer, T_δ . Once the boundary temperature is found, the rate of heat transfer from the particle to gas is calculated.

The Fuchs' model validated in Ref. [15] considered a mono-atomic gas and a definition of mean free path given by Eq. (6.3). A more generic definition for the mean free path, suitable for polyatomic gases is commonly considered, e.g. Ref. [16]:

$$\lambda'_{\text{MFP}} = \frac{4k_g(T_g)}{[9\gamma(T_g) - 5]P_g} [\gamma(T_g) - 1] \sqrt{\frac{\pi m_g T_g}{2K_B}} \quad (6.6)$$

In order to use the Fuchs' model validated in Ref. [15] to describe heat transfer in a polyatomic gas, Eq. (6.6) should replace Eq (6.3) while being corrected by a factor of ' $3/\sqrt{\pi}$ ', which is the difference between the two expressions when applied to a mono-atomic gas. Thus, the corrected Eq. (6.6) was used in this model. Properties of dry air [22] including the adiabatic index, γ , and thermal conductivity, k_g , were used. An accommodation coefficient of $A = 0.85$ for Al particle [23] was used. Figure 6.4 shows Nusselt number as a function of Knudsen number or particle diameter for a selected combination of particle and gas temperatures. The dashed curve was

calculated in Ref. [15] for mono-atomic gas and was reproduced here. The solid line, used in the present ignition model, shows a modified dependency taking into account properties of air as a diatomic gas.

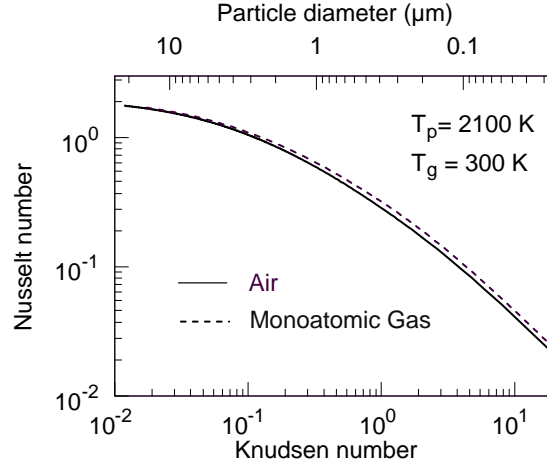


Fig. 6.4. Nusselt number as a function of Knudsen number (or particle diameter) is calculated for transition regime heat transfer using Fuchs' two layer model [15]. Calculations for mono-atomic gas are reproduced and the model is adapted for dry air.

Laser Heating Term

To determine the energy delivered to a particle from the laser beam, consider a particle that crosses a horizontal beam while moving along the vertical axis, z . The laser energy delivered to the particle is a function of the particle absorption efficiency, η , and laser spatial power density $I(z)$, and can be calculated as:

$$\dot{Q}_{Laser} = \frac{1}{4} \pi D^2 \eta(\lambda, D, f) I(z) \quad (6.7)$$

where η is the particle's laser absorption efficiency [19, 20] depending on the laser wavelength, λ , particle diameter, D , and material's complex refractive index, f . The laser power density $I(z)$, is commonly described by a Gaussian profile [14] and can be expressed as:

$$I(z) = \frac{W}{2\pi\sigma^2} \exp(-z^2/2\sigma^2) \quad (6.8)$$

where W is the total beam power and σ is the standard deviation for the beam's Gaussian function centered around $z=0$. The value of σ (or 6σ approximately equal to the beam diameter, D_{beam}) was varied as the model's adjustable parameter, as further discussed below.

The laser energy absorption efficiency as a function of particle size and temperature has been described in the literature for spherical metal particles [19, 20]. The absorption efficiency was calculated for the temperatures below the particle's melting point using the Mie's scattering theory. Drude's model was used to find the complex refractive index as a function of temperature. The computations presented in Ref. [19] were reproduced here for aluminum particles, as shown in Fig. 6.5. The calculations were also performed for other metals and it was observed that for a specific laser wavelength (10.6 μm for CO_2 laser), the absorption efficiency calculated using the Mie's scattering theory [19, 20], peaks at nearly the same particle size ($D \approx 3.37 \mu\text{m}$) for different metals. Because of this particle size selective heating, only the particles

with the peak absorption efficiency ignite at the threshold laser power in the present experiments. It should be noted that particle of diameter $3.37\text{ }\mu\text{m}$ is theoretically most efficient absorber of CO_2 laser energy and assumed to ignite first but practically there is a very narrow range of particle igniting at the threshold laser power. This range is sensitive to the size of laser power steps used to calculate the threshold. The use of $3.37\text{ }\mu\text{m}$ particle size for modeling the experiment is considered a good assumption.

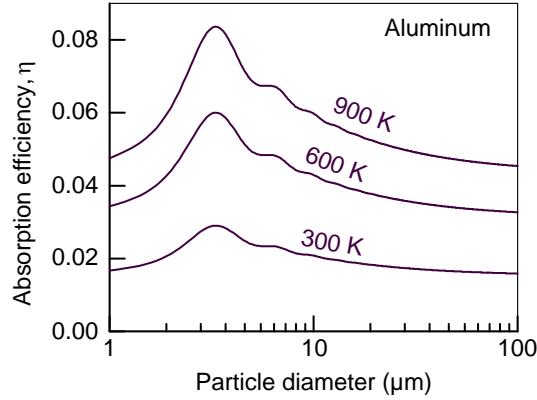


Fig. 6.5. CO_2 laser beam absorption efficiency as a function of aluminum particle size for different temperatures. The results are obtained in this work and reproduce the data reported earlier [19]. The peak efficiency occurs for the metallic particle diameter of $3.37\text{ }\mu\text{m}$, nearly independently of material.

The model was further modified to account for the effect of melting on the absorption efficiency [21]. On melting, the particle density changes abruptly [22] and the absorption efficiency experiences a jump as shown in Fig. 6.6.

The overall absorption efficiency for a particle undergoing melting was calculated as a weighted average of the efficiencies for its solid and liquid parts.

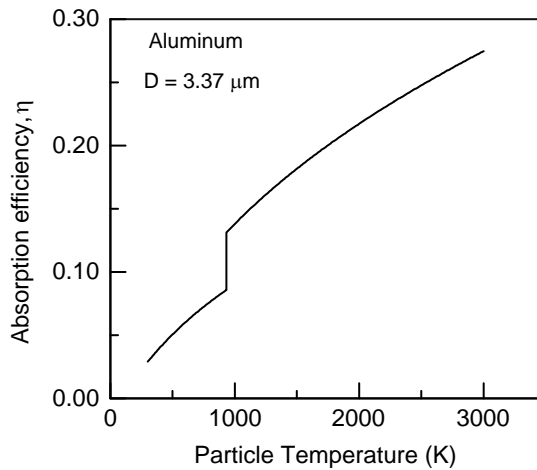


Fig. 6.6. CO_2 laser beam absorption efficiency as a function of aluminum particle temperature. The jump occurring upon melting is described in Ref. [21].

Chemical Term

For Al powder used in the experiments, the ignition model described recently [9 – 12] was used. The model calculates the rate of oxidation that is limited by the rate of transport of oxygen or aluminum through the protective surface oxide layer. As the particle temperature increases, different polymorphs of Al_2O_3 become stable [9, 24] and the model considers the kinetics of respective polymorphic phase transitions. The transformations accompanied by significant increase in density of alumina, such as amorphous to γ -alumina and γ - to α alumina can also be accompanied by disruptions in continuity of the protective oxide. Thus, the oxidation rates and respective heat release rates are predicted to increase rapidly when such phase changes occur. Further details of the oxidation model for aluminum particles are available in Ref. [12].

6.5. Results and Discussion

The model was used to predict the temperature history for a particle crossing a laser beam. The calculations were performed for different particle velocities, corresponding to the experimental aerosol jet velocities. For each calculation, the laser power was allowed to vary to find the threshold power at which ignition was predicted to occur. Figure 6.7 shows calculated Al particle temperature histories at three different particle velocities. The dashed curves show the particle temperatures when the laser power is just under the ignition threshold. The heating up and cooling down parts of the curves correspond to the particle's entrance to and exit from the laser beam. The solid curves, showing the particle temperature histories at the threshold power, are closely following the dashed curves during the initial heating period. The curves diverge as the particle temperature increases and the role of term $\dot{Q}_{\text{Chemical}}$ becomes increasingly significant.

The calculations were performed until the particle temperature reached the alumina melting point of 2320 K. Above this temperature, the analysis of heterogeneous processes rate limited by diffusion through the oxide layer is no longer relevant. Furthermore, the oxide coating can no longer remain protective and so the particles reached this temperature considered ignited.

Three cases illustrated in Fig. 6.7 correspond to different heating rates (or different velocities at which the particles crossed the laser beam.) It is clear that at lower heating rates, the predicted ignition threshold laser power is also lower.

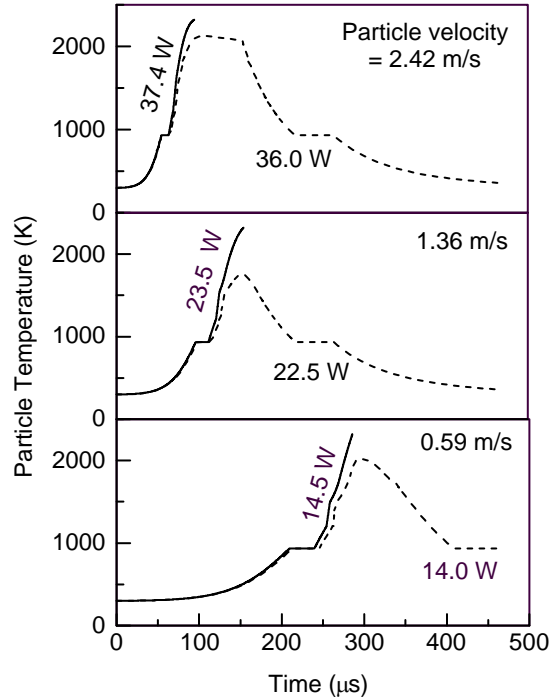


Fig. 6.7. Temperature histories for laser-heated 3.37 μm diameters Al particles calculated for three different particle velocities. The dashed lines show the cases when the laser power is just below the ignition threshold and the solid lines show the cases with the laser power at the threshold.

The breakup of particle heat balance is shown in Fig. 6.8 for the case of particle crossing the laser beam at 0.59 m/s and laser power at 14.5 W. The figure shows the laser and chemical heat input along with radiation and convection heat losses. Radiation heat loss is not significant as it is always less than 1 % of the laser heat input. Convection heat loss is responsible for almost all the heat loss by the particle. The chemical heat input comes into play only after the particle reaches certain temperature. The sharp increase after the melting plateau illustrates gas phase diffusion allowed by phase transformation of amorphous oxide to gamma oxide on particle surface. Once the gamma layer heals, the gas phase diffusion stops and shows up as sudden decrease in chemical heat input. Chemical heat release thereafter is calculated by diffusion through gamma oxide layer and its transformation to alpha oxide [9, 10].

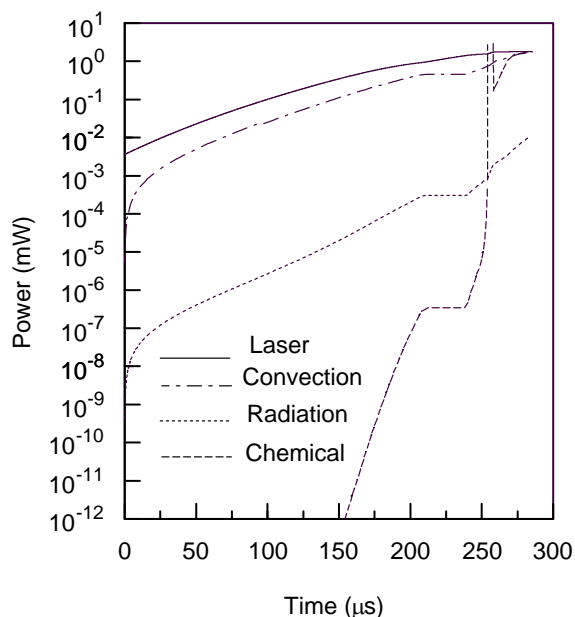


Fig. 6.8. Heat balance breakup of an Al particle of $3.37\ \mu\text{m}$ diameter crossing the CO_2 laser beam at $0.59\ \text{m/s}$. Convection heat loss is responsible for almost all the heat loss from the particle while radiation is always less than 1 % of the laser heat input. The shape of chemical heat input curve reflects phase transformation mechanism responsible for particle ignition.

Experimental laser power thresholds for ignition of Al powder at three different particle velocities are shown in Fig. 6.9. The powder ignited at $14.5\ \text{W}$, $23.5\ \text{W}$, and $37.4\ \text{W}$ for the particle velocities of $0.59\ \text{m/s}$, $1.37\ \text{m/s}$, and $2.42\ \text{m/s}$ respectively. For each pre-set laser power level, the ignition was detected optically, using the PMT ignition peaks. At the threshold power, at least one particle was observed to ignite during a period of 8 second. This ignition statistics is reasonable considering a small number of particles with diameters of about $3.37\ \mu\text{m}$ among polydispersed aluminum particles fed into the aerosol jet. In addition, only a fraction of the particles in the jet crossed the laser beam close to its centerline while the particles crossing the beam at its periphery were heated to a much lower temperature. The error bars for the threshold laser power show the step size used to adjust the laser power experimentally as well as the experimental error in the laser power setting. The error bars shown for the particle velocities represent the standard deviation for the velocity measurements based on the multiple recorded particle streaks.

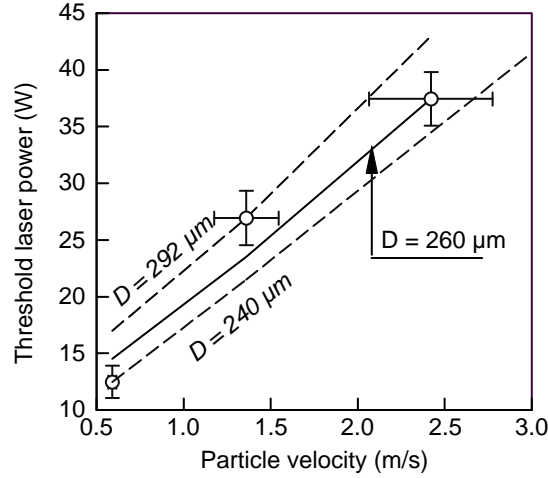


Fig. 6.9. Experimental results and calculated laser power thresholds for ignition of Al particles for different particle velocities (at different heating rates). Each line is calculated by selecting $6\sigma \approx D_{beam}$ to match one of the experimental points.

The adjustable parameter, 6σ , describing the width of the Gaussian profile for the energy distribution across the laser beam was varied between 240 μm and 292 μm to match the experimental laser threshold powers at different heating rates. For each measured threshold laser power corresponding to a specific heating rate, the value of 6σ was found at which the predicted laser power matched the experiment. This value was then used to predict the laser threshold powers for the entire range of heating rates used in experiments. Thus, the three resulting calculated lines are shown in Fig. 6.9; each line, as described above, was selected to match one of the experimental points exactly. Most importantly, for all three cases the overall predicted dependencies of the laser threshold power on the heating rate (or particle velocity) match well the experimental trend. The value of $6\sigma = 260 \mu\text{m}$, selected for the laser threshold power at the highest heating rate, appears to match the experimental points at different heating rates best and is considered as the final selection for the model's adjustable parameter.

The developed model describes the experiment adequately and the calibrated heat transfer term describing the CO_2 laser heating of metallic particles can now be used to determine the unknown ignition kinetics for powders other than spherical aluminum used in these experiments. The unknown term $\dot{Q}_{Chemical}$ can be found by matching the experimental and calculated trends for the laser power ignition threshold as a function of the heating rate and using the terms \dot{Q}_{Laser} , $\dot{Q}_{Radiation}$, and $\dot{Q}_{Convection}$ determined above.

6.6. Conclusions

A new experimental technique and respective heat transfer model, using transition regime heat transfer, have been developed for studying ignition kinetics of metallic powders at high heating rates. An experimental setup, in which aerosol particles are heated in a CO_2 laser beam was built and tested. The heating rates on the order of 10^6 K/s were achieved, which are close to

those occurring in many practical applications of metal-containing energetic materials. Because the experiment uses a CO₂ laser to heat micron-sized metallic particles, which are comparable to the laser beam wavelength, the heating is most efficient for the particles of a specific diameter, close to 3.37 μm . This particle size-selective heating simplifies dramatically the theoretical analysis of the heat transfer while allowing one to use regular polydispersed powders in experiments. The developed heat transfer model includes radiation, convection in the transition regime, and a detailed analysis of the heat transfer from a laser beam to metal particles. The model was calibrated comparing the calculations and experimental data acquired for spherical Al particles, for which the ignition kinetics parameters were determined elsewhere. The developed experimental technique and the heat transfer model enable one to quantify the kinetics of ignition of a metallic particle in a gaseous environment of interest. The heat transfer term describing the unknown ignition kinetics can be determined by matching the experimental and predicted laser power thresholds necessary for particle ignition at different velocities at which the particles cross the laser beam and, therefore, for different heating rates.

6.7. References

1. Evans, J.P., Borland, W., and Mardon, P.G., "Pyrophoricity of Fine Metal Powders," *Powder Metallurgy*, 19 (1), 1976, pp. 17-21.
2. Dugam, A.G., Muttalib, A., Gandhi, H.J., Phawade, P.A., John, A., and Khare, R.R., "Effect of Fuel Content and Particle Size Distribution of Oxidizer on Ignition of Metal-based Pyrotechnic Compositions," *Defence Science Journal*, 49 (3), 1999, pp. 263-268.
3. Rogers, R.N., "Thermochemistry of Explosives," *Thermochimica Acta*, 11 (2), 1975, pp. 131-139.
4. Pickard, J.M., "Critical Ignition Temperature," *Thermochimica Acta*, 392-393, 2002, pp. 37-40.
5. Annamalai, K., and Durbetaki, P., "A Theory on Transition of Ignition Phase of Coal Particles," *Combustion and Flame*, 29 (2), 1977, pp. 193-208.
6. Almada, S., Campos, J., and Gois, J. C., "Ignition and Pyrolysis of Explosive Components," *Proceedings of International Pyrotechnics Seminar*, 24th, 1998, pp. 827-831.
7. Ward, T.S., Trunov, M.A., Schoentiz, M., and Dreizin, E.L., "Experimental Methodology and Heat Transfer Model for Identification of Ignition Kinetics of Powdered Fuels," *International Journal of Heat and Mass Transfer*, 49 (25-26), 2006, pp. 4943-4954.
8. Shoshin, Y.L., Trunov, M.A., Zhu, X., Schoenitz, M., and Dreizin, E.L., "Ignition of Aluminum-Rich Al-Ti Mechanical Alloys in Air," *Combustion and Flame*, 144 (4), 2006, pp. 688-697.
9. Trunov, M.A., Schoenitz, M., and Dreizin, E.L., "Ignition of Aluminum Powders Under Different Experimental Conditions," *Propellants Explosives and Pyrotechnics*, 30 (1), 2005, pp. 36-43.
10. Trunov, M.A., Schoenitz, M., Zhu, X., and Dreizin, E.L., "Effect of Polymorphic Phase Transformations in Al₂O₃ Film on Oxidation Kinetics of Aluminum Powders" *Combustion and Flame*, 140 (4), 2005, pp. 310-318.
11. Trunov, M.A., Umbrajkar, S.M., Schoenitz, M., Mang, J.T., and Dreizin, E.L., "Oxidation and Melting of Aluminum Nanopowders," *Journal of Physical Chemistry B*, 110 (26), 2006, pp. 13094-13099.

12. Trunov, M.A., Schoenitz, M., and Dreizin, E.L., "Effect of Polymorphic Phase Transformations in Alumina Layer on Ignition of Aluminum Particles," *Combustion Theory and Modeling*, 10 (4), 2006, pp. 603-624.
13. Shoshin, Y., and Dreizin, E., "Production of Well-Controlled Laminar Aerosol Jets and Their Application for Studying Aerosol Combustion Processes," *Aerosol Science and Technology*, 36 (9), 2002, pp. 953-962.
14. Yilbas, B.S., "Laser Heating Process and Experimental Validation," *International Journal of Heat and Mass Transfer*, 40 (5), 1997, pp. 1131-1143.
15. Filipov, A. V., and Rosner, D. E., "Energy Transfer between an Aerosol Particle and Gas at High Temperature Ratios in the Knudsen Transition Regime," *International Journal of Heat and Mass Transfer*, 43, 2000, pp. 127-138.
16. Lin, F., Dann, K. J., Snelling, D. R., and Smallwood, G. J., "Heat Conduction from a Spherical Nano-particle: Status of Modeling Heat Conduction in Laser-induced Incandescence," *Applied Physics B*, 83, 2006, pp. 355-382.
17. Fuchs, N.A., "On the Stationary Charge Distribution on Aerosol Particles in a Bipolar Ionic Atmosphere," *Geophys. Pura Appl.*, 56, 1963, pp. 185-193.
18. Fuchs, N.A., *The Mechanics of Aerosols*, Pergamon Press, Oxford, 1964 (Dover Publications, New York, 1989).
19. Qiu, T. Q., Longtin, J. P., and Tien, C. L., "Characteristics of Radiation Absorption in Metallic Particles," *Journal of Heat Transfer*, 117 (2), 1995, pp. 340-345.
20. Bhormen, C. F., and Huffman, D. R., *Absorption and Scattering of Light by Small Particles*, Wiley, New York, US, 1983, pp.126-129, Chap. 4.
21. Graham, S. Arnold, "Absorptivity of Several Metals at 10.6 μm : Empirical Expressions for the Temperature Dependence Computed from Drude Theory," *Applied Optics*, 23 (9), 1984, pp. 1434-1436.
22. Weast, R.C., editor, *CRC Handbook of Chemistry and Physics*, 58th Edition, CRC Press, Cleveland OH, 1977
23. Saxena, S. C., and Joshi, R. K., *Thermal Accommodation and Adsorption Coefficients of Gases*, Hemisphere Pub. Corp., New York, US, 1989.
24. Levin I, and Brandon D., "Metastable Alumina Polymorphs: Crystal Structures and Transitions Sequences," *J. Am. Ceram. Soc.*, 81, 1998, pp. 1995-2012.

7. Aluminum Particle Ignition in Different Oxidizing Environments

7.1. Introduction

Aluminum powder is widely used as a fuel additive in solid propellants, explosives, and pyrotechnics. Ignition and combustion of aluminum particles have been extensively studied in the past, e.g., [1 – 3] with early work reviewed in ref. [4]. Initial combustion models were developed following the hydrocarbon droplet combustion formalism and then expanded to include condensed reaction products and their transfer between the particle and the flame zone [5 – 8]. Noticeably less attention was paid to aluminum particle ignition processes which could be equally or even more important for practical applications. Most commonly, ignition is assumed to occur at a specific temperature, varied from 1350 K [9] to 2370 K [10, 11] Despite extensive previous research, many of the aluminum ignition and combustion processes are not understood sufficiently well to enable their quantitative modeling. Currently, research of aluminum ignition and combustion in various configurations is very active involving both experimental [12-15] and

modeling [16-18] efforts. Quantitative description of particle ignition processes is of specific importance for the practical applications, in which such processes determine ignition delays and bulk burn rates for aluminum. Recently, an ignition model for aluminum particle in oxygen was suggested based on detailed thermo-gravimetric (TG) studies of aluminum powders oxidation [16]. Oxidation was established to occur in several steps, including growth of the initial amorphous oxide layer, a phase change from the amorphous to $\gamma\text{-Al}_2\text{O}_3$ polymorph accompanied by an increase in the oxide density and formation of discontinuities in a thin alumina scale, growth of $\gamma\text{-Al}_2\text{O}_3$ and its transformations into θ - and later $\alpha\text{-Al}_2\text{O}_3$ polymorphs. Each alumina polymorph presents a specific diffusion resistance and thus is oxidized at a specific rate. The polymorphic phase transitions result in stepwise changes in the oxidation rate. The rates of mass transfer processes accompanying oxidation of different alumina polymorphs and rates of polymorphic phase changes occurring in alumina were quantified based on the TG measurements [12]. Combining the quantitative description of heterogeneous oxidation processes with the heat transfer analysis for aluminum particles introduced in a hot gas environment or heated by another source (e.g., laser beam) enables one to predict the ignition delay as a function of the particle size and external conditions. The model was validated experimentally for aluminum particles rapidly heated and ignited in air using a CO_2 laser [19].

However, in many practical applications oxygen is not the primary oxidizer available for ignition of aluminum powders. Instead, ignition occurs in CO_2 and H_2O environments [20, 21]. This paper describes an experimental study of ignition of aluminum particles heated rapidly in well-controlled environments with H_2O and CO_2 being the primary oxidizers. The laser ignition experimental methodology is similar to that for ignition experiments in air as described in ref. [19]. The experimental setup is modified to enable studies of aluminum ignition in water vapor, carbon dioxide, and mixed oxidizers.

7.2. Experimental

The experimental approach is similar to the earlier experiments conducted in air [19]. A threshold CO_2 laser power required to ignite a particle is measured for a set of particle jet velocities in different gas environments. A narrow, low number density particle jet is fed through the focal spot of a CO_2 laser. The laser power is increased in steps, until ignition is detected. The minimum ignition threshold indicates that the particles passing through the center of the laser beam are heated sufficiently to transition to the self-sustained combustion, detectable optically. Particles passing through the beam periphery will not be heated as much as those passing through the beam center, so that only a small fraction of the powder particles ignites upon achieving the ignition threshold.

The experimental setup is described in detail elsewhere [19]; its modified version is schematically shown in Fig. 7.1. It includes an aerosol jet generator, a 125 W CO_2 laser (by Synrad, Evolution 125 series) with a ZnSe convex lens (0.75" aperture and 4" focal length), and a modulated green laser (SUWTECH model DPGL-3000 by Photop Technologies, Inc.) operated with a set of a semi-cylindrical and convex glass lenses to produce a laser sheet for the jet visualization. A photomultiplier tube (PMT) by Hamamatsu (model PMT C7247) was used to measure emission traces of the heated and ignited particles.

The device used to produce the aerosol jet was described in detail elsewhere [22, 23]. Its main part is a parallel plate capacitor with a conductive (e.g., metal) powder placed onto the bottom electrode. The bottom electrode has a concave shape and the top electrode has a small hole in its center. A DC voltage in a range of 1-15 kV is applied and conductive particles acquire electric charge. They are repelled from the bottom electrode and attracted to the top electrode, at which they re-charge upon collision. The motion of the charging and re-charging particles continues so that an aerosol is produced in the space between the capacitor's electrodes [22]. The applied voltage is used to control the particle number density in the produced aerosol. The space between the capacitor's electrodes was enclosed in a chamber. A controlled gas flow measured by a gas mass flow meter (M-200SCCM-D by Alicat Scientific Inc.) and fed into the space between the electrodes exits through the opening in the top electrode. Thus, an aerosol jet issues from the capacitor. In these experiments, as in ref. [19], a low number density of the produced aerosol was maintained so that the number of particles fed into the aerosol jet was of the order of 1000 per second. The carrier gas flow rate was adjusted to control the aerosol jet speed in the range of 0.1 - 3 m/s. An additional plate with a built-in electric heater is placed above the top electrode. The space between the electrode and the plate is enclosed, and the plate has an opening coaxial with that of the nozzle in the top electrode. The size of the opening is greater than the electrode nozzle, as illustrated in Fig. 7.1. A separate gas mixture is fed between this plate and the top electrode to generate a shroud gas jet around the central aerosol jet, as shown in Fig. 7.1. The shroud gas jet stabilizes the central aerosol jet as well as shields it from the room environment. For experiments with the only oxidizer being H_2O , the central jet comprised of N_2 while the shroud jet was a mixture of N_2 and superheated steam. For the mixed $\text{H}_2\text{O}/\text{O}_2$ oxidizing environments, the steam mixture with air and/or air as the central jet carrying gas could be used. Note that argon could not be used as the central jet carrier gas because of its low electric breakdown potential, further reduced at elevated temperatures [24]. The steam gas flow tubes as well as the space between the top electrode and the additional plate were heated to about 150°C to eliminate water condensation.

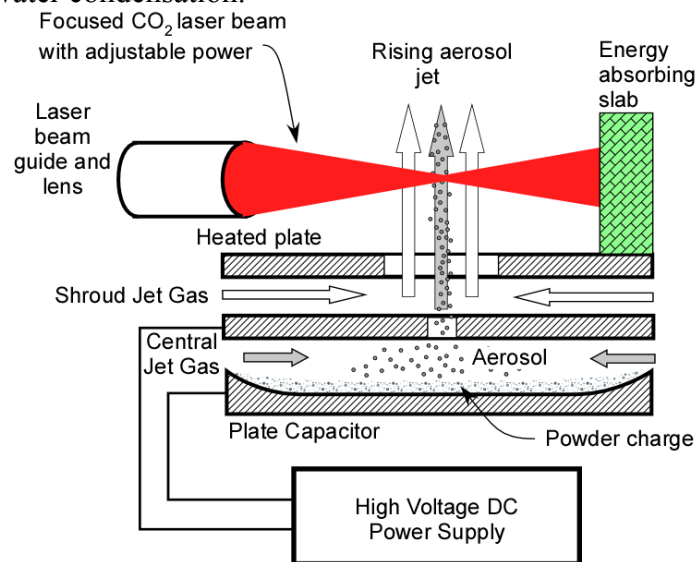


Fig. 7.1 Schematic diagram of the experimental setup. (Note modification of the setup compared to that shown in Fig. 6.1: heated plate is added to pre-heat the shroud jet.)

In experiments involving H₂O, superheated steam was generated using a customized steam generator. A peristaltic pump (Variable Speed Pump by Control Company) supplied a metered amount of liquid water (typically, 0.1 ml/min) into a steel tube (3.1 mm diameter, 5 m overall length) coiled inside a tube furnace (Tube Furnace 21100 by ThermoLyne). Prior to entering the furnace, the tube was connected to a tee and a second tube to which a metered nitrogen (or air) flow was supplied. Both the carrier gas (nitrogen or air) and water were pumped through the furnace. The furnace was pre-heated to 400 °C so that a superheated steam, mixed with the carrier gas at a controlled ratio, issued from the coiled tube exiting the furnace. The steam/carrier gas mixture was fed through a heated hose maintained at about 150 °C, to the aerosol jet generator (with its respective components also pre-heated). The shroud jet and the main particle carrying gas mixed rapidly as discussed in more detail below, so that a well-controlled gas environment was generated in the area where the particles entered the laser beam.

For experiments with CO₂ serving as an oxidizer, the shroud gas was pure CO₂ and the heaters for hoses and components of the aerosol generator were turned off. CO₂ was also used as the central jet carrier gas. For mixed CO₂/O₂ environments, a premixed CO₂/O₂ mixture was used for both shroud and central gas flows.

Threshold CO₂ laser power required for particle ignition was measured for three different jet velocities for each environment, similar to the experiments in air [19]. The variation in the jet velocity is equivalent to changing the particle heating rate in the laser beam, which is useful for identification and/or validation of the ignition kinetics. The aerosol jet velocity was measured using particle image velocimetry. A vertical green laser sheet modulated with a frequency in the range of 300 to 3000 Hz illuminated the aerosol jet, with the higher frequencies selected for higher jet speeds. Produced particle streaks were recorded using a digital camera and the streak lengths were measured to determine the jet velocity.

For each experiment, a stable aerosol jet was established and the CO₂ laser was fired continuously for 8 seconds, at a preset power level. Visible radiation generated by heating and/or ignition of particles was monitored using a PMT connected to a PC-based data acquisition system. The experiment was repeated with the laser powers gradually increased until ignition events were clearly detected (see data processing section below). The measurements for both the jet velocity and the laser power were made immediately before each ignition experiment.

Spherical aluminum powder, 99% pure by Alfa Aesar with nominal particle size of 4.5 – 7 μm was used in this study. Figure 7.2 shows the particle size distribution of the powder as measured by low angle laser light scattering (Beckman Coulter LS-230). Note that while the particle size distribution does not peak around 3.4 μm (the particle size heated by the CO₂ laser most effectively [19]), the number of particles with this size is substantial.

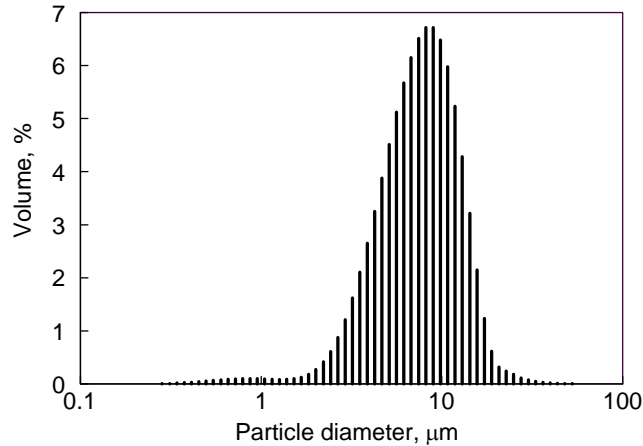


Fig. 7.2 Particle size distribution of spherical aluminum powder, 99% pure aluminum by Alfa Aesar with nominal particle size of 4.5 – 7 μm , measured by Coulter LS-230.

7.3. Simulation of gas mixing for ignition experiments

A numerical simulation was used to establish the gas concentrations in the mixed flows used in experiments. Gambit, a pre-processing software, was used to model the geometry of the aerosol generator outlet. Experimental geometry of the axisymmetric, cylindrical central jet nozzle and the shroud flow nozzle was directly introduced into the code. For the calculations, the space was covered by 2 different meshes with quadrilateral elements. The first, internal mesh had a node-to-node distance of 0.1 mm and described the central zone where the concentration gradients were likely to be high. The second, external mesh had a 5 mm distance between nodes, and was used for the ambient gas. Computational fluid dynamic (CFD) code Fluent was used for numerical calculations. Calculations assumed laminar gas flow and considered a gas jet neglecting the presence of particles. This analysis is adequate for the current experiments, considering the very low particle number densities used.

The gases were introduced into the system using mass flow inlets, corresponding to the mass flow rate measured in experiments. The heat transfer to the walls was neglected and walls were assumed to be at the same temperature as the adjacent gas elements.

The results of calculations for a specific case are presented for example in Figs. 7.3 and 7.4. These calculations used an N_2 flow rate of 100 ml/min at 293 K in the central jet and a mixture of $\text{H}_2\text{O}/\text{N}_2$ comprising 0.085 ml/min of liquid H_2O and 100 ml/min of N_2 at 293 K in the shroud jet. These flowrates are representative of experimental settings. The temperature of all entering gases was set at 400 K. The final mixture consisted of 57.5 mass % of N_2 and 42.5 mass % of H_2O . The environment was air at 293 K. The environment along the axis of the jet was nearly uniform across the rising jet after about 10 mm from the jet exit. Following the calculation results, in experiments, the laser spot was focused on the jet 12 mm above the nozzle, so that the particle ignition occurred in a relatively well-established and homogeneous gas mixture.

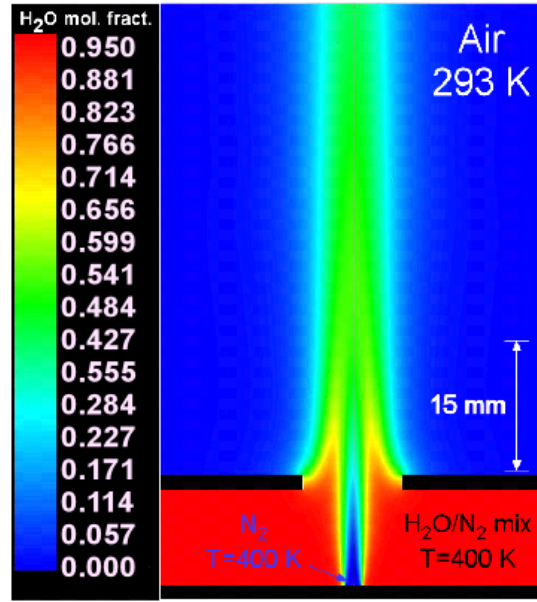


Fig. 7.3 Mole fraction of water as a function of vertical and horizontal coordinates for the produced mixed jet. The specific conditions are: Flow rate of N_2 (central jet): 100 ml/min at 293 K; Flow rates of H_2O/N_2 mixture represent 100 ml/min of N_2 at 293 K and 0.085 ml/min of liquid water. Temperature of all entering gases is 400 K. The final mixture consists of 57.5 mass % of N_2 and 42.5 mass % of H_2O . The environment is air at 293 K.

Figure 7.3 shows that mixing of the starting H_2O/N_2 gas coming as a shroud jet with the central nitrogen jet is nearly completed about 10 mm above the nozzle and that the water concentration across the jet is nearly uniform in vicinity of the focal spot of the laser beam. The specific water concentration at which ignition is studied is well quantified by this calculation.

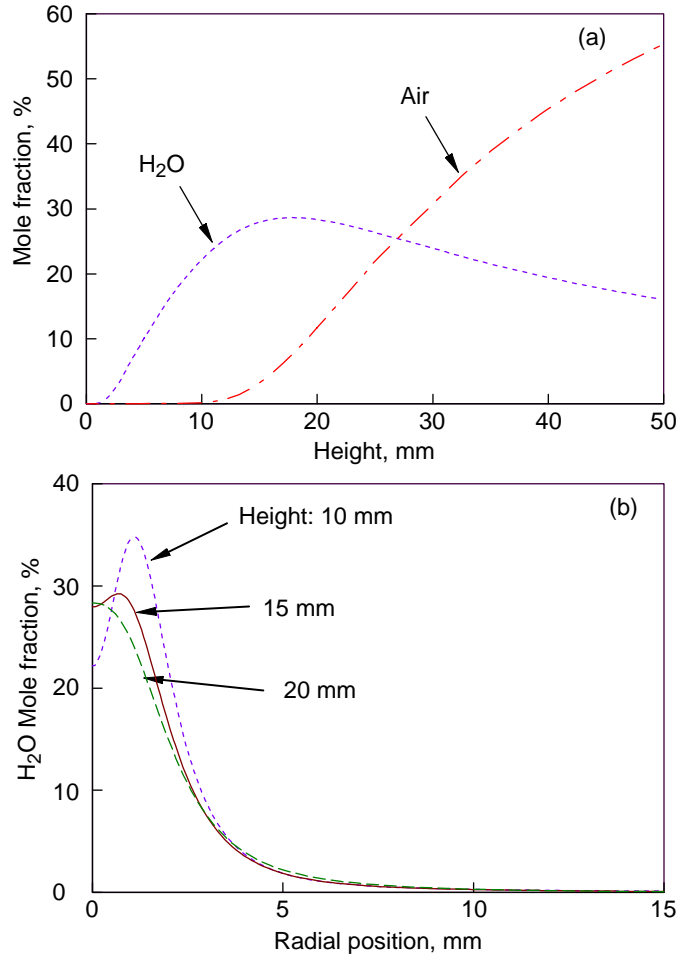


Fig. 7.4 Concentration profiles for flow conditions presented in Fig. 7.3; (a) H₂O and air mole fractions along the jet's axis; (b) H₂O mole fractions at three different heights plotted as a function of the distance from the jet axis.

Mole fraction profiles for H₂O and air are shown in Fig. 7.4 (a). There is effectively no contamination of surrounding air up to 12 mm along the jet axis where the CO₂ laser was focused. Figure 7.4 (b) shows H₂O mole fraction as a function of distance from the jet axis. H₂O concentration changes only slightly within 2-3 mm of the jet axis which is more than the width of the particle jet.

Specific experimental conditions used in experiments are presented in Table 7.1. For each of the shown gas flow rate combination, a detailed Fluent calculation was performed and specific gas concentrations present in vicinity of the laser focal spot were found and also shown in Table 7.1.

Table 7.1 Volumetric compositions (%) of gases in vicinity of the laser focal spot.

Environments	Air	CO ₂	H ₂ O / N ₂	H ₂ O / N ₂ / O ₂	CO ₂ / O ₂
N ₂	79	-	65	51	-
O ₂	21	-	-	14	21
CO ₂	-	100	-	-	79
H ₂ O	-	-	35	35	-

7.4. Experimental data processing

Two methods were combined to detect particle ignition, both based on the anticipated substantial difference in the emission signature of the ignited particle vs. particle that is simply heated by the laser beam. This approach assumed that the emission signatures are substantially different for ignited vs. unignited particles. This assumption is justifiable for particles burning in the vapor phase, however, it may not be useful when particles combust heterogeneously. The cases of intermediate combustion regime also require specific attention. For the particle burning with a standoff vapor phase flame, as commonly expected for aluminum, the emission signature is primarily generated by the flame rather than the particle surface. The flame temperature, limited by the alumina boiling point, is substantially greater than the particle temperature, limited by the boiling point of metallic aluminum; thus the flame-produced emission is much stronger than the emission from heated particles. Even more importantly, a burning particle produces an emission pulse with a detectable plateau (which may or may not be overlapped with an oscillatory pattern), unlike the particles that are simply heated and cooled off, for which the optical signal decrease immediately follows its rise. The plateau corresponds to the combustion period when the vapor-phase flame is maintained, and it results in a substantial extension in the overall pulse duration. Thus, the separation of particles burning with a vapor-phase flame from unignited particles based on their optical signatures is relatively straightforward when radiation intensity pulses produced by particles are visually inspected. However, developing an automated procedure for separating pulses for ignited vs. unignited particles proved to be very difficult due to substantial variation in both amplitudes and shapes of the pulses.

In order to understand results presented below, it is important to stress that detection of aluminum particles burning heterogeneously using their optical signatures is nearly impossible. Indeed, any particle heated in an oxidizing environment is reacting heterogeneously, but this reaction may remain undetected if it does not lead to a full-fledged flame. Even if the reaction is capable of balancing heat losses to the room temperature environment, the particle boiling point limits the temperature of reaction. Therefore, the emission produced by such particles is similar in intensity to that produced by particles heated in the laser beam, but not capable to maintain their high temperature. Furthermore, unlike the case of vapor-phase reaction, when most of the combustion products are formed away from the particle, for a heterogeneously reacting particle, combustion products are formed on its surface and immediately mixed in. This inevitably slows down the heterogeneous reaction, and causes the particle temperature to decay. Respectively, the emission pulse may not include a detectable plateau. Therefore, a detailed analysis of the

produced emission signature combined with the knowledge of the initial particle diameter for each individual particle is needed to discern between the heterogeneously reacting metal particles that are or are not capable of self-sustaining combustion. Such analysis is beyond the scope of the present study, so only particles burning with a stand-off vapor phase flame could be detected as described below.

The first method is based on the visual inspection of shapes of particle emission pulses as in earlier experiments [19]. Figure 7.5 shows typical examples of the recorded PMT output pulses produced by particles crossing the CO₂ laser beam (39.3 W) in air at a speed of 2.63 m/s. The peak shape on the left has a plateau following the initial signal increase, indicative of an ignition and combustion event. The peak on the right does not have a noticeable plateau and is typical for a particle that was heated by the laser beam without ignition. The minimum ignition threshold was registered if at least one ignition event was detected during an 8-s period the laser was fired. For each laser power setting the laser was fired three times. The laser power setting is confirmed to ignite the powder if ignition events are observed in all three 8-s runs.

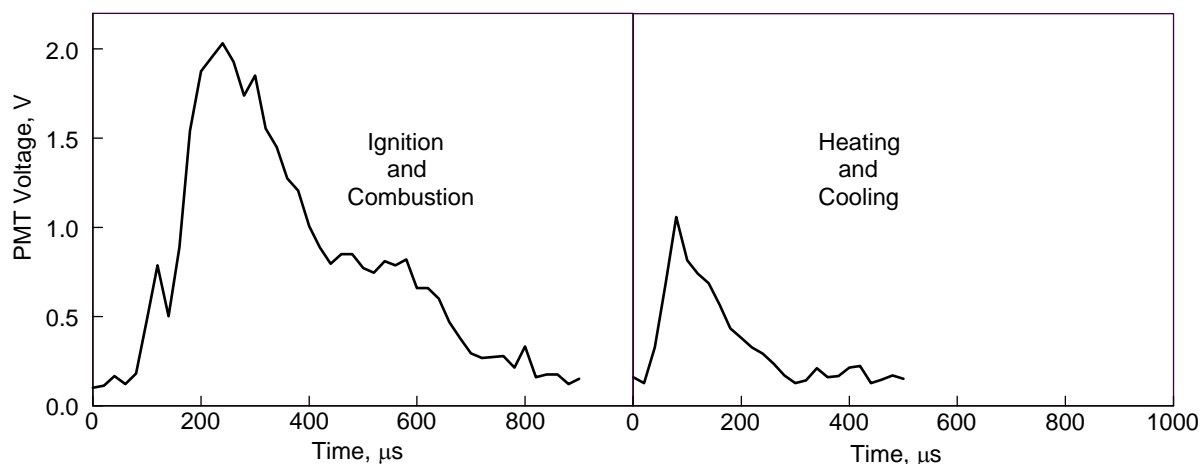


Fig. 7.5 Typical examples of PMT signals recorded for Al particles in air crossing the CO₂ laser beam (at 39.3 W) in air at a speed of 2.63 m/s. The peak on the left has a characteristic plateau indicative of combustion. The peak on the right shows heating and cooling of an un-ignited particle.

In the second method, the PMT peak data were analyzed statistically for the peak width of the ignition/heating pulses. Short pulses observed at low laser powers were attributed to particles that were heated but not ignited. As the laser power increased, appearance of longer pulses was expected to indicate ignited particles, producing emission signatures extended in time due to a self-sustaining reaction. Figure 7.6 shows the frequency distribution of peak widths for pulses accumulated during 24 s (three 8-s runs) for different CO₂ laser powers at the fixed jet velocity of 1.5 m/s in air. Only a very few narrow peaks are detected at the laser power of 12.1 W. Increase in the laser power to 14.8 W produces greater number of peaks and the peak widths begin forming a bell-curved distribution around 300 μs. Upon further increase in the laser power to 18.1 W, peaks with substantially greater durations, around 900 μs, first appear as a tail of the peak widths distribution. The appearance of the wider peaks and respective change in the overall distribution among peak widths is considered to indicate the ignition threshold.

The visual peak shape inspection for this experiment (according to the first method described above) gives the threshold laser power to be at 20 W (between 18.1 and 21.9 W). Thus, for the example shown in Fig. 7.6, the ignition threshold detected at 18.1 W based on the frequency distribution of peak widths is in agreement with the ignition threshold identified based on visual inspection of the peak shapes.

It is interesting that as the power increases, more and more particle combustion events are detected with the respective peak durations close to 900 μs . Because of the particle size-selective heating in the CO_2 laser beam [19], it is reasonable to attribute this combustion duration to the burn time of the 3.4 μm diameter particles most efficiently heated by the laser. Using a burn time correlation proposed in Ref. [25] for combustion of aluminum aerosol, $t=310d$, the burn time of a 3.4 μm particle is 1054 μs . This is in good agreement with the measured time of about 900 μs , which, in fact, is expected to be shorter than the predicted time because of a faster reaction expected for the particle while it is crossing the laser beam.

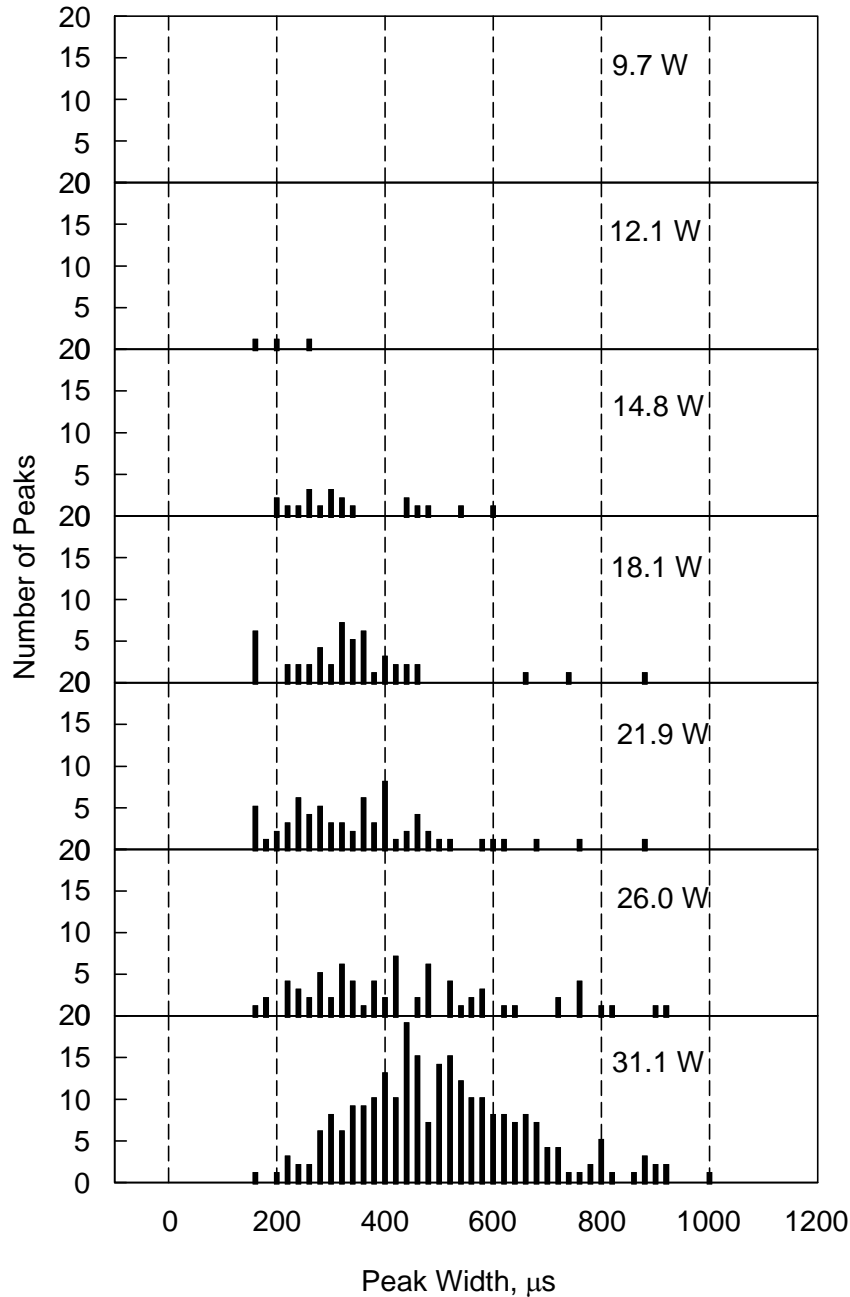


Fig. 7.6. Frequency distribution of peak widths produced by emission of Al particles crossing the CO₂ laser beam in air. The aluminum aerosol jet speed is 1.5 m/s.

7.5. Results and discussion

The initial set of experiment was performed in air. The threshold laser power needed for ignition measured for air was slightly lower than shown in ref. [19] which was attributed to a better focusing of the CO₂ laser beam. In earlier measurements [19], the particle jet was placed in the visually identified focal spot of the auxiliary red laser (0.65 μm wavelength), which resulted in a less focused CO₂ beam (10.6 μm wavelength). In this work, the particle jet was placed at the focal spot calculated using the actual CO₂ emission wavelength. The current measurement in air

was processed using a similar fitting procedure of matching the measured experimental laser threshold with that calculated as described in ref. [19] and using the beam diameter as an adjustable parameter. The fitting gave the focused beam diameter equal to 200 μm (compare to 260 μm found to best describe similar experiments with a less focused beam [19]). The 200 μm beam diameter was used for processing all experiments in mixed environments discussed in this paper. We note that the beam diameter was also assessed experimentally using both luminescent thermal image plates illuminated by an ultraviolet lamp to visualize the beam profile and imprints left by the focused beam of a target metal substrate. These assessments have a limited accuracy of about $\pm 50 \mu\text{m}$. Within that uncertainty, the focused beam diameter is equal to 200 μm , supporting our selection of this value as an adjustable parameter for the model.

The experiments in air were repeated while turning on the heaters in the shroud jet hoses and in the elements of the aerosolizer. It was observed that pre-heating the shroud gas to about 150 $^{\circ}\text{C}$ did not result in a meaningful difference in the measured laser power ignition thresholds.

Fig. 7.7 shows the threshold laser power measured for all five different environments. For each environment, threshold powers are measured for three different jet velocities, thus producing three different heating rates. An increase in the jet velocity increases the threshold power. CO_2/O_2 environment has the lowest threshold and $\text{H}_2\text{O}/\text{N}_2$ environment has the highest. Threshold for air is slightly higher than that for CO_2/O_2 mixture, which is likely due to a higher concentration of oxidizer. However, threshold for pure CO_2 environment is higher than that for air indicating O_2 to be a better oxidizer than CO_2 . In mixed $\text{H}_2\text{O}/\text{O}_2/\text{N}_2$ environments, the ignition threshold depends strongly on the presence of O_2 . Adding 14 % by volume of O_2 to the environment with 35 % of H_2O lowered the ignition threshold to effectively the same as for pure CO_2 .

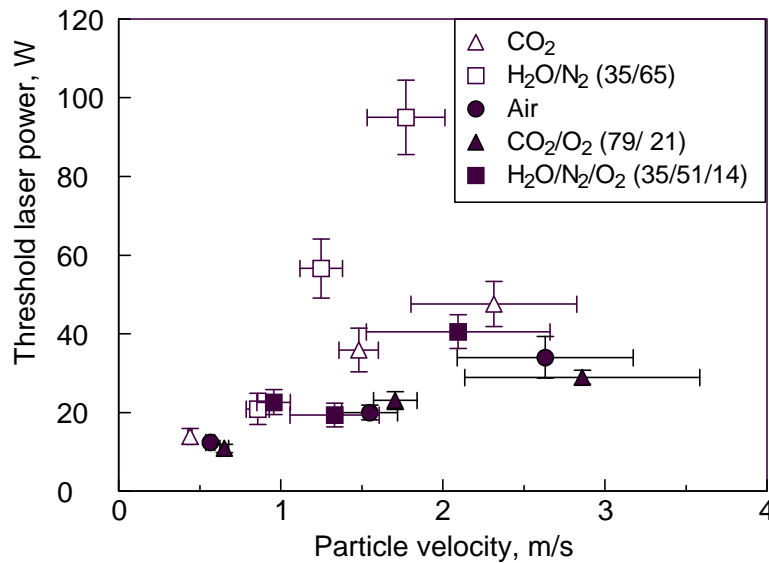


Fig. 7.7 Threshold laser power required for ignition of aluminum particles crossing the laser beam in different gas environments (refer to Table 7.1 for environment details).

It was considered whether a simplified Arrhenius ignition model approach could be useful for describing the ignition threshold results shown in Fig. 7.7. The heat balance of a single particle can be described as:

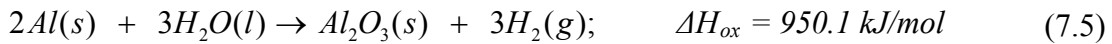
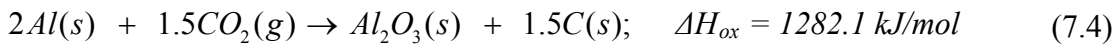
$$MC \frac{\partial T_p}{\partial t} = \dot{Q}_{Laser} + \dot{Q}_{Chemical} - \dot{Q}_{Radiation} - \dot{Q}_{Convection} \quad (7.1)$$

where M is the particle mass, C is its specific heat, T_p is its temperature; \dot{Q}_{Laser} is the heat transfer rate to the particle from the laser beam, $\dot{Q}_{Chemical}$ is the chemical heat generation rate, and $\dot{Q}_{Radiation}$ and $\dot{Q}_{Convection}$ are the radiation and convection heat transfer rates, respectively. Convection term is given by the Fuchs model described in ref. [26]. \dot{Q}_{Laser} and $\dot{Q}_{Radiation}$ are described in detail in ref. [19]. For a simplified approach, the chemical term is described by a single term Arrhenius ignition model,

$$\dot{Q}_{Chemical} = A_r \Delta H_{ox} P_{ox} (\pi d^2) \exp \left[\frac{-E_a}{RT_p} \right] \quad (7.2)$$

where A_r is the Arrhenius pre-exponent, ΔH_{ox} is the oxidation enthalpy (per mol of fuel), d particle diameter, P_{ox} oxidizer partial pressure, E_a activation energy and T_p particle temperature. For a given environment i.e. specific values of A_r , ΔH_{ox} and E_a , equations 7.1 and 7.2 can be used to calculate temperature history of a particle of given diameter d . For environments with several oxidizers, it is proposed that the chemical term can be treated as a sum of the respective terms given by Eq. 7.2 with kinetic parameters found for individual oxidizers.

Taking into account the selective heating of particles of around 3.4 μm by the CO_2 laser, these particles were expected to ignite first at the measured threshold laser power. Thus, equations 7.1 and 7.2 were used to calculate threshold laser power to best fit the experimental results in Fig. 7.7 using A_r and E_a as variable parameters for each environment. The oxidation enthalpy, ΔH_{ox} , for each environment was calculated assuming oxidation of Al to Al_2O_3 , given by the global reactions:



Note that the reaction (7.4) is unlikely and a more viable scenario of Al combustion in CO_2 would lead to formation of Al_2O_3 and CO. However, to maximize the oxidation enthalpy, and to remain consistent with the assumption of the complete oxidation implied by reactions (7.3) and (7.5), reaction (7.4) was considered. When applied to different environments, this simple approach was capable of describing the ignition threshold measurements for air and CO_2/O_2 . However, this approach was found to be problematic for other environments used in this study. It was observed that the heat transfer model presented above predicted that the 3.4 μm diameter

particles will be heated to the temperature exceeding aluminum boiling point at the laser powers well below the measured ignition threshold, even if no chemical heat generation was included in the calculation, i.e., $\dot{Q}_{Chemical} = 0$. The results of this analysis are illustrated in Fig. 7.8. Experimental points are shown for each environment separately. For each environment, the dashed lines show the calculated laser powers required to achieve 2792 K (the aluminum boiling point) with no chemical reaction allowed. Reaching the boiling of aluminum is considered to be an indicator of beginning of the vapor-phase combustion; in other words if the particle temperature reaches 2792 K, it is assumed that further analysis of heterogeneous reaction leading to ignition becomes irrelevant.

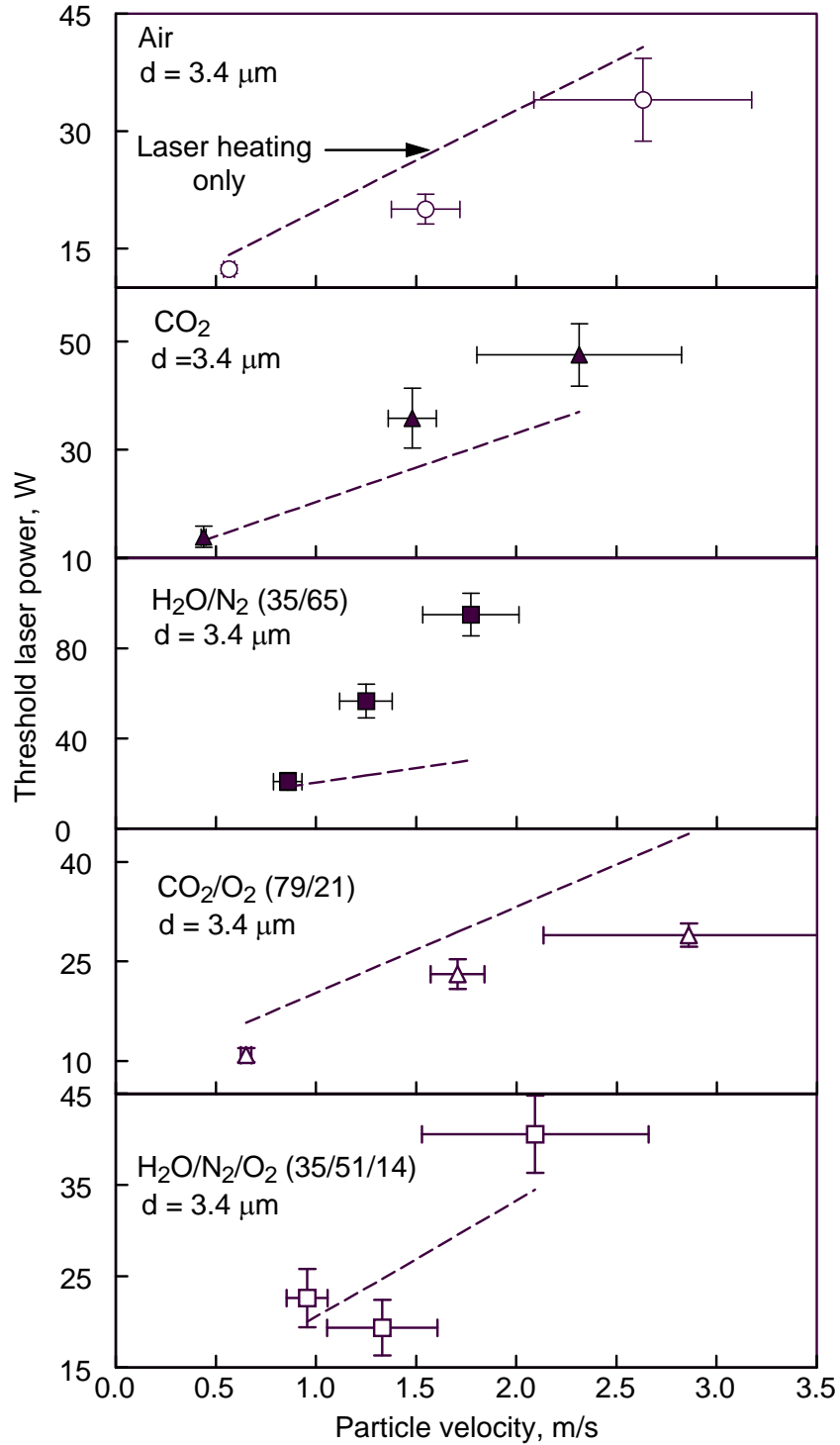


Fig. 7.8 Experimental data for the laser ignition thresholds and calculated laser powers required to heat 3.4 μm Al particle to the Al boiling point (2792 K) with no chemical reaction allowed.

Note that mismatch between the experimental and calculated trends is increasing for higher particle velocities. The slopes of the calculated curves for the laser threshold power vs. particle velocity (shown in Fig. 7.8 as dashed lines) are strongly dependent on the size of the particles

considered in the calculation. This effect is illustrated in Fig. 7.9, where laser powers required to heat the particles to the aluminum boiling point with no chemical reaction allowed are shown for $\text{H}_2\text{O}/\text{N}_2$ environment for different particle sizes. The slopes of the calculated curves become close to that of the experimental trend for the laser ignition power threshold for $\sim 13\ \mu\text{m}$ particle size. In calculations, the primary effect of the added chemical reaction term is a shift of the entire curve down; the change in slope of the predicted trend is relatively minor. Thus, calculations illustrated in Fig. 7.9 suggest that adding a chemical term would enable one to match the experimental trend considering ignition of particles of about $13\ \mu\text{m}$ diameter.

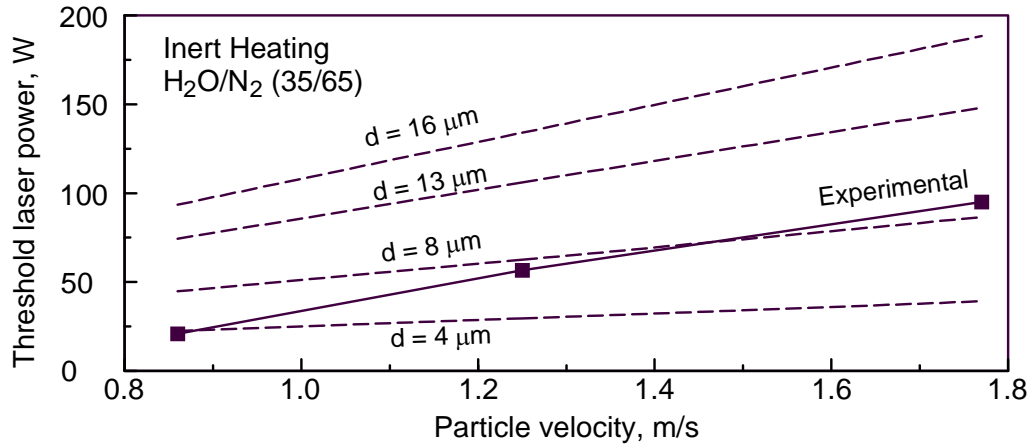


Fig. 7.9 Dashed lines show calculated laser powers required to heat Al particles of different diameters moving at different velocities to the aluminum boiling point in an $\text{H}_2\text{O}/\text{N}_2$ environment with no chemical reaction allowed. Solid line shows an experimental laser power ignition threshold for the same environment.

The above analysis suggests that the assumption used in ref. [19] that only $3.4\ \mu\text{m}$ particles ignite at the threshold power may not be suitable for all environments considered in this paper. Indeed, as described above, the optical identification of ignited particles is only useful for the particles burning in the vapor phase. It is well known, however, that heterogeneous reactions become increasingly important as the particle sizes decrease. Recently, it was shown that a simple heat transfer balance between the standoff flame, particle surface, and surrounding room temperature gas restricts the particle sizes capable of the purely vapor-phase combustion [27]. The restrictions are more severe for the oxidizing environments with lower adiabatic flame temperatures, i.e., for the same partial pressure of oxidizer, smaller particles can sustain the vapor phase flame in oxygen than in the mixtures containing CO_2 or H_2O . Therefore, even if the laser heating is the most effective for the particles of $3.4\ \mu\text{m}$ diameter [19], the exothermic reaction for such particles would remain undetected in the present experiments unless it results in a vapor phase flame. In other words, the ignition thresholds detected in this research are for the smallest particles capable of maintaining the vapor phase flame, so that their dimensions depend on the oxidizing environment and are not known in advance. The following analysis treats the diameter of the igniting particle as an adjustable parameter to match the calculated and measured laser power ignition thresholds for different particle velocities.

7.6. Arrhenius model parameter for Al ignition in different environments

Based on the above discussion, the size of the particle observed to ignite using the particle's optical signature, is a function of the oxidizing environment. Thus, to extract the Arrhenius model parameters for ignition kinetics, i.e., A_r and E_a , the experimental trend for the threshold ignition power is matched using Equations 7.1 and 7.2 considering A_r , E_a and d as adjustable parameters. Calculations were run to fit the experimental data for different gradually increasing particle diameters, activation energies and pre-exponents. For mixed environments, the experimental curves were not matched varying all three adjustable parameters. Instead, Arrhenius parameters determined for individual oxidizers were used as per Equation 7.2 with contributions from different oxidizers added taking into account their respective partial pressures. The only adjustable parameter varied for mixed oxidizer experiments was the particle diameter. Thus, matching the experimental data for mixed oxidizers validates the Arrhenius parameters selected for individual oxidizers. Figure 7.10 shows the same experimental results as presented in Fig. 7.8 together with the curves calculated using the selected adjustable parameters A_r , E_a and d for all environments tested. The adjustable parameters selected to fit the experiments are shown in Table 7.2.

Table 7.2 Arrhenius parameters for different environments

Environments	Air	CO ₂	H ₂ O / N ₂	H ₂ O / N ₂ / O ₂	CO ₂ / O ₂
d (μm)	3.4	5.0	12.0	9.0	3.0
A_r (s/m)	5.63E+03	3.94E+02	1.55E+10	-	-
E_a (kJ/mol)	179	154	192.5	-	-

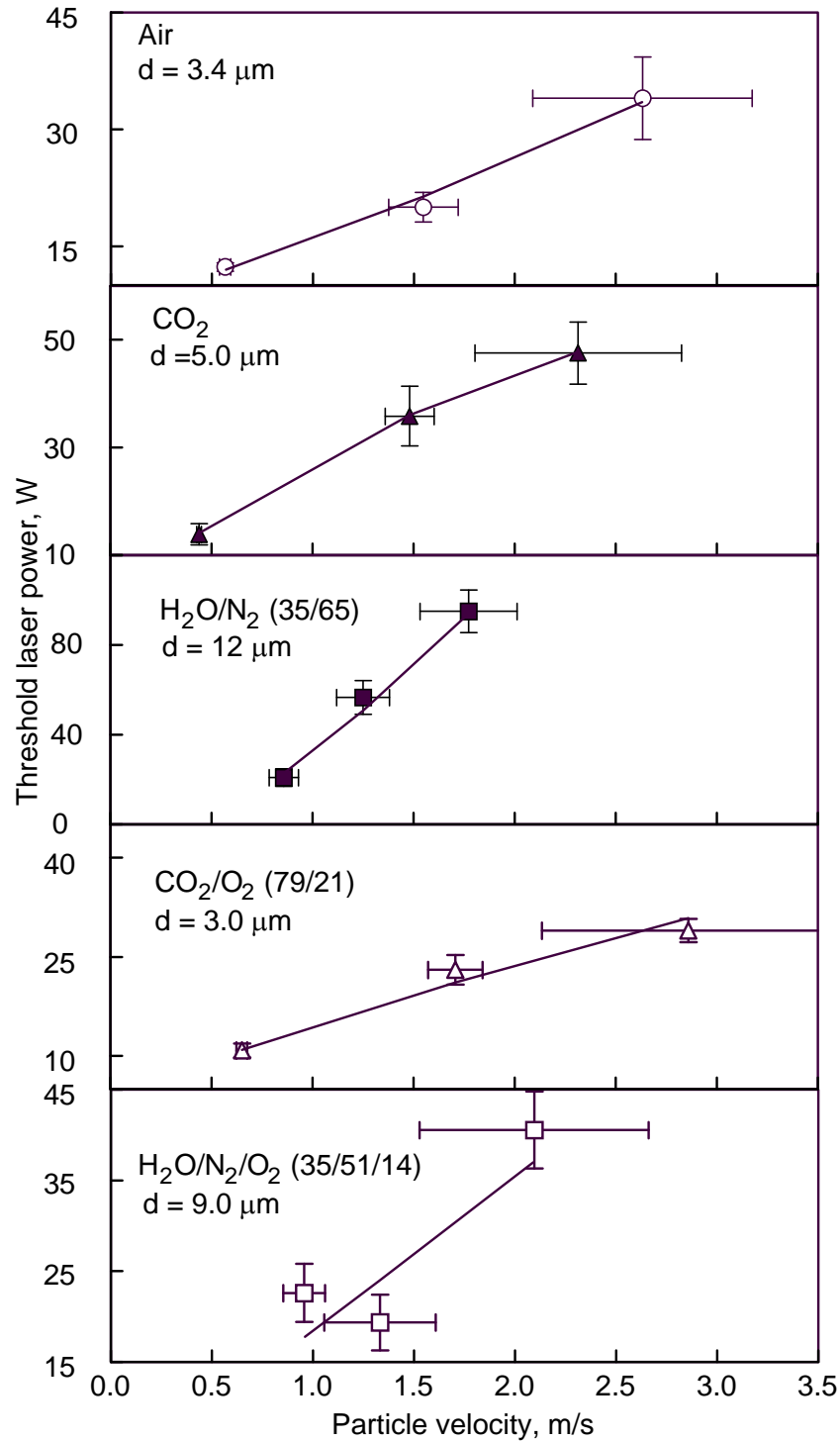


Fig. 7.10. Experimental data and calculated laser ignition thresholds; the particle diameters found as adjustable parameters are shown in the respective plots. Arrhenius reaction kinetics parameters extracted from experiments with individual oxidizers are tabulated in Table 7.2. Experimental data for mixed oxidizers are fitted adjusting the particle diameter and using the linear superposition of individual oxidizer kinetic parameters corrected by the partial pressures of the individual oxidizers.

Figure 7.10 shows that the match between the experimental and predicted laser ignition thresholds is equally good for pure oxidizers, for which Arrhenius kinetics was selected directly and for mixed environments, for which the Arrhenius kinetics obtained for individual oxidizers was used considering respective particle pressures, according to Eq. 7.2.

The Arrhenius parameters shown in Table 7.2 indicate that H_2O as an oxidizer is associated with a faster reaction kinetics than either O_2 or CO_2 . Note that it has the lowest oxidation enthalpy, which makes ignition in pure H_2O most difficult.

It is concluded that in the $\text{H}_2\text{O}/\text{N}_2$ environment, 12 μm sized particles ignite at the ignition threshold laser power. For the $\text{O}_2/\text{H}_2\text{O}$ environment, the particles detected to ignite at the threshold laser power are slightly smaller, 9- μm diameter, which is reasonable considering that the flame temperature is expected to be higher when oxygen is added as an oxidizer. For other environments (O_2 , CO_2 and mixed O_2/CO_2 oxidizers) the particle size selected as an adjustable parameter is quite close to 3.4 μm , the particle size that is most effectively heated in the CO_2 laser beam.

The difference in the activation energies found to be adequate for different environments (see Table 7.2) is relatively minor. The pre-exponents differ significantly, however, with the pre-exponent for H_2O being many orders of magnitude greater than the values found to describe ignition for CO_2 and O_2 , serving as oxidizers.

7.7. Conclusions

Aluminum particle laser ignition experiments were conducted in five different oxidizer environments (Table 7.1). Three environments included a single oxidizer: O_2 , CO_2 or H_2O , and the other two environments included mixtures of two oxidizers i.e., $\text{H}_2\text{O}/\text{O}_2$ and CO_2/O_2 . CO_2 laser ignition threshold power was measured for three different particle jet velocities for each environment.

The approach described in ref. [19] for processing the experiments on metal particle ignition in CO_2 laser by considering only the particle size of 3.4 μm (because of the selective heating of this particle size) was modified to account for the effect of oxidizing environment on the minimum particle size, for which a vapor-phase flame can be maintained [27]. Because the vapor phase flame could not be sustained for fine particles in all environments tested, and because the optical ignition detection could only reliably establish the existence of the vapor-phase flames but not of heterogeneous reactions, the experimental data were processed considering particle diameter as one of the adjustable parameters.

Experimental results were processed considering particle heat balance and a simplified chemical kinetics model, including a single Arrhenius term. The Arrhenius parameters, pre-exponent A_r and activation energy E_a for Al ignition in O_2 , CO_2 , and H_2O were determined (Table 7.2). Despite the highest measured laser power threshold required for ignition of Al particles in H_2O , the data indicate the fastest kinetics of heterogeneous reaction leading to ignition and vapor phase combustion for H_2O as compared to other oxidizers. Thus, the difficulty of igniting Al in H_2O is associated with the relatively low heat release upon Al oxidation in H_2O rather than with

the respective reaction kinetics. Kinetic parameters for heterogeneous reactions leading to Al ignition in O₂ and CO₂ are of similar order of magnitude. For environments where two different oxidizers were mixed, the experimental results are successfully described using a sum of the Arrhenius reaction terms describing ignition of Al particles in environments with individual oxidizers corrected by the partial pressures of these oxidizers.

7.8. References

1. R. Friedman and A. Macek, Combust. Flame 6 (1962) 9-19.
2. J.L. Prentice, Combust. Flame 9 (1965) 208-210.
3. J.L. Prentice, L.S. Nelson, J. Electrochem. Soc. 115 (1968) 809-812.
4. I. Glassman, I. "Combustion," 3rd Edition, Academic Press, Orlando, Ch. 9, 1996.
5. M.K. King, Proc. Combust. Inst. 17 (1979) 1317-1328.
6. C.K. Law, Combust. Sci. Technol. 7 (1973) 197-212.
7. C.K. Law, Combust. Sci. Technol. 12 (1976) 113-124.
8. J.F. Widener, Y. Liang, M.W. Beckstead, CPIA Pub. 680 (JANNAF 35th Combustion Subcommittee Meeting, Vol. 1) (1998) 577-592.
9. K. Benkiewicz, A. K. Hayashi, Fluid Dynamics Research 30 (2002) 269-292.
10. K.P. Brooks, M. Beckstead, J. Prop. Power 11 (1995) 769-780.
11. V.M. Boiko, S. V. Poplavski, Shock Waves 11 (2002) 289-295.
12. M.A. Trunov, M. Schoenitz, X. Zhu, E.L. Dreizin, Combust. Flame 140 (2005) 310-318.
13. T. Bazyn, H. Krier, N. Glumac Proc. Combust. Inst. 31 (II) (2007) 2021-2028.
14. Y. Huang, G.A. Risha, V. Yang, R.A. Yetter, Proc. Combust. Inst. 31 (II) (2007) 2001-2009.
15. A. Dokhan, E.W. Price, J.M. Seitzman, R.K. Sigman, Proc. Combust. Inst. 29 (2) (2002) 2939-2945.
16. M.A. Trunov, M. Schoenitz, E.L. Dreizin, Combust. Theor. Model. 10 (2006) 603-624.
17. P.E. DesJardin, J.D. Felske, M.D. Carrara, J. Prop. Power 21 (2005) 478-485.
18. E.B. Washburn, J.N. Trivedi, L. Catoire, M.W. Beckstead Combust. Sci. Technol. 180 (2008) 1502-1517.
19. S. Mohan, M.A. Trunov, E.L. Dreizin, J. Prop. Power 24 (2008) 199 – 205.
20. E.W. Price, Progress in Astronautics and Aeronautics 90 (1984) 479-513
21. S.D. Gilev, V.F. Anisichkin, Combust. Explo. Shock. 42 (2006) 107-115.
22. Y. Shoshin, E. Dreizin, Aerosol Sci. Tech. 36 (2002) 953-962.
23. Y. L. Shoshin, E. L. Dreizin, AIAA J. 42 (2004) 1416-1426
24. I. V. Bozhko, N. I. Glazkov, S. R. Troitskii, N.I. Falkovskii, Zhurnal Prikladnoi Mekhaniki I Tekhnicheskoi Fiziki 1 (1980) 20-27. (in Russian)
25. Y.L. Shoshin, E.L. Dreizin, Combust. Flame 145 (2006) 104505-105505.
26. S. Mohan, M. A. Trunov, E. L. Dreizin, J. Heat Transf. 130 (2008) 104505 – 104509.
27. S. Mohan, M. A. Trunov, E. L. Dreizin, Combust. Flame 156 (2009) 2213-2216.

8. Oxidation of aluminum powders at high heating rates

8.1. Introduction

Advances in computational capabilities enable increasingly more detailed modeling of combustion dynamics in various energetic systems. Respective fluid dynamics and heat transfer processes are being described more and more accurately using both novel modeling approaches [1-3] and detailed numerical schemes [4, 5].

However, contemporary combustion models still rely on very simplified and often inaccurate submodels to describe the dynamics of ignition and combustion of metals present in energetic formulations. For aluminum, the most common metallic additive in both propellants and explosives, ignition is commonly described by a somewhat arbitrarily chosen fixed ignition temperature as reviewed in ref. [6] and combustion is modeled to fit the “d-power law” inferred from a modified hydrocarbon droplet combustion model [7]. Many experimental studies, e.g., [8-10] have shown such simplified descriptions for both ignition and combustion of aluminum to be inadequate. In particular, recent research on aluminum particle ignition has shown that it is controlled by diffusion processes of oxygen and aluminum through the surface oxide, and that this diffusion is critically affected by polymorphic phase changes occurring in alumina upon heating [11,12]. A quantitative oxidation model was developed [12] describing ignition of aluminum particles in O₂/N₂ environments reasonably well [13]. This oxidation model was developed based on thermoanalytical measurements that were performed with heating rates less than 40 K/min. While shown to be capable to predict ignition for individual Al particles heated by a laser beam [13], the model developed in ref. [12] uses a number of adjustable parameters and additional validations and improvements of that model are needed to reliably describe ignition in environments with varied oxygen concentrations and for broader range of particle sizes and ignition stimuli. There are several orders of magnitude between the heating rates used in thermal analysis (traditionally less than 1 K/s) and encountered during ignition ($>10^6$ K/s). Direct observation of changes in the surface oxide of aluminum particles or detection of any other signs of the ongoing oxidation at heating rates approaching to or even exceeding 10^6 K/s are not experimentally feasible. Alternatively, it is possible to extend the range of heating rates over which thermal analysis can be performed, so that the oxidation model can be verified, and if needed refined. The present study is aimed to provide experimental thermoanalytical data at heating rates up to 500 K/min (8.3 K/s) with the specific goal to extend the experimental support for the oxidation model previously developed.

8.2. Experimental

Thermogravimetric (TG) measurements of aluminum oxidation were conducted in an Ar + 50 vol-% O₂ mixture with heating rates of 50, 200, and 500 K/min using a TA Q5000-IR thermogravimeter. Aluminum powder (Alfa Aesar, 98 %) with a nominal size of 3-4.5 μ m was loaded in an alumina sample pan. Particle agglomeration above the melting point of aluminum was a concern, since this could drastically reduce the surface area available for oxidation, and distort the results. In order to minimize particle-particle contacts, a suspension of the powder in pyridine was painted into the sample pan. After drying the pyridine, a sample mass of 0.5-1 mg was typically left so that the surface of the sample pan was coated with a thin powder layer. Examining the samples after heating through the Al melting point revealed no signs of agglomeration. The gases were mixed externally, and their combined flow was adjusted to 25 mL/min by a mass flow controller built into the thermogravimeter.

Oxidation is not complete at 1473 K, the maximum temperature of the instrument. However, with such small sample masses it is necessary to collect a baseline by heating the fully oxidized sample. Therefore the samples were held for 30 min at 1473 K to oxidize them to a substantial degree, if not fully, so that no measurable oxidation would occur on second heating. The second heating experiment was then subtracted from the first heating experiment to obtain the actual sample mass vs. temperature curve that is due only to the oxidizing sample. This method of baseline correction does not require handling the sample holder between the actual measurement and the baseline measurement. Initial experiments where an empty crucible was used instead of a fully (or substantially) oxidized sample were found to be less reproducible.

The sample temperature of the thermogravimeter was calibrated using a set of Curie point standards (alumel®, Ni, Co) as well as a set of high purity metal melting point standards (In, Sn, Bi, Zn, Al, Ag, Au). The difference between recorded and actual sample temperature depends linearly on heating rate and follows a second order polynomial with respect to temperature. At low heating rates, the temperature is estimated to be accurate to within ± 2 K, while at 500 K/min, the accuracy decreases to ± 15 K.

8.3. Results and Discussion

The measurements, shown in Fig. 8.1, qualitatively resemble earlier experiments [11] in that an initial stepwise weight increase of less than 5 % is followed by a larger stepwise weight increase at higher temperatures. Note that the oxidation rate in none of these experiments shows any increase near the aluminum melting point at 933 K. The first oxidation step shifts to higher temperatures with an increase in the heating rate, as is expected for a thermally activated reaction. However, this shift appears to be smaller at greater heating rates and when the onset temperature approaches the aluminum melting point. A final step, leading to (near) complete oxidation that was observed in experiments [9] where the maximum temperature was 1773 K is not seen here due to the lower maximum temperature in the present experiments.

In order to quantitatively relate the new measurements to previous investigations of oxidation of aluminum powder, oxidation kinetics were determined according to a formalism first developed for measurements at lower heating rates [11, 12]. Particles are assumed to be spherical and oxidation is assumed to occur as a series of individual diffusion processes through the growing surface oxide layer. In this model, at any given time the rate of oxidation is limited by a single, thermally activated mass transfer process, such as diffusion of one species. The rate of mass increase due to oxidation, dm/dt , is described by the equation

$$dm/dt = C_A^* \exp(-E/RT) (1/r_{Al} - 1/r_{ox})^{-1} \quad (8.1)$$

where T is temperature, C_A^* is the combined oxidation constant depending on the reaction stoichiometry, the initial sample mass, and the type of the diffusing species; r_{Al} and r_{ox} are the radii of the aluminum core and oxide shell, respectively; E is the activation energy; and R is the universal gas constant. Rearranging allows processing the recorded TGA traces according to the following equation:

$$\frac{E}{RT} = \ln C_A^* - \ln \left(\frac{dm}{dt} \right) - \ln \left(\frac{1}{r_{Al}} - \frac{1}{r_{ox}} \right) \quad (8.2)$$

The sample mass, m , as well as the radii of the aluminum core and the oxide shell can be expressed in terms of the reaction progress α [14].

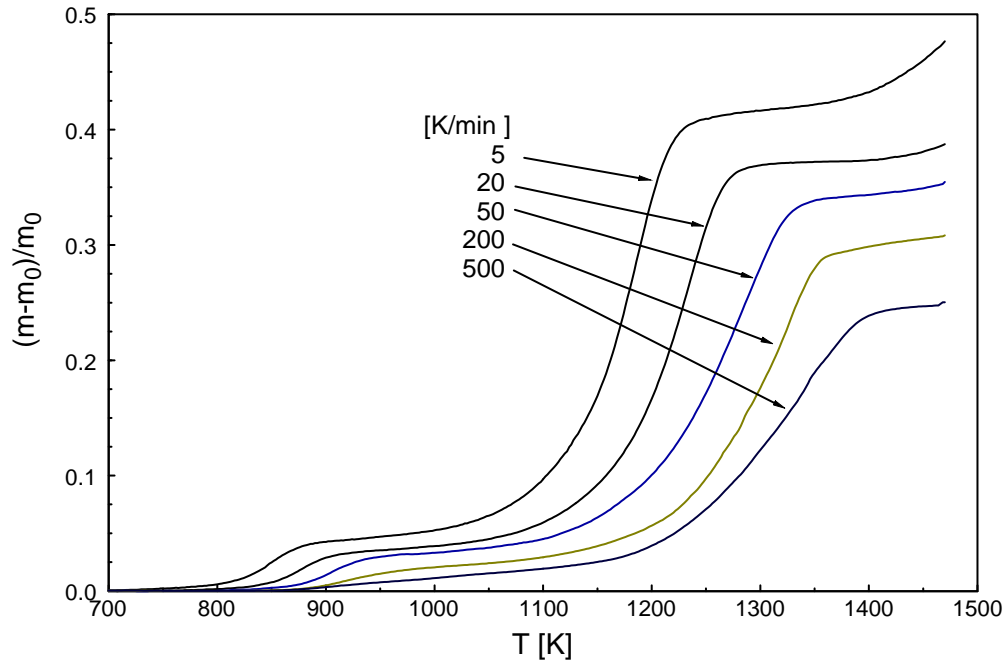


Fig. 8.1. TGA measurements of aluminum powder oxidizing in oxygen-argon mixtures. The nominal heating rates are indicated.

$$\alpha = (m - m_0) / (m_f - m_0)$$

$$-\ln(r_{Al}^{-1} - r_{ox}^{-1}) = \ln\left((1 - \alpha)^{-1/3} - (1 + c \cdot \alpha)^{-1/3}\right) \quad (8.3)$$

Where m_o and m_f are the initial and final masses of the oxidizing particle, respectively, and the constant c accounts for the differences in molar weight and in density between the metal core and the oxide shell.

Therefore, the right hand side of Eq. (8.2) depends only on the experimental reaction progress, and is readily plotted vs. inverse temperature to identify regions that can be described by a positive slope. Respective plots for the thermogravimetric measurements performed at 50, 200, and 500 K/min as presented in Fig. 8.1 are shown in Fig. 8.2.

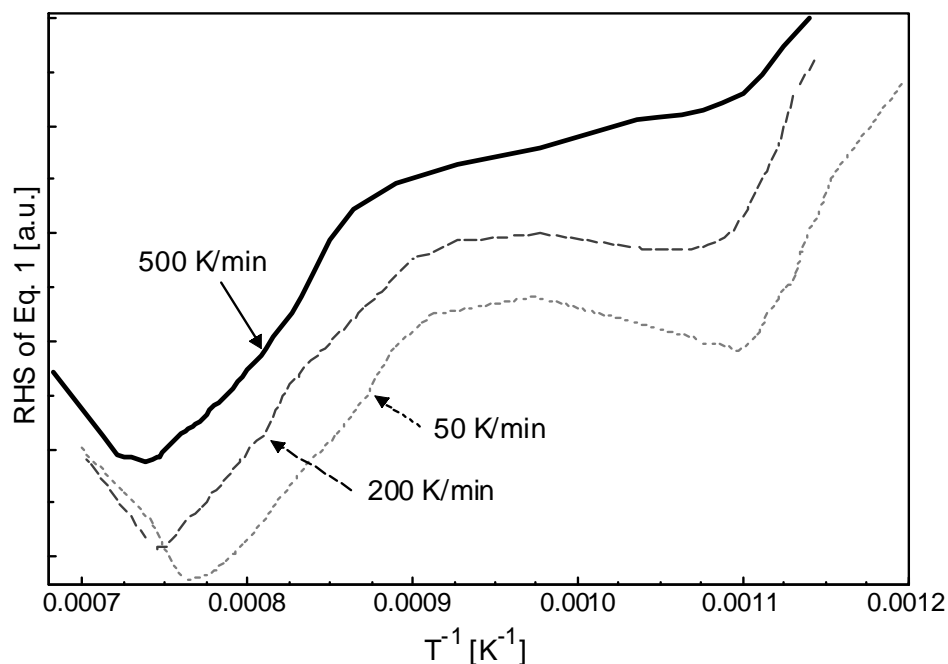


Fig. 8.2. Kinetic processing of a series of measurements at different heating rates. Curves are vertically offset from each other for easier comparison.

For regions where the curves appear as straight lines with positive slopes, the assumption about the reaction rate being controlled by a single thermally activated process and used to derive Eq. (8.2) is considered valid. Therefore, the slopes represent the effective activation energies of the specific reaction processes governing oxidation at the respective values of the reaction progress. For consistent data processing, the slope can be calculated at each value of T^{-1} , or T , or α . This results in characteristic curves of E vs. any parameter that varies monotonously with time. The curves illustrating changes in the activation energy as a function of T and α are shown in Fig. 8.3. In both plots, the activation energy curve produces two humps corresponding to the first and second oxidation steps. The curves are relatively “noisy” because they are obtained from the slopes of such plots as shown in Fig. 8.2. Most of the observed noise represents small, random changes in the experimental thermogravimetric traces rather than actual variations in the activation energy. The activation energy plotted as a function of T shows the temperature shift of the oxidation steps with increasing heating rate. The activation energy plotted as a function of α shows that the steps occur over about the same ranges of the reaction progress.

Data for experiments with different heating rates are processed independently so that the resulting activation energies can be compared directly to one another. The activation energies determined from different experiments should coincide if the same oxidation processes control the reaction in corresponding oxidation stages. This reasoning remains valid when the current measurements performed at higher heating rates are compared to earlier data [11].

Shown in Table 8.1 are average values for the activation energy determined for each group of data points in Fig. 8.3 – corresponding to the first and second oxidation steps, respectively. The activation energy was considered representative if the value was above the 20th percentile in each respective group. The limits in T and α were determined as the points where the E value rose above, and dropped below the 20th percentile, respectively. The data in Table 8.1 are also shown

in Figs. 8.4 – 8.7. In addition, Figs. 8.4 – 8.7 include processed data from earlier experiments [11].

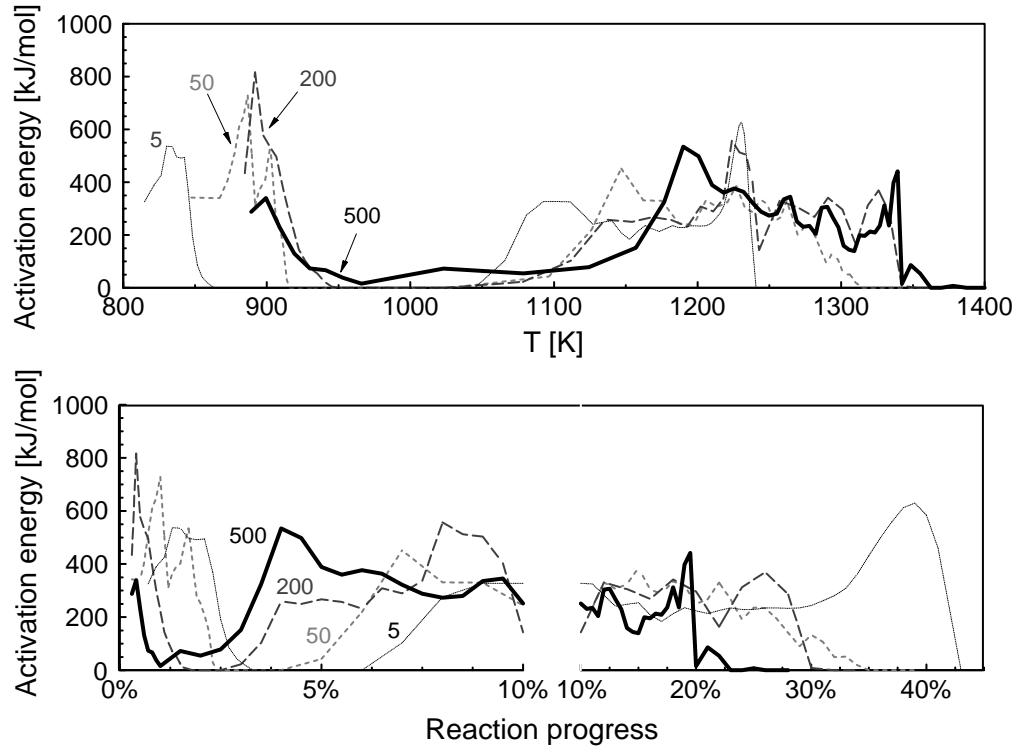


Fig. 8.3. Activation energies of aluminum particle oxidation as a function of temperature (top) and reaction progress (bottom). For clarity, the bottom plot is broken into two parts with different horizontal scales. Nominal heating rates are indicated.

Table 8.1. Summary of observations from Fig. 8.3

Heating rate [K/min]	First observable oxidation step: amorphous-to γ transition			Second observable oxidation step: γ alumina growth		
	T [K]	α	E_A [kJ/mol]	T [K]	α	E_A [kJ/mol]
5	802 – 850	< 2.8 %	393 ± 108	1063 – 1190	8.0 – 34	341 ± 105
20	815 – 882	< 2.4 %	383 ± 155	1106 – 1237	7.0 – 31	345 ± 54
50	847 – 904	< 1.8 %	458 ± 123	1126 – 1294	6.0 – 30	269 ± 82
200	885 – 930	< 1.3 %	372 ± 230	1136 – 1334	4.0 – 28	318 ± 103
500	889 – 941	< 0.8 %	188 ± 115	1177 – 1340	3.5 – 19.5	291 ± 95

Some systematic trends became apparent. The (inverse) temperatures bracketing the oxidation steps (onset and end) shift nearly linearly with the logarithm of the heating rate (Fig. 8.4). This is expected for thermally activated processes. The data from the earlier, lower heating rate measurements [11] appear to correlate with the newly produced measurements at higher heating rates. The temperature shift of the first oxidation step appears to be slightly stronger over the observed range of heating rates.

The extent of oxidation during each observable step decreases with increasing heating rates (Fig. 8.5). As a result, the onset of the second observable step occurs at lower degrees of oxidation, and for 500 K/min, the RHS of Eq. 8.2 never has a negative slope between the first and second observable steps. The end of the second oxidation step also occurs at lower degrees of oxidation at higher heating rates. This trend indicates an increased influence of the second oxidation step (and, respectively, reduced effect of the first oxidation step) on the oxidation kinetics for greater heating rates, of interest to practical ignition situations.

The activation energies calculated for the second oxidation step are consistent at an average value of 300 kJ/mol between the current set of experiments and also previous measurements at lower heating rates (Fig. 8.7). This gives further support to the idea that the growth of γ alumina on the surface of the aluminum particles is the only process responsible for this oxidation step [11, 12], and that within the resolution of the measurement/data processing, the mechanism of oxidation remains unchanged up to the highest heating rates covered in this study.

In contrast, the activation energy of the first oxidation step (Fig. 8.6) varies more with a substantial decrease towards higher heating rates, and also has larger error bars. This can be understood when one takes the nature of this oxidation step into account. According to the current oxidation model, this oxidation step includes at least three distinct processes: the growth of amorphous alumina, the transition of amorphous to a porous layer of γ alumina, and the eventual ‘healing’ of the porous γ alumina layer to form regular polycrystalline γ alumina coating [11, 12]. Therefore, the average activation energy is a composite value that shifts as the relative influence of the component processes changes. Furthermore, it is possible that the activation energy of the transition from the amorphous to γ - Al_2O_3 polymorph is not constant and is affected by the thickness of the oxide layer in which this transition occurs.

The consequence of the decrease in the activation energy of the first oxidation steps at higher heating rates is that the temperature shift with increasing heating rates becomes more pronounced. This may, at very high heating rates, lead to the second oxidation step occurring at lower temperatures than the transition between amorphous and γ alumina. This would necessarily mean that γ alumina starts growing on or within the amorphous alumina before the amorphous surface layer transforms to γ alumina. This potential effect, combined with the observed decrease in the degree of reaction at the end of the first oxidation step (see Table 8.1 and Fig. 8.5), further suggests that the ignition of aluminum particles (at least for the particle sizes covered) is controlled by the processes dominating in the second oxidation step.

The activation energies that are reported depend on, and are strictly valid only for the specific particle oxidation model developed in Ref. 12. To independently assess the activation energies for the growth of amorphous and γ alumina, an isoconversion analysis [15] was performed on all current measurements. The result, an apparent activation energy as a function of the degree of oxidation α , is shown in Fig. 8.8. As expected, the region where amorphous-to- γ transition occurs ($\alpha < 3\%$) can be distinguished from the interval where γ alumina grows ($\alpha > 5\%$). However, the detecting transitions between these intervals, as well as the upper end of the γ growth interval are problematic.

As can be seen in Figs. 8.1 and 8.5, the end of the amorphous-to- γ transition and the beginning of γ growth occurs at decreasing degrees of oxidation as the heating rate increases. A similar effect is seen at the end of the γ growth step. This causes the isoconversion analysis in the affected intervals to break down, since at, e.g. 2 % reaction progress, the amorphous-to- γ transition at 5 K/min is considered the same “degree of conversion” as the γ growth at 500

K/min, while these different processes clearly are characterized by different activation energies. This breakdown is recognized in Fig. 8.8 as the wide depression of the activation energy near 3 % and before 25 %, and as a result, no meaningful activation energy can be determined by isoconversion analysis for the amorphous-to- γ transition. On the other hand, in the interval where γ growth is the only process for all heating rates, at least from 10 % to 20 % reaction progress, the activation energies obtained by isoconversion analysis are very consistent with the values shown in Fig. 8.7.

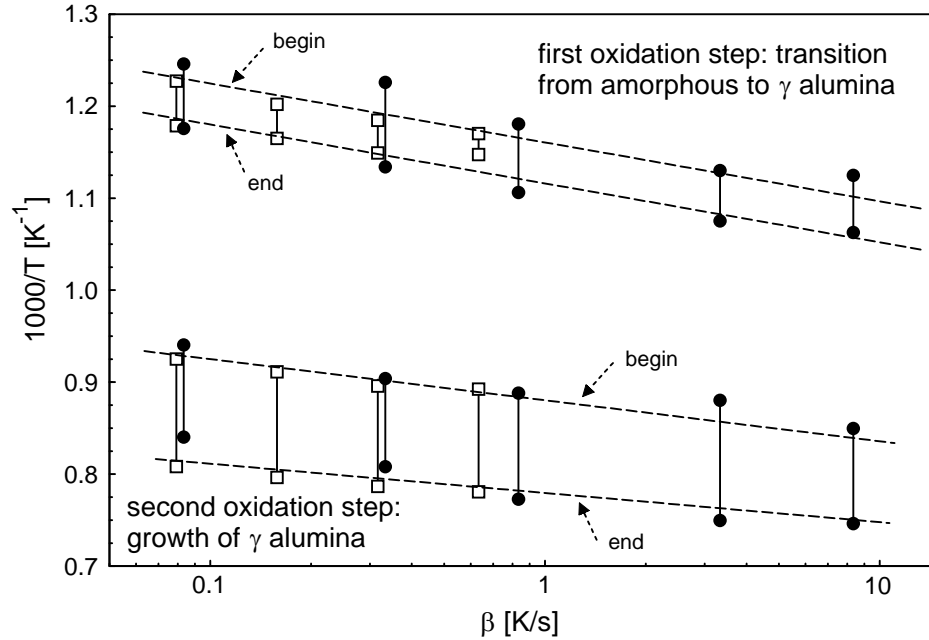


Fig. 8.4. Reciprocal onset and end temperatures of the oxidation steps shown in Fig. 8.1. The figure is calculated from data in Table 8.1, including measurements at 5, 10, 20, and 40 K/min from a previous investigation [11] (open symbols, shifted in β for display) and at 5, 20, 50, 200, and 500 K/min from current work (filled symbols).

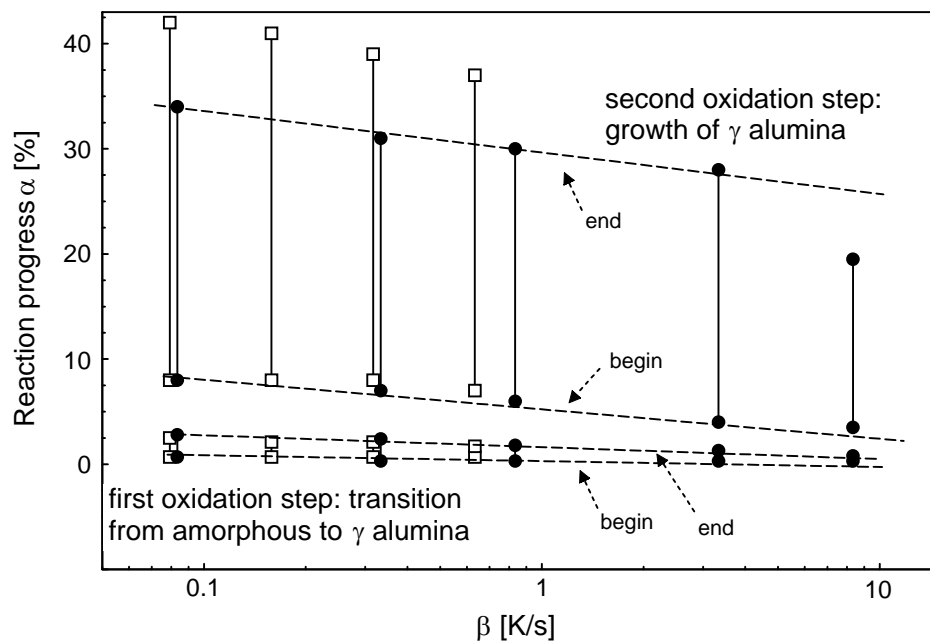


Fig. 8.5. Initial and final values of the reaction progress of the oxidation steps shown in Fig. 8.1, using data in Table 8.1. See Fig. 8.4 for explanation of symbols.

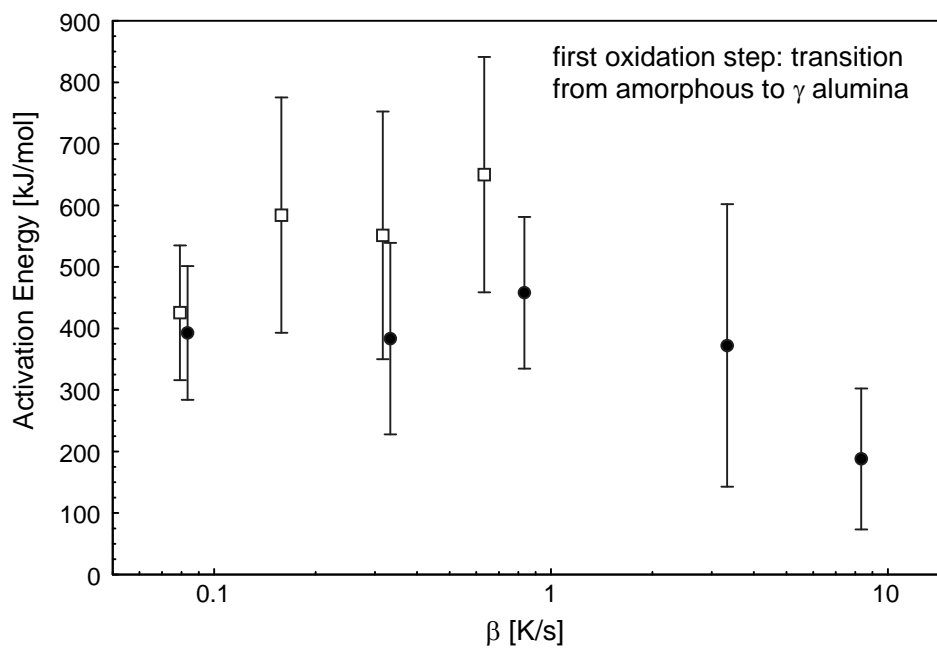


Fig. 8.6. Average activation energies of the first oxidation step, from data in Table 8.1. See Fig. 8.4 for explanation of symbols.

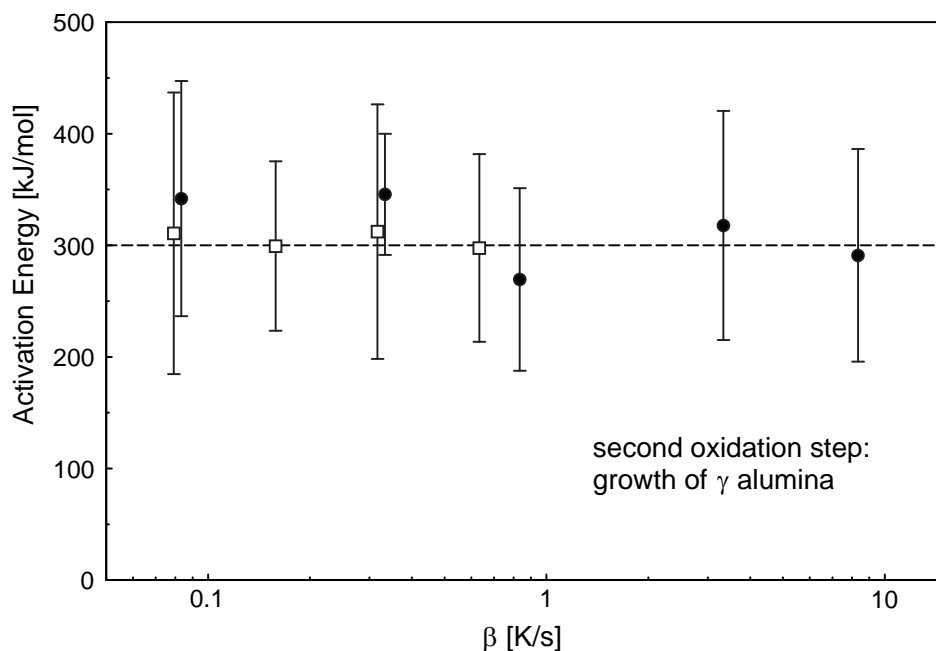


Fig. 8.7. Average activation energies of the second oxidation step, from data in Table 8.1. See Fig. 8.4 for explanation of symbols.

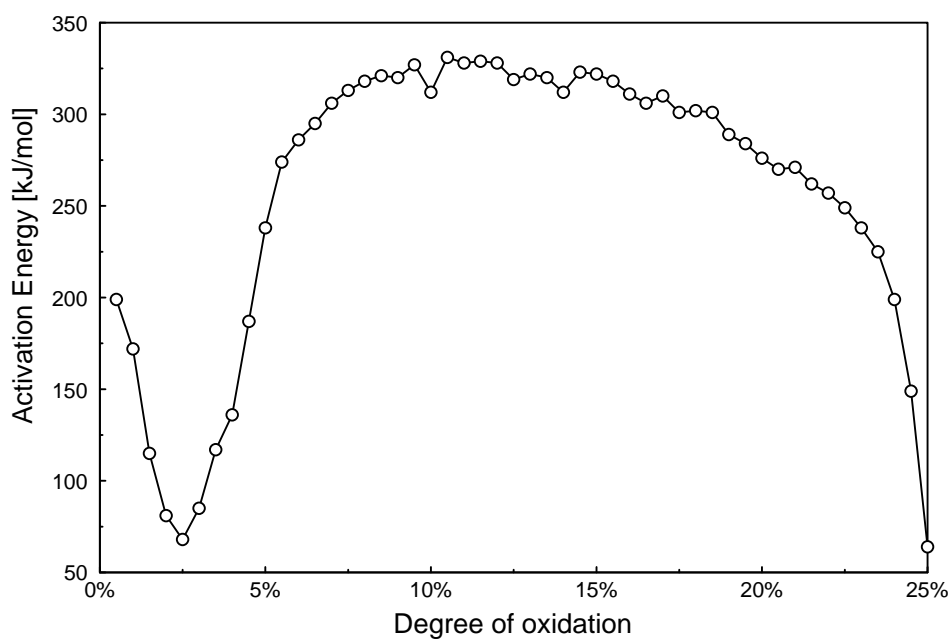


Fig. 8.8. Results of isoconversion analysis of the TGA measurements from 5 – 500 K/min.

8.4. Refining and validation of the oxidation model

To refine the oxidation model by direct comparison with the extended set of TG measurements performed in this study, a set of computed TG curves was prepared following an algorithm

developed earlier [12]. The algorithm includes a large number of empirical parameters (see Table 3 in ref. [12]) and is briefly summarized below.

The oxidation rate of an aluminum particle is exclusively determined by the state of the oxide layer on the particle surface. At any given time there may be more than one oxide polymorph present in the surface oxide layer. To simplify calculations the different polymorphs are modeled as concentric shells or sublayers. The parent oxide according to the transition sequence *amorphous* $\rightarrow \gamma \rightarrow \alpha$ is always located adjacent to the aluminum core, and the newly formed product oxide is located on the outer surface of the particle. The growth of an individual oxide shell is summarily described by the diffusion of a relevant chemical species (e.g. oxygen inward or aluminum outward) using Eq. (8.1), which requires as coefficients a pre-exponent and an activation energy.

The transition from one alumina polymorph with decreasing stability to the next more stable polymorph, e.g., amorphous alumina transforming to γ alumina, is expressed in terms of the interface between the alumina polymorphs moving across the oxide layer, consuming the parent oxide, and leaving the product behind. All polymorphic transitions are described using the same formalism as presented below for the amorphous to γ transition [12]. The velocity of the movement of the interface, $v_{am \rightarrow \gamma}$, requires an activation energy and a pre-exponent (different from those describing growth of oxide by diffusion through the growing layer). In addition to the transformation rate increasing with increasing temperature, the stability of the parent polymorph decreases with increasing layer thickness, and therefore the pre-exponent describing the interface velocity is modeled as a function of both, temperature and parent oxide thickness:

$$v_{am \rightarrow \gamma} = F_{am \rightarrow \gamma} T \left[1 - \exp(-K_{am \rightarrow \gamma} h_{am} / RT) \right] \exp(E_{am \rightarrow \gamma} / RT) \quad (8.4)$$

where h is the layer thickness, and F and K are empirically determined coefficients. The newly formed γ oxide sublayer is assumed to not pose any diffusion resistance until it reaches a minimum thickness $h_{\gamma, \min}$. This means that before that thickness is reached, γ alumina grows exclusively by transformation from amorphous alumina. Once that thickness is reached, the calculated diffusion resistance of γ alumina is compared to the diffusion resistance of the shrinking amorphous oxide sublayer. Of the two sublayers, only the sublayer with a higher diffusion resistance is allowed to grow by diffusion. Consequently once diffusive growth is turned on for γ alumina, the amorphous sublayer will be consumed by the transformation reaction (Eq. 8.4) and disappear within a relatively short time.

Further, γ alumina is considered to have reached its full diffusion resistance only after it reaches a critical thickness, $h_{\gamma, \max}$. Until that occurs, the pre-exponent describing the diffusive growth of γ alumina (see Eq. (8.1)) is modeled as a linear function of its thickness, h_{γ} :

$$C_{\gamma} = C_{\gamma}^* \left[X_{\gamma} - \frac{h_{\gamma} - h_{\gamma, \min}}{h_{\gamma, \max} - h_{\gamma, \min}} (X_{\gamma} - 1) \right] \quad (8.5)$$

where X_{γ} is yet another parameter empirically determined in ref. [12] to fit the measured TG oxidation curves. The minimum thickness $h_{\gamma, \min}$ was set to 5 nm, and the maximum transition thickness $h_{\gamma, \max}$ is determined as a function of the heating rate according to the equation

$$h_{\gamma,\max} = 2h_{\gamma,\min} + G_{\gamma} \exp(-L_{\gamma} \cdot dT / dt) \quad (6)$$

The coefficients G_{γ} and L_{γ} are determined from the relation of the γ layer thickness vs. heating rate at the beginning of the region where γ is the only polymorph. The γ layer thickness was estimated from the sample TG curve at the temperature where dm/dt has a minimum after the first weight increase step (see Fig. 8.1). For further details, please see Ref. [12].

This model was used to reproduce computationally the TG curves measured in this study at heating rates up to 500 K/min (8.33 K/s). The comparison of the model calculations and the measurement is shown in Fig. 8.9, using a heating rate of 50 K/min as example. The experiment is shown as a bold line. Several options existed regarding the treatment of the set of coefficients needed for Eqs. (8.1), (8.4) and (8.5). First, the TG curve calculated directly using the original set of coefficients given in Ref. [12] (p. 611 and Table 3), is shown as the dotted line in Fig. 8.9. The original set of coefficients was determined from measurements in the range 5 – 40 K/min, and under the simplifying assumption that the powder can be described by a single particle size corresponding to a particle with the specific surface area that was measured by BET for the entire powder.

The particle size of the Al powder used here has been measured previously using low-angle laser light scattering (Beckman Coulter - LS 230 Analyzer) [16] making it feasible to calculate TG curves for the specific size distribution rather than for a single size. To account for the size distribution, the oxidation profile $m = f(T)$ was calculated for each size bin, and then all profiles were averaged using the volume-based size frequencies as mathematical weights. Figure 8.9 shows the calculated TG curve for a powder with the full size distribution as the dashed line. Taking the size distribution into account increases the calculated weight change (by a small amount) at the temperatures covered by the experiments. However, the general difference to the measured curve is not significantly affected.

As noted above, the model uses a large number of coefficients. Potentially, the TG curves could be fitted perfectly if all coefficients were allowed to vary. To not over-interpret the measurements, the kinetic parameters describing the diffusion through the growing oxide layer, and describing the phase transition, i.e., the respective activation energies and pre-exponents identified in Ref. [12] were not varied. The activation energies identified in Table 8.1 have too large uncertainties to give compelling reasons to change the model parameters from those given in Ref. [12]. Within their error bars they are consistent with the earlier parameters. However, the greater range of heating rates covered by the current set of experiments allows one to determine the critical thickness parameter $h_{\gamma,\max}$ (Eq. 8.6) with greater confidence than before.

The thin dash-dot and solid lines in Fig. 8.9 represent the set of coefficients with updated $h_{\gamma,\min}$, G_{γ} and L_{γ} coefficients and a single BET-derived particle size, and the full size distribution, respectively. From the method used to determine $h_{\gamma,\min}$, G_{γ} and L_{γ} , it is not surprising that the updated thickness relations achieve a significant improvement in the fit between computation and experiment.

An updated list of adjustable parameters and their refined values based on the current experiments is given in Table 8.2.

Table 8.2. Parameters used in the kinetic model of aluminum oxidation. Original parameters are from Ref. [12]. Parameters that were updated in this manuscript are marked.

E_{am} : 120 kJ/mol	C_{am} : 5.098×10^{-8} kg/(m·s)	
E_{γ} : 227 kJ/mol	C_{γ} : 4.0784×10^{-3} kg/(m·s)	
E_{α} : 306 kJ/mol	C_{α} : 2.3791×10^{-2} kg/(m·s)	
$E_{am \rightarrow \gamma}$: 458 kJ/mol	$K_{am \rightarrow \gamma}$: 1×10^{12} J/(mol·m)	$F_{am \rightarrow \gamma}$: 2×10^{15} m/(s·K)
$E_{\gamma \rightarrow \alpha}$: 394 kJ/mol	$K_{\gamma \rightarrow \alpha}$: 1×10^8 J/(mol·m)	$F_{\gamma \rightarrow \alpha}$: 5×10^6 m/(s·K)
$h_{\gamma, \min}$: 3.47 nm [†]	G_{γ} : 14.1 nm [†]	L_{γ} : 0.360 s/K [†] X_{γ} : 200
$h_{\alpha, \min}$: 61.1 nm [†]	G_{α} : 98.5 nm [†]	L_{α} : 0.563 s/K [†] X_{α} : 150

Figure 8.10 shows the comparison of current measurements at 5, 50, and 500 K/min to calculated TG curves using the real size distribution, and kinetic coefficients with updated $h_{\gamma, \max} = f(dT/dt)$ relations. The calculations fit the measurements reasonably well. The shift of the amorphous-to- γ transition step below 1000 K as a result of the change in heating rate is reproduced very well, as is the degree of oxidation after the transition step. The calculations overestimate the shift of the γ growth step, although the degree of oxidation after the γ -to- α transition is also reproduced well. The ability of the kinetic model to directly reproduce new experiments with the extended range of heating rates in terms of sequence and timing of the phase transitions and in terms of growth of individual polymorphs is encouraging.

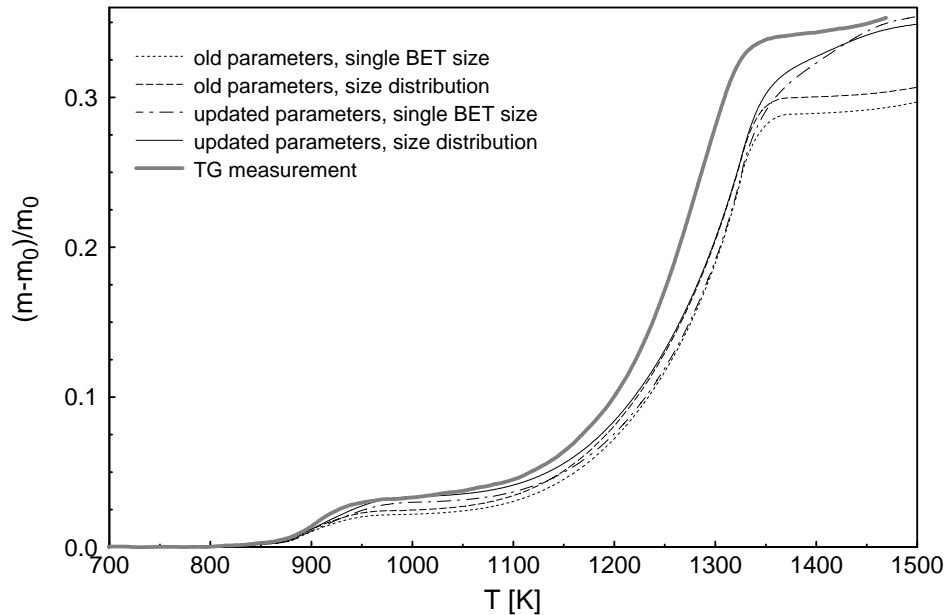


Fig. 8.9. Comparison of the TG curve at 50 K/min with model calculations using different sets of coefficients (see text for detailed explanation).

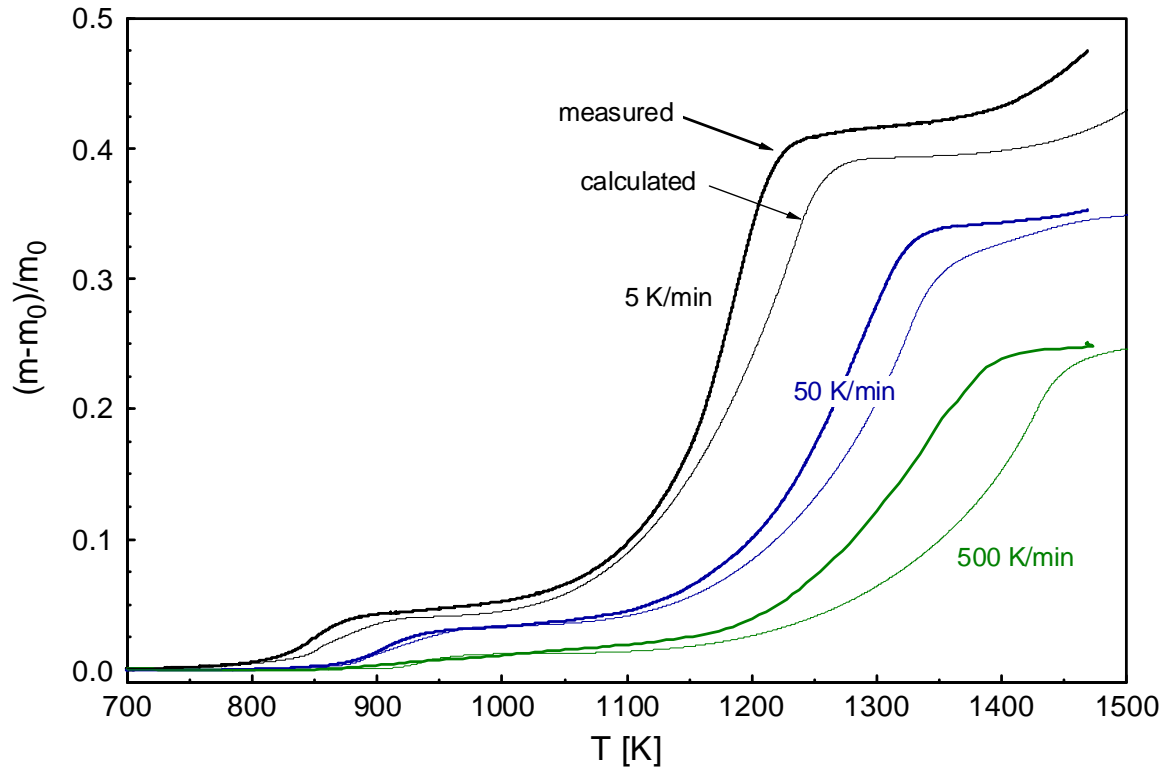


Fig. 8.10. Comparison of experiments and model calculations over the covered range of heating rates.

Although the calculations in the range of heating rates covered by the experiments show that the oxidation rate is always limited by diffusion through the growing surface oxide layer, this is not necessarily the case for higher heating rates. At the stage when all of the parent oxide has disappeared two qualitatively different cases can be distinguished. At low heating rates the thickness of the product layer will have exceeded $h_{i,min}$, and oxidation will be rate limited by diffusion through the growing product oxide layer. As mentioned, all TG experiments represent this mode of oxidation. At high heating rates, however, the product layer may not have reached the minimum thickness $h_{i,min}$, and will therefore remain porous even after the parent layer have disappeared. In the latter case, diffusion resistance of the product oxide layer is negligible so that the fresh, unoxidized aluminum surface is exposed. The oxidation rate will be limited by diffusion in the surrounding gas phase only. In the current model calculations this situation is predicted to occur at heating rates above 10^3 K/s. Figure 8.11 shows the qualitative difference in the oxidation behaviors below and above this critical heating rate.

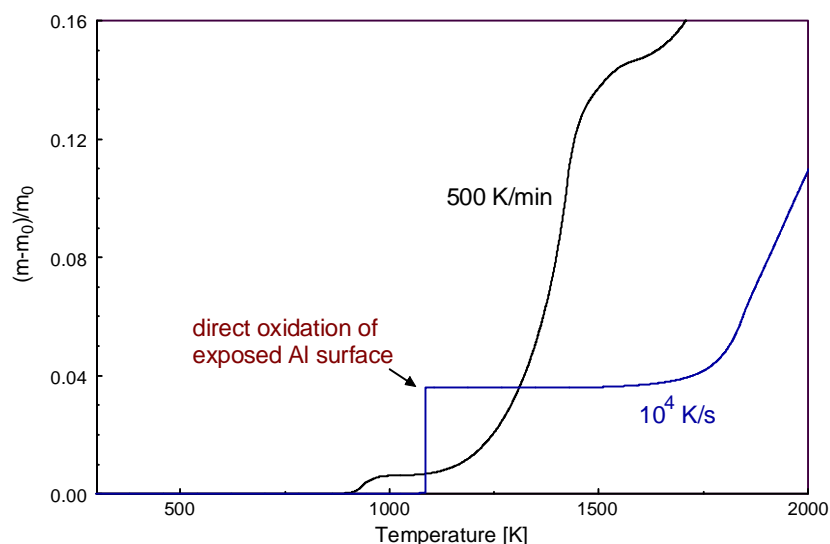


Fig. 8.11. Oxidation behavior at heating rates just below and above which gas phase diffusion becomes a rate limiting factor.

Although this situation is not achievable in the current TG experiments, the calculations can be compared to ignition experiments at high heating rates. A single particle ignition experiment has been described previously [13, 17] where a $3.4\ \mu\text{m}$ diameter particle is moved in air across the focal spot of a stationary CO_2 laser beam with variable velocities, achieving heating at variable rates in the range $0.5 \cdot 10^6 - 3 \cdot 10^6\ \text{K/s}$.

For a detailed description of the experiment and calculations of the particle temperature history while heated by the laser beam, please refer to Refs. [13, 17]. In a previous report [17], the ignition behavior was approximated by a simplified zeroth order reaction without attempting to account for physical processes on the particle surface. This simplified description reproduced the ignition behavior observed in experiments. In particular, the model reproduced the variation in the laser power required to ignite particles crossing the laser beam at different speeds, and thus heated at different rates. The calculated temperature reached by the particle just before the thermal runaway due to the exothermic reaction, referred to as ignition temperature, was not sensitive to the heating rate for the relatively narrow range of heating rates covered by the experiments. Particle ignition was always observed when particles were heated to $\sim 1150\ \text{K}$. However, the extended oxidation model used in the present manuscript can be validated if it predicts the same ignition temperature for the range of heating rates and under the heat transfer conditions of the laser ignition experiment.

To approximate the conditions of the ignition experiment, an aluminum particle with $3.4\ \mu\text{m}$ diameter is suspended in room temperature air, and a constant heating rate is imposed. The heat generated by the surface oxidation is then balanced against convective heat losses of the particle. Convection is the dominant heat loss mechanism at the ignition temperatures, exceeding radiation by about 3 orders of magnitude (see Fig. 8.8 in ref. [13]), and therefore other contributions to the heat loss can be neglected. Figure 8.12 shows the result of this comparison at a heating rate of $10^6\ \text{K/s}$. It is apparent that the convective heat loss rate is only exceeded at the stage in the oxidation process where fresh unoxidized aluminum surface is exposed, which allows a relatively straightforward determination of the ignition temperature due to the sharp increase in the heat generated. Once the convective heat losses are exceeded, the reaction becomes self-sustained and can continue even if the external heat source (laser beam in this case)

is removed. Note that once the heat release due to heterogeneous oxidation exceeds the convective heat losses, it is expected that the vapor phase reaction becomes significant and further contributes to the particle heating. Because vapor phase reactions are not included in the present analysis, the sharp spike in the heat release shown in Fig. 8.12 is followed by the drop in the heat release rate, indicating the thickening of the parent oxide layer. In order for this analysis to remain relevant after the instant the convective heat losses are exceeded, vapor phase reactions must be added to the heat balance calculations, which is beyond the scope of the present paper.

Figure 8.13 shows the ignition temperature determined as the instant when the reaction heat release exceeds the convective losses at a number of heating rates in comparison to the temperature at which aluminum particles are observed to ignite in the laser heating experiments in air reported in [13, 17]. The oxidation model predicts the ignition temperature that is identical to that implied by direct processing of the experimental data with the maximum difference between calculated and experimental ignition temperatures less than 30 K. The model calculations presented in this manuscript, specifically regarding the transition from amorphous to γ alumina, are therefore consistent with experimental observations at heating rates in the 10^6 K/s range.

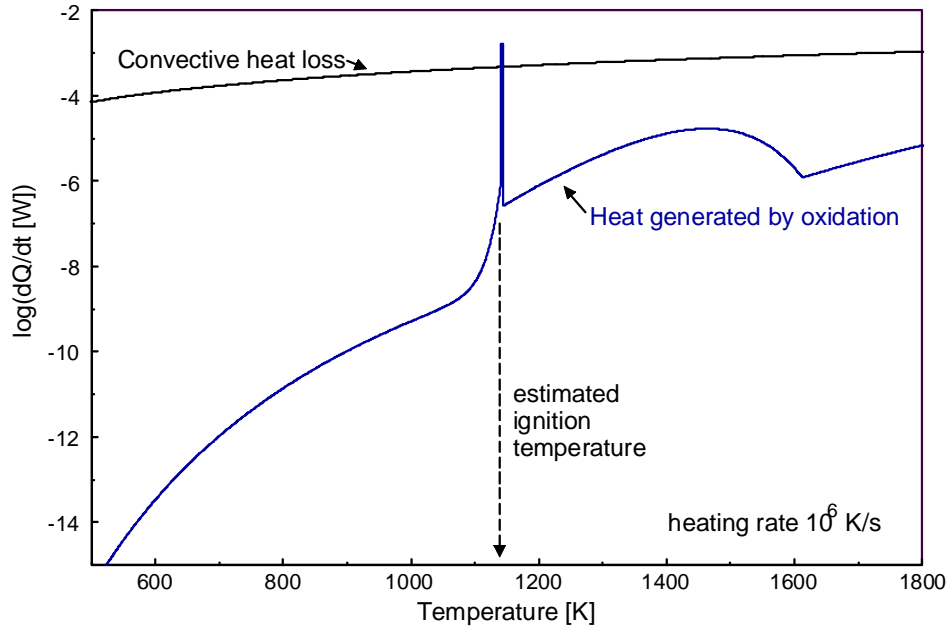


Fig. 8.12. Predicted rates of heat release due to oxidation and heat losses due to convection for a $3.4 \mu\text{m}$ diameter aluminum particle heated at 10^6 K/s.

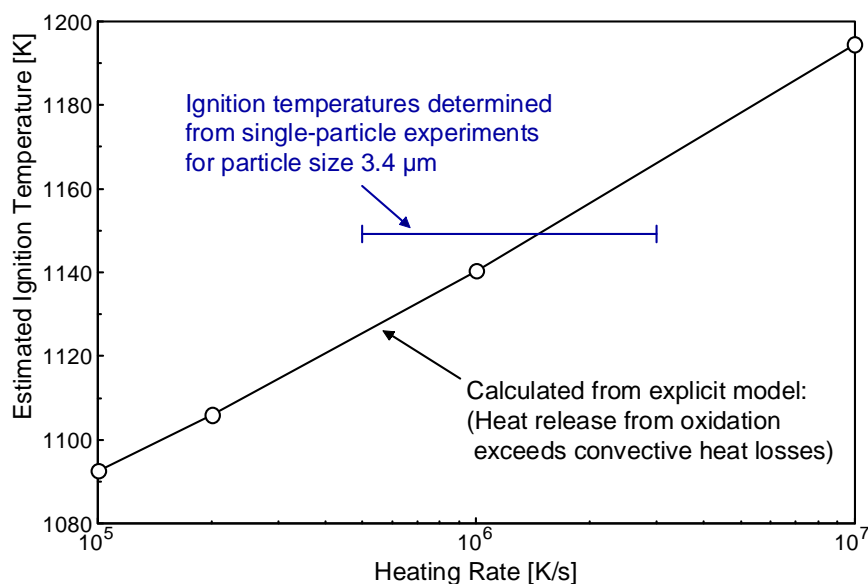


Fig. 8.13. Comparison of the predicted ignition temperature as a function of the heating rate and the ignition temperature inferred from the laser ignition experiments with the heating rates varied in the range of $0.5 \cdot 10^6 - 3 \cdot 10^6$ K/s.

8.5. Conclusions

Aluminum particle oxidation in an argon/oxygen mixture was studied experimentally at heating rates up to 500 K/min and temperatures up to 1473 K. The previously established aluminum oxidation model considering consecutive changes in the surface oxide layer was confirmed qualitatively. The results were processed to extract the activation energy associated with the stages of the oxidation model. The values have relatively large uncertainties but agree substantially with previous results based on experiments performed at lower heating rates. New experimental data refined parameters describing the transition of amorphous to γ alumina, where the initial formation of γ appears to become less dependent on heating rate as the heating rate increases. The predictions of the refined oxidation model are found consistent with the results of recent laser ignition experiments in which aluminum particles were heated in air at about 10^6 K/s. The present results indicate that ignition of laser-heated micron-sized aluminum particles occurs when the integrity of the protective oxide layer is disrupted by a polymorphic phase change between amorphous and γ - Al_2O_3 .

8.6. References

1. Frost, D.L., Ornthanalai, C., Zarei, Z., Tanguay, V., Zhang, F. 2007 *Journal of Applied Physics* 101 (11), art. no. 113529
2. Baer, M. R. *Thermochimica Acta* 384 351–367 (2002)
3. Eakins D.E., N.N. Thadhani, N.N., *Acta Materialia* 56 1496–1510 (2008)
4. Fang, T. 2008 *Journal of Thermophysics and Heat Transfer* 22 (2), pp. 313-315
5. Yoh, J.J., Kim, K.-H. 2008 *Journal of Applied Physics* 103 (11), art. no. 113507
6. Trunov, M.A., Schoenitz, M., and Dreizin, E.L., *Propellants Explosives and Pyrotechnics*, V. 40, No 1, pp. 36-43 (2005)
7. Beckstead, M.W. 2005 *Combustion, Explosion and Shock Waves* 41 (5), pp. 533-546
8. Dreizin, E.L., *Combustion and Flame*, 105:541-556 (1996)

9. Dreizin, E.L., *Combustion and Flame* 117:841-850 (1999)
10. Brooks, Kristen P., Beckstead, Merrill W. *Journal of Propulsion and Power* 11 (4), pp. 769-780 (1995)
11. Trunov, M.A., Schoenitz, M., Zhu, X., Dreizin, E.L., *Combustion and Flame*, V. 140 No 4, pp. 310-318 (2005)
12. Trunov, M.A., Schoenitz, M., Dreizin, E.L., *Combustion Theory and Modeling*, 10 (4) pp. 603-624 (2006)
13. Mohan, S., Trunov, M.A., and Dreizin E.L. *Journal of Propulsion and Power* 24 (2) pp. 199 – 205 (2008)
14. Zhu, X., Schoenitz, M., and Dreizin E L. In *Energetic Materials. Characterisation, Modelling and Validation; 40th International Conference of ICT*, June 23-26, 2009, Karlsruhe, Germany, pp. 34-1 – 34-11, 2009
15. Vyazovkin, S., J. *Computational Chemistry* 22(2) (2001) 178-183
16. Eapen B. Z., Hoffmann V. K., Schoenitz M., Dreizin E. L., *Combustion Science and Technology*, 176 (7): 1055-1069 (2004)
17. Mohan S., Furet L., Dreizin E.L. *Combustion and Flame*, 157 pp. 1356–1363 (2010).

9. On possibility of vapor-phase combustion for fine aluminum particles

9.1. Introduction

Metal powders are widely used as high energy density additives in propellants, pyrotechnics and explosives. There is growing interest in using finer metal powders and nano-powders [1 – 3] to increase the reactive surface area and achieve higher burn rates, more compatible with the burn rates of conventional monomolecular energetic formulations. However, combustion of metal particles with dimensions of 0.01 – 10 μm is not well understood and may differ substantially from that of coarser particles. In most practical codes, combustion of metal particles is described by one or another variant of “ d^2 -law”, e.g., [4 – 6], an analog of expression derived for diffusion-limited combustion of liquid droplets. It is, however, well understood that for finer particles, both heat and mass transfer processes shift towards free molecular regimes and surface reaction kinetics starts playing an increasingly important role. In the first approximation, this shift is being treated by simply adjusting the exponent in the “ d^n law”, with $n=1$ corresponding to the kinetically controlled combustion. However, this treatment may be inadequate, and it remains unclear just how the exponent should be adjusted for different size particles. Substantial corrections to other combustion parameters may need to be considered as well. One important example is the flame temperature, and recent results [7] suggest that the flame temperatures decrease for fine Al particles; it was also observed that nano-Al powders can burn at temperatures substantially lower than the Al boiling point. Clearly, the role of vapor-phase combustion processes is substantially reduced under such conditions, resulting in burn rates and reaction kinetics different from those implied by conventional “droplet combustion” model. Models for both heat and mass transfer processes as well as for both gas phase and surface reaction kinetics are needed for accurate combustion description. Practically useful models can be simplified if it can be shown that some of the involved processes can be safely neglected. This paper presents a simplified analysis of heat transfer for a burning metal particle resulting in a critical condition establishing the feasibility of a vapor-phase flame. It is shown

that for each environment, there is a minimum particle size capable of maintaining a purely vapor phase flame. For particles smaller than this critical size, additional heat should be released by reactions directly on the particle surface for the vapor phase combustion to remain sustained. Estimates for the minimum Al particle size necessary to maintain the vapor phase flame are made for three oxidizing environments: air, CO₂ and H₂O, all considered to be at room temperature.

9.2. A simplified heat transfer model for an Al particle burning in the vapor phase

A single spherical Al particle of diameter d_p at the aluminum boiling point ($T_p = 2792$ K) is assumed to be surrounded by a vapor phase flame. The flame is treated as a hypothetical gas surface of diameter d_f at temperature T_f . The flame itself is surrounded by ambient gas at room (or environment) temperature, T_e ($T_e < T_p < T_f$). This situation is illustrated in Fig. 9.1. The flame heat balance considers the heat transfer from the flame to both cold gas outside the flame, \dot{Q}_e , and to the particle inside the flame, \dot{Q}_p . The heat flux to the particle surface supports evaporation of Al, while the rate of evaporation determines the rate of the heat release due to the Al combustion. A quasi-steady situation is considered for micron-sized particles because the particle combustion time (of the order of ms) is much greater than the characteristic time of heat or mass transfer in the surrounding gas (less than 1 μ s) that is estimated as d_p^2/D_g or d_p^2/κ_g , where D_g and κ_g are gas diffusion coefficient and thermal diffusivity, respectively. For self-sustaining vapor phase combustion, the following inequality should always be satisfied:

$$\dot{Q}_C \geq \dot{Q}_e + \dot{Q}_p \quad (9.1)$$

where the heat of combustion \dot{Q}_C is the heat released as a result of oxidation of all of the evaporated aluminum. The value of \dot{Q}_C is defined by the rate of evaporation, which itself depends on the heat transferred from the flame to the particle. It can be calculated as:

$$\dot{Q}_C = \frac{\dot{Q}_p}{H_{ev}} \Delta H_{ox} \quad (9.2)$$

where, H_{ev} is the latent heat of evaporation for aluminum and ΔH_{ox} is the heat of oxidation of aluminum in a given environment.

Treating the vapor-phase flame as a spherical surface placed in the gas, assuming that the flame diameter is much greater than the mean free path of the gas molecules, and neglecting radiation, the heat loss from the flame to the environment can be estimated using a continuum regime heat transfer expression given as [8]:

$$\dot{Q}_e = 2\pi d_f \int_{T_e}^{T_f} k(T) dT \quad (9.3)$$

where k is the thermal conductivity of the surrounding gas. Its dependence on temperature, $k(T)$ is obtained from ref. [9].

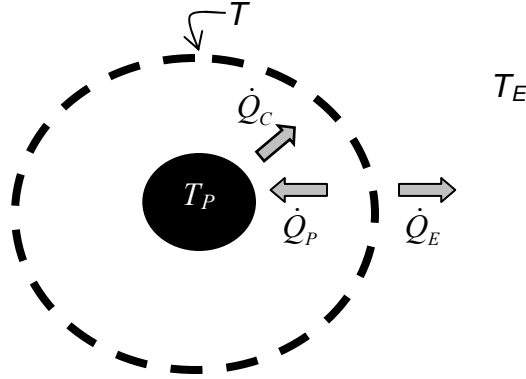


Fig. 9.1 Configuration showing an Al particle at temperature T_P , a hypothetical flame surface at temperature T_F in a gaseous environment at temperature T_E .

Because of the high flame temperature and small size of the burning particles considered in this study, the mean free path of gas molecules can be comparable to the particle diameter. Therefore, neglecting radiation, the heat transfer rate between the flame and particle is estimated using three different approaches: continuum, free molecular and transition regimes [8, 10, and 11]. For the continuum regime, expression for heat conduction between two concentric shells [12], i.e., droplet surface and flame, is used:

$$\dot{Q}_P^{Continuum} = \frac{2\pi}{\left(\frac{1}{d_P} - \frac{1}{d_F}\right)} \int_{T_P}^{T_F} k(T) dT \quad (9.4)$$

For free molecular regime, \dot{Q}_P is calculated as [8, 10 and 11]:

$$\dot{Q}_P^{Free\ Molecular} = \alpha \pi d_P^2 P_E \sqrt{\frac{k_B T_F}{8\pi m_g}} \frac{\gamma^* + 1}{\gamma^* - 1} \left(1 - \frac{T_P}{T_F}\right) \quad (9.5)$$

where α is the accommodation coefficient, m_g is the mass of a gas molecule, k_B is the Boltzmann constant, and P_E is the ambient gas pressure. The superscript ‘*’ indicates that the value of γ is averaged over the temperature range of $(T_P - T_F)$. The accommodation coefficient equal to one was used to maximize the heat flux. In general, the free-molecular heat transfer regime described by Eq. (9.5) is valid for surfaces separated by a distance equal to or smaller than the mean free path of the gas molecule. For the present estimate, this limitation can be relaxed in order to assess the maximum possible heat flux to the particle.

For transition regime, \dot{Q}_E is calculated using a well-known [13] and recently validated [8, 10 and 11] Fuchs model for the heat transfer. The Fuchs model introduces Langmuir layer with thickness δ around the particle and the heat transfer inside this layer is calculated using the free molecular regime while the heat transfer outside of it is calculated using continuum convection model. This model is adapted here by introducing the Langmuir layer between the particle surface and the flame. The Langmuir’s layer thickness $\delta(T_\delta)$ is approximately equal to

the mean free path $\lambda(T_\delta)$ [8]. The heat transfer within the Langmuir layer is calculated using Eq. (9.5) as:

$$\dot{q}_{in} = \alpha \pi d_p^2 P_E \sqrt{\frac{k_B T_\delta}{8\pi m_g}} \frac{\gamma^* + 1}{\gamma^* - 1} \left(1 - \frac{T_p}{T_\delta} \right) \quad (9.6)$$

Outside of the Langmuir layer, the heat transfer is calculated considering continuum regime for the configuration of two concentric shells, similar to Eq. (9.4):

$$\dot{q}_{out} = \frac{2\pi}{\left(\frac{2}{d_p + 2\delta(T_\delta)} - \frac{1}{d_F} \right)} \int_{T_\delta}^{T_F} k(T) dT \quad (9.7)$$

Because there is no additional heat sources or sinks in the Fuchs model, Eqs. (9.6) and (9.7) are solved for T_δ assuming,

$$\dot{q}_{out} = \dot{q}_{in} \quad (9.8)$$

after which, the heat transfer rate $\dot{Q}_E = \dot{Q}_P^{Fuchs} = \dot{q}_{in}$ or $= \dot{q}_{out}$ can be found using either of the Eqs. (9.6) or (9.7), respectively. It can be seen that the total heat loss from the flame i.e., $(\dot{Q}_E + \dot{Q}_P)$, is a function of the flame diameter. For a given particle size, a larger flame is harder to sustain because a greater flame diameter means increased heat losses to the environment and reduced heat transfer to the particle. From this heat transfer perspective only, Eq. (9.1) can be used to estimate the maximum flame diameter expected for a given particle size and flame temperature. To estimate the maximum flame diameter, the flame is considered to be at the maximum possible temperature, which is the adiabatic flame temperature for Al reacting in a given environment. Using the adiabatic flame temperature for T_F in the equations presented above, the maximum flame diameter can be estimated applying Eq (9.1). Because of the three different approaches used to estimate the heat transfer between the flame and the particle, according to Eqs. (9.4), (9.5), and (9.6 – 9.8), three separate estimates for the maximum flame diameter are presented below.

9.3. Maximum vapor phase flame diameter for Al particles burning in different environments

The maximum flame diameter is calculated for three different environments: air, CO₂ and H₂O and as a function of the particle diameter. Figure 9.2 shows the adiabatic flame temperatures for different environments as a function of the equivalence ratio. These temperatures were obtained using CEA code (CEA2, version 2, [14]) and considering a constant pressure combustion case (at 1 atm). The adiabatic flame temperature correlates with the oxidation enthalpy for different environments and peaks, for each environment, around the equivalence ratio of 4. For further analyses, the flames are assumed to be at the maximum predicted adiabatic flame temperatures corresponding to each environment, air: $T_F=4009$ K; CO₂: $T_F=3893$ K; and H₂O: $T_F=3590$ K.

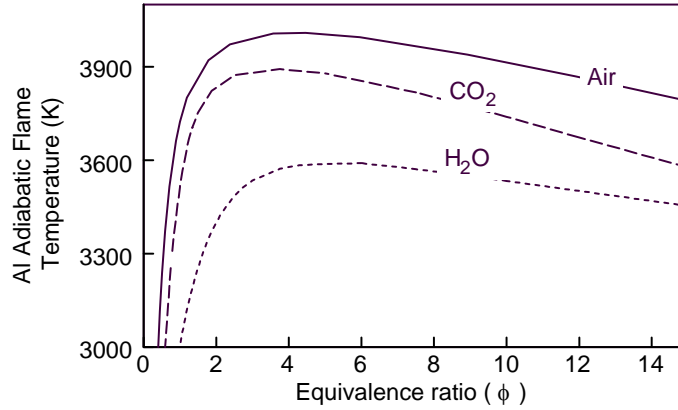


Fig. 9.2 Adiabatic flame temperatures of aluminum combustion plotted as a function of equivalence ratio for different environments.

Figure 9.3 shows the dimensionless flame diameter, D , defined as a ratio of the calculated maximum flame diameter over the Al particle diameter, as a function of the Al particle diameter for air, CO₂ and H₂O. For each environment three curves shown represent three different approaches used to calculate \dot{Q}_E : continuum, free molecular, and transition regimes. The dimensionless diameter D calculated for the continuum heat transfer approach does not depend on the particle size. Its value is affected only by the combustion enthalpy, metal heat of evaporation, and flame temperature. D equals to 2.4, 2.1 and 1.7 for air, CO₂ and H₂O environments, respectively. The continuum approach is applicable for very large particles, when the distance between the flame and droplet surface is much greater than the mean free path of gas molecule. On the other hand, in case of very small particles, when the distance between the particle surface and the flame approaches the mean free path of gas molecules, free molecular approach should be used. For a given temperature difference and assuming the accommodation coefficient, $\alpha = 1$, the free-molecular approach predicts the maximized heat transfer rate possible in the gas phase, so that a high-end estimate for the maximum flame diameter is produced. In this case, the ratio D becomes proportional to square of the particle diameter. The value of D equal to 1 is predicted for a specific particle diameter for each environment, as shown in Fig. 9.3. The diameter $D = 1$ means that the maximum flame diameter equals to the particle diameter, or that the flame exists right on the particle surface. Thus, the values of $D < 1$ indicate a non-physical situation, which implies that self-sustaining purely vapor phase flames cannot be established for respective particle sizes. In other words, the particle diameter corresponding to the value of $D = 1$ is a critical diameter below which the purely vapor phase combustion is not possible, based on the assumed thin flame zone approximation. The critical particle diameters predicted for air, CO₂ and H₂O environments at 1 atm are close to 6.1 μm , 7.2 μm and 15.1 μm , respectively. Note that the actual flame zones for metal combustion are extended due to the formation of relatively stable suboxides, e.g., AlO, Al₂O and AlO₂ for aluminum combustion. The heat losses from extended flame zones will be generally greater than those estimated here for the thin flame zone. At the same time, the inner boundary of the flame zone can approach the particle surface, enhancing the heat transfer from the flame to the particle. Analysis of the heat transfer for the extended flame zones is rather complicated, but it will similarly result in the existence of a critical particle size for which the purely vapor phase flames are impossible.

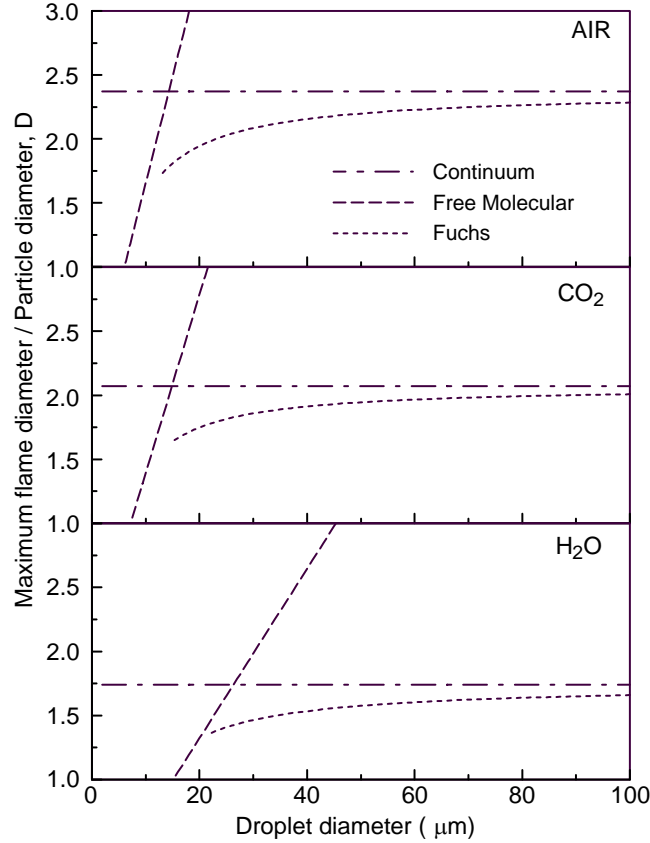


Fig. 9.3 Ratio of maximum flame diameter to Al droplet diameter as a function of Al droplet diameter in different gas environment i.e. air, CO₂ and H₂O. Flame diameter is calculated using continuum, free molecular and Fuchs heat transfer model approaches.

The Fuchs model takes into account the particle size-dependent heat transfer and approaches the free molecular regime for smaller particles and the continuum for increasing particle sizes. Because the Langmuir layer is placed between the particle surface and the flame, the model cannot be used when the distance between the particle and the flame becomes smaller than approximately three mean free paths of the gas molecules.

9.4. Discussion

The simplified model discussed here is not intended to describe multiple heat and mass transfer processes occurring in metal particle combustion. It highlights a striking effect of taking into account changes in the convection heat transfer occurring when particle sizes are reduced to become comparable with the mean free path of gas molecules.

One of the most important omissions in the discussed heat transfer model is neglecting the radiation heat transfer. The significance of this omission can be assessed based on a simplified estimate. Note that for a metal vapor phase flame most of the radiation is produced by the condensed combustion products (smoke). The strongest effect of the radiation heat transfer is the reduction in the flame temperature compared to the adiabatic flame temperature. For

example, the flame temperature for a single Al particle was recently measured to be close to 3200 K [15, 16]. The reduction in the flame temperature results in the reduced rate of heat transfer by conduction from flame to the particle. In turn, this leads to an increase in the critical particle size, below which the purely gas phase combustion is not sustainable. On the other hand, despite the reduced flame temperature, radiation may also intensify heat transfer from the flame to the particle, which would result in reduction in the critical particle size. To compare these two opposite effects, an additional calculation was performed. This calculation assumed the flame to be a thin surface with emissivity equal to one. The radiation contributions were added for both \dot{Q}_p and \dot{Q}_e terms. For the particle emissivity, a value of 0.06 reported for molten Al, was used [12]. The environment and surfaces surrounding burning particle remained at room temperature. To estimate the effect of flame temperature on the value of critical particle size, calculations were performed for two flame temperatures for the case of aluminum combustion in air. For the adiabatic flame temperature of 4009 K, accounting for radiation increased the critical particle size to 6.6 μm compared to 6.1 μm obtained neglecting radiation. For the experimental flame temperature of 3200 K, the critical particle size increased to 12 μm compared to 11 μm obtained neglecting radiation. Thus, even though the effect of radiation heat transfer is not negligible, due to its competing contributions to heat loss to the environment and heating the particle, the value of the critical particle size is not affected significantly. The most important conclusion is that the existence of the critical particle size is predicted by heat transfer models with and without radiation. Clearly, more detailed modeling will result in a better defined critical particle size, while the simplified analysis presented here is aimed to establish the existence of such a critical diameter conceptually.

It is interesting to compare predictions of the present model with the experimental observations. Detailed measurements of the flame zone size are available for large Al particles. Experimental data cited in early refs. [17, 18] suggest that for atmospheres with water, the dimensionless flame diameter is 1.5 and for atmospheres with oxygen, the dimensionless flame diameter varies between 2.5 and 3, depending on the oxygen concentration. In ref. [19], the luminous zone size of about 0.4 mm was observed for the 165 μm diameter Al particles burning in air. The ratio of the flame size to the particle size $D=2.42$, which is very close to that predicted by the continuum approach, adequate for such large particles. Detailed SEM images of the condensed combustion products collected around Al particles burning in CO_2 are shown in refs. [20] and [21]. In both cases, the condensed products are observed to form at the dimensionless flame diameters just above 2, again, consistent with the prediction shown in Fig. 9.3. Thus, the dimensionless flame size predicted for large particles in different environments is in reasonably good agreement with the available experimental data.

Similar data for fine particles are not available, while it is generally expected that the flame would move closer to the particle surface. A more important outcome of the model is the prediction of fairly large critical particle sizes below which the vapor-phase combustion becomes unsustainable. In an apparent contradiction to the above conclusion, smaller Al particles have been reported to burn with the observable vapor-phase flames [22] or, more precisely, extended luminous zones. The contradiction is easily resolved considering that the observed extended luminous zones may be indicative of the combined vapor phase and surface reactions. Indeed, formation of the extended luminous zone is possible, while both heterogeneous and vapor phase reactions contribute to the heat release and affect the heat balance between the particle, its extended flame zone, and surrounding environment. In fact, even for such a metal as Mo, with the metal boiling temperature exceeding its adiabatic flame temperature, an extended flame zone

and respective combustion products were reported to form around a particle burning in air [23], indicative of a combination of the surface and vapor phase combustion processes. Clearly, however, such combustion regime is very different from the classic vapor-phase droplet combustion.

The simple heat transfer analysis presented here suggests that for micron-sized Al particles, combustion always includes surface reactions substantially affecting the heat balance in the flame, respective evaporation rate of metal, and the overall particle burn rate. Note that for a more complete model, a similar analysis of the mass transfer governing fuel and oxidizer diffusion towards the flame should also be considered. Similarly to heat transfer, mass transfer rates will also be affected by reduction in the burning particle size and respective reduction in the length scales involved. Respective estimates will also require use of free-molecular or transition mass transfer regimes.

Note that the presented critical particle sizes are estimated for Al combustion at 1 atm; these sizes will be reduced for elevated pressures. Finally, it should be emphasized that the analysis presented here applies to single particles only. In an aerosol, when the particle interaction is substantial, the situation can change dramatically. For a particle in the middle of an aerosol cloud, the environment temperature would be close to the flame temperature, T_F , so that losses from the flame are greatly reduced. Therefore, the critical particle size capable of maintaining the vapor phase flame can be substantially reduced as well.

9.5. Conclusions

A simplified heat transfer model applicable for vapor-phase combustion of individual fine metal particles predicts existence of a critical particle diameter, below which the vapor phase flame alone cannot be self-sustaining. Other heat generation mechanisms (i.e. surface oxidation) should complement the vapor phase flame. The predicted critical particle diameter is a function of the flame temperature and pressure. Decrease in the flame temperature results in an increase in the critical particle diameter, while the increase in pressure reduces the critical particle diameter. The estimates of the critical particle diameter are made for Al combustion in air, CO₂ and H₂O at 1 atm. The simplified estimates suggest that particles less than 6.1 μm , 7.2 μm and 15.1 μm will not sustain vapor phase flames in air, CO₂ and H₂O environments, respectively. These numbers are not expected to be precise but they are useful as indicators of the Al particle size ranges for which combustion will be governed by combination of heterogeneous and vapor phase combustion processes. Respectively, substantial changes in the burn rates and combustion regimes for such particles are expected as compared to larger size Al particles.

9.6. References

1. M.M. Mench, K.K. Kuo, C.L. Yeh, Lu, Y.C, Combustion Science and Technology 135 (1-6) (1998) 269-292.
2. Y. Huang, G.A. Risha, V. Yang, R.A. Yetter, Combustion and Flame 156 (1) (2009) 5-13.
3. L. Galfetti, L.T. De Luca, F. Severini, L. Meda, G. Marra, M. Marchetti, M. Regi, S. Bellucci, Journal of Physics Condensed Matter 18 (33) (2006) S1991-S2005.
4. L.F. Ernst, F.L. Dryer, R.A. Yetter, T.P. Parr, D.M. Hanson-Parr, Symposium (International) on Combustion 28 (1) (2000) 871-878.

5. C.T. Richmond, AIP Conference Proceedings 845 I (2006) 495-498.
6. Y. Shoshin, E. Dreizin, Combustion and Flame 133 (3) (2003) 275-287.
7. T. Bazyn, H. Krier, N. Glumac, Proceedings of the Combustion Institute 31 II (2007) 2021-2028.
8. A. V. Filipov, D. E. Rosner, International Journal of Heat and Mass Transfer 43 (2000) 127-138.
9. P. Linstrom, W. Mallard, NIST Chemistry WebBook: National Institute of Standards and Technology Gaithersburg, MD, 1997.
10. F. Liu, K. J. Daun, D. R. Snelling, G. J. Smallwood, Appl. Phys. B 83 (2006) 355–382.
11. S. Mohan, M. A. Trunov, E. L. Dreizin, Journal of Heat Transfer 130 (10) (2008) 104505-104509.
12. J. P. Holman, Heat Transfer, McGraw-Hill, New York, 1981.
13. N.A. Fuchs, Geophys. Pura Appl. 56 (1963) 185-193.
14. B. J. McBride, S. Gordon, NASA RP 1311 Users Manual and Program Description, 1996.
15. N.I. Poletaev, A.V. Florko, Combustion, Explosion and Shock Waves 43 (4) (2007) 414-422.
16. N.I. Poletaev, A.V. Florko, Combustion, Explosion and Shock Waves 44 (4) (2008) 437-443.
17. P.F. Pokhil, A.F. Belyayev, Y.V. Frolov, V.S. Logachev, A.I. Korotkov, Moscow: Nauka; 1972; Engl Transl Rept FTD-MT-24-551-73, Wright-Patterson AFB, OH: Foreign Technology Division; 1972.
18. R.P. Wilson Jr., F.A. Williams, Proc. Symposium (International) on Combustion 13(1) (1971) 833-845.
19. E.L. Dreizin, Combustion and Flame 116 (3) (1998) 323-333.
20. P. Bucher, R.A. Yetter, F.L. Dryer, E.P. Vicenzi, T.P. Parr, D.M. Hanson-Parr, Combustion and Flame 117 (1-2) (1999) 351-361.
21. S. Rossi, E.L. Dreizin, C.K. Law, Combustion Science and Technology 164 (2001) 209 – 237.
22. Y. Shoshin, E. Dreizin, Aerosol Science and Technology 36 (9) (2002) 953-962.
23. E.L. Dreizin, A.V. Suslov, M.A. Trunov, Combust Science and Technology 90 (1993) 79-99

10. Combustion times and emission profiles of micron-sized aluminum particles burning in different environments

10.1. Introduction

Aluminum is an important energetic component of many solid propellants, explosives, and pyrotechnic formulations [1 – 4]. One critical parameter of aluminum combustion, universally important for all applications, is the particle burn time, τ_b , as a function of the particle diameter, D . For practical purposes the burn time is commonly expressed as a power law $\tau_b \sim D^n$, with the exponent n and pre-exponent factor depending on the oxidizing environment, temperature, and

pressure, e.g., [5 – 8]. Various D'' type trends were reported by different authors based on a diverse set of experiments. Generally, laboratory experiments in well-characterized environments reported in the literature can be broadly divided into two groups: experiments using individual metal particles, e.g., [9 – 14], and experiments employing aerosolized powders or clouds, e.g., [7, 15 – 19]. For individual particles, the measurements of combustion times are often direct, while indirect methods and data analyses are used to extract the information on particle burn times or burn rates from the cloud combustion experiments. It is also worth noting that single metal particle combustion experiments in general, and direct measurements of combustion times for individual aluminum droplets in particular, were restricted to relatively large particles, with sizes 50 μm or greater. However, most practical applications deal with finer aluminum powders with particle sizes on the order of, or finer than, 20 μm . It is also interesting that in many experimental configurations, aluminum particles burn in combustion products of hydrocarbon fuels. In such cases, the oxidizers are mixtures of CO_2 , H_2O , and O_2 in various proportions. While this situation imitates some practical applications, the specific oxidizer mixtures produced in laboratory burners and in practical energetic formulations differ from one another substantially. Laboratory experiments with mixed oxidizers are also not particularly useful for extracting the information about efficiency of individual oxidizing species, which is required to model the practical configurations. The information on aluminum combustion in CO_2 and H_2O is very limited [9, 20, 21], with most data coming from experiments in mixed oxidizers, where the effects of different oxidizers are somewhat difficult to uncouple.

Considering the limitations of the available data on aluminum combustion, the goal of the current work was to directly measure optical signatures and burn times of individual, micron-sized aluminum particles. The focus of these experiments was to establish a direct correlation between particle diameters and their optical signatures and burn times for particles under 20 μm . The measurements were performed in well-characterized oxidizing environments with individual oxidizers including O_2 , CO_2 , and H_2O . These measurements are expected to serve as a foundation for development of a mechanistic aluminum combustion model. The model should account for multiple processes occurring in aluminum combustion and is not expected to be limited to a quasi-steady description. At the same time, the model should be relatively simple to enable its implementation in practical calculations. The measurements reported in this paper are expected to help to identify the most important reaction mechanisms and processes to be included into the mechanistic model of aluminum combustion.

10.2. Experimental

Apparatus

The experimental setup used in this study is schematically shown in Fig. 10.1. The apparatus, experimental procedure, and data processing steps have been described in detail in a recent publication [22], and only a brief summary is presented here for completeness. Metal powder, comprised of spherical particles, was fed by an electrostatic particle generator [7, 19, 22] so that a narrow, vertically rising particle jet with a low number density is produced. The particles were carried by an oxidizing gas stream. The particle jet crosses two laser beams. First, particles intercept a 785-nm laser beam. For each particle, the scattered light intensity is proportional to its area and is used to measure the particle diameter. Two millimeters above the 785 nm laser beam, the particles traverse a focused CO₂ laser beam (~0.3 mm beam waist) in approximately 0.5 ms (i.e., particle velocities ~0.6 m/s). In the CO₂ beam, particles are rapidly heated and ignited. Emission from the incandescent and burning particles was measured to determine the particle burn times. The emission was collected by a wide angle quartz fiber, passed through a 500 nm band-pass filter, detected by a photomultiplier tube, converted to a digital signal, and stored for further analysis.

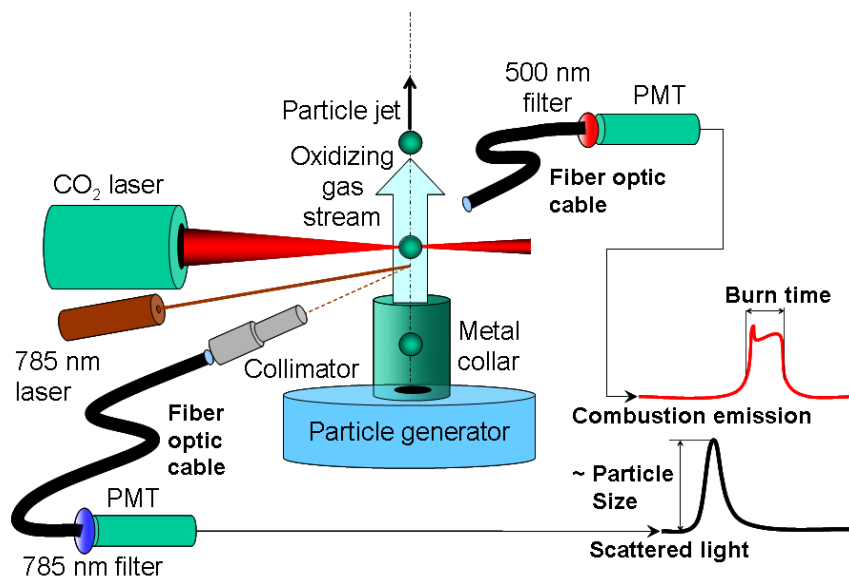


Fig. 10.1. Schematic diagram of the experimental setup

There are three significant modifications to the apparatus previously described in ref. [22].

First, a set of small inner diameter telescoping tubes, labeled “collimator” in Fig. 10.1 were attached to the fiber optic viewing the 785 nm scattered light. The field of view of the detection system was reduced to $< 4.5^\circ$ (full angle) and these tubes eliminated all emission produced by incandescent or burning particles from reaching the scattered light detector.

Second, experiments were performed in various oxidizing environments. The compositions of the oxidizers included mixtures of N₂/O₂, N₂/CO₂, and N₂/H₂O (all at 1 atm.) A thin-walled

aluminum collar (“metal collar” in Fig. 10.1) was added to the particle generator. This restricted outside air from mixing with the oxidizing gas streams. This collar is 8 mm in height and it has an outer diameter of 8.9 mm (inner diameter = 6.4 mm). High purity, dry gases were used for these experiments. Gases were metered through needle valves and flows were measured with mass flow meters (Alicat Scientific; Model M200SCCM-D) to $\pm 1\%$ accuracy. Carbon dioxide and water vapors interfere with the operation of the particle generator; so for experiments with these oxidizers, particles were fed with a pure nitrogen stream, and oxidizers were supplied in a shroud jet [22, 23] not shown in detail in Fig. 10.1. Detailed calculations using FLUENT software, for the gas flows in this apparatus, show that the inner and outer gas streams are well-mixed at the height where the particles intercept the CO₂ laser beam. These results are presented in Ref. [23] where the same experimental configuration was employed to study ignition of aluminum particles in different oxidizers. For oxygen/nitrogen gas mixtures, both the inner gas flow passing through the particle generator and the shroud jet had the same gas composition. Individually metered oxygen and nitrogen gas streams were mixed by passing them through a 3.0 m length of plastic tubing (1/4” od). To generate water vapor, a calibrated peristaltic pump (Control Company; Model 3384-CC) fed liquid water (3.3 mg/s) into a tube furnace held at a temperature of 200-250°C. The gas transfer lines and a top flange of the particle generator were maintained at 120°C to prevent condensation.

Specific environments used in experiments, gas flows, and calculated flow velocities are shown in Table 10.1. Particle flow velocities along the centerline were measured using square-wave modulated (500Hz; 50% duty cycle) green laser sheet illumination. This yielded particle velocities of about 0.6 m/s at 5 mm above the collar rim (13 mm above the particle generator outlet) and these velocities agree with those estimated from the offset time found when correlating the scattering peaks with the corresponding ignition peaks (see below for details).

Table 10.1. Gas Environments and Flow Rates for Ignition Experiments. Jet Velocities are Calculated at the Exit Plane of the Respective Orifice.

Inner Jet Gas	Outer Jet Gas	Collar ?	Flow Rate, cc/min		Jet Velocity, m/s	
			Inner	Outer	Inner	Outer
Air	Air	No	73.0	158	1.61	0.09
O ₂ :N ₂ 1:9	O ₂ :N ₂ 1:9	Yes	62.3	141	1.38	0.08
O ₂ :N ₂ 2:3	O ₂ :N ₂ 2:3	Yes	64.9	125	1.43	0.07
N ₂	CO ₂	Yes	73.6	165	1.63	0.09
N ₂	H ₂ O:N ₂ 9:1	Yes	67.5	386	1.49	0.21

Lastly, a 14-bit data acquisition board (DAC, National Instruments, Model PCI-6133) replaced the 12-bit, sequential DAC used in prior work. The new DAC has eight independent D/A converters and a maximum sampling rate of 3.0 MS/s (0.33 μ s per sampling event). In the current experiments, the sampling rate was 100 kS/s; or 10 μ s per data point; except for the experiments with air, where the sampling rate was increased to 500 kS/s. For each scan, the time during which sequences of pulses of both scattered light and light produced by incandescent particles were continuously collected, was 10 s. Typically, 50-150 scans were collected for a set of experiments with a selected oxidizing gas mixture.

Materials

Spherically shaped micron sized aluminum particles were used for these experiments (Alfa Aesar, 10-14 μm nominal particle size). Prior to experiments, the powder was dried in a glass vial at 65-85°C under vacuum for more than 2 hours. The vial was quickly capped after opening the vacuum oven and after a cooling period, the sample vial was roll-milled (i.e., milled with an aluminum or Teflon solid rod, 1cm diam.) for approximately 20 min. This procedure reduced the number of agglomerated particles, but did not deform the shape of the particles - as confirmed by electron microscopy.

Measurements, processing, and interpretations

Prior to each combustion experiment, the particle sizing system was calibrated, as described elsewhere [22]. In these calibrations, particle size distributions measured by a commercial analyzer, LS230 by Beckman-Coulter, was matched with the size distributions determined from the scattered light pulses. Please see ref. [22] for details including the particle size distribution for the aluminum powder used in this work.

In each measurement, two separate pulse sequences were acquired simultaneously. In the first sequence, each pulse was produced by the scattered light and its amplitude was proportional to the particle surface area. In the second pulse sequence, each pulse represented an incandescent particle and its duration was equal to the time the particle remained incandescent. The two pulse sequences were correlated with each other to determine the emission duration for each individually sized particle. The details of the correlation procedure are given elsewhere [22]. It is based on matching the two sequences of pulses to each other while determining the “offset time” by which one pulse sequence needs to be shifted in time relative to another one to achieve the match. The offset time was compared to the time a particle travels between the two laser beams, which could be readily found from the average particle velocity and distance between the beams. When the two times were sufficiently close, the experimental results were further processed. A typical experiment includes collecting both pulse sequences during 50 - 150 separate 10-s intervals. There were typically 500-2000 scatter signal pulses and 50-100 particle emission pulses in each pair of the collected pulse sequences. After the overlapping peaks are removed and two sequences are correlated, approximately 20-50 pulses remain in each pulse sequence, representing the number of particles for which both sizes and burn times were determined.

Measurement of the particle size is very straightforward based on the scattered light intensity and calibration [22]. However, interpretation of the pulse durations produced by the incandescent particles is more difficult. To illustrate the problem with this interpretation and how it is addressed, consider a cartoon shown in Fig. 10.2. It schematically shows three particles of the same diameter crossing the laser beam at different locations. In one possible scenario, particle 1 is not heated to ignition, particle 2 ignites and starts burning within the laser beam, and particle 3 is heated so that it ignites just when it exits the beam. In such a case, the durations of pulses produced by incandescent particles 1 and 2 would be shorter than the combustion time of interest. For particle 1, duration of emission is simply defined by the time the particle cools off. (Note that cooling times are very short for particles moving in a room temperature gas. An

estimate shows that a 20 μm particle at 2793 K will cool to 933 K in about 5.8 ms, but the particle incandescence at 500 nm (spectral detection window) will drop 3 decades in light intensity (our detection limit) in about 1.5 ms. This is substantially shorter than the observed burn times discussed below). For particle 2, part of its combustion was assisted by the laser beam so that the rate of reaction is accelerated. Thus, only the longest pulse measured for particle 3 represents the burn time of interest. Because this consideration is valid for particles of any dimensions, it is concluded that for each particle size, only the longest measured pulse durations represent the burn times of interest. Considering that majority of particles do not cross the laser beam at the very specific location required to ignite, but not burn the particle while in the beam, it becomes clear that only a small fraction of the recorded emission pulses carries the useful information about the burn time of interest. In other words, many pulses need to be collected and processed so that the fraction of the pulses reflecting the burn time of interest becomes representative.

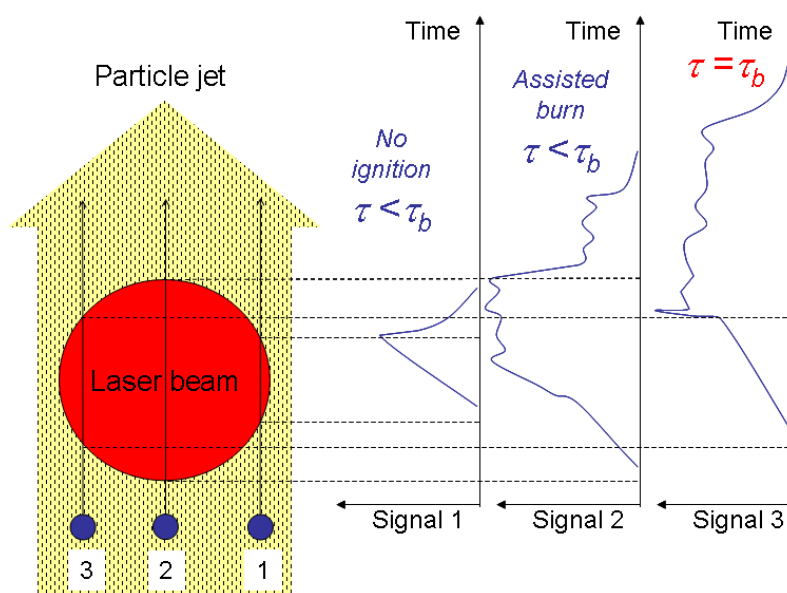


Fig. 10.2. Cartoon illustrating formation of pulses of different duration by particles of the same size crossing the laser beam at different locations.

A limitation on the shortest burn time that can be measured reliably is implied by the time a particle crosses the laser beam, so that it may be heated rapidly and remain incandescent while moving within the beam. Roughly, this limitation can be estimated as the ratio of the laser beam waist ($\sim 300 \mu\text{m}$) over the average particle velocity ($\sim 0.6 \text{ m/s}$) giving a heating time of about 0.5 ms.

10.3. Results

Emission Profiles

The emission intensity profiles from burning Al particles provide information about the processes and reactions occurring during combustion. Characteristic emission profiles for particles burning in different environments are shown in Figs. 10.3 – 10.7. The profiles shown

are not selected to represent only the longest pulses for each particle size; instead, representative samples of profiles of different durations are shown for all environments.

The profiles measured for Al combustion in oxygen/nitrogen mixtures are collected in Figs. 10.3 – 10.5. The profiles look similar to one another and always begin with a relatively sharp initial peak. A closer examination of the peak fronts shows that for many pulses, the rate of the initial signal rise exhibits a sharp, step-wise increase, possibly indicating particle ignition within the laser beam. For particles burning in 10% O₂, Fig. 10.3, the first emission peak is relatively sharp and is followed by a steadily decaying emission signal. The decay is followed by a characteristic oscillatory emission pattern preceding the particle quenching. For particles burning in 21% O₂, the first emission peak becomes wider, while still being followed by a period of nearly steady decay in the emission signal. The oscillatory pattern is less clearly visible, and in many cases the oscillations are reduced to one or two spikes in the emission signal. While the burn time trends are discussed below, it is interesting to note here that the emission pulse durations in general are substantially reduced as the oxygen concentration increases from 10 to 21 %. For particles burning in 40% O₂, the first emission peak is very broad and the oscillatory emission patterns often appear nearly immediately following the peak. The oscillations continue for the entire burn time while the particle extinction is often preceded by a sharp jump in the emission intensity. No significant reduction in the measured pulse durations is noticed as compared to the pulses obtained in the 21% O₂ environment.

The emission profiles for carbon dioxide and water are presented in Figs. 10.6 and 10.7, respectively. The carbon dioxide profiles exhibit a broad first peak followed by a long, slow decay. The leading edges of the first peaks are substantially less sharp compared to those observed for oxygenated environments. Most profiles have small but identifiable oscillations in the tail of the profile. The oscillations are overlapped with a decay in the overall emission intensity.

Inspecting the water profiles shown in Fig. 10.7, it appears that the initial peaks are substantially greater in intensity than the rest of the emission signal. The leading edges of the initial peaks are sharper than in CO₂. The overall duration of the initial peaks is comparable to the estimated time the particles are crossing the laser beam. Thus, it appears that immediately after the laser source is removed, the emission drops rapidly to a very low level, which is substantially lower than that observed for any of the other environments. However, the emission remains reliably above the baseline level for a while, suggesting a relatively steady exothermic reaction that is accompanied by emission that is much weaker compared to reactions in O₂ and CO₂.

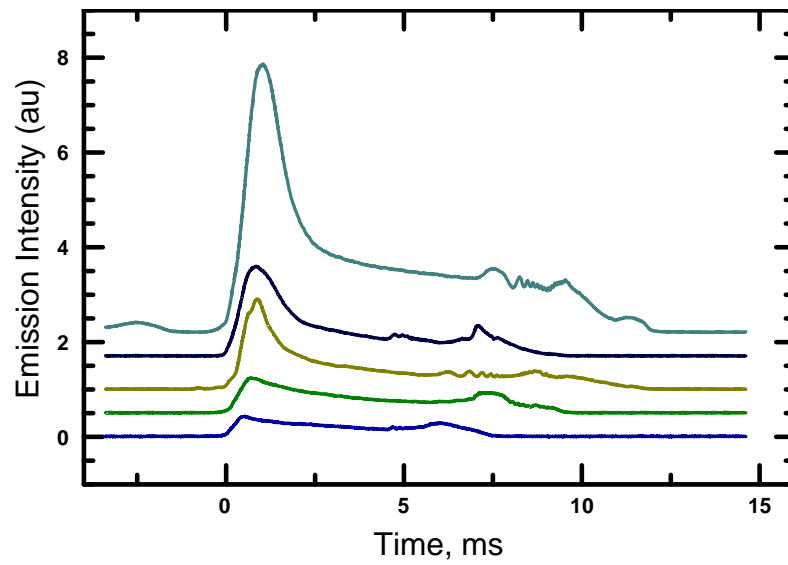


Fig. 10.3. Emission profiles for Al particles burning in a 10/90 O_2/N_2 mixture.

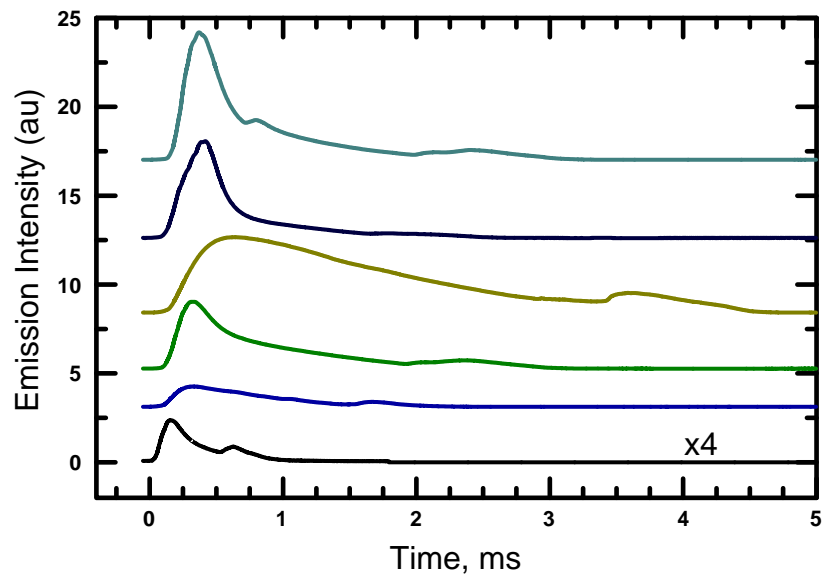


Fig. 10.4. Emission profiles for Al particles burning in a 21/79 O_2/N_2 mixture (air).

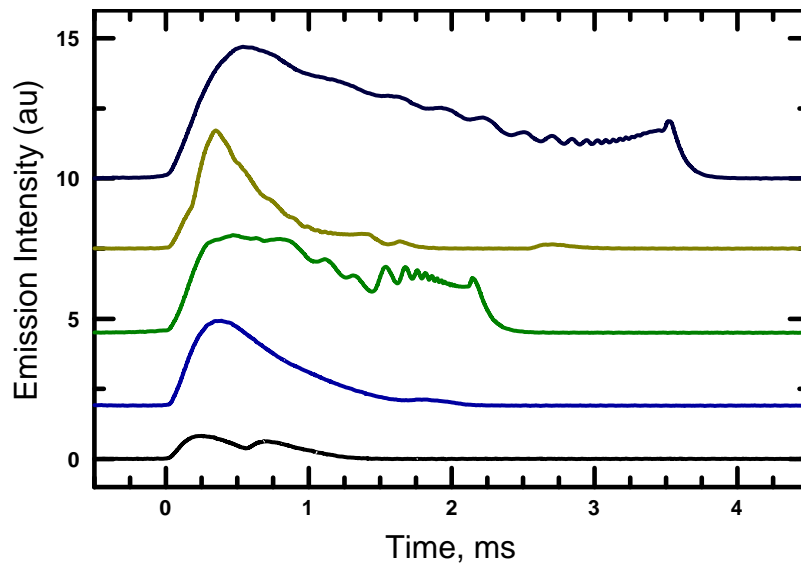


Fig. 10.5. Emission profiles for Al particles burning in a 40/60 O_2/N_2 mixture.

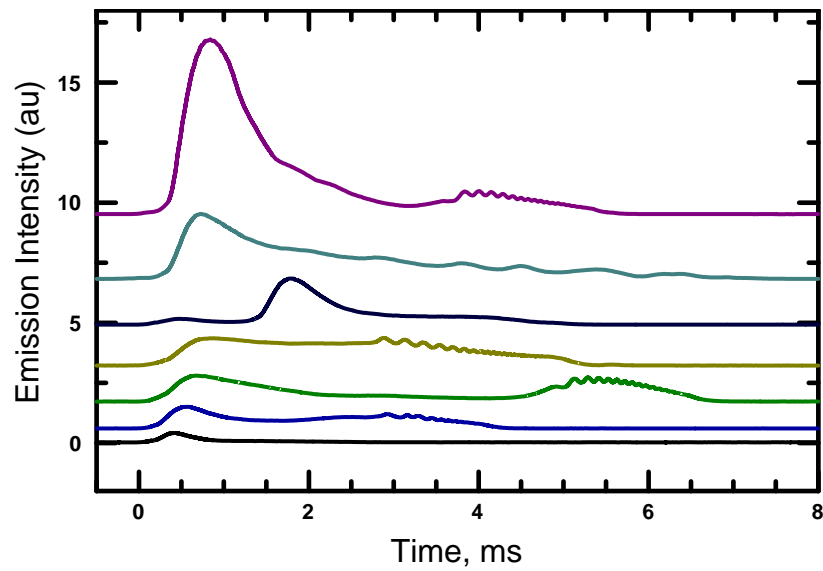


Fig. 10.6. Emission profiles for Al particles burning in a 73/27 CO_2/N_2 mixture.

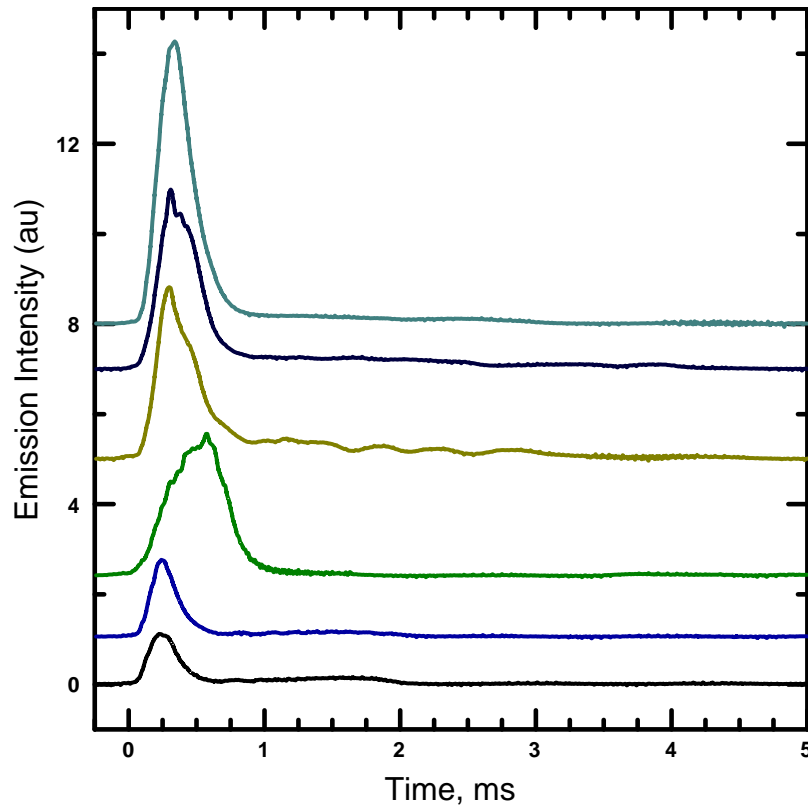


Fig. 10.7. Emission profiles for Al particles burning in a 77/23 H₂O/N₂ mixture.

Burn Times

Burn times are presented in Figs. 10.8 – 10.12, where all experimental data points are shown. Each point represents a particle, for which the diameter is measured from the scattered pulse sequence, and the burn time is inferred from the duration of the correlated emission pulse. In other words, each point represents a pair of pulses measuring particle emission and scattered light, which are correlated in time to ensure that both pulses were produced by the same particle. As discussed above, the majority of the measured pulse durations do not represent the burn times of interest. Only the longest measured pulse durations for each particle size can be interpreted as the burn times for a self-sustained particle combustion that was not assisted by laser. For each set of experimental data points, a trendline showing the D^n fit is also shown as a solid line. The fit is obtained for data points representing the longest measured pulse durations for each particle size range. The particle size ranges and the respective longest pulse durations are selected manually and somewhat subjectively from all the measured data points. The points used to calculate the trendline are shown as filled symbols while the rest of the experimental data points are presented as open symbols. Note that each data point used in the “power-law” fits, was inspected additionally to confirm that for each such matched pair of emission and scattered light peaks both peaks were well separated from their neighbors, were clearly above the noise level, and that the emission profile was typical of aluminum combustion in the respective environment. Despite an elaborate automated peak processing routine described in ref. [22], some outlier points were still identified by this additional inspection, which were likely caused by ignition of

agglomerated particles or particles closely following each other in the jet. Such outlier points were removed from Figs. 10.8 – 10.12.

In addition to the experimental points and solid trendlines, three dashed lines are also shown for each plot. The dashed lines show particle burn times predicted for each specific environment as a function of the particle diameter using three different D^n trends reported in the literature for aluminum combustion. For all trends, the particle diameter, D , is entered in mm and the burn time, τ_b , is calculated in ms.

The first trend, given by Eq. (10.1), comes from a review of published experimental results, primarily for coarser Al particles, compiled by M. Beckstead [5].

$$\tau_b = \frac{7.35D^{1.8}}{(C_{O_2} + 0.6C_{H_2O} + 0.22C_{CO_2})P^{0.1}T^{0.2}} \quad (10.1)$$

In Eq. (10.1) and below, C is the concentrations of oxidizer given by the respective subscript, P is pressure, and T is the environment temperature.

The second trend is described by the set of Eqs. (10.2) and was proposed by N. Glumac et al. [6] based on measurements using aerosolized Al particles ignited in a shock tube. These measurements identified average combustion times of narrowly size-classified Al powders. The burn times were obtained from the widths of the optical emission peaks produced by the powders ignited in a gas heated by the shock wave.

$$\tau_b = a_0 C_{OX}^{a_1} \left(\frac{P}{P_0} \right)^{a_2} D^n$$

$$n = 2 \exp(-4.3C_{OX}) \left(\frac{P}{P_0} \right)^{-0.3} \quad (10.2)$$

$$\tau_{b,mix} = \left(\sum_{i=1}^n \frac{1}{\tau_{b,i}} \right)^{-1}$$

Similarly to Eq. (10.1), Eqs. (10.2) describe effects of oxidizer concentration and ambient pressure. The reference pressure that should be used in Eqs. (10.2) is $P_0=8.5$ atm. The effect of the oxidizer type is given by the choice of constants a_0 , a_1 , and a_2 , as described in Table 10.2. Unlike Eq. (10.1), there is no effect of ambient temperature in Eqs. (10.2). However, it should be noted that the measurements used to obtain Eqs. (10.2) were performed in hot ambient gases.

Table 10.2. Selection of constants as a function of oxidizer for use in Eq. (10.2) [6].

Oxidizer	a_0, ms	a_1	a_2
O ₂	200	0.5	-0.5
CO ₂	500	0.6	0.3
H ₂ O	86	-1.7	0.75

Finally, the third trend used for reference calculations of the burn time is given by Eq. (10.3) and was taken from ref. [7] by Shoshin and Dreizin, where the particle burn times were measured using a lifted laminar flame burner. The experiments were performed in air only, so Eq. (10.3)

does not take into account effects of ambient pressure, temperature, oxidizer type or concentration.

$$\tau_b = 310 \cdot D \quad (10.3)$$

Results for burn time for aluminum in the 10% oxygen mixture are shown in Fig. 10.8. Both Eqs. (10.1) and (10.3) substantially underestimate the particle burn times, while Eqs. (10.2) predict much longer burn times than observed in experiments. Note that experimental points appear for particles greater than about 3 μm , indicating that the smaller particles were difficult to identify based on the measured scattered light pulses. This restriction is due to a smaller peak to noise ratio for the scattered signal from the small scattered light peaks produced by small particles.

A relatively weak increase in the burn time for increased particle sizes is observed and it is reasonably well described by a $D^{0.32}$ trendline.

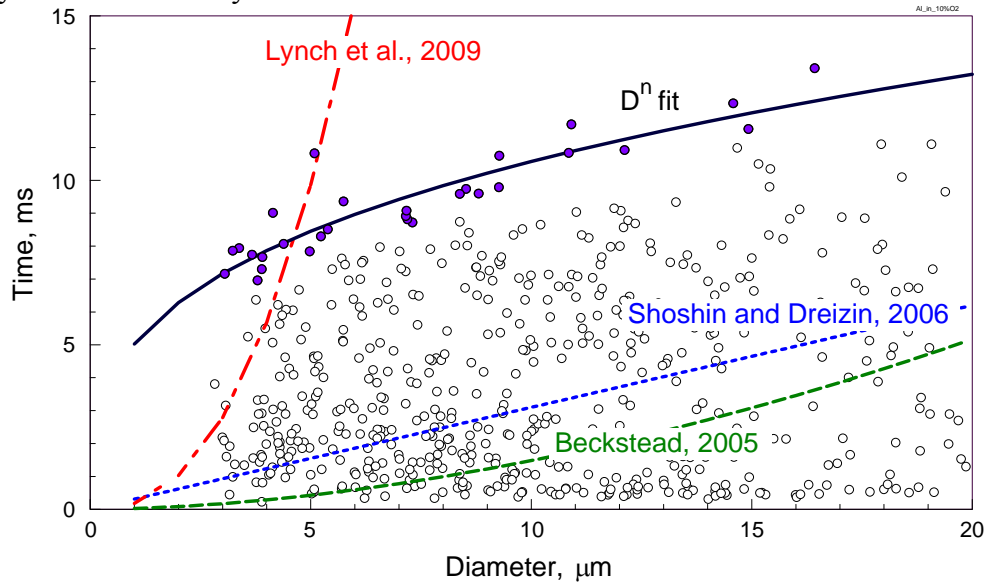


Fig. 10.8. Particle combustion times as a function of the particle diameters for Al burning in a 10/90 O_2/N_2 mixture. Here and in Figs. 10.9 – 10.12, open and closed symbols: experimental points; closed symbols used for the D^n fit shown by solid line ($n=0.32$). Dashed lines show D^n trends reported in the literature (see text).

As already noted from examination of individual emission traces, the burn times are substantially reduced when the concentration of oxygen is increased to 21% as shown in Fig. 10.9. For this case, Eq. (10.1) continues to under-predict the particle burn times and Eqs. (10.2) still predict longer burn times than observed experimentally. It is interesting that Eq. (10.3) appears to work rather well and for the set of data available the predicted trend nearly coincides with the directly calculated best match line.

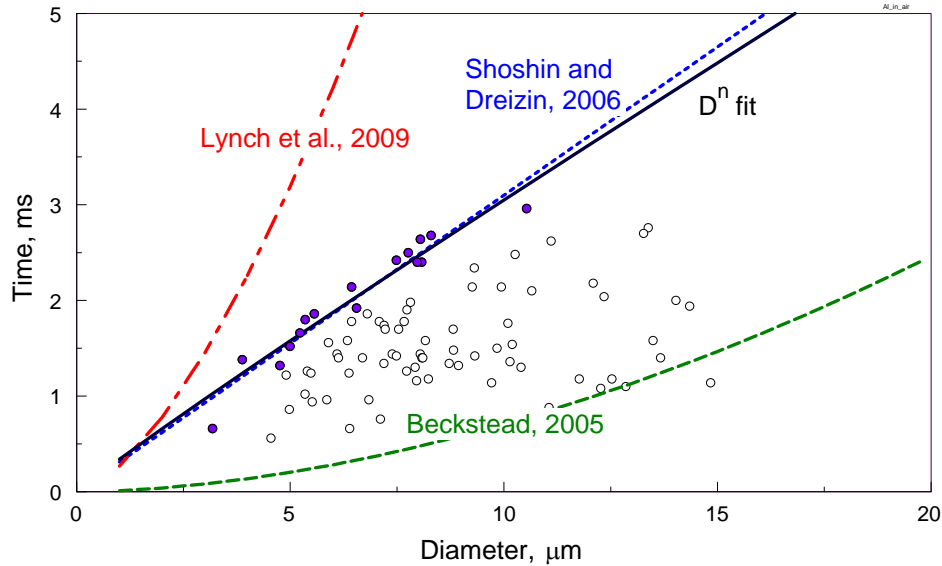


Fig. 10.9. Particle combustion times as a function of the particle diameters for Al burning in a 21/79 O₂/N₂ mixture (air). D^n fit is shown by a solid line ($n=0.95$).

The results for the 40% oxygen mixtures are shown in Fig. 10.10. It is interesting that despite substantially increased oxygen concentration, the burn times do not decrease noticeably compared to the 21% oxygen case. Calculations by both Eqs. (10.1) and (10.2) for this case predict shorter burn times than observed experimentally. Calculation by Eq. (10.3) somewhat over-predicts the observed burn times and the curve directly matching the experimental data is described by a $D^{0.57}$ trendline.

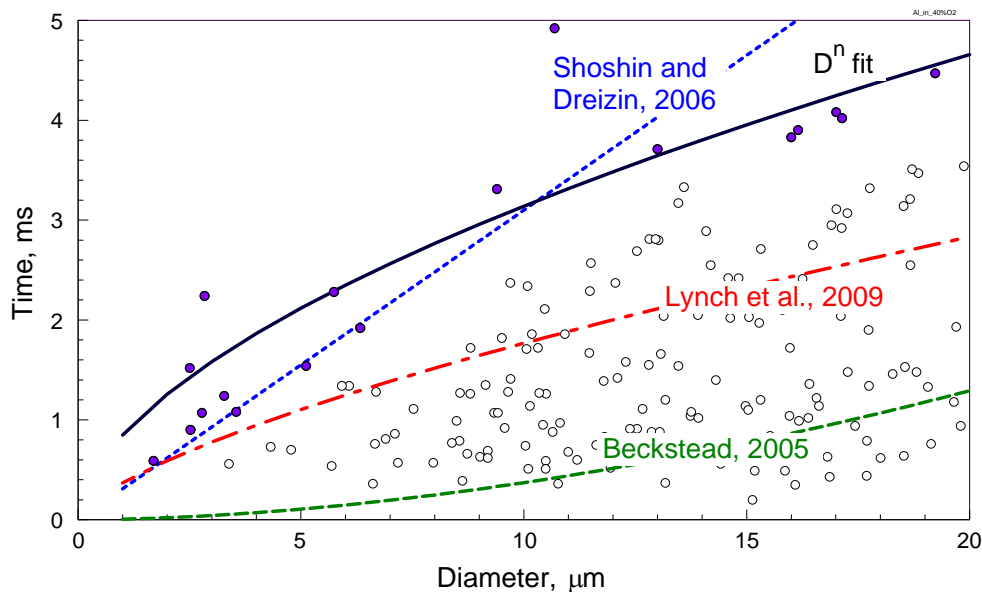


Fig. 10.10. Particle combustion times as a function of the particle diameters for Al burning in a 40/60 O₂/N₂ mixture. D^n fit is shown by a solid line ($n=0.57$).

Burn times for aluminum particles in 73% CO₂ mixture are shown in Fig. 10.11 and are quite long, despite a very high concentration of the oxidizing gas. All reported trends, Eqs. 10.1 –

10.3, substantially under-predict the combustion times as compared to the current measurements. The experiments are described by a trendline similar to that used to describe the data for the 10% O₂ mixture.

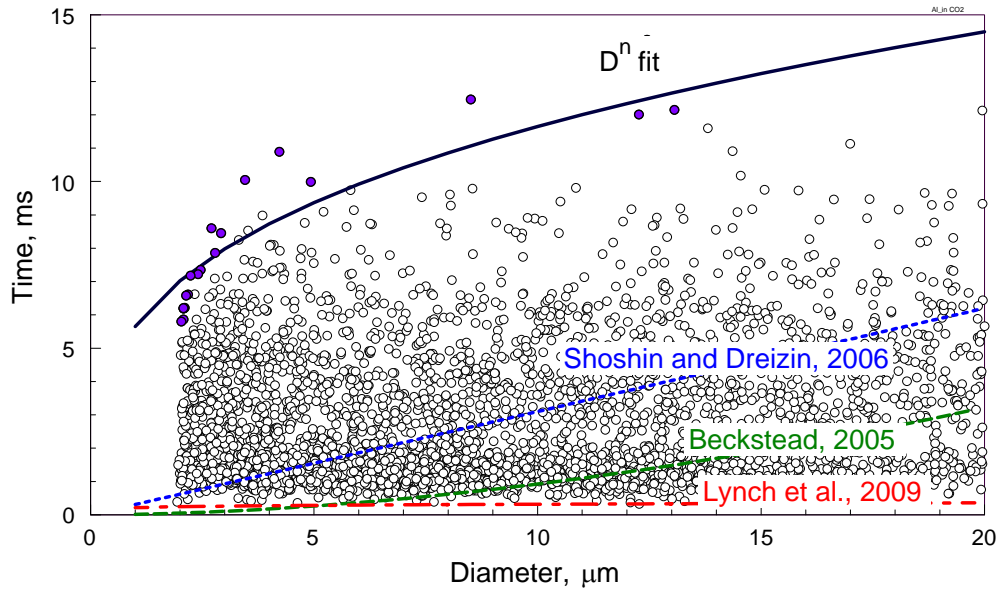


Fig. 10.11. Particle combustion times as a function of the particle diameters for Al burning in a 73/27 CO₂/N₂ mixture. D^n fit is shown by a solid line ($n=0.32$).

Finally, for aluminum combustion in 77% of H₂O vapor, the burn times are somewhat shorter than for CO₂, but longer than in oxygen. Once again, all reported trends significantly underestimate the combustion times.

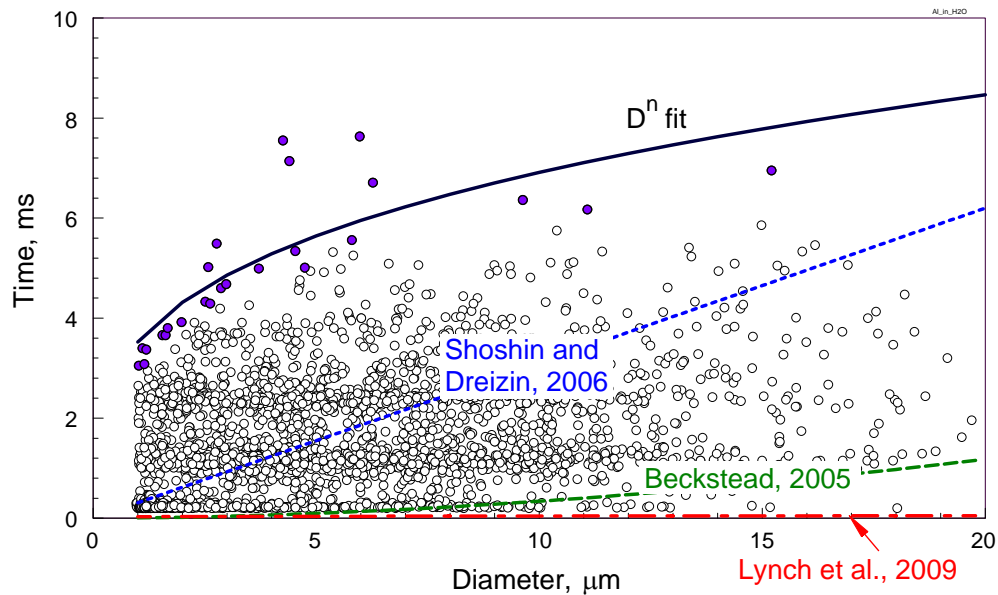


Fig. 10.12. Particle combustion times as a function of the particle diameters for Al burning in a 77/23 H₂O/N₂ mixture. D^n fit is shown by a solid line ($n=0.29$).

Table 10.3 gives the exponents and pre-exponents for all the power law fitting functions used for these experiments. It is interesting that in no case an exponent greater than 1 is observed. At the same time, very small exponents, around 0.3, are observed for three cases: H_2O , CO_2 and 10% O_2 environments.

10.4. Discussion

This work presents, for the first time, detailed emission traces produced by individual burning aluminum particles in the size range of 3 – 20 μm . Previously, similar traces were reported for much larger particles burning in air and other environments, e.g., [12 – 14]. Previous work established that multiple peaks and oscillatory emission patterns produced by burning aluminum particles are associated with non-uniformities in the particle composition developed during combustion. Specifically, pure Al particles become saturated with the dissolved combustion products (e.g., oxidized Al species, nitrogen oxides, and more complex compounds formed in presence of CO_2 and other oxidizers) which results in separation of molten aluminum into two or more liquid solutions [12 – 14, 24]. Each solution component evaporates at a different rate resulting in an asymmetric flame and associated oscillatory emission pattern. Furthermore, continuing oxidation results in the formation of oxide caps producing yet another oscillatory emission pattern, typically observed by the end of combustion. The described above processes were identified from comparisons between the particle emission profiles and morphologies and compositions of aluminum particles rapidly quenched at different stages of their combustion [14, 24]. Such quenching experiments and analyses of the particle morphologies are extremely difficult for finer aluminum particles commonly used in practical applications. However, current results suggest that the emission profiles for finer Al particles are qualitatively identical to those observed earlier for greater size particles, suggesting that the same combustion processes occur and determine the rate of metal consumption and associated heat release. Specifically, current observations of oscillatory emission patterns occurring in a sequence similar to that reported earlier for coarse Al particles, suggest that heterogeneous processes play a substantial role in Al combustion even in environments comprising 40 % O_2 .

The particle emission profiles measured in experiments performed with H_2O as an oxidizer are qualitatively different from those recorded in other environments. A very low and relatively steady level of emission suggests that the vapor phase flame is very weak or non-existent, while the particle continues to react exothermically, remaining weakly incandescent. This emission behavior suggests a surface reaction, suggesting that Al combustion in H_2O is primarily heterogeneous. Interestingly, recent estimates presented in Ref. [25] indicated that a relatively low heat release for aluminum oxidation by water is insufficient for maintaining a standoff vapor-phase flame for micron-sized particles burning in room temperature environment, as in the present experiments. Thus, present observations indicative of the surface combustion for aluminum particles in H_2O are consistent with the predictions of ref. [25].

Reviewing measured particle burn times as compared to the predictions of Eqs. (10.1 – 10.3), it becomes clear that none of the currently reported trends are suitable for practically useful and reasonably accurate prediction. In particular, the discrepancies are greatest when the

experimental conditions are different from those used to establish the specific trend. In that sense, the best match fits found in this work and summarized in Table 10.3 are as limited as any other proposed trends. As with other trends, they are only suitable for calculation of the particle burn times for experimental conditions similar to those used to find the respective relations.

More specifically, it is suggested that Eq. (10.1) based on Beckstead's analysis of multiple experimental results is heavily biased to experiments with much larger particles. Thus, estimating burn times for finer particle sizes is challenging, and, as observed here, results in substantial errors. Eqs. (10.2) are based on experiments performed at relatively high pressures and temperatures. It is also worth noting that Eqs. (10.2) are based on the measurement of the emission peak produced by a group of burning particles, so that the peak duration is dominated by larger particle sizes, even if the number of smaller particles is significant. Alternatively, only smaller particles could have ignited in selected shock tube experiments resulting in very short combustion peaks, whereas larger particles present in the system may not have ignited. Corrections for such effects and for the effect of high environment temperature are difficult, and without such corrections Eqs. (10.2) do not predict combustion times accurately. Finally, Eq. (10.3) is very simplistic and does not account for oxidizer concentration, type, or any other experimental condition. In fact it is somewhat surprising how well it described the current experimental data for mixtures with 21% O₂, for which it was initially proposed. Because Eq. (10.3) was obtained based on aerosol combustion experiments, it is suggested that the particle interaction effects in Al aerosol combustion are relatively weak so that the particle burn rates for single particles and particles burning in an aerosol effectively coincide with each other. Alternately, the particle number density could have been below the levels where such effects would be measurable.

Finally, to comment on the specific burn times measured in this work for different environments, it is interesting to compare these times to one another. To streamline such a comparison, all "best fit" trendlines are plotted together in Fig. 10.13. A small difference between the burn times measured for Al in 21% and 40% O₂ mixtures is remarkable and indicative that in these environments, the aluminum combustion may be relatively well described by a heat transfer limited droplet combustion model with a stand-off flame [26], where the rate of combustion is determined by the transfer number B , which is not affected by the oxidizer concentration and is defined as:

$$B = \frac{\Delta h_c / \nu + C_p (T - T_{boil})}{L} \quad (10.4)$$

where Δh is the heat of oxidation, L is the latent heat of evaporation, C_p is specific heat, ν is the stoichiometric coefficient, and T and T_{boil} are the temperatures of the hot environment (assumed here to be equal to the flame temperature) and particle surface, respectively. It is somewhat unexpected that a bit longer burn times are anticipated for the particles less than 10 μm at 40% O₂ as compared to 21% O₂. This effect may simply represent an experimental uncertainty. It is also possible that the dimensions of extinguished particles are reduced at greater oxygen concentrations, resulting in somewhat longer overall reaction times. Additional measurements and, possibly, analyses of the combustion products would be needed to address this issue in the future.

Table 10.3. Fitting coefficients for particle diameter power law: fitting eqn.: $\tau_{burn} = a \cdot D^n$.

Gas environment (remainder N ₂)	<i>a</i>	<i>n</i>	Correlation Coefficient, <i>r</i> ²
10% Oxygen	5.03	0.32	0.82
21% Oxygen (Air)	0.34	0.95	0.93
40% Oxygen	0.85	0.57	0.81
73% Carbon Dioxide	5.65	0.32	0.86
77% Water Vapor	3.52	0.29	0.68

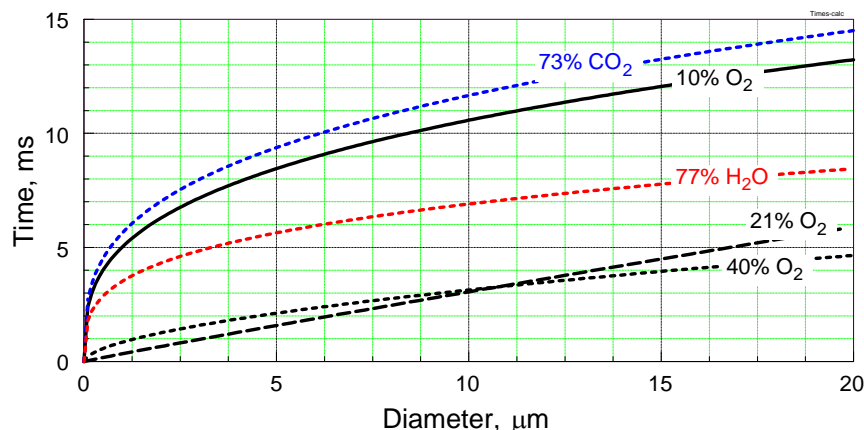


Fig. 10.13. Calculated burn times based on the best matches with experimental results presented in Figs. 10.8 – 10.12 for aluminum particle combustion in different oxidizing environments.

For reduced oxygen concentration, the combustion times increase substantially, suggesting that a different rate limiting process is at play. Most likely this rate-limiting process is the heterogeneous oxidation occurring on the particle surface. The overall emission level also decreased suggesting a reduction in the size of the vapor phase flame and an increasing contribution from surface reaction processes.

For CO₂ and H₂O environments, the role of surface processes is expected to be substantial for micron-sized particles, based on the heat balance estimates presented in ref. [25]. Respectively, long particle combustion times are measured despite high oxidizer concentrations in both cases. The significance of surface processes is particularly pronounced for combustion in H₂O as discussed above. Therefore, aluminum combustion models taking such processes into account need to be developed and validated by comparisons with the current and future experiments. It is interesting that the exponent close to 0.3 was found to describe the observed trends for all cases when heterogeneous reactions deem to be important. While this value of exponent indicates a very weak effect of particle size on the burn time, it can also indicate that particles of different dimensions combust in different regimes. Specifically, heterogeneous reactions, which occur at lower temperatures and generally lower rates, prevail for smaller particles, resulting in extended burn times. As the particle size increases, vapor phase reactions play an increasingly greater role, resulting in a faster burn and thus shorter burn times. Note that results summarized in Fig. 10.13 describe experiments performed at atmospheric pressure. In many practical systems involving metal combustion the pressures are elevated, so that the particle dimensions

for which the vapor phase reactions are important will be smaller than in this work. It is anticipated that descriptive models of metal combustion dynamics can be developed and validated based on measurements similar to those presented in this paper. These combustion dynamics should be incorporated into the models so that the effects of pressure and environment composition could be predicted with reasonable accuracy.

10.5. Conclusions

A new experimental setup enables measurements of optical emission signatures and combustion times for individually sized metal particles with diameters between 3 and 20 μm . The measurements can be carried out in various oxidizing environments, including oxygen, carbon dioxide, and water mixed with nitrogen or other inert diluent. Extending the set of environments using mixed oxidizers and, possibly, elevated pressure, are possible avenues of future work.

Optical signatures of individual micron-sized aluminum particles burning in different environments show characteristic oscillatory patterns previously observed for much larger particles. Such optical signatures highlight the importance of the heterogeneous processes in aluminum combustion. Heterogeneous reactions result in variation of surface properties of the burning droplets, which, in turn, cause formation of asymmetric flames and repeatable changes in particle emission intensities. For aluminum burning in water vapor, the optical signature of the particle is substantially weaker than in other environments, possibly indicating a primarily surface oxidation.

Results presented in this paper show that the current simplified D^n correlations for aluminum combustion time reported in the literature cannot be usefully applied for the conditions beyond the narrow ranges, for which such correlations were developed initially. It is observed that for oxygenated environments with oxygen concentrations in excess of 21%, the effect of oxygen concentration on combustion time of micron-sized aluminum particles is weak. However, combustion times increase substantially for lower oxygen concentrations. Aluminum particle combustion times are generally longer than predicted for experiments with water and carbon dioxide oxidizers. For all environments, the observed effect of particle size is relatively weak and the exponents in the descriptive D^n relations appropriate for the current experiments vary approximately from 0.3 to 1. An exponent close to 0.3 describes well the burn-times for aluminum in oxidizing environments for which heterogeneous reactions appear to dominate.

10.6. References

1. E. Price, R.K. Sigman, in: *Progress in Astronautics and Aeronautics* (2000), Combustion of Aluminized Solid Propellants, Georgia Inst. Technol., Atlanta, GA, 2000, pp. 663–687.
2. B. Palaszewski, L.S. Ivanovski, P. Carrick, *J. Prop. Power*, 14 (1998) 641-648.
3. R. H. W. Waesche, *J. Prop. Power*, 15 (1999) 919-922.
4. F. Zhang, S.B. Murray, K.B. Gerrard, *Shock Waves* 15 (2006) 313-324.
5. M.W. Beckstead, *Combust. Explo. Shock+* 41 (2005) 533–546.
6. P. Lynch, H. Krier, N. Glumac, *Proc. Combust. Inst.* 32 (2009) 1887–1893.
7. Y.L. Shoshin, E.L. Dreizin, *Combust. Flame* 145 (2006) 714–722.
8. Y. Huang, G.A. Risha, V. Yang, R.A. Yetter, *Combust. Flame* 156 (2009) 5-13.
9. P. Bucher, R.A. Yetter, F.L. Dryer, E.P. Vicenzi, T.P. Parr, D.M. Hanson-Parr *Combust. Flame* 117 (1999) 351-361.
10. M. Marion, C. Chauveau, I. Gökalp *Combust. Sci. Technol.* 115 (1996) 369 – 390
11. S.E. Olsen, M.W. Beckstead, *J. Prop. Power* 12 (1996) 662-671.
12. E.L. Dreizin, *Combust. Flame* 117 (1999) 841-850.
13. E.L. Dreizin, *Combust. Flame*, 116 (1999) 323-333.
14. E.L. Dreizin, *Combust. Flame*, 105 (1996) 541-556.
15. Y. Huang, G.A. Risha, V. Yang, R.A. Yetter, *Proc. Combust. Inst.* 31 II (2007) 2001-2009.
16. N.I. Poletaev, A.V. Florko, *Combust. Explo. Shock+* 44 (2008) 437-443.
17. S. Goroshin, M. Kolbe, J.H.S. Lee, *Proc. Combust. Inst.* 28 (2000) 2811-2817.
18. S. Goroshin, J. Mamen, A. Higgins, T. Bazyn, N. Glumac, H. Krier, *Proc. Combust. Inst.* 31 II (2007) 2011-2019.
19. Y. Shoshin, E. Dreizin, *Combust. Flame*, 133 (2003) 275-287.
20. S. Rossi, E.L. Dreizin, C.K. Law, *Combust. Sci. Technol.* 164 (2001) 209 – 237.
21. J. Servaites, H. Krier, J.C. Melcher, R.L. Burton, *Combust. Flame* 125 (2001), 1040-1054.
22. R.J. Gill, S. Mohan, E.L. Dreizin *Rev. Sci. Instrum.* 80 (2009) 064101-1 – 064101-7.
23. S. Mohan, L. Furet, E.L. Dreizin, *Combust. Flame* (2010), article in press
doi:10.1016/j.combustflame.2009.11.010
24. E.L. Dreizin, *Prog. Energ. Combust.* 26 (2000) 57-78.
25. S. Mohan, M.A. Trunov, E.L. Dreizin, *Combust. Flame* 156 (2009) 2213-2216.
26. I. Glassman, R.A. Yetter, *Combustion*. Fourth Edition. Academic Press, Burlington MA, 2008.

11. Characteristics of aluminum combustion obtained from constant volume explosion experiments

11.1. Introduction

In this chapter, a systematic experimental investigation of combustion of aluminum powders in different gaseous environments using CVE technique is presented. The experimental setup is based on a 9.2-l, nearly spherical explosion vessel. Experiments with widely varied aluminum aerosol number densities are performed in different environments comprising N_2/O_2 and $\text{N}_2/\text{O}_2/\text{CH}_4$ mixtures. Spherical aluminum particles with different particle sizes varied in the range of 5 – 20 μm are used. An analytical model developed earlier for CVE experiments and described in detail in ref. [1] is used to estimate the burning velocity and other flame characteristics of aluminum aerosol combustion based on the recorded pressure traces. Additional assumptions are made to evaluate the flame thickness. Role of various heat transfer processes in sustaining the aerosol flame is discussed based on the retrieved flame characteristics.

11.2. Experimental

The powders tested in this project are the same spherical Al powders as used in a previous study [2], specifically, nominal 1-5 μm aluminum by Atlantic Equipment Engineers, aluminum powder X-65 by Toyal America, Inc, and spherical Al powder with nominal sizes 10 – 14 μm by Alpha Aesar. The SEM images showing the spherical shapes of these particles and their particle size distributions measured using low angle laser light scattering were reported in ref. [2]. The volume mean diameters obtained from the measured particle size distributions for 1-5 μm , X-65, and 10-14 μm aluminum powders are 9.38, 10.87, and 20.33 μm , respectively. For interpretation of combustion experiments, it may be more appropriate to use the mean particle sizes based on the surface area, which are 5.4, 7.4, and 16.3 μm for the 1-5 μm , X-65, and 10-14 μm powders, respectively. Experiments with the same mass load were performed for different Al powders, and experiments with different mass loads were performed for one powder (1-5 μm nominal size). The mass loads 2.89 g, 4.34 g, 5.78 g and 8.67 g (respective equivalence ratios are about 1, 1.5, 2, and 3 for the 21% O_2 /79% N_2 environment at 1 atm in the 9.2 l combustion vessel) were used in experiments with the finest, 1-5 μm powder. In earlier efforts [2] experiments with all three powders were performed at the mass load 4.65 g and some of these earlier experiments were reprocessed here for comparison with the current results.

The experimental setup used in this project was described elsewhere [2, 3, 4] and only a brief summary is given below. The setup uses a nearly spherical vessel with volume of 9.2 liters. At the bottom of the vessel, there is a gas port. A pipe elbow is mounted under this gas port to serve as a powder container. Prior to experiments, the vessel is open, weighed powder load is placed into the pipe elbow and a semi-spherical nozzle (15 mm diameter, containing 37 holes, 0.25 mm diameter each) is mounted above the pipe elbow. The powder is introduced into the initially evacuated vessel through the nozzle together with a gas blast produced using a solenoid valve connecting the vessel to a 7-liter high-pressure gas reservoir. Depending on the desired

oxidizing gas environment, compressed dry air, nitrogen, oxygen, methane, and mixtures of thereof are used to fill the pressure reservoir. The combustion vessel is initially evacuated and then partially filled with the desired gas mixture prior to the gas blast initiating the experimental sequence. The initial pressures in the combustion vessel and high pressure reservoir are kept constant at 0.25 atm and 5.86 atm, respectively for all experiments. The gas blast duration is 200 ms and the target pressure in the combustion vessel by the end of the gas blast is 1 atm. After the gas blast and a short, 300 ms delay necessary to reduce turbulence in the combustion vessel, the aerosol is ignited by an electrically heated tungsten wire mounted at the center of the vessel. The wire is heated by a discharge current of a capacitor battery with the overall capacitance of 130,000 μF charged initially to 50 V. The combustion pressure is measured by a PX5500 Omegadyne transducer (pressure range: 0-500 psia; accuracy: ± 0.1 % of the full scale). After each experiment, the vessel was allowed to cool for at least 2 min after which the final pressure in the vessel was measured.

11.3. Thermodynamic equilibrium calculations

Equilibrium calculations were performed using NASA's CEA (Chemical Equilibrium with Applications) software [5] to establish a reference framework for the analysis of experimental results. The calculations were performed for the assigned specific volume, a case equivalent to the CVE experiment. Three aluminum powder mass loads used in experiments were also considered for these calculations. The specific volumes were evaluated for each of the powder mass loads considering densities of aluminum and of the gases present in the environment. All components were assumed to be initially at 25 °C. The results of calculations are summarized in Table 11.1 showing adiabatic flame temperatures and respective pressures.

Table 11.1. Adiabatic flame temperatures and pressures predicted for CVE experiments by equilibrium calculations.

Gas Environment (balance: N ₂)	Temperature, K for mass load:			Pressure, atm, for mass load:		
	2.89 g	5.78 g	8.67 g	2.89 g	5.78 g	8.67 g
21% O ₂	4032	3412	2900	12.34	11.93	10.62
21% O ₂ with 6% CH ₄	3703	2847	2868	12.74	10.97	10.82
40% O ₂	4092	4335	4496	12.44	13.95	15.05
40% O ₂ with 6% CH ₄	4030	4208	3998	13.42	14.94	15.51

11.4. Experimental results

Individual Pressure Traces

Characteristic pressure traces recorded in the CVE experiments are shown in Fig. 11.1. Each trace is a typical example of at least three runs performed for each experimental condition. The traces shown in Fig. 11.1 illustrate the effect of oxidizing environment, while other varied experimental parameters included powder type (particle size distribution) and its mass load.

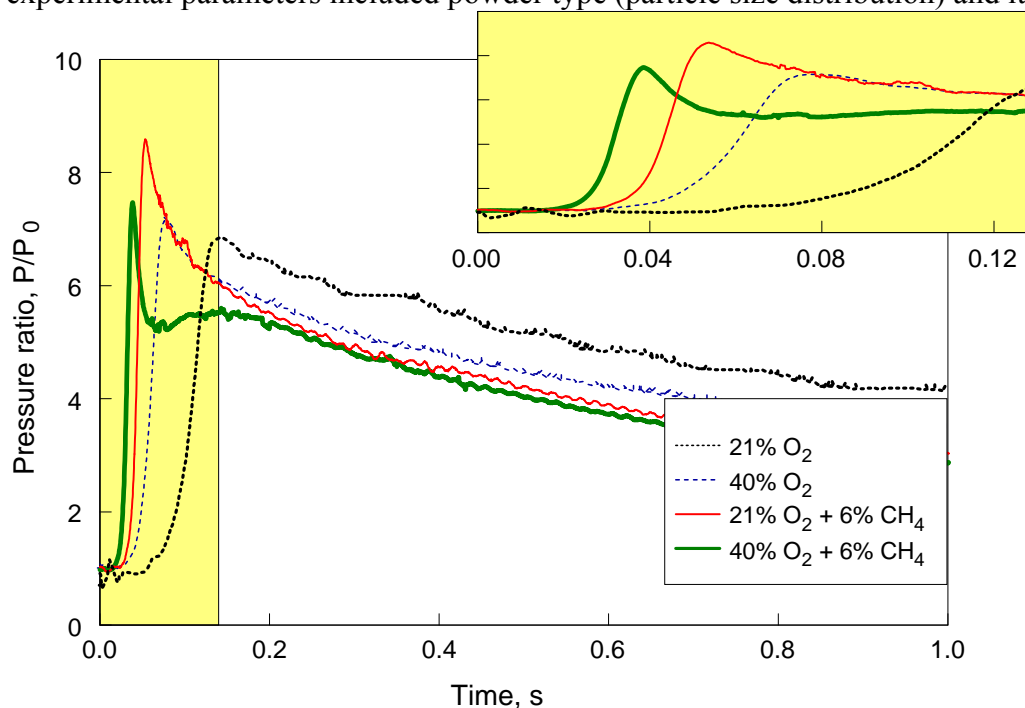


Fig. 11.1. CVE pressure traces illustrating the effect of oxidizing environment on combustion of 1-5 μm Al powder; mass load 2.89 g. The inset shows the shaded portion of the pressure traces with the expanded temporal scale.

Dashed lines in Fig. 11.1 show experiments with varied oxygen concentrations balanced with nitrogen. Solid lines indicate experiments, in which methane was added to the oxidizing environment. To correct for small differences in the initial pressure P_0 from 1 atm measured in different experiments, the pressure ratios, P/P_0 are shown. Both the maximum pressure ratios,

P_{max}/P_0 , and the rates of pressure increase, dP/dt , are higher for the runs with added methane. The shaded portion of the plot is expanded in the inset to better illustrate the parts of the signal corresponding to the increasing pressure and thus to the propagating flames. The rate of pressure rise is the highest when the environment with 40% O₂ and added 6% CH₄ is used. For the runs with added methane, higher values of P_{max}/P_0 are observed for runs with 21% O₂ compared to those with 40% O₂, which is opposite to the situation predicted in equilibrium (cf. Table 11.1). However, for the runs without added CH₄, the maximum pressures are somewhat higher at greater oxygen concentration, as predicted by the equilibrium calculations. Note that the absolute values of the pressures measured in experiments are substantially lower than the equilibrium predictions.

The shapes of the pressure pulses are remarkably different for the experiments performed with and without methane. This difference is striking in particular for the experiments with 40% O₂ when the pressure peak for the run with added CH₄ is sharper and, most interestingly, the first sharp peak is followed by an extended pressure hump (with the maximum just past 0.20 s in Fig. 11.1). Such a combination of a sharp initial peak followed by the second pressure hump was observed in most experiments with 1-5 μm Al powder ignited in the environments containing 40% O₂ and 6% CH₄. A single peak was observed at lower oxygen concentrations for the 1-5 μm Al powder and for coarser Al particles ignited in all environments. To understand the effect of methane on the formation of the double pressure peak, a test run in which the environment was maintained as 40% O₂ with 6% CH₄ was conducted without any powder. The obtained pressure trace is shown in Fig. 11.2 together with the respective traces measured for aluminum combustion in the environments with the same oxygen concentrations with and without CH₄. In addition, traces showing the rates of pressure change, dP/dt , for the same experiments are also shown.

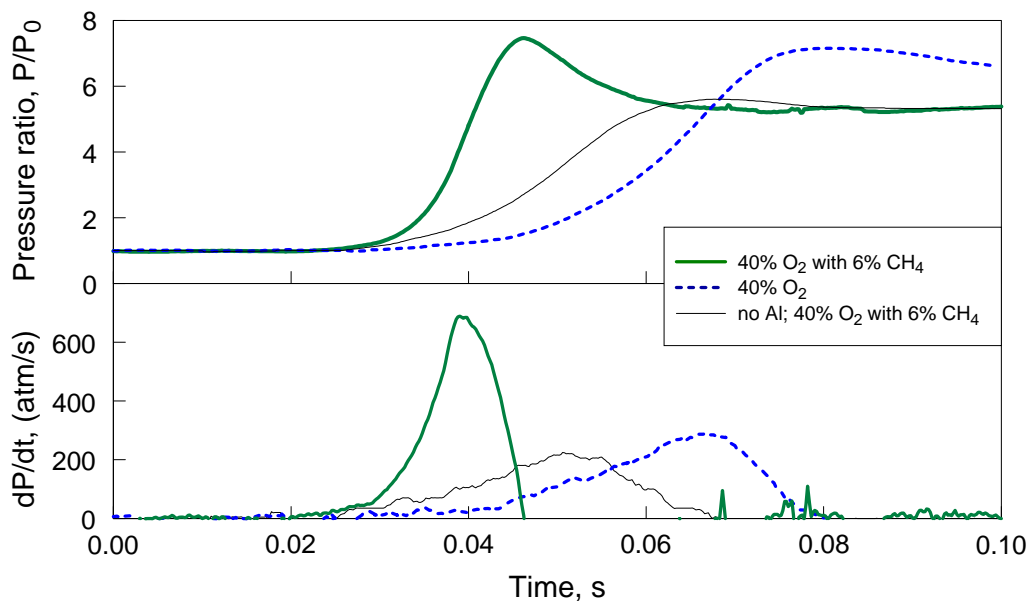


Fig. 11.2. Pressure traces and respective traces showing the rates of pressure change comparing combustion of Al and CH₄ in environments with 40% O₂; two of the three presented experiments use 1-5 μm Al powder, mass load 2.89 g.

A somewhat unexpected observation made based on the result presented in Fig. 11.2 (just one of several qualitatively similar sets of pressure traces obtained for different Al mass loads and for experiments on combustion of methane without Al) is that the rate of pressure rise for the combustion of methane with no aluminum added is lower than that for any experiment using aluminum fuel with the same concentration of oxygen, including experiments with no methane. This observation suggests that the pressure double peak is not explained by initial combustion of the gaseous fuel. Instead, the higher rates of pressure increase in experiments with mixed solid (Al) and gaseous (CH₄) fuels appear to be driven by aluminum combustion. Formation of the following pressure hump could be due to a slow equilibration of products of the initial reaction in a quickly cooled, post-combustion environment. Overall, the processes responsible for the formation of the secondary pressure hump remain poorly understood and it is likely that a detailed analysis of reaction kinetics for both Al and CH₄ would be required to interpret these observations quantitatively. Therefore, interpretation of the results reported here cannot simply assume that Al particles burned in the combustion products of methane; instead, the performed CVE measurements represent simultaneous combustion of solid and gaseous fuels.

Summary of results

The results are presented in terms of maximum pressures, generally reflecting the reaction energy, the rate of pressure rise corresponding to the rate of reaction, and the final pressure in the vessel, indicating consumption of gaseous oxidizer (oxygen) and thus the reaction completeness. All pressure values are divided by the initial pressure to account for the small (less than 0.1 atm) variation in the initial pressures from run to run. Also shown is the measured ignition delay, or induction period leading to the rapid pressure increase. The induction period is defined as the time from the ignition instant (when the voltage is applied to the ignition wire in the center of the vessel) to the time the aerosol in the vessel is observed to burn, as indicated by an increase in the measured pressure from its initial level to 10% of its maximum value. This induction time can be associated with the establishment of a steadily propagating flame. The effects of particle mass load and oxidizing environment for the experiments with fixed particle size distribution (1 – 5 μm nominal size Al) are shown in Fig. 11.3.

The increase in the powder load from 2.89 to 5.78 g always resulted in a substantial increase in both the maximum pressure and in the rate of pressure rise for all environments except the 21%O₂/79%N₂ case. For the latter gas mixture, there was an increase in the maximum pressure and in the rate of pressure rise when the load was increased to 4.65g (cf. Fig. 11.3). Corresponding further increase in the powder load is much less efficient and results only in minor changes in both P_{max} and dP/dt_{max} for all cases.

The induction period leading to powder combustion is affected noticeably by increased Al mass load for the experiments in environments with no methane. The effect is less pronounced for the experiments employing environments with added methane. The induction period always decreases when methane is added, as noted comparing experiments with the same Al mass loads and the same oxygen concentrations. Therefore, it can be suggested that a substantial role of methane additive is in reducing the critical volume of the aluminum cloud that can sustain quasi-steady flame propagation.

The trends for the final pressure in the vessel for methane-free environments indicate a greater consumption of oxygen when more fuel is present in the mixture. It can also be concluded that partial consumption of nitrogen occurred for the highest aluminum powder load (8.67 g) in the methane-free experiments with the environment initially containing 21% of O_2 . Results presented in Fig. 11.3 show that in these experiments, the final pressure in the vessel was about 70% of the initial one. A trend for the final pressure is less clear for the experiments with mixed Al/ CH_4 fuels used, which can be explained by partial competition of methane and aluminum for oxygen consumption. It can be hypothesized that at lower Al mass loads, methane consumes oxygen more effectively, while as the powder loads increase most of the oxygen becomes consumed by aluminum.

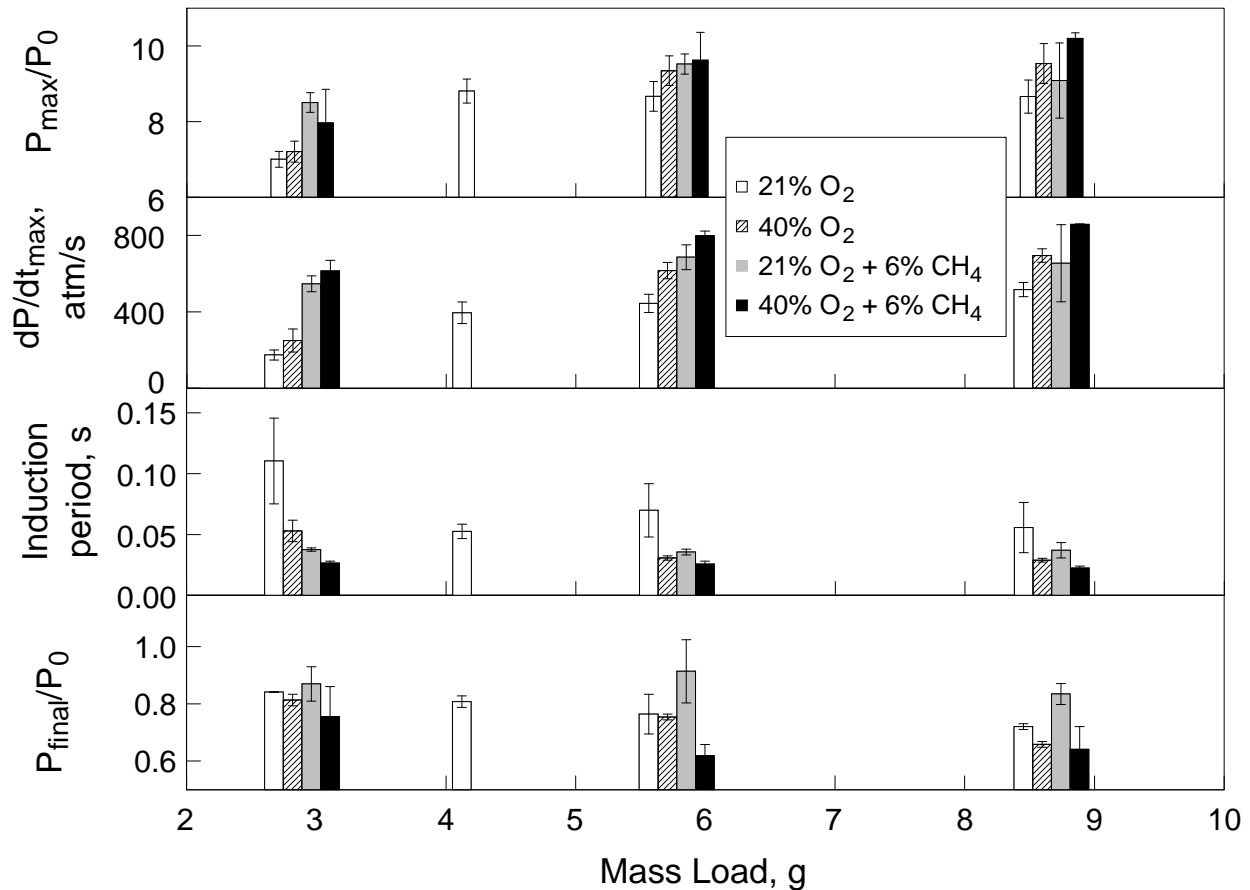


Fig. 11.3. Combustion characteristics directly obtained from the measured pressure traces in CVE experiments as a function of the mass load of powder and combustion environment (1-5 μm Al powder).

The effect of particle size on combustion is illustrated in Fig. 11.4. Finer particles produce higher combustion pressures and greater rates of pressure rise. In addition, combustion of finer particles results in a more complete reaction, based on the reduced final pressure in the vessel. It is interesting that the effect of particle size is substantial, especially for the rate of pressure rise, for a relatively minor difference in the mean particle sizes, i.e., comparing particles with 1-5 μm

nominal sizes (surface area based mean size 5.4 μm) and X-65 powder (surface area based mean size 7.4 μm).

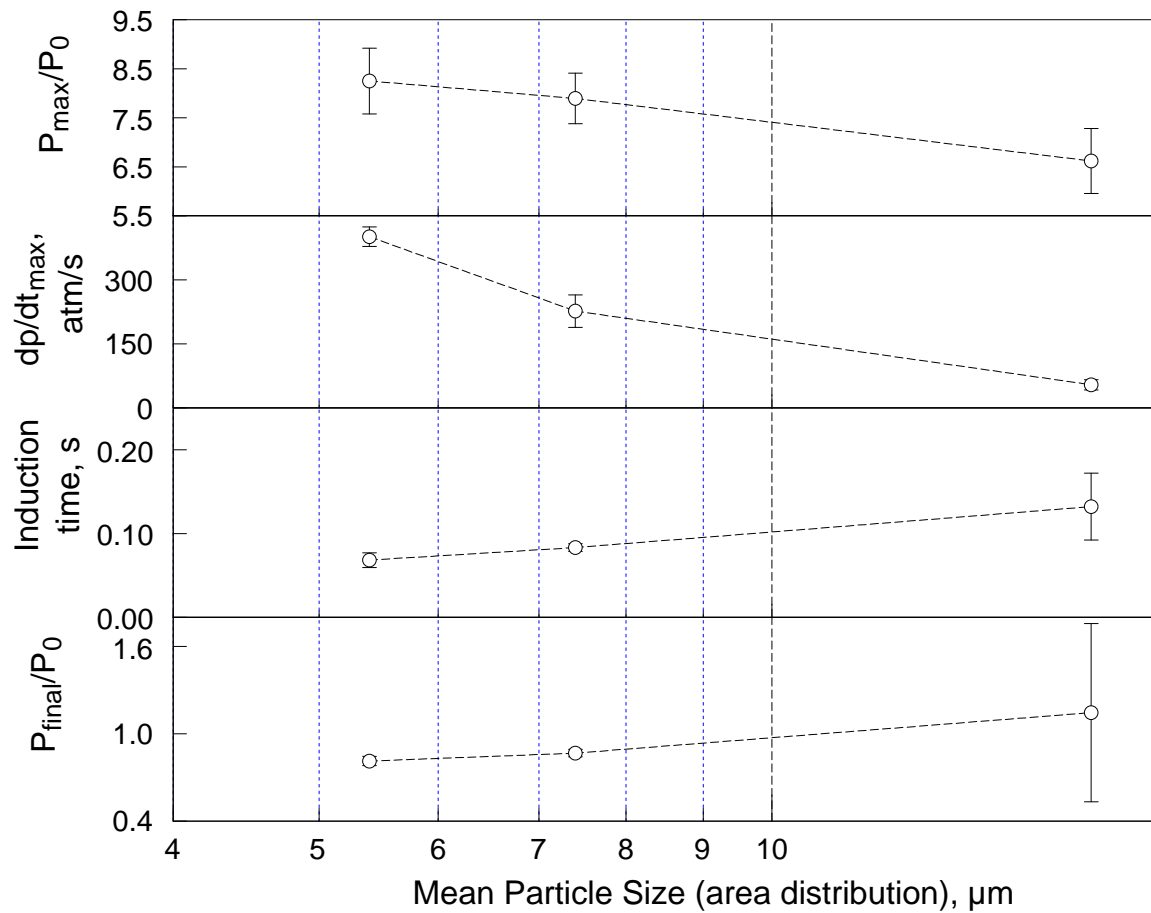


Fig. 11.4. Combustion characteristics directly obtained from the measured pressure traces in CVE experiments as a function of the particle size distribution. Results are shown for 4.65 g mass load (different Al powders) and fixed 21% O_2 , 79% N_2 environment.

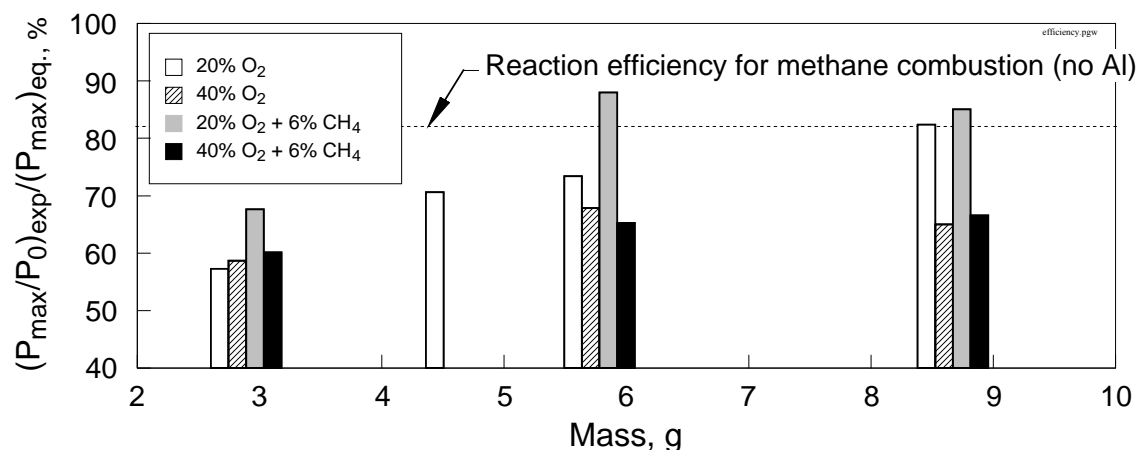


Fig. 11.5. Comparison of the experimental pressure ratios vs. the values implied by the equilibrium calculations for different environments and different mass loads of powder; experimental data for 1-5 μm Al.

The reaction efficiency can be assessed comparing the experimental combustion pressures to those predicted for respective conditions by the equilibrium calculations (cf. Table 11.1). In particular, comparing the ratios P_{max}/P_0 from the CEA calculation with the same ratio obtained from the data analysis of CVE results is indicative of how efficient the combustion was. This comparison is illustrated in Fig. 11.5. Note that for the methane only case (no Al fuel), the reaction efficiency implied by the same ratio is greater than 82 %, as shown by a dashed line in Fig. 11.5.

For the environments with 21% O₂, the efficiency is increased with addition of CH₄; the effect of CH₄ is negligible for the environments with 40 % O₂. It is also noted that for the methane-free experiments with 21% O₂, the efficiency increases with the increase in the aluminum powder load. This trend is not maintained for the mixed O₂/CH₄ environments. The highest efficiency of 88% is observed for the case with 21% O₂, 6% CH₄, and intermediate aluminum load (5.78 g.) Except for the case of 2.89 g powder load ignited in the methane-free environments, it appears that the higher oxygen concentration results in a lower efficiency.

The results presented in Fig. 11.5 can be put in context considering the effect of the predicted equilibrium flame temperature on the assessed reaction efficiency, as shown in Fig. 11.6. The trend apparent in Fig. 11.6 shows that greater reaction efficiencies are generally attained when the predicted equilibrium flame temperatures are relatively low. Indeed, it is unreasonable to expect the flame temperatures approaching 4000 K, simply because of the tremendous radiation heat losses not considered by the equilibrium calculation. Thus, the pressure ratios shown in Figs. 11.5 and 11.6 may not represent uniformly the true combustion efficiency for the experimental conditions with very different predicted adiabatic flame temperatures. Such ratios are more accurate indicators of the combustion efficiency for the cases when the adiabatic flame temperature is attainable in experiment. For the cases when a very high adiabatic flame temperature is predicted, a different equilibrium calculation would be desired, with superficially reduced flame temperature, to obtain more useful equilibrium prediction for the combustion products and the anticipated maximum pressure.

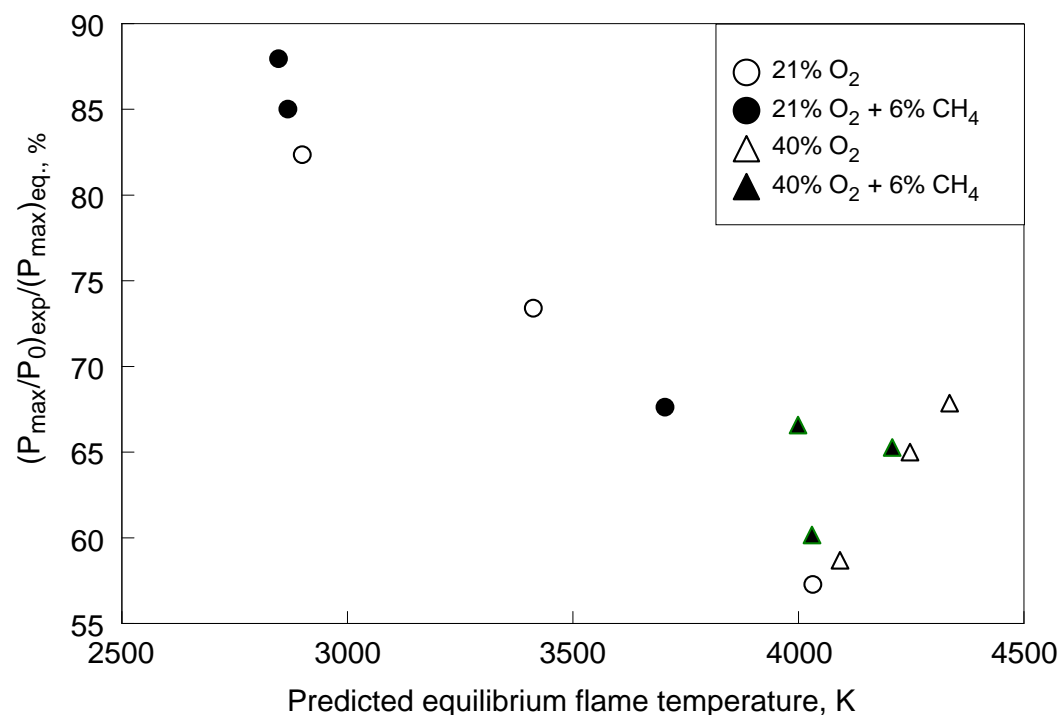


Fig. 11.6. Effect of the predicted equilibrium flame temperature on the reaction efficiency defined from the ratio of the experimental pressure ratios over the values implied by the equilibrium calculations. Presented are the same results as in Fig. 11.5. Note that each specific symbol represents one gas environment for three different aluminum mass loads.

11.5. Discussion

The double pressure peak observed for high oxygen concentrations and added methane as illustrated in Fig. 11.1 cannot be described by any simplified model for a CVE experiment and requires detailed analysis of kinetics for various reactions occurring in the system. In particular, comparison of rates of aluminum and methane combustion reactions is needed. While methane is one of the slowest reacting hydrocarbon fuels, the observation of the double pressure peak in CVE experiments may suggest that kinetic analysis of multiple reactions is also needed for accurate prediction of some of the anaerobic metal reactions in practical explosives. A simplified data processing discussed below is focused on the first rapid pressure increase observed in any experiment. The description remains meaningful with the caveat that for the experiments with O₂/CH₄ gas mixtures, the actual gas environment in which aluminum combustion occurred remains poorly defined.

Burning velocity implied by CVE experiments

A simplified model for the propagating premixed flame is used, with the following main assumptions:

1. The propagating flame is spherically symmetric.

2. The temperature field inside the combustion vessel (radius R_0) can be described by two zones: a centrally located core zone with radius r_b containing burned aerosol (or combustion products) at a constant temperature T_b , or flame temperature, surrounded by the second, shell-like zone representing the unburned aerosol placed between r_b and R_0 .

3. Combustion occurs adiabatically.

Following classic analysis [6], the model assumes a linear correlation between the mass fraction burnt and experimental pressure. It enables expressing instantaneous values of burning velocity, S_L and other flame characteristics through the measured pressure, P and rate of pressure rise, dP/dt without analyzing heat and mass transfer processes in the propagating flame. Recently, more accurate correlations between the combustion characteristics and pressure traces for constant volume explosion experiments were derived [7, 8]. However, the inaccuracies resulting from using the earlier model are small and considered to be negligible for the treatment presented here. In fact, the present treatment incurs substantially greater errors by applying a set of assumptions developed for premixed gas phase flames to the case of aluminum aerosol combustion. In particular, the flame zone is assumed to be very thin. Further, it is assumed that when the flame propagates and gas is transferred from the external unburned gas shell into the central core zone of combustion products, no changes in the number of moles of gas or in the molar mass of gas are occurring. Equilibrium calculations predicting the compositions of the combustion products show that this assumption results in an error of about 10 – 15 % for the number of moles of gas, and thus in the related gas density and temperature. This error is considered acceptable for the simplified analysis presented here but it can be corrected in the future considering the compositions of the combustion products predicted by thermodynamic equilibrium calculations. Following the simplified model [1] the burning velocity is expressed through the rate of pressure rise, dP/dt and pressure, P , as:

$$S_L = \frac{dP}{dt} \frac{R_0}{3} \frac{\rho_0}{\rho_u} \frac{1}{(P_e - P_0)} \left[1 - \left(\frac{P_0}{P} \right)^{1/\gamma} \frac{P_e - P}{P_e - P_0} \right]^{-\frac{2}{3}} \quad (11.1)$$

where P_0 is the initial pressure in the combustion vessel, P_e is the theoretically predicted maximum pressure achievable in the experiment, ρ_0 and ρ_u are densities of the flammable mixture prior to the experiment and after adiabatic compression, respectively, and $\gamma = C_p/C_v$. C_p

and C_v are specific heats of the unburned gas taken at the constant pressure and volume, respectively. For diatomic gases, such as N_2 and O_2 representing the bulk of the unburned gas mixture, $\gamma = 7/5$, so the value of $7/5$ was used neglecting the change in γ due to the addition of methane. The values of P_e corresponding to different conditions are calculated using NASA CEA code by [5] (see Table 11.1). The ratio of densities of the flammable mixture before and after adiabatic compression is calculated as:

$$\frac{\rho_0}{\rho_u} = \frac{P_0}{P} \cdot \frac{T_u}{T_0} \quad (11.2)$$

Where the temperature of the adiabatically compressed unburned gas T_u is calculated as

$$T_u = T_0 \left(\frac{P}{P_0} \right)^{\frac{\gamma-1}{\gamma}} \quad (11.3)$$

In order to interpret various values of the burning velocity observed during a single run, it is also interesting to track down the position of the flame front. The radius of the propagating flame can also be expressed using the measured pressure [1] as:

$$r_b = R_0 \left[1 - \left(\frac{P_e - P}{P_e - P_0} \right) \left(\frac{P_0}{P} \right)^{1/\gamma} \right]^{1/3} \quad (11.4)$$

A representative example of the burning velocity calculated for a CVE experiment is shown in Fig. 11.7. Also shown are a respective pressure trace, a trace of the rate of pressure rise, dP/dt , and values of T_u and r_b varied during the run.

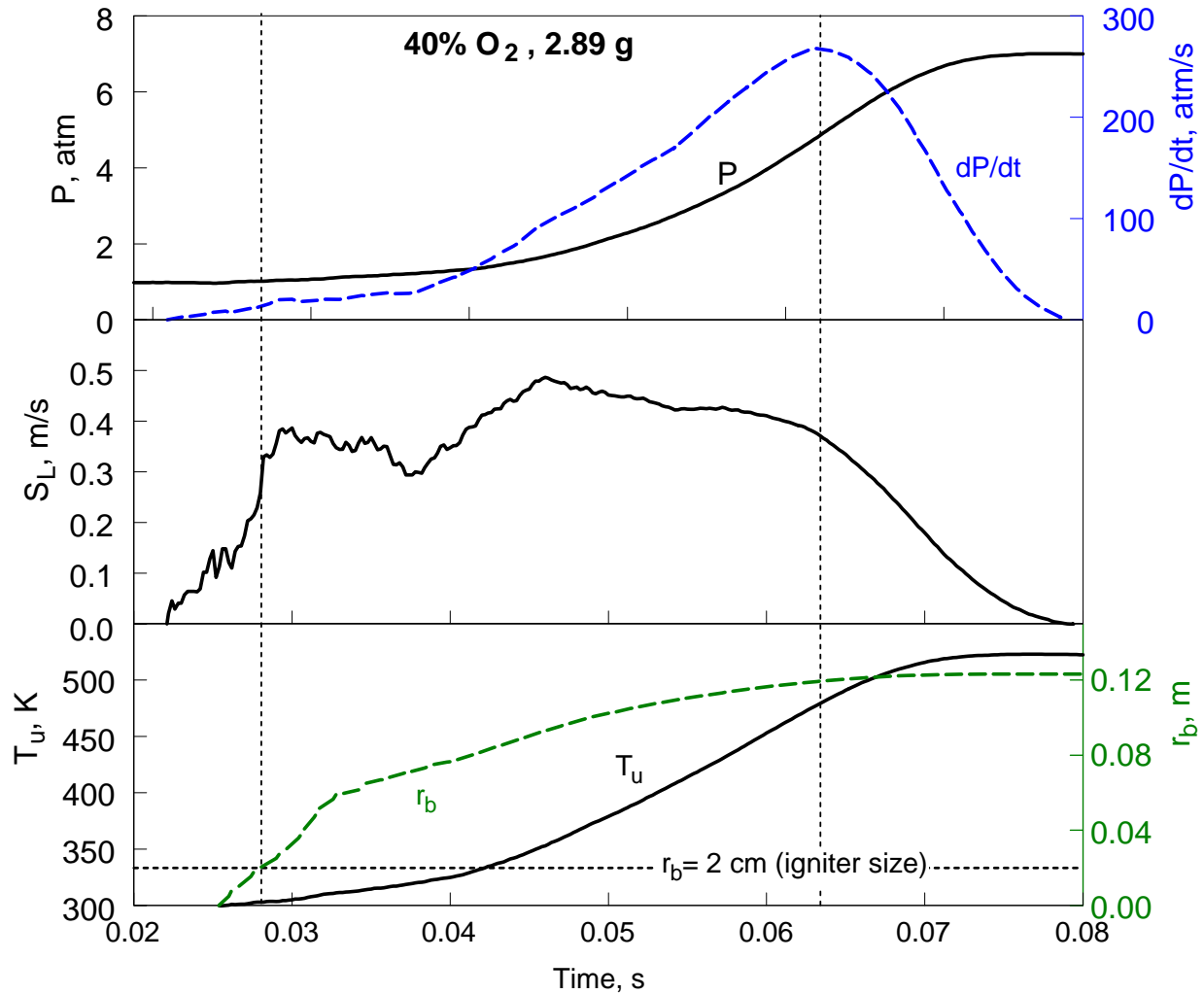


Fig. 11.7. Pressure traces and inferred characteristics of a CVE experiment. Rate of pressure rise, burning velocity, radius of the expanding flame, and the temperature of the adiabatically compressed unburned mixture are shown.

Two vertical dashed lines in Fig. 11.7 select the time period between them for which the most meaningful interpretation of the experimental results can be obtained. The first dashed line corresponds to the instant the flame radius calculated using Eq. (11.4) exceeds 2 cm, which is the size of the igniter wire. Once the flame exceeds this dimension, it can be expected that a self-

sustaining flame developed. The second vertical line marks the instant when the maximum rate of pressure rise is observed. Reduction in the rate of pressure rise in a CVE experiment suggests that a quenching effect of the vessel walls becomes significant. It is interesting that the burning velocity calculated using Eq. (11.1) is relatively stable between the vertical lines, varying from 0.3 to 0.5 m/s for this specific example. It becomes even more stable after reaching its maximum value and it decreases substantially only after dP/dt_{max} is observed. It is also interesting to note that the temperature of the adiabatically compressed unburned gas is increased by about 200 K during the experiment.

Note that use of the theoretically predicted maximum pressure achievable in the experiment in Eq. (11.1) does not take into account that part of the fuel is never combusted, so that the burning velocity obtained is somewhat underestimated. In fact, based on the comparison of the measured and predicted pressures for the case illustrated in Fig. 11.7, one concludes that the combustion completeness is less than 60. The unburned metal is compressed in a shell-like volume near the vessel wall and is likely quenched by heat losses to the wall. A small part of the powder load might also have been trapped in the powder reservoir. To account for such losses, which cannot be avoided in experiments, a higher limit for the burning velocity can be assessed using Eq. (11.1) with the P_e value replaced with the maximum experimental pressure. It is likely that the actual burning velocities are between these two limiting values.

Thickness of the flame front

Thickness of the flame front cannot be estimated without making an additional assumption for the characteristic particle burn time, τ . This time can be roughly assessed using one of several correlations available in the literature for aluminum particles, e.g., [9 – 11]. The flame front is defined as a layer sandwiched between the unburned mixture shell and burnt gas core, within which fuel particles are fully consumed. The unburned mixture enters the flame front with the speed S_L . The flame front could be further separated on two areas: preheat zone, where the mixture temperature increases rapidly from the temperature of the unburned aerosol, T_u , to the aerosol ignition temperature, T_i ; and combustion zone where the actual combustion of aluminum particles takes place, and where the temperature increases up to T_b . Neglecting the change in mass of the gas phase passing through the flame, it is easy to see that due to the temperature driven gas expansion, the speed of aluminum particles in the frame of reference attached to the flame front, scales with the increased mixture temperature. Therefore, when temperature increases from the temperature of the unburned aerosol, T_u , to an arbitrary value T^* , ($T_u < T^* < T_b$), the relative gas velocity increases from S_L to S^* :

$$S^* = S_L \frac{T^*}{T_u} \quad (11.5)$$

Recognizing that during the particle burn time, the particle moves within the flame front from the location where the temperature equals to T_i to the location where temperature reaches T_b , the average particle velocity (S_p) during its combustion can be estimated as:

$$S_p = S_L \frac{T_i + T_b}{2T_u} \quad (11.6)$$

Respectively, the thickness of the combustion zone (δ) in the flame front (or the thickness of the flame) can be estimated as a product of this velocity and characteristic particle burn time, τ , as:

$$\delta = \tau S_L \frac{T_b + T_i}{2T_u} \quad (11.7)$$

Plugging in an empirical expression for the Al particle burn time (in ms) [10],

$$\tau = 310 \cdot d \quad (11.8)$$

where d is the particle diameter (in mm), we obtain an estimate for the flame thickness. The characteristic ignition and combustion temperatures employed for this estimates were $T_i=1900$ K and $T_b=3000$ K. The ignition temperature was evaluated based on the summary of experimental data presented in ref. [12] and the combustion temperature was from recent measurements [13, 14].

The resulting flame thickness is shown in Fig. 11.8 for the experiment presented in Fig. 11.7. Note that the surface based mean diameter was used in this calculation. The vertical dashed lines mark the same instants as marked in Fig. 11.7. Because the change in T_u is minor, the changes in the estimated flame thickness directly reflect predicted changes in S_L , while the value of δ varies from 3.8 to 5.5 mm. Although it is certainly much thicker than a typical gas-phase premixed flame, this flame thickness is still substantially less than the diameter of the combustion vessel, partially justifying the thin-flame assumption required for derivation of Eqs. (11.1) and (11.4).

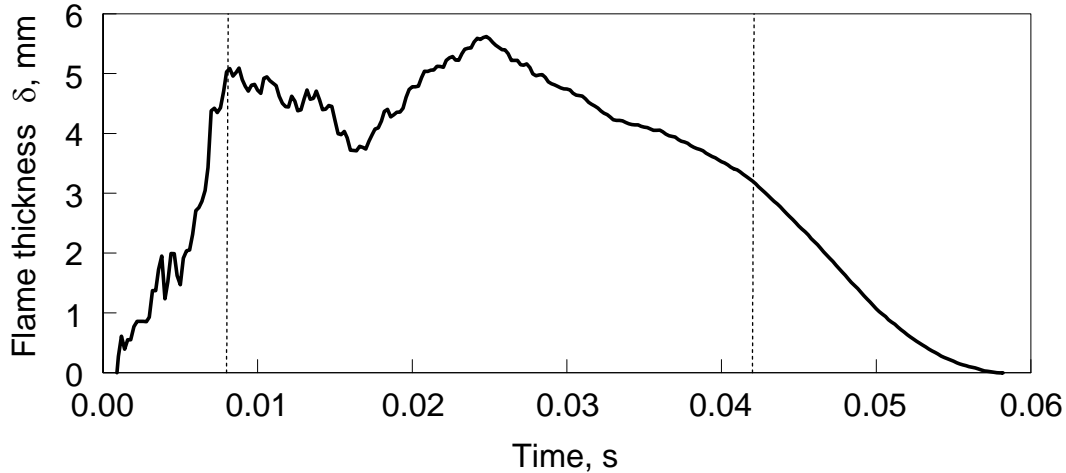


Fig. 11.8. Flame thickness as a function of time. The data processed for the run presented in Fig. 11.7.

Effect of gas environment and powder mass load on the burning velocity and flame thickness

Data collected for all CVE experiments were processed as illustrated in Figs. 11.7 and 11.8. Resulting burning velocities and flame thicknesses were averaged between the characteristic instants illustrated in Figs. 11.7 and 11.8 by vertical lines to obtain representative values for various CVE experiment parameters. These average values are shown in Fig. 11.9 where the error bars represent the standard deviation for the values obtained from the repeat runs.

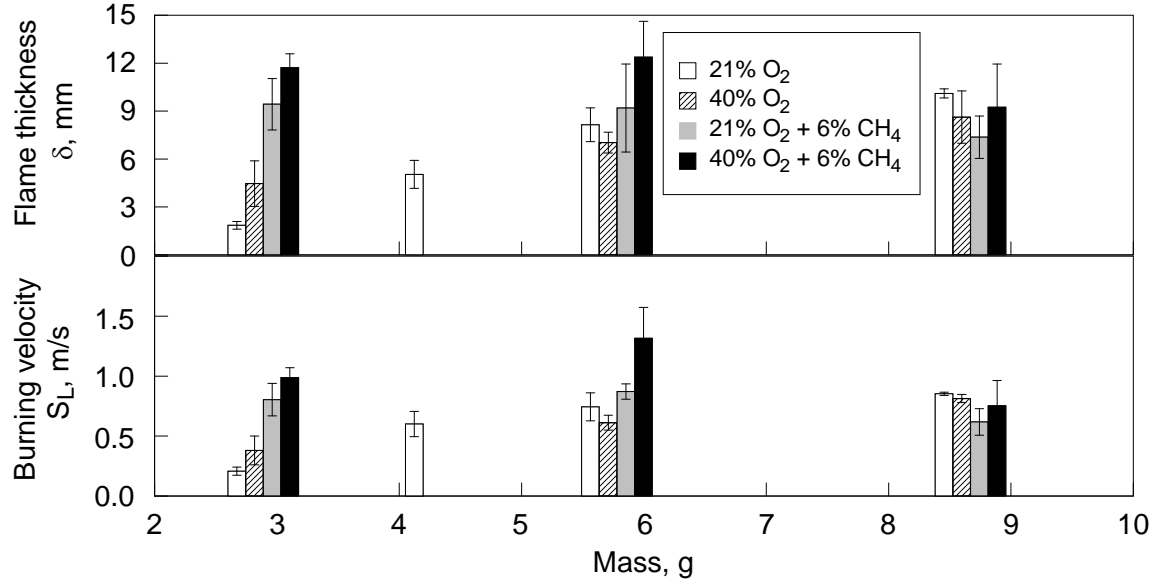


Fig. 11.9. Average values of flame thickness and burning velocity for various powder loads burned in CVE experiments in different gas environments.

Several interesting trends are observed from the obtained burning velocity values. For the methane-free experiments, the burning velocity increases with the increased mass load. The velocity at 21 % O₂ is less than that at 40 % for the lowest mass load, while this situation reverses as the mass loads increase. Note that at higher mass loads and higher oxygen concentrations, the discrepancy between the predicted in equilibrium (and used in Eq. (11.1)) maximum pressure and the actual combustion pressure observed in the experiments increases. Therefore, as explained above, the burning velocity obtained from Eq. (11.1) is more and more underestimated. Consistently correcting the maximum pressure in Eq. (11.1) would likely result in higher burning velocities at higher oxygen concentrations for all mass loads used in experiments.

For the experiments with added methane, the effect of aluminum mass load is even less pronounced. Higher burning velocities are consistently observed for higher oxygen concentration, with the most substantial difference in S_L as a function of oxygen concentration observed at the mass load of 5.78 g.

Burning velocities obtained here can be compared to the flame speeds reported for similar aluminum particles elsewhere [15, 16]. Recently, a model for flame propagation in aluminum aerosol was presented and a summary of the experimental data was given in ref. [15]. For aluminum burning in air, the burning velocities were not predicted to vary substantially. Equivalence ratios in the range of 0.7-1 and were shown to produce flame speeds of 0.3 – 0.4 m/s for particles with dimensions of 5 – 7 μm , similar to the particles used in this study. Flame

speeds in the range of 0.2-0.8 m/s, essentially matching those presented in Fig. 11.9, were measured in ref. [16] for aluminum aerosol burning in oxygen/nitrogen mixtures with oxygen concentrations varied from 10 to 60%. No comparable measurements have been reported in environments comprising the mixtures of oxygen, nitrogen, and methane.

The predicted flame thickness simply mirrors the values of the calculated S_L (with a small correction due to changes in T_u) as evident from Eq. (11.7). The flame thickness varies from about 2.5 to 12 mm for the slowest and fastest flames, respectively. This analysis does not take into account possible variations in the particle burn time as a function of the powder load or the environment.

Heat transfer in the flame

Considering obtained values of the flame thickness and used characteristic temperatures T_i and T_b , it becomes possible to roughly evaluate the role of various heat transfer processes in the propagating flame. Assuming the quasi-steady flame propagation and a linear temperature gradient throughout the flame zone, the conductive heat flux (\dot{q}_C) within the flame zone can be estimated as

$$\dot{q}_C = k \frac{T_b - T_i}{\delta} \quad (11.9)$$

where k is the thermal conductivity of the gas mixture. Note that the heat flux determined from Eq. (9) is not equal to the conductive heat flux from the flame to unburned gas. The radiation heat flux (\dot{q}_R) from the developed part of the flame with temperature T_b to area where metal particles ignite, with characteristic temperature T_i , can be estimated as

$$\dot{q}_R = \sigma \varepsilon (T_b^4 - T_i^4) \quad (11.10)$$

where σ is Stefan-Boltzmann constant and ε is the effective flame emissivity. Equation (11.10) assumes that the various parts of flame zone absorb radiation as a black body.

It was observed that the conduction heat flux calculated from Eq. (11.9) is four to five orders of magnitude smaller than the right hand side of Eq. (11.10). Thus, radiation is the dominant heat transfer mechanism within the flame zone. This estimate also shows that radiation must be included in the heat transfer model for energy exchange between the flame zone and unburned mixture. Unfortunately, development of the respective heat transfer model requires assessing a number of poorly known flame characteristics, and it is outside the scope of the present article. Specifically, the emissivity of the flame is not known, but is expected to be affected substantially by aluminum mass load and by the oxidizing environment, resulting in different types of condensed products formed. Further, the thickness of the layer in which the gas temperature decreases from T_i to the temperature of the unburned mixture T_u is not known, and it is difficult to evaluate without taking into account both convective and radiation modes of heat transfer. Finally, the optical thickness of the preheat zone is poorly characterized, so it is unclear what portion of the flame's emission is absorbed there and which portion penetrates further into (or through) the unburned aerosol. It is proposed that future theoretical analysis might be useful to further elucidate the heat transfer model for the burning metal aerosol.

11.6. Conclusions

A set of experiments on aluminum powder combustion in a constant volume explosion chamber showed that at increased oxygen concentrations, the kinetics of Al combustion may be faster than that of gas phase combustion of methane. This observation may be important for analysis of metal combustion at elevated pressures and/or increased partial pressures of oxidizers. In particular, it indicates that under certain conditions, a common assumption that aluminum particle combustion is a rate-limiting process in many aluminized energetic formulations should be questioned. It is suggested that future experimental studies of the flame structure in the combustion systems containing both solid metal and gaseous hydrocarbon fuels are of significant interest.

A simplified flame propagation model for CVE experiments applied for aerosolized solid fuel enables processing the experimental pressure curves to recover the burning velocity. A period of nearly constant burning velocity during the explosion is observed, validating the quasi-steady treatment of the flame propagation assumed in the model. The burning velocities measured in this work compare well with those reported earlier for similar size Al powders. Making additional assumptions regarding the particle burn time, ignition and combustion temperatures, allows one estimating the thickness of the flame front. This thickness varies from 2.5 to 12 mm and always remains much smaller than the diameter of the combustion vessel.

It is observed that addition of methane always results in reduced induction times and increased experimental pressures and rates of pressure rise for identical mass loads and oxygen concentrations. Also, adding methane results in increased burning velocities for Al aerosol for lower powder loads. This effect diminishes for higher powder mass loads (or very fuel rich conditions). The results further suggest that the adding oxygen always results in higher rates of pressure rise, shorter induction periods, and shorter aerosol combustion times.

Laminar conductive heat transfer cannot explain the experimentally observed rates of flame propagation in aluminum aerosols. Radiation heat transfer must be included in the model. In fact, radiation heat transfer may be the predominant mechanism for the energy transfer from the flame to the unburned heterogeneous mixture.

11.7. References

1. Bradley, D., Mitcheson, A. (1976) Mathematical solutions for explosions in spherical vessels. *Combustion and Flame* **26**(C), 201-217
2. Eapen B. Z., Hoffmann V. K., Schoenitz M., Dreizin E. L. (2004) Combustion of Aerosolized Spherical Aluminum Powders and Flakes in Air. *Combustion Science and Technology*, **176**(7), 1055-1069
3. Schoenitz, M., Dreizin, E.L., and Shtessel, E. (2003) Constant Volume Explosions of Aerosols of Metallic Mechanical Alloys and Powder Blends. *Journal of Propulsion and Power*, **19**(3), 405-412

4. Trunov, M.A., Hoffmann, V.K., Schoenitz, M., Dreizin E.L. (2008) Combustion of Boron-Titanium Nanocomposite Powders in Different Environments. *Journal of Propulsion and Power* **24**(2), 184-191
5. McBride, B. J. and Gordon, S., (1996), *NASA RP 1311*, Computer Program for Calculation of Complex Chemical Equilibrium Compositions and Applications II. Users Manual and Program Description.
6. Lewis B., von Elbe G. (1961) Combustion, flames and explosions of gases, 2nd edition, Academic Press New York.
7. Luijten, C.C.M., Doosje, E., van Oijen, J.A., de Goey, L.P.H. (2009a) Impact of dissociation and end pressure on determination of laminar burning velocities in constant volume combustion. *International Journal of Thermal Sciences* **48**(6), 1206-1212
8. Luijten C.C.M., Doosje E., de Goey L.P.H. (2009b) Accurate analytical models for fractional pressure rise in constant volume combustion. *International Journal of thermal Sciences*, **48**(6), 1213-1222
9. Beckstead, M.W. (2005) Correlating aluminum burning times. *Combustion, Explosion and Shock Waves* **41**(5), 533-546
10. Shoshin, Y.L., Dreizin, E.L. (2006) Particle combustion rates for mechanically alloyed Al-Ti and aluminum powders burning in air. *Combustion and Flame* **145**(4), 714-722
11. Lynch, P., Krier, H., Glumac, N. (2009) A correlation for burn time of aluminum particles in the transition regime. *Proceedings of the Combustion Institute* **32**(II), 1887-1893
12. Trunov, M.A., Schoenitz, M., and Dreizin, E.L. (2005) Ignition of Aluminum Powders under Different Experimental Conditions. *Propellants Explosives and Pyrotechnics*, **40**(1), 36-43
13. Poletaev, N.I., Florko, A.V. (2007) Radiative characteristics of an aluminum dust flame. Condensed phase. *Combustion, Explosion and Shock Waves* **43**(4), 414-422
14. Poletaev, N.I., Florko, A.V. (2008) Spectral studies of the gas component of an aluminum dust flame. *Combustion, Explosion and Shock Waves* **44**(4), 437-443
15. Huang, Y., Risha, G.A., Yang, V., Yetter, R.A. (2009) Effect of particle size on combustion of aluminum particle dust in air. *Combustion and Flame* **156**(1), 5-13
16. Shoshin, Y.L., Dreizin, E.L. (2004) Laminar Lifted Flame Speed Measurements for Aerosols of Metals and Mechanical Alloys. *AIAA Journal*, **42**(7), 1416-1426